

Towards the development of a systems pharmacology model for vitiligo

by

Pooja Dnyane
10BB18A26028

A thesis submitted to the
Academy of Scientific & Innovative Research
for the award of the degree of
DOCTOR OF PHILOSOPHY
in
SCIENCE

Under the supervision of
Dr. Chetan Gadgil



CSIR-National Chemical Laboratory, Pune.

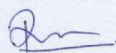


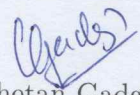
Academy of Scientific and Innovative Research
AcSIR Headquarters, CSIR-HRDC campus
Sector 19, Kamla Nehru Nagar,
Ghaziabad, U.P. – 201 002, India.

May 2023

CERTIFICATE

This is to certify that the work incorporated in this Ph.D. thesis entitled, "*Towards the development of a systems pharmacology model for vitiligo*" submitted by *Pooja Avinash Dnyane* to the Academy of Scientific and Innovative Research (AcSIR) in fulfillment of the requirements for the award of the Degree of *Doctor of Philosophy in Science*, embodies original research work carried out by the student. We, further certify that this work has not been submitted to any other University or Institution in part or full for the award of any degree or diploma. Research material(s) obtained from another source(s), illustration(s), figure(s), table(s) etc., used in the thesis from other source(s), have also been duly cited and acknowledged.


Pooja Dnyane
(Student)


Dr. Chetan Gadgil
(Supervisor)

STATEMENTS OF ACADEMIC INTEGRITY

I Pooja Dnyane, a Ph.D. student of the Academy of Scientific and Innovative Research (AcSIR) with Registration No.10BBA1826028 hereby undertake that, the thesis entitled "*Towards the development of a systems pharmacology model for vitiligo*" has been prepared by me and that the document reports original work carried out by me and is free of any plagiarism in compliance with the UGC Regulations on "*Promotion of Academic Integrity and Prevention of Plagiarism in Higher Educational Institutions (2018)*" and the CSIR Guidelines for "*Ethics in Research and in Governance (2020)*".

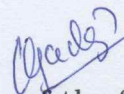


Signature of the Student

Date: 27/05/2023

Place: Pune.

It is hereby certified that the work done by the student, under my/our supervision, is plagiarism-free in accordance with the UGC Regulations on "*Promotion of Academic Integrity and Prevention of Plagiarism in Higher Educational Institutions (2018)*" and the CSIR Guidelines for "*Ethics in Research and in Governance (2020)*".



Signature of the Supervisor

Name: Dr. Chetan Gadgil

Date: 27/5/23

Place: Pune.

Acknowledgement

I am grateful to everyone who has supported and guided me throughout my Ph.D. First and foremost, I would like to express my sincere gratitude to my Ph.D. advisor, Dr. Chetan Gadgil, for his constant support, guidance, and patience during my doctorate journey. I am grateful to him for providing me with several opportunities to interact with experimental labs and participate in conferences. The discussions we have had over the years have helped me to be self-critical and think and work independently. I'm also thankful to him for listening to me and supporting me through tough times. I couldn't have asked for a better advisor and mentor for my Ph.D. studies.

I am also grateful to the members of my Doctoral Committee; Dr. Sarkar, Dr. Narlikar and Dr. Ajithkumar for reviewing my work and for their valuable comments. I would like to acknowledge and thank all the collaborators and students from Dr. Gokhale's labs at IGIB and NII in Delhi. I thank Dr. Natrajan (JNU, Delhi) and Dr. Ganju (Ahhamune Biosciences Pvt. Ltd.) for patiently listening to my presentation and giving valuable insights into the disease model.

I am deeply grateful to the former members of our lab, Sucheta, Shraddha, Priyanka, Dimpal, and Bharat, who warmly welcomed me into the lab when I initially joined as a Project Assistant. I express my gratitude to Shraddha for her assistance with my initial work and manuscript. Furthermore, I want to thank Anushua for her unwavering support. She has been an invaluable companion throughout my Ph.D. journey. I will always cherish our scientific and informal discussions. I would also like to express my gratitude to the current members of our lab, Ashley, Indrani and Aparna for a supportive work environment. Special thanks to Anuja and Shikha for helping me when I was unwell and otherwise.

I would like to extend my gratitude to all the staff members from the students' office, accounts, bills section, and C & P section as well as Mr. Raheja and Mr. Palash for their administrative support. My sincere thanks go to CSIR-NCL for providing me with a research platform and to CSIR for the research fellowship. I am grateful to the Directors and department HODs at NCL for giving me the opportunity to work at NCL.

I express my gratitude to Aditi and Gajanan for always having my back. I thank them for listening to me and helping me during tough times. Finally, I am immensely grateful to my parents for their constant support and belief in me. They have continuously encouraged me to pursue my passions and have been supportive of all my decisions.

Abstract

The human skin is a complex organ made up of a large number of different cell types which proliferate, differentiate, get eliminated, and interact with each other in a highly coordinated manner to maintain homeostasis of skin thickness, composition, and pigmentation. When skin is exposed to UV radiation, keratinocytes excessively synthesize biochemical substances such as α -MSH, endothelin and prostaglandin. These keratinocyte-derived factors are transported to melanocytes in a paracrine manner and induce activation of the transcription factor MITF through a series of events. MITF activates the expression of key melanin-forming genes including genes for tyrosinase family enzymes. Tyrosinase converts tyrosine to dihydroxyphenylalanine (DOPA). Eventually, DOPA is polymerized into Eumelanin and Pheomelanin. This process of skin pigment synthesis is called Melanogenesis. The synthesized pigment is packed into melanosome and transported to nearby keratinocyte cytoplasm via dendrites where they are strategically placed over nuclei to protect DNA.

An imbalance in molecular events that regulate melanogenesis could result in a skin depigmentation disorder such as vitiligo. According to recent data, the worldwide occurrence of vitiligo is estimated to be between 1-2%. However, there are differences in the prevalence of vitiligo according to geographical regions, with the highest prevalence reported in India (8.8%), Mexico (2.64%), and Japan (1.68%). The disorder can be psychologically and emotionally damaging. Unfortunately, it is incurable and the underlying pathogenesis mechanism is still unclear. The available therapeutic options for vitiligo are unsatisfactory for many patients as they are complex, time-consuming and ineffective. To develop optimal treatment protocols, an integrated understanding of drug distribution kinetics and disease kinetics is required. This implies understanding the molecular network underlying melanogenesis and the effects leading to loss of pigmentation. To this end, we developed models, and adapted existing models, at molecular, cellular, and organ level to achieve an integrated perspective on skin depigmentation and treatment.

The first part of this thesis focuses on understanding the transcriptional regulation and molecular rewiring underlying the process of pigmentation. We used the B16 cells autonomous pigmentation model. This model effectively simulates the transition of cells from a depigmented state to a pigmented state within a span of six days. Through the analysis of the time-course expression data, we have identified differentially expressed genes during pigmentation. The analysis has highlighted the involvement of the fatty acid metabolism pathway in melanogenesis. Results indicate that elevated levels of MITF play a crucial role in triggering the uptake of glucose, which in turn supports the biogenesis of melanosomes - an organelle responsible for melanin production. As the pigmentation progresses, upregulation of genes associated with fatty acid synthesis, metabolism, and oxidation, is observed leading to the accumulation of lipid droplets and an increase in fatty acid oxidation facilitated by mitochondrial respiration.

The second part of the thesis involves understanding the keratinocyte-melanocyte interaction and metabolism. A 265-node Boolean model for melanogenesis was developed and compared to

a smaller existing model. The new model encompasses more comprehensive information about molecular interactions and incorporates components that were previously missing. Analysis revealed that the majority of common nodes in both models exhibit similar responses to UV stimulation. Furthermore, sensitive nodes with significant impacts on melanin and BCL2, the output nodes, were identified. In order to analyze the network, two new dynamic function perturbation methods were formulated, which successfully identified previously unreported sensitive nodes. In summary, the larger model presented in this study serves as a valuable tool for simulating and analyzing the intricate interplay between keratinocytes and melanocytes during melanogenesis.

The third and last part of this thesis is about the formulation of the first disease model for vitiligo. We developed a model that incorporates multiple mechanisms responsible for melanocyte death in vitiligo, along with their correlation to clinical outcomes. Results show a correlation between increasing levels of reactive oxygen species (ROS) and the gradual increase in vitiligo severity, supporting prior studies on the role of oxidative stress in vitiligo pathogenesis. Furthermore, the effect of stress on different skin cells, immune cells, and cytokines is investigated. According to the findings, increased ROS levels had a negative effect on keratinocyte and melanocyte levels, with melanocyte levels declining earlier than keratinocytes due to lower melanin levels. The simulation also reveals changes in the dynamics of dendritic cells (DC), T cells, and cytokines in response to stress. Moreover, we also simulated drug effects through parameter variations. Simulations demonstrate that increasing the formation rate of melanocytes is more effective in reducing the Vitiligo Area Scoring Index (VASI) compared to increasing the rate of Regulatory T-cell differentiation. This suggests that drugs targeting melanocytes may be more successful in vitiligo treatment than immune cell modulators. Overall, the disease model outlined in this part provides a framework for understanding vitiligo pathogenesis and holds the potential for developing more effective treatment strategies.

There are very few models even at one scale, and none to my knowledge spanning scales in the public domain. Through this work, we have tried to provide a qualitative interpretation of disease dynamics at various levels. As a step further, the disease model can be extended to a quantitative system pharmacology (QSP) model by including a physiology-based pharmacokinetic (PBPK) model. We believe that this combination of the skin disease model and the PBPK model will serve as a unique framework for checking the effect of multiple drugs used in treating vitiligo and optimizing treatment protocols.

List of Tables

3.1	Types of interactions and their distribution in the network	33
3.2	Individual interactions for MC1R_melan as defined by (Raghunath et al., 2015)	33
3.3	Individual interactions for NFkB1_kerat as defined by (Raghunath et al., 2015)	34
3.4	Individual interactions for CREB1_melan as defined by (Raghunath et al., 2015)	34
3.5	Sensitive nodes identified in both models	44
3.6	Perturbation Impact on Melanin, BCL2M, and BCL2K Activities: Node Analysis and Sensitivity	47
3.7	Sensitivity Comparison: Nodes Identified by Function Perturbation and Transient Perturbation/Gene Mutation Methods	49
4.1	Steady state level of species at healthy state	67
4.2	Parameter description and values	69
A.1	Parameter definitions and values	85
A.2	Various interaction scenarios and their corresponding regulatory parameter values used during simulation	85

List of Figures

1.1	Skin’s epidermis and dermis	3
1.2	Metabolic synthesis of melanin in melanosome	5
1.3	Core molecular pathways regulating melanin production in melanocytes	6
2.1	B16 cell-autonomous pigmentation model (Natarajan et al., 2014)	19
2.2	New setup of B16 cells resulting in the transition of melanocyte from depigmented (day 0) to pigmented state (day 6) followed by sequencing	20
2.3	Differentially expressed genes in the melanogenesis pathway.	23
2.4	KEGG pathway enrichment analysis for differentially expressed genes.	24
3.1	Methods of function perturbation with an example	37
3.2	Qualitative, individual input–output relationships in the Boolean model of melanogenesis network	39
3.3	The qualitative relationships between individual inputs-outputs (remaining 7 outputs) in the melanogenesis network	40
3.4	Comparing the effect of UV radiation on the few selected nodes in the existing model and the newly developed Boolean model	41
3.5	Comparing the effect of UV radiation on the few negatively correlated nodes in the existing model and the newly developed Boolean model	42
3.6	Distribution of coefficient correlation (R) values in the new model.	43
3.7	Effect of function perturbation of selected nodes on UVB-induced skin pigmentation and BCL-2 expressions	48
4.1	Illustration of the development of chemical-induced vitiligo	58
4.2	Neuronal hypothesis for segmental vitiligo (van Geel et al., 2012)	59
4.3	Different pathways triggered by oxidative stress in vitiligo	61
4.4	Autoimmune theory of vitiligo showing both cell-mediated and humoral autoimmune responses Laddha et al. (2013)	62
4.5	A systems model for vitiligo	65
4.6	Change in Vitiligo Area Severity Index (VASI) in response to increasing ROS for different days of exposure	70
4.7	Change in the level of skin cells in response to increasing ROS for different days of exposure	71
4.8	Change in the level of immune cells and cytokines in response to increasing ROS for different days of exposure	72
4.9	Changes in VASI during drug treatment	73
5.1	Concept diagram of Physiology Based Pharmacokinetic Model for Vitiligo	81

A.1	Schematic presentation of drug-drug interaction model	84
A.2	Bifurcation Diagram and Oscillatory Behavior	86
A.3	Bifurcation Diagram and Bistability	87
A.4	Bistability and Periodicity: Codimension-two Bifurcation Plots for k_{11}, k_{21} with Varying k_{12}	88
A.5	Oscillating Concentrations: Codimension-two Bifurcation Plots for k_{11}, k_{21} with Varying k_{12}	89
A.6	Bistability and Oscillations: Codimension-two Bifurcation Plots for $k_{11}, k_{21}, k_{12}, k_{22}$, and $\widehat{k_{in}}$	90

Abbreviations

ACTH	Adrenocorticotropic hormone
ADCY4	Adenylate Cyclase 4
AKT	RAC-alpha serine/threonine-protein kinase
ASK	Apoptosis signal-regulating kinase
ASK1	Apoptosis signal-regulating kinase 1
BCL2	B-cell lymphoma 2
CASP3	Caspase-3
CI	cubitus interrupters
CREB1	cAMP response element-binding protein 1
CRT	Calreticulin
CXCL	Chemokine (C-X-C motif) ligand
DDI	Drug-drug interaction
DEG	Differentially expressed genes
DFFA	DNA fragmentation factor subunit alpha
DHICA	2-carboxy-5,6-dihydroxyindole
DHI	5,6-dihydroxyindole
DOPA	L-3,4-dihydroxyphenylalanine
EGFR	Epidermal growth factor receptor
EN	Engrailed
ERK	Extracellular signal-regulated kinases
ET1	Endothelin 1
ETR	Ethylene receptor
FAS	Fas Cell Surface Death Receptor
HH	hedgehog
HMGB	High mobility group box
HRAS	GTPase HRas, from "Harvey Rat sarcoma virus"
IFN γ	Interferon gamma
IKBKA	Nuclear factor of kappa light polypeptide gene enhancer in B-cells inhibitor, alpha
IL1	Interleukins 1
IP3	Inositol trisphosphate
JNK	c-Jun N-terminal kinases
MAPK1	Mitogen-Activated Protein Kinase 1
MC1R	Melanocortin 1 Receptor
MITF	Microphthalmia-associated transcription factor
MKK	Mitogen-Activated Protein Kinase
NFKB1	Nuclear Factor Kappa B Subunit 1

NGF	Nerve growth factor
NPY	Neuropeptide Y
PASI	Psoriasis area severity index
PDK1	Pyruvate dehydrogenase kinase 1
PI3	Peptidase Inhibitor 3
PI3K	Phosphoinositide 3-kinases
PKC	Protein kinase
PLC	Phospholipase C
PMEL	Premelanosome protein
PRKACA	Protein Kinase C Alpha
PRKG	Protein Kinase CGMP
PTPN	Protein tyrosine phosphatase non-receptor
PTC	patched
RAF	c-Raf proto-oncogene serine/threonine-protein kinase
ROS	Reactive Oxygen Species
RPS6KA1	Ribosomal Protein S6 Kinase A1
RYR1	Ryanodine receptor 1
SMO	Smoothed
SOS	Son of Sevenless gene set
GRB2	Growth Factor Receptor Bound Protein 2
SHC1	SHC Adaptor Protein 1
TNF	Tumor necrosis factor
TP53	Tumor Protein P53
TYR	Tyrosinase
TYRP	Tyrosinase related protein
USF	Upstream Stimulatory Factor
UV	Ultraviolet radiarion
VASI	Vitiligo Area Severity Index
WT	Wild Type
cAMP	Cyclic adenosine monophosphate
4HNE	4-Hydroxynonenal Protein
α -MSH	alpha-Melanocyte-stimulating-hormone

Contents

Certificate	iii
Statement Of Academic Integrity	v
Acknowledgement	vii
Abstract	ix
List of Tables	xi
List of Figures	xiii
List of Abbreviations	xv
1 Introduction	1
1.1 The human skin: architecture and components	2
1.1.1 Epidermis	2
1.1.2 Melanocyte and melanosomes	4
1.1.3 Melanin	4
1.2 Signaling pathways regulating melanin synthesis	5
1.3 Human skin pigmentation and related disorders	7
1.3.1 Variation in human skin color	7
1.3.2 Alteration in constitutive pigmentation	7
1.4 Vitiligo: diagnosis and treatments	9
1.4.1 Vitiligo disease scoring methods	9
1.4.2 Available treatments for vitiligo	11
1.5 Existing mathematical and systems pharmacology models related to skin biology	13
1.6 About the thesis	15
2 Data analysis to understand metabolic rewiring during melanogenesis	17
2.1 Introduction	18
2.1.1 Intracellular signaling and metabolism associated with melanogenesis . . .	18
2.1.2 Objective of this study	19
2.2 Transcriptional analysis to delineate the signaling network underlying pigmentation	19
2.2.1 Transcriptome Analysis of B16 cells following Pigmentation	19
2.2.2 Pre-processing and assessment of RNA-seq data	21
2.2.3 Alignment	21
2.2.4 Read Quantification	22

2.2.5	Differential Analysis	22
2.2.6	Pathway analysis and GO Enrichment Analysis	22
2.3	Melanogenesis involves the transcriptional activation of metabolic genes	23
2.4	Conclusion	25
3	Boolean modeling of melanogenesis pathway	27
3.1	Introduction	28
3.1.1	Existing mathematical models of melanogenesis	28
3.1.2	Identification of essential nodes in melanogenesis	30
3.2	About this work	32
3.3	Methodology	32
3.3.1	Building the Boolean model	32
3.3.2	Comparison with existing model	35
3.3.3	Perturbation Analysis	36
3.3.4	Two new function perturbation methods	36
3.4	Results	38
3.4.1	New model for melanogenesis captures the response of the system to UV	38
3.4.2	Comparison with the Lee model	39
3.4.3	Identification of sensitive nodes in the new model	41
3.4.4	Effect of function perturbations in the Lee model	44
3.4.5	Effect of function perturbations in <i>D. melanogaster</i> segment polarity network	45
3.5	Discussion	49
3.6	Conclusion	53
4	A systems model for vitiligo	55
4.1	Introduction	56
4.1.1	About vitiligo	56
4.1.2	Theories of vitiligo pathogenesis	57
4.2	About this study	63
4.3	The first disease model for vitiligo	64
4.3.1	Model construction and simulation	64
4.3.2	Equations for cells and cytokines	65
4.4	Results	69
4.4.1	Vitiligo model captures the system response to varying levels of stress	69
4.4.2	Effect of stress on skin cells, immune cells and cytokines	70
4.4.3	Simulating the drug effect	72
4.5	Discussion	74
4.6	Conclusion	75
5	Summary and Future Perspective	77
A	Appendix	83
A.1	Understanding drug-drug interactions: mechanisms, risk factors, and existing models	83
A.2	Model for drug-drug interaction	84
A.2.1	Simulation Methodology	86
A.3	Continual drug infusions may alter the system's behavior	86
A.3.1	Incoherent regulation may lead to oscillations	86
A.3.2	Double negative regulation may lead to bistability	87

CONTENTS

A.4 Codimension-two bifurcation analysis of motif 2 and 3	87
A.5 Codimension-two bifurcation analysis of motif 4	88
A.6 Conclusion	89
ABSTRACT	115
List of Publications	117
Conference poster presentations	119
Copy of all SCI publication	121

CHAPTER 1

Introduction

This chapter presents a review of the published literature relevant to the work in the thesis. The introduction is broadly divided into five sections. The first section of the introduction focuses on the details of the architecture and components of the human skin epidermis. The second section gives the details of the signaling pathways regulating melanin synthesis. An overview of human skin pigmentation and related disorders is given in the third section. The fourth section contains clinical scoring methods and available treatments for vitiligo. The last section of the introduction is a summary of existing systems pharmacology models and mathematical studies related to human skin pigmentation.

1.1 The human skin: architecture and components

Skin is the largest organ of the human body that apart from acting as a physical barrier has immune and sensory properties. It is mainly divided into three layers: the lowermost hypodermis, middle dermis and topmost epidermis. The hypodermal layer is mainly composed of adipose tissue which stores fat globules and controls body temperature. Along with hosting blood vessels and nerves, it also connects muscle and bone to the upper layer. The dermis is mainly composed of fibroblasts, macrophages, and adipocytes, and contains sebaceous glands, sweat glands, hair follicles, nerve endings, and blood vessels. The nerve endings help in sensation and blood vessels provide nourishment to the top layer. The outermost epidermal layer consists of continuously differentiating keratinocytes, pigment-producing melanocytes, immune-related Langerhans cells, and Merkel cells.

1.1.1 Epidermis

This thesis primarily deals with some of the activities in the epidermis. The epidermis is itself multilayered and subdivided into five layers that continuously rebuild the skin's surface. The stratum corneum, the topmost layer of the skin, is composed of keratin-filled dead cells that protect the skin from mechanical damage. Stratum lucidum is the next layer. It is also composed of dead cells that contain lipid-rich eleiden, which keeps out water. Stratum granulosum is the middle layer that mostly contains mature keratinocytes migrated from the bottom layer. The second layer from the bottom is the stratum spinosum. It contains keratinocytes as well as Langerhans cells that inform the immune system about invading pathogens. The deepest layer of the epidermis is the stratum basale. It contains continuously dividing basal cells, which differentiate to form keratinocytes. This layer also contains pigment-producing melanocytes. These cells rest on a basement membrane (BM) that separates the epidermis from the dermis that lies beneath. The basement membrane plays an important role in the differentiation of keratinocytes (Bergstresser et al., 1978). After the division in the basal layer, stem cell keratinocytes move upward and begin to differentiate. The upper four layers of the epidermis contain keratinocytes at varying stages of differentiation. The keratinocytes from the outermost corneum layer are denucleated and have no cell organelles. They are flattened and contain sheets of keratin filaments that form the skin's protective barrier (Costin and Hearing, 2007). After differentiation, keratinocytes in the suprabasal layer migrate upward to the skin surface. On reaching the surface, cells shed in a process known as desquamation. Figure 1.1 depicts a section of the multilayered epidermis and dermis. Across individuals, epidermal thickness at a particular body location is generally the same. However, there is inter-site variation in thickness at various body regions,

1.1 The human skin: architecture and components

with the palms and soles of the feet having the thickest epidermis. In a study involving 71 human participants, the thickness of the stratum corneum and the remaining layers of the viable epidermis was examined (Lock-Andersen et al., 1997). This study found a negative correlation between the number of years of smoking and stratum corneum thickness. However, it has been found that the blood volume of an individual positively correlates with the thickness of viable layers, with males having thicker viable layers than females (Sandby-Møller et al., 2003).

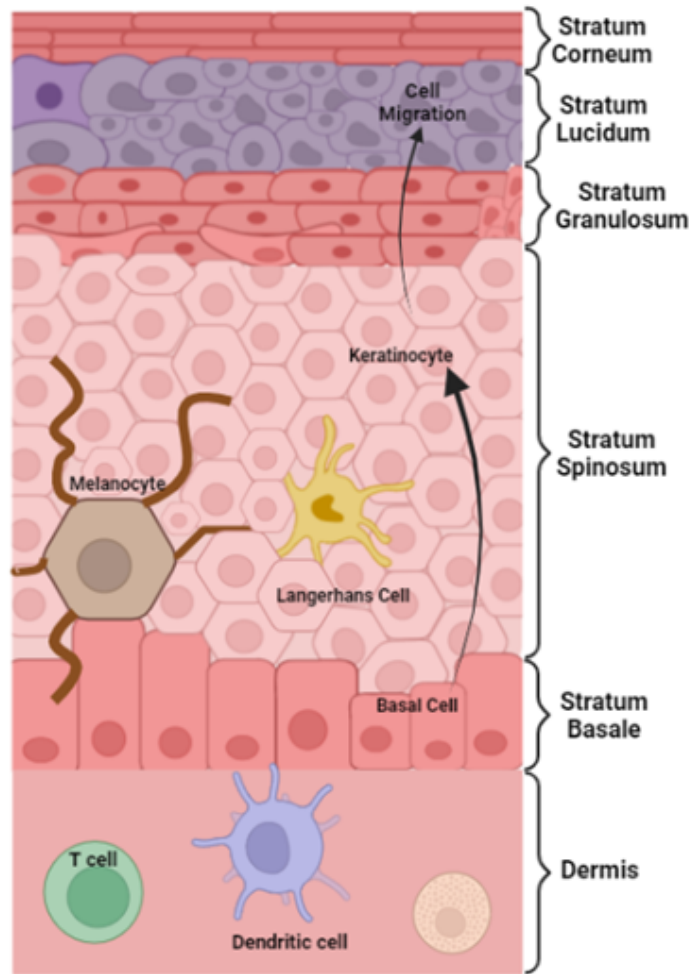


Figure 1.1: Skin's epidermis and dermis

Upon differentiation, keratinocytes move toward the skin surface. The time taken by the keratinocytes to travel along the epidermal layers is termed epidermal turnover time. In healthy skin, the keratinocytes take around 28-56 days to make the complete journey from the basal layer to the top of the corneum layer from where they are shed off (Halprin, 1972; Bergstresser and Richard Taylor, 1977; Iizuka, 1994). In a non-diseased, non-stimulated, baseline condition, the number of keratinocytes in the epidermis is at equilibrium. The keratinocytes in the epidermis are entirely replaced by the steady-state production and removal of the cells.

1.1.2 Melanocyte and melanosomes

Melanocytes are the second largest epidermal cell population after keratinocytes. Melanocytes are functionally connected to the dermal fibroblasts and the epidermal keratinocytes. These neural crest-derived cells are found in the epidermal layer's lowermost layer. Melanocytes are dendritic cells with finger-like extensions that extend into keratinocytes nearby. The density of melanocytes at a certain bodily place, such as the back of the hand, is the same in all people. However, inter-site variance is observed at multiple body sites of the same individual. Skin exposure to damaging ultraviolet radiation or hazardous substances can influence the density of constituent melanocytes in the skin. (Yamaguchi et al., 2007). Skin melanocytes multiply slowly under normal conditions and are resistant to apoptosis due to strong BCL2 expression (Goldschmidt and Raymond, 1972). Melanocytes include melanosomes, which are lysosomal-like organelles that synthesize and compact melanin. Melanosomes are usually classified into four stages. Stage I pre-melanosomes contain no internal structural components and no Tyrosinase activity, but Stage II melanosomes have Tyrosinase and the structural protein PMEL17. Melanin production and homogeneous deposition on interior fibrils characterize Stage III melanosomes (Costin and Hearing, 2007). Stage IV melanosomes are totally melanized and electron-opaque. Stage IV mature melanosomes migrate from the perinuclear region of the melanocyte to the tips of the dendrites. One melanocyte is believed to transfer melanosomes to 36 neighboring keratinocytes (Fitzpatrick and Breathnach, 1963). The mechanism of melanosome transfer from melanocytes to keratinocytes is thought to be either cytophagocytosis, filopodial mediated melanosomal transfer, or the discharge of melanosomes into extracellular space followed by phagocytosis (Van Den Bossche et al., 2006; Singh et al., 2010). Melanosomes taken up by keratinocytes cover the nucleus. The size of melanosomes influences their dispersion in keratinocytes. Large melanosomes are distributed singly in keratinocytes, whereas small melanosomes tend to cluster into aggregates (Atkins et al., 2002; Thong et al., 2003).

1.1.3 Melanin

The melanosomes synthesize two types of melanins: black/brown eumelanin and red pheomelanin from the same precursor - tyrosine. OCA2 is a transmembrane protein that transfers tyrosine within melanosomes. Three enzymes oxidize tyrosine to melanin: tyrosinase, TRP1, and TRP2. The ratio of eumelanin to pheomelanin synthesized is determined by the availability of substrates for enzyme activity. The synthesis of melanin is separated into three stages. Tyrosine is transformed to cysteinyl-dopa in the first stage until enough cysteine is available. The conversion of cysteinyl-dopa to pheomelanin is the following step. When cysteinyl-dopa and

1.2 Signaling pathways regulating melanin synthesis

cysteine are depleted, the third stage includes the synthesis of eumelanin (Prota, 1988; Videira et al., 2013; D’Mello et al., 2016). Figure 1.2 depicts a visual representation of the metabolic mechanism of melanin formation.

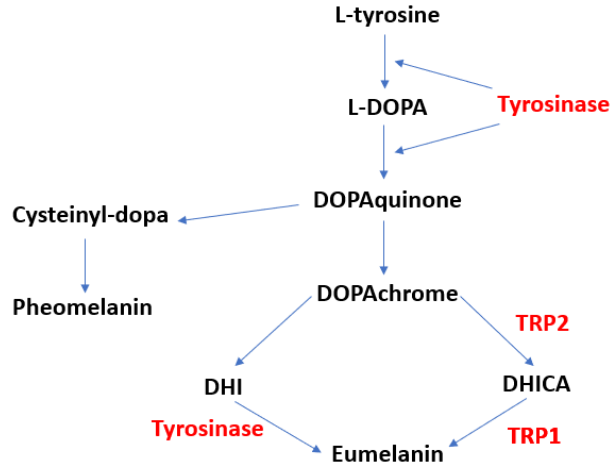


Figure 1.2: Metabolic synthesis of melanin in melanosome

The first step of the pathway of the conversion of tyrosine to dopaquinone is common to both eumelanin and pheomelanin synthesis. In a rate-limiting step, catalyzed by Tyrosinase, tyrosine is initially hydroxylated to L-DOPA and then oxidized to dopaquinone. If cysteine is available in the system, it reacts with dopaquinone to give cysteinyl-dopa, which is further oxidized and yields pheomelanin. On depletion of cysteine from the system, dopaquinone spontaneously converts to dopachrome. Dopachrome is further processed to form DHI which is polymerized to give eumelanin. Alternately, in the presence of TRP1 and TRP2, dopachrome is converted to DHICA which polymerizes to form eumelanin.

1.2 Signaling pathways regulating melanin synthesis

Many signaling mechanisms and transcription factors interact to initiate and control melanin production. A variety of key signaling pathways function upstream of pigmentation genes and transcription factors. The majority of the mechanisms involved in the control of melanogenesis are ligand receptor-mediated. Paracrine signals from neighboring keratinocytes and dermal fibroblasts bind to melanocyte receptors, activating the downstream signaling cascade. Figure 1.3 depicts some of the signaling networks involved in regulating melanogenesis. The α -MC1R route is known to be the primary pathway controlling melanin production. α -MSH (alpha melanocyte stimulating hormone) is produced by cleaving the precursor protein, pro-opiomelanocortin (POMC), which is secreted by the pituitary gland and surrounding keratinocytes.

α -MSH binds to the melanocyte-specific receptor (MC1R) and induces adenylate cyclase activation downstream via G-protein. Adenylate cyclase increases cyclic AMP from ATP, which activates protein kinase A (PKA). PKA phosphorylates and thereby activates CREB (cAMP response element binding protein). When CREB is activated, it phosphorylates MITF. Tyrosinase, TRP1, and TRP2 are important melanogenic enzymes that are induced by phosphorylated MITF (Costin and Hearing, 2007; D’Mello et al., 2016).

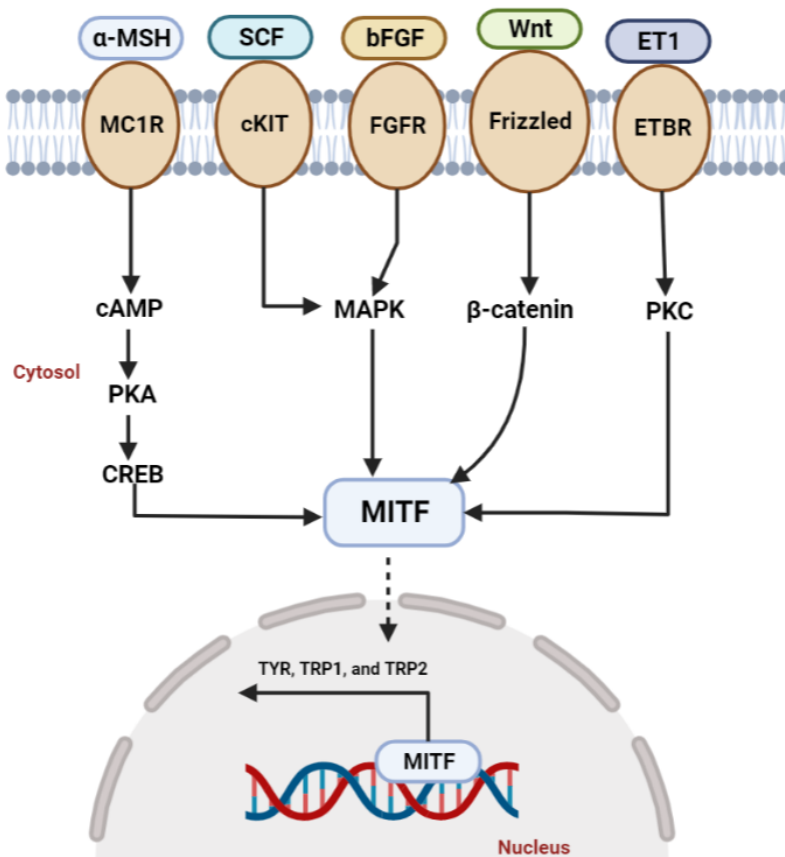


Figure 1.3: Core molecular pathways regulating melanin production in melanocytes

When stem cell factor (SCF) and basic fibroblast growth factor (bFGF) to their respective melanosomal receptors, c-KIT, and FGFR, the downstream MAPK signaling cascade is activated. The SCF/c-KIT and bFGF/FGFR pathways regulate melanocyte proliferation and dendritogenesis. Wnt ligands bind to Frizzled receptors on the cell surface, increasing the stability of cytoplasmic *beta*-catenin and causing its translocation into the nucleus, where it induces MITF transcription. The Wnt/*beta*-catenin signaling pathway regulates MITF transcription, which in turn controls the expression of TYR and other pigmentation enzymes. After UV exposure, endothelin-1 (ET1) released by keratinocytes binds to its G-protein coupled receptor (ETBR)

1.3 Human skin pigmentation and related disorders

and stimulates a cascade of signaling pathways involved in boosting melanocyte dendricity and migration (Costin and Hearing, 2007).

1.3 Human skin pigmentation and related disorders

At birth, humans have a basal skin color that is passed down genetically. The skin color results from the genetically determined, basal melanogenesis termed as constitutive pigmentation. Several factors contribute to constitutive pigmentation, including melanocyte density, enzyme activity, and the transfer and distribution of melanin-filled melanosomes from the melanocytes into adjacent keratinocytes (Yamaguchi et al., 2007).

1.3.1 Variation in human skin color

Human skin color range from fair white to dark black. Based on the color of human skin and the response of human skin to ultraviolet light, Thomas Fitzpatrick classified humans into six classes. When exposed to sunlight, phototype I individuals' skin never darkens, whereas phototype VI individuals' skin is black, and they do not show skin burn (Fitzpatrick, 1986, 1988). The kind and quantity of melanin, as well as the size and distribution of the melanosomes inside the suprabasal layers, define the color of the basal skin. The amount of melanin is seen to vary greatly across persons of the various phototypes while having almost comparable melanocyte densities at a specific region on the body (Alaluf et al., 2003; Tadokoro et al., 2003). Dark-skinned people have more eumelanin in vast, uniformly distributed melanosomes, while fair-skinned people have more pheomelanin contained in smaller, clustered melanosomes (Alaluf et al., 2003; Thong et al., 2003; Brenner and Hearing, 2008). Sebum and other skin-related factors have been demonstrated to have an impact on the skin's reflective property, which in turn affects the final appearance of skin color (Loy and Govindarajan, 2007).

1.3.2 Alteration in constitutive pigmentation

As the outermost covering of the body, the skin is continuously exposed to internal and external stresses. Internal stress can be genetic or endocrine whereas external stress affecting the skin can be physical, chemical, or environmental. Any form of stress on the skin often leads to a change in color which can be either temporary where the basal pigmentation is eventually restored or permanent like melasma, albinism or vitiligo.

Melasma is an acquired pigmentary condition characterized by light brown, dark brown and/or blue-gray patches on your skin. Hyperpigmentation patches appear most commonly on the cheeks, nose, chin, above the upper lip and forehead. It sometimes affects arms, neck and

back. In general, it affects mostly women and those with darker complexions (Fitzpatrick skin types III-V). The disease impairs social life of patients due to its frequent facial involvement. Its pathogeny is yet to be deciphered, while there are some known triggering factors like sexual hormones, sun exposure, pregnancy, inflammatory response elicited by the skin, and also associated with the use of steroids, cosmetics, and photosensitizing drugs. There is also a clear hereditary predisposition since more than 2/5th of patients reported to have relatives with the similar condition. Hydroquinone monotherapy and cream consisting of Tretinoin (0.05%), hydroquinone (4%), and mometasone furoate (0.1%) are predominantly used to treat melasma, whereas chemical peels, laser and light-based therapies are found to be at-par or less effective and are found to have higher risk of adverse effects. Oral tranexamic acid require more clinical validation (Ogbechie-Godec and Elbuluk, 2017; Aishwarya et al., 2020; McKesey et al., 2020).

Contrary to melasma, albinism is a genetic disease characterized by a congenital reduction or absence of melanin pigment. Albinism is manifested in several forms. Albinism's phenotypic variability is caused by several gene mutations impacting distinct locations within the melanin pathway, leading to varied degrees of declined melanin production. Oculocutaneous albinism is the most severe type of albinism. This kind of albinism is characterized by pink/white skin, iris, and hair. Patients also experience vision problems. Ocular albinism type 1 (OA1) is a different form of albinism that solely impacts the eyes. Typically, the person's skin tone and eye color fall within the normal range. However, a vision test will reveal that the retina is completely depigmented. A form of albinism Hermansky-Pudlak syndrome (HPS), is known to be caused by a change to a single gene. In addition to oculocutaneous hypopigmentation, HPS is characterized by ceroid accumulation and hypopigmentation. Furthermore, patients with this condition suffer from severe immune deficiencies, fibrosis of the interstitial lungs, granulomatous colitis, and mild bleeding disorders associated with platelet insufficiency. Given that the condition is a genetic disorder, albinism has no cure. The goal of existing treatments is to relieve symptoms which includes getting proper eye care and monitoring skin for problems (Mártinez-García and Montoliu, 2013; Marçon and Maia, 2019).

Vitiligo is the most common skin disorder leading to depigmentation which is characterized by the loss of melanocytes, which eventually leads to pigment reduction in the affected areas of the skin (Bergqvist and Ezzedine, 2020). The specific cause of vitiligo is unknown; however, autoimmunity and oxidative stress are found to have a significant impact. As per the literature published between 1964 to 2021, Vitiligo affects 1-2% of the population worldwide. There are, however, discrepancies in the frequency of vitiligo among geographical regions. Japan (1.68%), Mexico (2.6-4%), and India (8.8%) have the highest reported prevalence (Said-Fernandez et al., 2021). It is mainly classified into two types: segmental vitiligo (SV) and nonsegmental vitiligo

1.4 Vitiligo: diagnosis and treatments

(NSV). NVS is the most prevalent type and often affects acrofacial areas in a symmetrical fashion. SV, on the other hand, is localised to one segment of the skin and causes early skin whitening. Though vitiligo is often overlooked as a cosmetic issue, its psychological implications can be distressing and place a substantial strain on one's everyday life (Ezzedine et al., 2015). Many patients find the available treatment choices unsatisfying because they are time-consuming, complex, and unsuccessful. A deeper knowledge of the underlying causes should allow for the formulation of more targeted, and presumably more effective, treatments.

1.4 Vitiligo: diagnosis and treatments

Even though the skin is the biggest organ of the human body, there are no standard procedures for determining the severity of many skin diseases. A disease-scoring system is especially important for monitoring medication response and assessing the effectiveness of new drugs. Several scoring systems have been proposed in recent years to compare inter-individual variances in disease progression (Bhor and Pande, 2006). The Psoriasis Area Severity Index (PASI) is currently the preferred score for assessing the extent of psoriasis. It considers the severity (induration, erythema, and desquamation) as well as the proportion of the affected region (Fredriksson and Pettersson, 1978; Charman and Williams, 2000). The most generally used grading system for assessing the intensity of atopic dermatitis is SCORAD (noa, 1993). The score is calculated based on the extent, severity (erythema, edema, crusting, excoriation, lichenification, dryness) and sleep loss. There are other scoring systems used for skin disorders like scleroderma, hirsutism, acne vulgaris, melasma and vitiligo (Bhor and Pande, 2006). Vitiligo is a chronic depigmentary condition characterized by melanocyte malfunction or destruction (Picardo et al., 2015). To determine the effectiveness of treatment, reliable measurements of vitiligo regions would be required. Recently, some novel scoring methods were presented, which are discussed in the following section.

1.4.1 Vitiligo disease scoring methods

The Vitiligo European Task Force (VETF) proposed a method that integrates study of three vitiligo components: disease extent, stage, and progression (Taieb et al., 2013). The rule of nines is used to determine the extent (Wachtel et al., 2000). To determine how much area has been affected, the rule divides the surface area of the body into a percent of 9 or multiples of 9. In an adult, the front and rear of the head and neck account for 9% of the body's surface area, while the front and back of each hand and arm account for 9%, the front and backside of the torso or trunk account for 18% each, the front and back of both legs and foot account for 18%, and genitalia

contribute to 1%. Staging is measured and distinguished into three stages based on dermal and hair pigmentation in vitiligo patches: Stage 0 represents natural pigmentation, stage 1 indicates inadequate depigmentation, stage 2 suggests total loss of pigment with a maximum of 30% hair whitening, and stage 3 shows over 30% hair whitening. The final parameter, progression, is measured on a scale of -1 to 1, with 1 indicating progressive illness spread, 0 indicating stability, and -1 indicating regressive disease spread (Taieb et al., 2013) The Vitiligo Area Severity Index (VASI) determines the hand unit proportion of vitiligo involvement. The surface area of one hand is roughly equal to 1% of the entire body. Estimates of the degree of pigmentation are made to the nearest percentage of the following: 100% indicates total depigmentation; 90% indicates minor pigmentation; 75% indicates that the depigmented region is more than the pigmented area; 50% indicates that the two are equal; 25% indicates that the pigmented area is greater than the depigmented area; and 10% indicates the presence of only minor depigmentation. The product of the area of vitiligo in hand units and the degree of depigmentation within the hand unit yields the VASI for each body region (Hamzavi et al., 2004). Based on a person's perception of the current disease activity throughout time, the Vitiligo Disease Activity Score (VIDA) is a scale with six points for rating vitiligo activity. Expanding lesions or the emergence of new lesions are symptoms of active vitiligo. Following are the grades: VIDA score: +4 for activity lasting no more than six weeks, +3 for activity lasting between three and six weeks, +2 for activity lasting between three and six months, +1 for activity lasting between six and twelve months, and 0 for activity lasting for twelve months or longer. -1 for stable with random repigmentation lasting at least a year. A reduced level of activity is indicated by a smaller VIDA score (Njoo et al., 1999).

A new system called the Vitiligo Extent Tensity Index (VETI) scoring combines the examination of the level of extensity and severity of vitiligo to determine the depth of the condition (Feily, 2014). Similar to PASI, the composite score represents a constant replicable number. The rule of nines is used to quantify the proportion of extended involvement. Five phases of disease tensity (T) are used to score the five places afflicted, including the trunk (t), upper limbs (u), head (h), lower limbs (l), and genitalia (g): Stage 0 represents healthy skin; Stage 1 represents hypopigmentation (which includes trichrome and uniform lighter pigmentation); Stage 2 represents a complete loss of pigment with black hair and perifollicular pigmentation; Stage 3 represents complete loss of pigment with black hair along with no perifollicular pigmentation; Stage 5: Complete loss of pigment combined with significant hair whitening. Stage 4: Mixture of white and black hair either with or without perifollicular pigmentation. The following formula is employed to determine the total body VETI, taking all body regions into account:

$$(Ph \times Th) + (Pt \times Tt) \cdot 4 + (Pl \times Tl) \cdot 4 + (Pu \times Tu) \cdot 2 + (Pg \times Tg) \cdot 0.1$$

1.4 Vitiligo: diagnosis and treatments

P stands for percentage engagement, T for intensity level, h for head involvement, t for trunk involvement, u for upper limb involvement, l for lower limb involvement, and g for genitalia involvement. The coefficients listed in the above equation depend on the rule of nines' percentage of the skin surface. Accordingly, the coefficient of trunk and lower limb is 4 ($36:9=4$), upper limb is 2 ($18:9=2$), head is 1 ($9:9=1$) and the genitalia is almost 0.1 ($1:9=0.1$). If calculated, the VETI can have a maximum score of $5+20+10+20+1=55.5$.

In comparison to the other vitiligo scores mentioned above, the VETI score is more similar to the PASI score for psoriasis and, in contrast to other vitiligo scores, yields a reliable and consistent result. Unlike the PASI score, the VETF system is more complicated and has certain shortcomings with regard to inconsistent outcomes. Since the VIDA score is determined by the patient, there may eventually be a discrepancy. In clinical research, VASI offers a reasonably easy-to-use approach that is similar to the PASI.

1.4.2 Available treatments for vitiligo

The existing treatment options for vitiligo can be broadly categorized as medical and surgical methods. Medical treatment can be further classified into topical, systemic, and phototherapy approaches. As per the guidelines provided by the European Dermatology Forum, the initial course of action for segmental vitiligo involves the use of topical treatments. If the desired repigmentation is not achieved and the disease stabilizes, surgical options can be considered. Finally, phototherapy is employed to halt the progression of the condition and stimulate pigmentation. In contrast, for non-segmental vitiligo affecting extensive areas, phototherapy is administered for a minimum of three months to establish stability before transitioning to systemic medications or other immunosuppressants if there is no response (Taieb et al., 2013).

Topical corticosteroids function as both local immunomodulators and melanocyte stimulators. They work by binding to GC receptors, which reduces the production of cytokines like IL10, IFN- γ , and TNF- α , thereby inhibiting T cell activation (Njoo et al., 1999). Although corticosteroids are effective in treating non-segmental vitiligo, they come with various side effects. As a result, they are only suitable for intermittent and limited-duration use in treating areas beyond the face (Xing and Xu, 2012; Taieb et al., 2013). Topical calcineurin inhibitors, such as tacrolimus, also possess an immunomodulatory effect on cytotoxic T cells. They inhibit the production of IL-2 and IFN- γ while reducing systemic antioxidant stress, which aids in controlling the disease and promoting repigmentation in vitiligo (Felsten et al., 2011). Compared to corticosteroids, topical calcineurin inhibitors are safer, allowing for a longer duration of intermittent use in sensitive areas like the face and neck (Lubaki et al., 2010). Calcipotriol, a topical analog of Vitamin D, has not shown satisfactory results in treating vitiligo. However, when combined

with betamethasone dipropionate, it has demonstrated mild to moderate response (Parsad et al., 1999). Prostaglandin analogs like latanoprost induce tyrosinase and promote melanocyte proliferation. They have been found to be effective in treating periocular vitiligo, although they may cause mild irritation and burning as side effects (Kapoor et al., 2009; Anbar et al., 2015). Topical antioxidants such as catalase and superoxide dismutase are effective in inducing repigmentation when used in combination with other therapeutic options (Naini et al., 2012).

Phototherapy is considered the primary treatment option for vitiligo when more than 10% of the body's surface area is affected. The combination of broad band UVA (320-380nm) and either oral or topical psoralen is known to activate follicular melanocytes and release keratinocyte growth factors that support melanocyte growth (Shenoi and Prabhu, 2014). NB-UVB phototherapy functions by inducing the tyrosinase enzyme and enhancing melanosome expression. Numerous studies have demonstrated that NB-UVB phototherapy is more effective than PUVA phototherapy in stabilizing the condition and promoting repigmentation. Side effects of NB-UVB treatment, such as erythema, itching, and moderate burning, are generally transient and diminish within a few hours of treatment (Felsten et al., 2011; Bae et al., 2017). Monochromatic excimer laser (308 nm) has shown superior clinical outcomes compared to NB-UVB and can be further enhanced when used in conjunction with topical hydrocortisone and tacrolimus (Alhowaish et al., 2013). Additionally, heliumneon lasers (632.8 nm) have demonstrated efficacy in treating segmental vitiligo (Wu et al., 2008).

When topical medications or NB-UVB do not provide adequate relief, systemic corticosteroids are prescribed. A low oral dose of dexamethasone stabilizes the disease to a certain extent however relapse is also noticed in some cases (Majid and Imran, 2013). When combined with PUVA, Azathioprine induces more repigmentation than PUVA alone (Madarkar et al., 2019).

The outer root sheath of the hair follicle serves as a crucial reservoir of melanocytes, which is vital for the success of medical treatments. Surgical therapies aim to reintroduce harvested melanocytes into depigmented vitiligo lesions. There are two types of surgical procedures: tissue grafting and cellular grafting. In tissue grafting, specifically split-thickness skin grafting, a thin layer of the epidermis is obtained from a suitable donor area and transplanted onto the vitiligo lesion (Khunger et al., 2009). This method has shown outstanding results in terms of repigmentation and achieving a cosmetic match, surpassing other tissue grafting techniques such as blister roof grafting and mini punch grafts (Majid and Imran, 2013). Cellular grafting involves harvesting viable tissues from pigmented normal sites through tissue grafting. The individual cells of the epidermis are then separated to form a suspension, which is subsequently transferred onto de-epithelialized recipient vitiliginous skin (Felsten et al., 2011). Various techniques have been developed for cellular grafting, including melanocyte transplantation, keratinocyte

1.5 Existing mathematical and systems pharmacology models related to skin biology

and melanocyte transplantation, and transplantation of follicular epidermal cells. One major advantage of cellular grafting over tissue grafting is the ability to treat a significantly larger surface area in a single procedure (Chen et al., 2004).

1.5 Existing mathematical and systems pharmacology models related to skin biology

One effective way to investigate the complexity of biological systems is through mathematical modeling. The study involves representing the biological system as a set of equations or a network of connections and then applying the appropriate mathematical method to answer a specific question. Several aspects of skin biology have previously been studied using mathematical models, including melanocyte development, signaling, pigmentation, disease, barrier function, and immune function.

Melanoblasts are neural crest-derived cells that proliferate and then differentiate into melanocytes and migrate to the stratum basale of the epidermis. Luciani et al. developed a mathematical model to study the cellular mechanisms involved in melanoblast expansion, and its proliferation and migration from the dermis to epidermis (Luciani et al., 2011). Some models simulate keratinocyte proliferation and differentiation which is necessary to maintain homeostasis of the human epidermis (Grabe and Neuber, 2005; Klein et al., 2007). Smallwood et al. developed a multiscale integrated model of a human epidermis that links subcellular mechanisms to the cellular level which helps in investigating the influence of subcellular factors in epidermal wound healing (Smallwood et al., 2010).

There are very few models that incorporate intracellular metabolism relevant to skin pigmentation in keratinocytes and melanocytes. Rodríguez-Lopez et al. formulated a kinetic model for the melanin biosynthesis pathway. The pathway included metabolites from tyrosine to dopachrome. The model explained lower catalytic efficiency of the enzyme tyrosinase on monophenols (tyrosine) than on diphenols (Rodríguez-López et al., 1992). Emir and Kurnaz devised an integrated model for melanocyte-specific gene expression and melanogenesis. The model successfully showed that upon stimulation/inhibition of certain growth factors in the system, the melanin output can be upregulated/downregulated (Emir and Kurnaz, 2003). Thingnes et al. defined a model for the distribution of melanin in keratocytes during the process of skin tanning. It predicts the thickness of the epidermal layer and how far the melanocyte dendrite grows after exposure to UV radiation (Thingnes et al., 2009). A mathematical model developed by Oyehaug et al. explains how an extracellular signal triggers the switch between eumelanin and pheomelanin production. They supported Ito's hypothesis that melanogenic switching is a

result of covalent binding that occurs between intermediate dopaquinone and glutathione reductase (Øyehaug et al., 2002).

A mechanistic model for the aging of human skin accounts for the loss of elasticity, resilience and flexibility of the dermis. It also explains the appearance of wrinkles and the thinning of the epidermis which is associated with aging (Giacomini and Rein, 2004). A number of mathematical models have also been developed which consider epidermal wound healing, dermal extracellular matrix remodeling, wound contraction, and angiogenesis (Sherratt and Murray, 1991; Sherratt and Dallon, 2002; Wearing and Sherratt, 2000; Maggelakis, 2003; Mcelwain et al., 2009).

Hair, the visible appendage of the skin, has also been extensively studied. The structure and mechanical properties of hair are being explored by several groups. Akkermans et al. have carried out molecular dynamics to study hair mechanics (Akkermans and Warren, 2004). Researchers in Singapore created a simple physics model for animating human hair by grouping the strands into stripes (Koh and Huang, 2001). Hair removal and styling are also studied while keeping in mind the outlook towards these two topics. Kolinko and Littler developed a mathematical model for laser hair removal that predicts and optimizes the procedure (Kolinko and Littler, 2000). To predict human skin color, mathematical techniques such as regression analysis (Shimada et al., 2001), neural networks (Phung et al., 2001), and image analysis (Tsumura et al., 2003; Coelho et al., 2006) are used. The image analysis technique is used to analyze and determine areas of skin that have undergone repigmentation in particular, during the treatment of vitiligo (Nugroho et al., 2007). Signaling and metabolic pathways that mediate human skin pigmentation are studied using network analysis and boolean modeling techniques.

A comprehensive, systems-level network of skin pigmentation has been rebuilt by Raghunath et al. The 256-node large network includes the signaling and metabolic processes involved in the production of melanin, the development of melanosomes, the formation of dendrites, and the uptake of melanosomes by keratinocytes. The authors used shortest path analysis to locate new and alternative pigmentation-related signaling pathways (Raghunath et al., 2015). Another group has created a 62-node network in a similar manner for UV-induced skin pigmentation. The paracrine factor and MITF-mediated signaling pathways that are essential for skin pigmentation have been the focus of Lee et al's research. The output nodes of the reconstructed model are melanin and BCL2, an inhibitor of apoptotic cell death, and the input node is UVB. Their study's goal is to use boolean analysis to find specific treatments that decrease melanin synthesis while having little impact on the cell's apoptotic balance (Lee et al., 2015).

Quantitative systems pharmacology (QSP) is a computational framework that supports drug discovery and development by integrating knowledge from biological, physiological, pharmacological and clinical systems (Bradshaw et al., 2019). So far, QSP modeling has been utilized

1.6 About the thesis

throughout preclinical drug discovery to examine the therapeutic as well as toxic actions of drugs across several fields including neurology, metabolism, oncology and autoimmunity. The existing skin biology models and QSP models mainly focus on proliferative skin disorders like psoriasis, since preclinical models for such diseases are in high demand in the pharma industry. There is brief information available regarding the QSP for modeling the etiology of psoriasis and acne. In the case of acne, a QSP-based strategy was employed to comprehend the interaction between the pathogenesis-related processes, such as sebum generation, *P. acnes* growth, and inflammation (Bansal et al., 2014). A population of virtual patients was simulated to identify a subset that can benefit the most from the new treatment. The model compared the effectiveness of three new compounds at lessening the severity of acne to existing therapies and assessed the effectiveness of three new compounds. Three compartments were incorporated in a QSP model for psoriasis: the skin, the systemic circulatory system, and the lymph nodes (Bansal et al., 2015). This model elucidates the mechanisms associated with immune cell recruitment from lymph nodes and blood to the skin, the production of inflammatory mediators in the skin, and the activation of keratinocytes. It also establishes the correlation between these processes and the progression of the disease. The study helped in understanding the pathogenesis of psoriasis and evaluating the efficacy of drug compounds in disease treatment by identifying novel targets. As such, there is no QSP model available to understand skin pigmentation and other disorders.

In order to address a variety of vitiligo-related concerns, it was necessary to understand the biological processes involved in skin pigmentation at various scales. We present three independent studies in this thesis, in which we developed new and adapted existing models at the molecular, cellular, and organ levels to provide an integrated perspective on depigmentation of the skin.

1.6 About the thesis

The thesis describes the work on three different topics wherein we investigate skin pigmentation from the molecular to the organ level. Using data from the available literature, we first create a deterministic model for each study. Then the model is simulated to reproduce the known experimental or clinical observations. After the model has been validated against the available data, the model simulations are further utilized to support a theory or predict a possible mechanism for an unexplained observation.

Melanogenesis is widely studied to identify therapeutic targets for skin pigmentation-related disorders. It is important to study melanogenesis at the molecular level to identify genes/ proteins that control the level of melanin without affecting cell survival. Natarajan et al. demonstrated the role of IFN- γ in cellular hypopigmentation (Natarajan et al., 2014). When they

plated B16 melanoma cells at varied densities, many genes associated with melanin synthesis and melanosome maturation showed periodic changes. Low density plating of cells resulted in upregulation of pigmentation whereas downregulation of IFN- γ genes. In a recent experiment performed by the same group, transcriptomic studies were carried out to understand metabolic circuit rewiring during melanogenesis. we analyzed the raw data to identify differentially expressed genes and key pathways linked to melanogenesis.

A small number of models incorporate intracellular signaling and metabolism relevant to melanogenesis in keratinocytes and melanocytes. Lopez et. al. captured the kinetics of melanogenesis from L-tyrosine to dopachrome in a model with just 8 nodes (Rodríguez-López et al., 1992). The model developed by Lee et al. is relatively larger and includes dynamics of response to varying input levels Lee et al. (2015). It is, however, lacking important enzymes. Raghunath et al. formulated a larger, more detailed model of skin pigmentation (Raghunath et al., 2015). However, it is a static network model that does not depict the system's dynamics. We decided to convert this static network graph into a dynamic boolean model. This would help in understanding the dynamics of keratinocyte-melanocyte interaction, metabolism and signaling.

The final part of the thesis focuses on the development of the first disease model for vitiligo. Multiple mechanisms have been proposed for melanocyte destruction in vitiligo, including local neuronal injury, exposure to harmful chemicals, intrinsic defect of melanocytes, oxidative stress, genetic pre-disposition and autoimmune responses. It is possible that several processes work simultaneously to cause progressive loss of melanocytes and they involve immune attack, or cell damage and detachment. There are theories that explain the overall contribution of each of these processes but no study to our knowledge has integrated multiple mechanisms. In our disease model, we have integrated multiple mechanisms along with their correlation to clinical outcomes. Moreover, we also simulated the effects of drugs through parameter variations.

The thesis is divided into five chapters. This chapter gives an overview of the architecture and components of the human skin epidermis, signaling pathways regulating melanin synthesis, human skin pigmentation and related disorders, clinical scoring methods and available treatments for vitiligo and a summary of existing systems pharmacology models and mathematical studies related to human skin pigmentation. The second chapter is the study to understand metabolic rewiring during melanogenesis through data analysis. The third chapter presents the largest boolean model for melanogenesis that describes melanocyte-keratinocyte intercellular and intracellular signaling. The fourth chapter of the thesis is about the formulation of the first disease model for vitiligo and simulating the effect of drugs. The final chapter summarizes the whole thesis and presents insights into potential future directions and perspectives that can be explored based on the findings presented throughout the thesis.

CHAPTER 2

Data analysis to understand metabolic rewiring during melanogenesis

1 2

¹Work in this chapter has been published

²Sultan, F.; Basu, R.; Murthy, D.; Kochar, M.; Attri, K. S.; Aggarwal, A.; Kumari, P.; Dnyane, P.; Tanwar, J.; Motiani, R. K.; Singh, A.; Gadgil, C.; Bhavesh, N. S.; Singh, P. K.; Natarajan, V. T.; Gokhale, R. S. “Temporal Analysis of Melanogenesis Identifies Fatty Acid Metabolism as Key Skin Pigment Regulator”. *PLOS Biology*. 2022, 20 (5), e3001634.

2.1 Introduction

2.1.1 Intracellular signaling and metabolism associated with melanogenesis

Melanin, the primary pigment that affects skin tone and shields it from UV ray damage, is synthesized during the process of melanogenesis. In several pigmentation diseases, altered melanogenesis is seen. Disorders that cause hyperpigmentation are identified by elevated melanogenesis and melanin buildup. These include skin conditions like melasma, freckles, age spots, and sunspots, which are particularly prevalent in clinical dermatology. Furthermore, inflammation brought on by skin irritants frequently leads to both hyperpigmentation and hypopigmentation, as seen in vitiligo lesions.

Melanocytes are specialized cells that produce melanin and interact physically and functionally with other skin cells through paracrine and autocrine mechanisms. This includes over 150 genes and a number of signaling pathways that function at both the transcriptional and post-transcriptional levels (Hushcha et al., 2021). A variety of gene networks related to melanogenesis, proliferation, and survival are connected by MITF, the main transcription regulator of the melanocyte lineage. MITF controls the expression of many pigmentation-related genes, including PMEL17 and MART1, as well as the melanin production enzymes TYR, DCT, and TYRP1 to promote melanocyte differentiation. The process of UV-mediated activation of pigmentation involves the secretion of α -MSH by keratinocytes, which binds to the melanocortin 1 receptor (MC1R) on epidermal melanocytes and causes the synthesis of cAMP and CREB-mediated MITF transcription. Additionally, MITF is activated by coactivators like SOX10, but the transcriptional response is suppressed by suppressors such as TCF4 and ATF4. Apart from these key factors, regulators of bioenergetic pathways also seem to elevate during skin pigmentation. In a recent study, Seo et al. analyzed metabolomics of α -MSH-induced B16F10 cells at 1, 24, and 48 hours. Treatment with α -MSH showed a minimal increase in citric acid cycle pathways and some amino acid metabolisms (Seo et al., 2020). Numerous lines of evidence point to changes in mitochondrial activity during melanogenesis. For instance, after 48 hours of stimulation, activation of melanin formation in B16F10 melanoma cells reduces oxygen consumption without altering mitochondrial membrane potential (Meira et al., 2017). On the other hand, it has been suggested that cells with melanogenesis stimulation have larger mitochondrial mass. Some of these mitochondria have been shown to be in close proximity to melanosomes, where fibrillar bridges are thought to enable the exchange of small molecules between the two organelles (Daniele et al., 2014). Reactive oxygen species (ROS) levels are elevated when mitochondria are remodeled to accelerate fission; this can have a conflicting influence on melanogenesis (Kim

2.2 Transcriptional analysis to delineate the signaling network underlying pigmentation

et al., 2014; Tanwar et al., 2022). Hyperpigmentation is induced while targeting the F1F0-ATP synthase, which ought to also cause a buildup of ROS (Jung et al., 2005).

In order to cure pathological disorders and restore homeostasis, it is essential to specifically inhibit the pathways that dysregulate cellular activities. The function of dynamic metabolic programming in immune cell plasticity and function has been decoded using transcriptome analysis. This has aided in the discovery of numerous metabolic pathway inhibitors that can be used to treat autoimmune disease and inflammation (Berod et al., 2014; Pan et al., 2017; O'Sullivan et al., 2014). Similarly, it is crucial to investigate the molecular basis of skin pigmentation in order to pinpoint the potential genes, proteins, and metabolic pathways that can be targeted to control melanin production while preserving cell viability.

2.1.2 Objective of this study

The objective of this work is to study transcriptomic changes during pigmentation. Our experimental collaborators at CSIR-IGIB, New Delhi, have set up a B16 cell-autonomous pigmentation model where cells transit from basal depigmented to the pigmented state over a period of 6 days. To identify the genes and the key pathways that are activated during pigmentation, a transcriptional analysis was carried out. This work focuses on transcriptional analysis to identify the genes that are differentially expressed during depigmentation.

2.2 Transcriptional analysis to delineate the signaling network underlying pigmentation

2.2.1 Transcriptome Analysis of B16 cells following Pigmentation

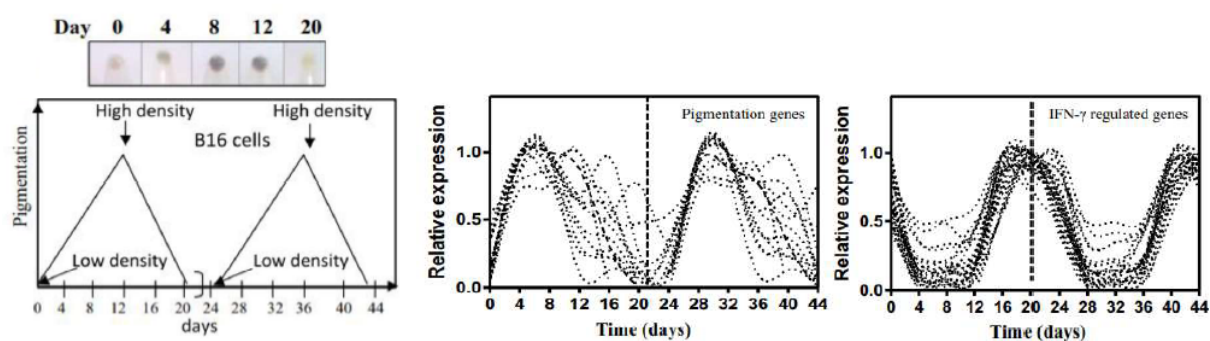


Figure 2.1: B16 cell-autonomous pigmentation model (Natarajan et al., 2014)

A bicyclic "cell" model was set up at CSIR-IGIB, New Delhi, to better understand the cellular alterations associated with the pigmentation-depigmentation process (Natarajan et al., 2014). An in vitro model was established by plating the B16 melanoma cells. By only varying the plating cell density, and without adding any external factor, the cells showed reversible pigmentation. When plated at a lower density of 10^2 cells per cm^2 , the depigmented cells showed repigmentation. Replating the cells in a fresh medium at a higher density of 104 cells per cm^2 reversed the repigmentation. The reversible pigmentation cycle was established twice, with each cycle lasting 20 days, in order to lessen the experiment's stochasticity. The cells were harvested every four days and replated at a higher density on day 12 of each cycle. Pigmentation peaked at day 12 and day 36. To identify the genes that are differentially expressed during the bicyclic in vitro model, transcriptional analysis was performed. Low-density plating of cells resulted in upregulation of pigmentation whereas downregulation of IFN- γ regulated genes. This is because IFN- γ causes cellular hypopigmentation by arresting melanosome maturation (Figure 2.1).

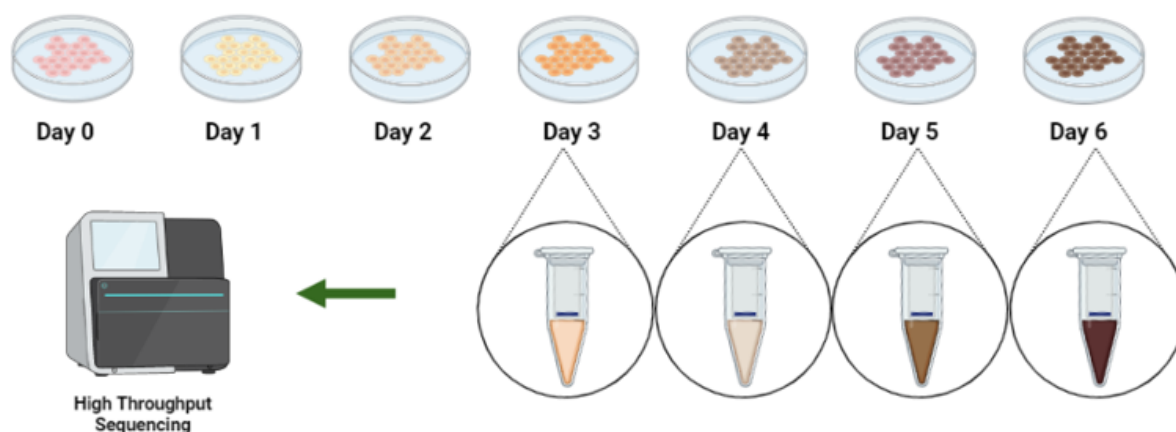


Figure 2.2: New setup of B16 cells resulting in the transition of melanocyte from depigmented (day 0) to pigmented state (day 6) followed by sequencing

In a recent experiment, B16 cells were seeded at a low density of 100 cells/ cm^2 and allowed to gradually pigment for 6 days of the model. The experiments were replicated at least twice to check the reliability and robustness of the findings. To ensure the consistency of experimental conditions, a correlation analysis was performed between samples. The resulting high correlation coefficients ranging from 0.98 to 0.99 among biological replicates confirmed the reliability of the data. Total RNA was isolated on days 3, 4, 5, 6. The sample was sequenced using Illumina NovaSeq 6000 platform. We analyzed the sequenced time-series transcriptome data at CSIR-NCL, Pune, to identify differentially expressed genes and key pathways linked to pigmentation.

2.2 Transcriptional analysis to delineate the signaling network underlying pigmentation

2.2.2 Pre-processing and assessment of RNA-seq data

The raw fastq files were used for quality assessment. Sequencing quality metrics play a crucial role in evaluating the accuracy of various steps involved in the sequencing process, such as library preparation, base calling, read alignment, and variant calling. The accuracy of base calling, which is the process of determining the sequence of bases in a DNA fragment, is commonly assessed using the Phred quality score (Q score). The Q score is a measurement of base calling accuracy and represents the probability of an incorrect base call made by the sequencer. It is defined as a logarithmic function of the base calling error probabilities (P). The Q score is calculated using the formula:

$$Q = -10 \log_{10} P$$

For instance, a base with a Q score of 30 (Q30) has a 1 in 1000 chance of being called incorrectly. This translates to a 99.9% base call accuracy. In comparison, a lower Q score of 20 (Q20) indicates that errors are likely to occur in every sequencing read of 100 base pairs with a base call accuracy of 99% and an inaccurate base call probability of 1 in every 100 calls. When the sequencing quality approaches Q30, the reads are almost error- and ambiguity-free and of the highest grade.

The FASTQC tool was used to perform the quality assessment on raw Fastq files, and a minimum average quality (Q) value of 20 was used. An overall high-quality read mapping set at 70% of 150bp DNA fragment size was also used. The quality stats were obtained and were used to calculate mean Phred scores. The per base quality values were calculated at each position from all the reads and their mean values from all samples were plotted.

2.2.3 Alignment

Filtered reads were aligned with HISAT2 alignment tool. GRCm38 was used as a reference genome. Default settings/parameters were deemed suitable while performing alignment using HISAT2. HISAT2 software is a highly cited short-read aligner. It scores above the other aligners like STAR, GSNAP, OLEgo and TopHat2 in terms of its speed of alignment and memory requirement (Kim et al., 2015). The graph-based data framework and alignment method implemented by HISAT2 allow for quick and accurate alignment of sequencing reads to a genome. Its mapping workflow involves two steps i.e. mapping unspliced reads to locate exons followed by splitting and alignment of unmapped reads to identify exon junctions. We also used HISAT2 to perform reference-based transcriptome mapping.

2.2.4 Read Quantification

HTSeq was used to quantify the reads for all genes. HTSeq is a Python based tool for processing high-throughput sequencing data. Other tools such as GenomicRanges Bioconductor and featureCount achieves fast runtimes because of being implemented in C but HTSeq is more accurate (Anders et al., 2015). The utility HTSeq-count was used to quantify the mapping of all genes in all the samples. The default settings/parameters were used. The tool takes the BAM files generated earlier and an annotation GTF file, with each model representing the structure of transcripts produced by a given gene as input and generates a text file that contains the raw count values.

2.2.5 Differential Analysis

After quantification, DESeq2 was used for differential gene expression analysis. Using negative binomial generalised linear models, the DESeq2 software offers techniques for detecting differential expression. The raw counts from HTSeq-count were used as input for DESeq2. The default settings/parameters were used for DESeq2 for analysis. DESeq2 uses a Gaussian Distribution of the raw counts for each sample to internally normalize the counts and negate outliers. 0.1 was chosen as the dispersion value. These normalised count values are used to compute differential expressions. There are different tools available for differential expression analysis such as edgeR, DESeq, baySeq, or EBSeq. While some of the differential expression tools can only perform pair-wise comparisons, DESeq2 can perform multiple comparisons and find more differentially expressed genes (Spies et al., 2017).

The results obtained through DESeq2 were in the form of a matrix that contained a log₂ fold change value for each gene. These values were used to identify genes that showed significant quantitative changes in expression levels over time.

2.2.6 Pathway analysis and GO Enrichment Analysis

The KEGG pathway analysis of all the differentially expressed genes for all three comparisons (Day 3 and Day 4, Day 3 and Day 5, and Day 3 and Day 6) was performed using the ClusterProfiler R package (version 3.10.1) by Mr. Ayush Aggarwal at IGIB. We employed the 'gage' package in R for gene enrichment analysis to identify pathways. Particularly, the package addresses the common occurrence of multiple genes being shared across different pathways. To manage this, it systematically considers the overlap between gene sets. In cases where a gene is linked to multiple pathways, its contribution to each pathway is taken into account in the enrichment analysis. Additionally, the Pathview package was utilized for the visualization of

2.3 Melanogenesis involves the transcriptional activation of metabolic genes

differential expression data. In this context, it was used for integrating log2 fold change data onto the pathway diagram.

2.3 Melanogenesis involves the transcriptional activation of metabolic genes

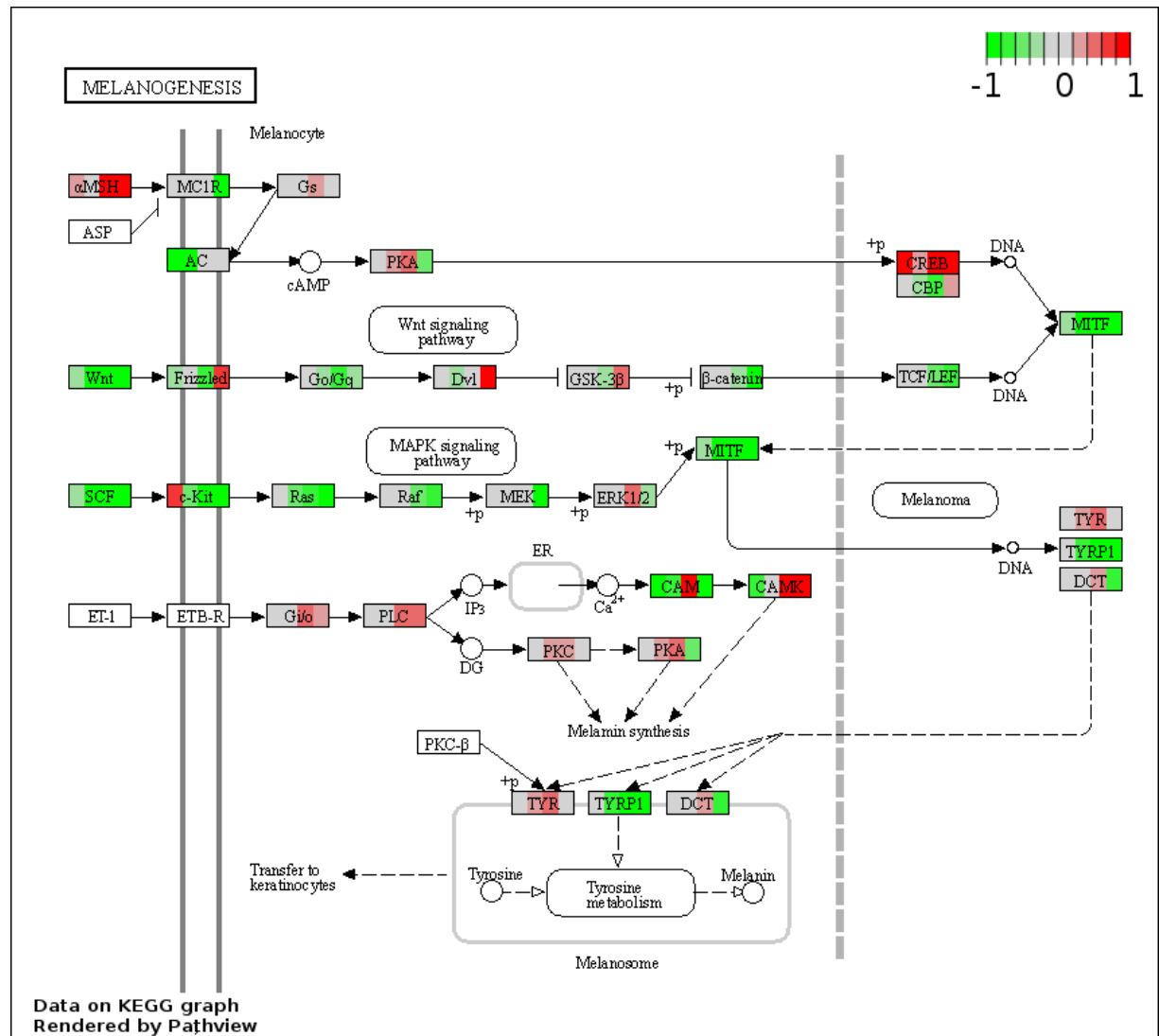


Figure 2.3: Melanogenesis pathway. Color scale represents a change in the expression value of genes over time on the scale of -1 to 1 (log2 fold change). Each cell is divided into four parts where the first part indicates day3 vs day4 expression change, the second part indicates day3 vs day5 expression change, the third part shows day3 vs day6 change and so on

A time series analysis of transcriptomic data of an independent pigmentation model of B16 cells was conducted to understand the differentiation programming of melanocytes from depig-

Data analysis to understand metabolic rewiring during melanogenesis

mented to pigmented state. A fine balance between the intrinsic needs of the cells and external constraints is thought to trigger melanogenesis in this model. A series of coordinated processes starting from transcriptional activation, melanosome biogenesis and melanin synthesis can be captured at the phenotypic and molecular levels. The phenotypic changes in the melanin are best observed and quantitated from days 3 to 6 (figure 2.3). At the molecular level, a higher MITF protein expression was observed on days 3 and 4. The classical MITF-mediated pigmentation targets show different trajectories of expressions during this period. PMEL17, a marker of early-stage melanosomes, is found to peak around days 4 and 5, indicating new melanosome formation as an early event that diminishes by day 6. This is followed by increased expression of tyrosinase, the rate-limiting enzyme in melanin synthesis, on days 5 and 6. In addition to these pivotal markers, various genes involved in the melanogenesis pathway demonstrate differential expression. Noteworthy among them are aMSH, MC1R, gs, AC, PKA, cAMP, CREB, CBP, MITF, TCF/LEF, DNA, B-catenin, GSK-3b, DVL, Go/Gq, Frizzled, Wnt, ERK1/2, MEK, Raf, Ras, c-Kit, SCF, Gi/o, PLC, PKC, CAM, CAMK, Melanin, TYR, TYRP1, DCT, and Tyrosine.

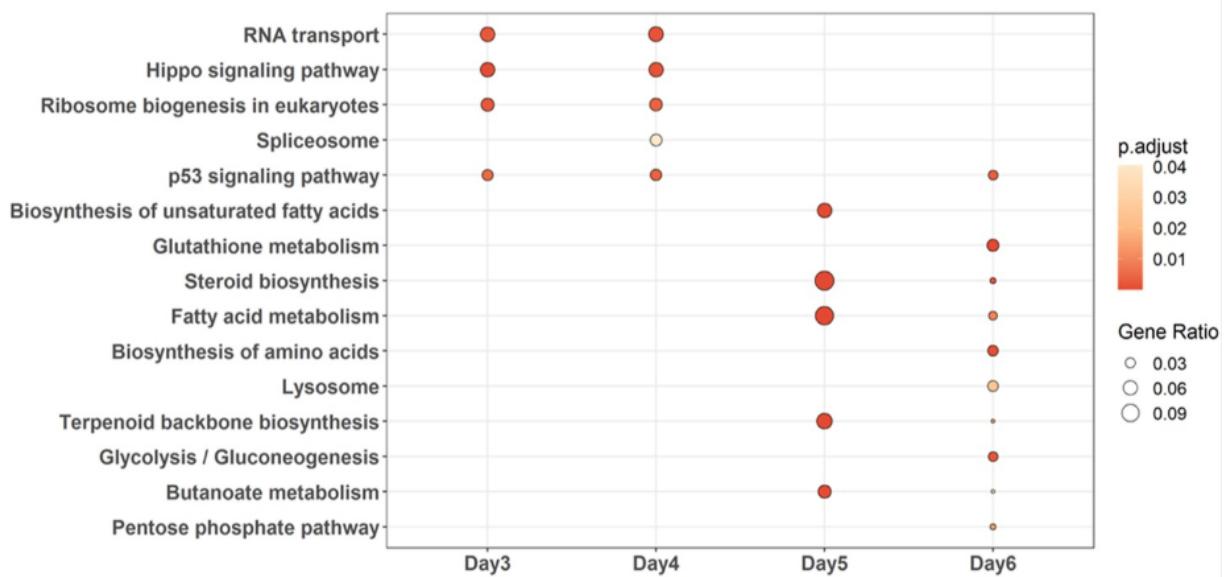


Figure 2.4: KEGG pathway enrichment analysis for differentially expressed genes. The size of the bubble represents the gene ratio and color represents the p-value. Gene ratio is the total number of DEGs in a given GO term (functionally alike gene group)

Pathway enrichment analysis using the KEGG database, illustrated as Bubble Plot (Figure 2.4), revealed pathways like RNA transport, ribosome biogenesis, and spliceosome enriched on days 3 and 4, indicative of transcriptional activation during early pigmentation phases. Day 5 showed up-regulation of metabolic pathways like steroid biosynthesis, unsaturated fatty acid

2.4 Conclusion

synthesis, and fatty acid metabolism. Enrichment of fatty acid metabolism along with the up-regulation of glycolysis and glutathione metabolism could be noted on day 6.

2.4 Conclusion

Numerous studies have stressed the significance of metabolic rewiring as the primary factor influencing cellular responsiveness. Berod et al. and Jha et al. have emphasized the significance of metabolism and metabolites as a driving factor and a crucial predictor of the quality and amount of immune response (Berod et al., 2014; Jha et al., 2015). However, little is known about metabolic rewiring in parenchymal cells like melanocytes. The majority of melanocytes in the epidermis of human skin are differentiated non-dividing cells. These cells must react effectively to physiological cues such as UV rays and/or cytokines to restore physiological equilibrium. Our collaborators at CSIR-IGIB, Delhi, developed a B16 cell pigmentation model that autonomously progresses from basic depigmentation to the pigmented state within six days. This study models various synchronized processes, including signaling, transcriptional activation, melanosome formation, melanin synthesis, and returns to homeostasis. Previous time-series analysis of this pigmentation model had resulted in the identification of interferon- signaling in defining the depigmentation phase of melanogenesis (Natarajan et al., 2014). Here, we analyzed the transcriptomic data of our collaborators to identify the involvement of other molecular pathways such as fatty acid metabolism in melanogenesis.

As expected, several key pigmentation-related genes like MITF, TYR, PMEL and TYRP1 were differentially expressed. The study also revealed that the high MITF levels act as a melanogenic trigger for the rapid uptake of glucose. During pigmentation, glucose is channeled to anabolic pathways that support melanosome biogenesis. Pathway enrichment analysis showed upregulation of fatty acid synthesis, metabolism and oxidation after day 5. The upregulation of fatty acids mediated by SREBF1 leads to the accumulation of lipid droplets and an increase in fatty acid oxidation through mitochondrial respiration. While this heightened bioenergetic activity supports the process of melanogenesis, it also negatively impacts mitochondria, causing a shift in metabolism towards glycolysis. As part of this recovery process, NRF2 detoxication pathways are activated.

In addition to defining a framework for understanding melanogenesis programming, the study identified the key role of SREBF1-mediated fatty acid metabolism during the melanogenic phase. Based on the guinea pig tanning model, our collaborators showed that inhibitors of fatty acid metabolism can resolve hyperpigmentary conditions. Through a topical formulation i.e. Orlistat, they were able to selectively target melanocyte function to treat hyperpigmentary diseases. To

Data analysis to understand metabolic rewiring during melanogenesis

conclude, our study reveals how melanocytes balance energetic and cellular stability by sensing external stimuli to elicit a physiological response during melanogenesis. This knowledge can help in determining how cutaneous pigmentary diseases develop as well as how to treat them.

CHAPTER 3

Boolean modeling of melanogenesis pathway

1 2 3

¹Work in this chapter has been published

²Dnyane P, Gadgil C. Boolean model for melanogenesis. *Phys Biol.* 2021 Feb 25;18(2):026004.DOI: 10.1088/1478-3975/abd3dd.

³Dnyane P, Puntambekar S, Gadgil C. Method for identification of sensitive nodes in Boolean models of biological networks. *IET Syst Biol.* 2018 Feb;12(1):1–6.DOI: 10.1049/iet-syb.2017.0039

3.1 Introduction

Biological pathways are frequently represented as networks, with the biomolecules acting as nodes and connections as edges. Dynamic models can describe how interactions between biomolecules cause their abundances to change over time. There are two types of dynamic modeling approaches: continuous and discrete. Sparse data in continuous dynamic models limit the number of nodes and reactions, which makes it difficult to identify kinetic parameters (Glass and Kauffman, 1973; Karlebach and Shamir, 2008; Thomas, 1973). The simplest type of discrete dynamic modeling is Boolean modeling with abundances represented by 0 (absence/low) and 1 (presence/high). It does not require knowledge of kinetic details. The only information needed is the logic of regulatory interactions such as the activating or inhibitory nature of genetic regulations. As a rule-based binary network, Boolean networks represent the interaction between nodes through logic rules. By updating node states in synchronized or asynchronous ways, the system dynamics can be simulated from a given set of initial node states (Wang et al., 2012). Boolean networks with 10 to 100 or more nodes have been used to study biological systems; a few of these are discussed here as examples.

A general representation of the mammalian cell cycle was converted into a logical regulatory graph of 10 nodes by Faure et. al. This model enabled them to evaluate synchronous versus asynchronous updating schemes in understanding the asymptotic behavior of regulatory networks (Fauré et al., 2006). Albert and Othmer developed a Boolean model of the embryonic segmentation gene network in *Drosophila* with 26 nodes. The model was able to mimic both the ectopic and wild-type expression patterns that were actually seen in different mutations (Albert and Othmer, 2003). An ensemble of random network structures known as random Boolean networks was used by Kauffman to examine the dynamic characteristics of the gene regulation network of 30 nodes in yeast (Kauffman et al., 2004). A T-cell boolean model comprised of 94 nodes was built by Saez-Rodriguez et. al. By transforming this logical model into an interaction graph, they were able to identify feedback loops, signaling routes, and network-wide interdependencies (Saez-Rodriguez et al., 2007). Fumia and Martins developed a Boolean dynamical system of 96 nodes by integrating the various signaling pathways involved in cancer. On a molecular level, this model reproduced some biologically relevant features of carcinogenesis (Fumiã and Martins, 2013).

3.1.1 Existing mathematical models of melanogenesis

There are currently very few models that take intracellular metabolism relevant to keratinocyte and melanocyte pigmentation in the skin into account. Each of these models is a unique kind

3.1 Introduction

that sheds light on the intricate regulatory system that controls melanogenesis at various levels.

Thingnes et. al. formulated a compact model of just 7 species that accurately depicts the dynamics of human skin tanning. The temporal distribution of melanin in the four epidermal layers i.e. basale, spinosum, granulosum, and conreum—following a UV pulse was modeled using differential equations. The degree of dendrification, or how far the melanocyte dendrites develop, has been discovered as a factor controlling phenotypic variance in skin color and tanning capacity (Thingnes et al., 2009). Emir and Kurnaz simulated the production of melanin in melanocytes using an 18 component computer-based model. Through kinetic modeling, they showed that upon growth factor stimulation, the activated MAPK pathway causes transcription factor activation and subsequent expression of melanogenic signal transduction, both of which result in high quantities of melanin being produced. In a separate module, the melanogenic pathway is suppressed with a tyrosinase inhibitor, ultimately reducing the system’s output of melanin. The in-silico effects of various inhibitors or drugs on the entire melanogenic system might be tested with this module (Emir and Kurnaz, 2003). Another model of the melanin biosynthesis pathway of 12 nodes includes metabolites for tyrosine to dopachrome. The model characterizes the kinetic behavior of the monophenolase activity of tyrosinase (Rodríguez-López et al., 1992). To better comprehend melanogenic switching i.e. the switching between eumelanin and pheomelanin synthesis based on the extracellular signaling context, Oyehaung et. al. created a mathematical model with 28 nodes. Their findings confirmed Ito’s theory that the level of tyrosinase activity plays a major role in regulating the transition between the two types of melanogenesis. Dopaquinone, a reactive intermediate in melanogenesis, is quantitatively transformed to glutathionyldopa, which only produces pheomelanin when tyrosinase activity is reduced because of a high amount of agouti. A surplus of dopaquinone is formed when tyrosinase activity is high, which is caused by a high amount of α MSH. This excess dopaquinone inactivates glutathione reductase and γ -glutamyl transpeptidase, two enzymes necessary for pheomelanogenesis. The result of these metabolic processes is eumelanogenesis (Øyehaug et al., 2002).

Raghunath et. al. constructed a network model for UV-mediated skin pigmentation in the epidermis, consisting of 265 components (nodes) with 429 directed interactions between them. This model captures the influence of one component on another and the flow of information within the network. By conducting graph theoretical analysis, they identified critical nodes in the network that, when removed, disrupt the signaling between the source (UV and other inputs) and target (pigmentation and survival) nodes (Raghunath et al., 2015). In a related context, Subramanian et. al. developed the ‘eSkin’ computational platform (Subramanian et al., 2018). The platform has about 2600 genes and a network of 35 manually defined pathways. The specialized platform was made to help with skin-centric omics data analysis and interpretation.

Similar to the Raghunath model, interactions here are characterized qualitatively as connections and edges, and dynamics are not simulated. Lee et. al. made a key contribution by constructing a Boolean model consisting of 62 nodes to represent the signaling network involved in melanogenesis. Through mathematical simulations, the researchers demonstrated that inhibiting β -catenin in melanocytes leads to a significant decrease in melanin production, without affecting the apoptotic equilibrium of the cells (Lee et al., 2015).

3.1.2 Identification of essential nodes in melanogenesis

Finding sensitive nodes in a regulatory network that, when perturbed, cause a significant change in the network output is frequently of interest. For instance, nodes that disproportionately impact survival are possible therapeutic targets in models for signaling or metabolic pathways in pathogens. Finding sensitive nodes in cancer cell pathways has the same rationale. A signaling network's robustness (or lack thereof) can be evaluated by identifying and examining all of its sensitive nodes. Every node or edge is perturbed in order to determine sensitivity and the impact on a collection of node states that have been predefined as the system output is calculated.

Previous studies on the robustness of Boolean networks have used perturbation methods that can be classified in three broad classes: state perturbations, function perturbations and update rule perturbations. A vast majority of studies use state perturbation to explain system properties including node sensitivity. Shmulevich et. al. explored the effect of random gene state perturbation on the entire network, i.e. any gene can flip its value for only one-time point from 0 to 1 or vice versa with probability p (Shmulevich et al., 2002). Lee et. al. performed node control analysis (constitutive state perturbation) to identify an effective target to reduce skin pigmentation. In this method, the state value of each internal regulatory node is fixed at either '0' for inhibition or '1' for constitutive activation and then the activity at steady-state of output nodes is measured (Lee et al., 2015). Fauré et. al. simulated the effect of loss of function and gain of function mutation in mammalian cell cycle by constraining selected nodes within specific value intervals (Fauré et al., 2006). Subramanian and Gadgil showed that transient state perturbation in the *Drosophila Melanogaster* segment polarity network leads to an ectopic expression pattern (Subramanian and Gadgil, 2010). Saadatpour et. al. introduced dynamic perturbation that entails setting the node status opposite to the existing state (diseased state) and normally updating other nodes (Saadatpour et al., 2010).

A node or group of nodes' truth table is altered by function perturbations. Additionally, sensitivity estimates have been made using function perturbations. According to Garg et. al., one gene (or one function) may be defective at any given moment. Another gene (or function) may be defective at a different point along the same trajectory. The function faults [stochasticity

3.1 Introduction

in function (SIF)] are further interpreted as employing a different truth table at that time point; the node faults [stochasticity in nodes (SINs)] are interpreted as a modification of the current state at that moment. They discovered that the SIN approach predicts biologically incoherent behavior while the SIF approach predicts robustness that is more biologically relevant (Garg et al., 2009). The 1 bit function perturbation, which involves flipping the value of a single row in the truth table of a probabilistic Boolean model, is tested by Qian and Dougherty (Qian and Dougherty, 2008). Similar methods were employed in a different study by the same authors, coupled with a change in a probabilistic parameter, namely a change in the likelihood of choosing each constitutive Boolean network in the probabilistic Boolean model and a change in the perturbation probabilities (Qian and Dougherty, 2009).

Change in updating scheme as a means of assessing robustness has been used by a few researchers. Chaves et. al. considered the effect of a perturbation in a synchronous update scheme on the dynamics of the model for the *D. melanogaster* segment polarity genes (Chaves et al., 2005). Perturbation in the time scales or using different kinds of updating schemes in combination with knockout strategies or state perturbation is also an effective way to identify sensitive nodes (Chaves et al., 2005; Kwon and Cho, 2008; Li et al., 2006b). Other studies demonstrate different kinds of perturbations not easily classifiable into these three categories. Structural perturbation strategies have been developed to identify essential nodes in a static network whose disruption can reverse the abnormal state of the signaling network (Saadatpour et al., 2011; Wang and Albert, 2011). Here, the topological intervention involves the ranking of the nodes by the effects of their loss (knockout) on the connectivity between the network's inputs and outputs. There are also many reports studying the effect of function perturbation on an ensemble of Boolean networks but not on a specific Boolean network (Aldana and Cluzel, 2003; Kauffman et al., 2004).

A few researchers have utilized change in updating schemes as a way to measure robustness. The dynamics of the model for the *D. melanogaster* segment polarity genes were examined by Chaves et. al. in relation to the impact of a perturbation in a synchronous update system. Another efficient method to find sensitive nodes is to disturb the time scales or use various updating techniques in conjunction with knockout tactics or state perturbation (Chaves et al., 2005; Kwon and Cho, 2008; Li et al., 2006b). Other investigations show other disturbances of diverse types that are difficult to categorize within these three groups. In order to determine which nodes in a static network are crucial and whose disruption can change the network's aberrant state, structural perturbation algorithms have been devised.

3.2 About this work

The existing dynamic models of melanogenesis do not include the intricate details of the signaling network. Having such a model would help in the simulation and analysis of the complex interplay between keratinocytes and melanocytes. Here, we describe the formulation of a Boolean model based on the nodes included in the Raghunath et al network. The interactions of the 265 nodes in that network were described using 23 different terms (activation, phosphorylation, etc.). Through additional manual curation of the reported interactions, we have converted this description into a set of Boolean rules and formulated the largest Boolean model for melanogenesis reported to our knowledge. In addition, we also carried out a perturbation analysis of the network through node deletion and constitutive activation to identify the sensitivity of outcomes such as melanin to individual nodes and compared the nodes identified as important to previous reports for smaller melanogenesis networks.

3.3 Methodology

3.3.1 Building the Boolean model

A comprehensive network model of UV-mediated skin pigmentation developed by Raghunath et. al. (Raghunath et al., 2015) was used as a basis for our boolean model. The system consists of 265 nodes with 429 directed interactions between them. These 265 nodes represent proteins, small molecules, complexes, biological processes and environmental factors. Of these nodes, 20 are source/input nodes and 9 are output nodes. Detailed literature references provided by Raghunath et. al. for individual interactions served as an excellent starting point for converting this model into a Boolean model. In Raghunath et. al. network, edges are directed based on the functional nature of their interaction, such as phosphorylation or activation. Likewise, there are a total of 23 interaction types (Table 3.1).

We have gone back and reviewed each interaction, and we have added more precision by formulating Boolean rules. Our goal in doing this is to improve the biological relevance of the model and make it possible to simulate system dynamics, including how the system responds to different levels of UV. For instance, when multiple nodes positively influence the activity of a target node, we have created rules that allow either one or all of the inputs to change the activity level of the target node (using either an OR gate or an AND gate, respectively). However, it is also possible that some nodes are required, while others are redundant, which would call for a combination of AND and OR rules. We have carefully examined relevant literature to

3.3 Methodology

S. No.	Expression relation	Frequency	S. No.	Expression relation	Frequency
1	Increases level	23	12	Catalysis	7
2	Induces	25	13	Decreases	1
3	Inhibits	24	14	Decreases expression	1
4	Activates	195	15	Dissociates to	7
5	Associates	1	16	Forms complex	18
6	Binds	1	17	Gets converted to	16
7	Increases expression	82	18	Induces complex dissociation	6
8	Increases	3	19	Induces complex formation	3
9	Inhibits expression	1	20	Increases release	6
10	Involved in	1	21	Increases stability	1
11	Regulates	5	22	Phosphorylates/activates /degrades	3

Table 3.1: Types of interactions and their distribution in the network

determine which mode of interaction best represents biology, and we have not made any general assumptions when formulating our Boolean rules. We have included a few examples of how we have defined interactions (refer to Tables 3.2–3.4) to develop these rules.

Input node	Target node	Interaction type
ACTH_kerat_kerat	MC1R_melan	activates
USF1_melan	MC1R_melan	increases
MITF_melan	MC1R_melan	increases expression
α _MSH_kerat	MC1R_melan	activates

Table 3.2: Individual interactions for MC1R_melan as defined by (Raghunath et al., 2015)

The α _MSH ligand of MC1R is a crucial factor in UV-induced tanning in humans. When the skin is exposed to UV light, α _MSH expression is strongly induced in keratinocytes, and its binding to MC1R stimulates the activation of MC1R and downstream signaling proteins (D’Orazio et al., 2006). α _MSH is a peptide derived from ACTH that is produced in the pituitary gland and other tissues, including the skin. Wakamatsu et. al. found that ACTH peptides might also work as natural ligands for MC1R receptors in melanocytes, suggesting that they might regulate melanocyte activity along with α _MSH (WAKAMATSU et al., 1997). The transcription factor MITF regulates the expression of genes essential to cell differentiation, proliferation, and survival. MITF binds specifically to M and E boxes (motifs) found in the promoters of target genes such as tyrosinase (TYR). Analysis of the MC1R promoter reveals the presence of an E box immediately upstream of the transcriptional initiation site. This motif suggests that MC1R gene expression may be regulated by MITF (which can increase MC1R activity up to five-fold) (Aoki and Moro, 2002). MC1R expression following UV induction is dependent on the presence of the USF1 transcription factor, whereas constitutive gene expression is not (Corre et al., 2004). Hence the rule for MC1R_melan is:

$$\text{MC1R_melan} = (\text{ACTH_kerat AND USF1_melan AND MITF_melan}) \text{ OR } \alpha_MSH_kerat$$

Input node	Target node	Interaction type
DNA_Damage_kerat	NFKB1_kerat	activates
IKBKA_kerat	NFKB1_kerat	activates
MC1R_kerat	NFKB1_kerat	inhibits
PKC_kerat	NFKB1_kerat	activates
PRKCZ_kerat	NFKB1_kerat	activates

Table 3.3: Individual interactions for NFKB1_kerat as defined by (Raghunath et al., 2015)

Binding of α _MSH to MC1R results in elevated intracellular cAMP levels and reduced NFKB activity (Garcin et al., 2009). ACTH serves as a precursor for α _MSH and α _MSH binding stimulates MC1R but it is only MC1R that interacts and inhibits basal NFKB levels in keratinocytes. IKBKA inhibits/destabilizes NFKB by phosphorylating it at ser-932 (Heissmeyer et al., 1999). DNA-damaging agents activate NFKB in a canonical IKK complex-dependent fashion. Upon activation of the IKK complex, the IKK β subunit directly phosphorylates NFKB-associated IKBKA, leading to its proteasomal degradation and release of p65/p50 heterodimer. Free NFKB then translocates into the nucleus and regulates gene transcription (Beals et al., 1997; Hirotani et al., 2004). phosphorylation of p50 and p65 by the catalytic subunit of protein kinase a (PRKACA) and PRKCZ is essential for NFKB DNA binding and transactivation activity (Goon Goh et al., 2008; Perkins, 2007; Guan et al., 2008; Duran et al., 2003).

Taking together all the information, the Boolean rule for NFKB1_kerat can be written as:

$$\text{NFKB_kerat} = \text{IKBKA_kerat AND (NOT MC1R_kerat) AND PKC_kerat AND PRKCZ_kerat AND DNA_Damage_kerat}$$

Input node	Target node	Interaction type
AKT1_melan	CREB1_melan	Activates
MAPK14_melan	CREB1_melan	Activates
PRKACA_melan	CREB1_melan	Activates
PRKG1_melan	CREB1_melan	Activates
PRS6KA1_melan	CREB1_melan	Activates

Table 3.4: Individual interactions for CREB1_melan as defined by (Raghunath et al., 2015)

In order to activate the transcription factor CREB1, it is must be phosphorylated. There are two possible pathways to achieve this: through cAMP/PRKACA signaling or through the involvement of Akt, MAPK14, PRKG1, and PRS6KA1 (D'Mello et al., 2016; Berthon et al., 2015; Zhang et al., 2012b; Pugazhenthii et al., 2000; She et al., 2002). CREB1 activation can be achieved by either cAMP or PRKACA alone. If these are absent, Akt, MAPK14, PRKG1, and PRS6KA1 are all required for activation via serine-133 phosphorylation. As a result, the Boolean rule for CREB1 is:

3.3 Methodology

$$\text{CREB1_melan} = (\text{cAMP_melan OR PRKACA_melan}) \text{ OR } (\text{AKT1_melan AND MAPK14_melan AND PRKG1_melan AND RPS6KA1_melan})$$

Likewise, rules were formulated for all 265 nodes through manual curation. The simulations were performed using MATLAB 9.5 (R2018b, Mathworks) and synchronous updating was used throughout. The simulations of both the Lee model and the new model were conducted with varying percentages of UV input, where the percentage of updating steps when the UV node state is on was fixed to match the UV percentage. For each UV level, the activity at steady-state of the output node was calculated as a sum of the last 100 of 1000 updating steps for each of 100 random initial conditions. The sequence of zeros and ones representing the on and off states was randomized using the MATLAB function `randperm` to ensure that there was no discernible pattern.

3.3.2 Comparison with existing model

The largest known Boolean model for melanogenesis so far is the one created by Lee et al, which comprises 62 nodes (Lee et al., 2015). By comparing the networks used by Lee et al and this work, it was discovered that 56 nodes are common between them. The sensitivity of these 56 common nodes was compared to the sensitivity reported by both studies. Lee et al. used simulations of their Boolean model to predict how individual nodes would respond to varying levels of UV input. Similarly, we performed simulations with synchronous updating and calculated the similarity in profiles for the 56 common nodes in terms of the Pearson correlation coefficient for their UV response. To determine the correlation between a node in the new model and the corresponding node in the Lee model, we calculated the Pearson correlation coefficient for steady-state values/output using the equation $R_i = \text{correlation}(S_i^l, S_i^n)$, where R is the Pearson correlation coefficient, S_i^l is a vector representing activity at steady-state of node i in the Lee model for all levels of UVB inputs, and S_i^n is a vector representing activity at steady-state of the same node (i) in the new model. It is important to note that the Pearson correlation coefficient is a rough measure for comparing the results of a qualitative model that has been simulated with a random input sequence for each UV level. Therefore, its interpretation is intended to be qualitative in nature (i.e., roughly similar, indicated by a substantially positive value, or anticorrelated, indicated by a large negative value) rather than as a quantitative similarity measure.

3.3.3 Perturbation Analysis

The analysis of Boolean networks involves identifying nodes that have a significant impact on a specific output when perturbed. Here, we have come up with two novel methods of function perturbation, which we have utilized to identify sensitive nodes in two specific networks. Our methods are widely applicable to any Boolean model or probabilistic Boolean model. We applied these perturbations to the melanogenesis signaling network (Lee et al., 2015) and *D. melanogaster* segment polarity network (Albert and Othmer, 2003). The two new function perturbation methods to identify sensitive nodes will be described below, followed by the application of these methods on existing Boolean networks.

3.3.4 Two new function perturbation methods

In a network, each node j is associated with a variable $x_j(t)$ that describes its expression level at time t . In Boolean models with synchronous updating, the future state of node j $x_j(t + 1)$, is determined by a logic rule that uses the current states of its regulators (inputs). This rule is denoted by i.e., $x_j(t + 1) = F_j[x(t)]$, where F_j is a Boolean rule and x is the vector of all node states.

The natural environment for biological processes is inherently noisy, so we conducted a simulation to study the effects of two permanent defects in the regulatory network. These defects occur in nodes when input signals are misinterpreted or output calculations are incorrect, even when the inputs are received correctly. To capture these perturbations, we used two methods: the function of not (FoN) and not of function (NoF), as shown in Figure 3.1A. Biological regulatory networks are similar to electrical circuits, where nodes are components that receive inputs and produce an output based on the input. The NoF perturbation simulates a defective node that reads inputs correctly but produces incorrect output. For example, a node that is activated by the binding of two components would be deactivated in a malfunctioning node with an NoF perturbation if both inputs are present. The FoN perturbation simulates a node that functions properly in logic but misreads the inputs, resulting in a node that is active only when both inputs are absent. We incorporated these perturbations by flipping the output of the function (NoF) or by flipping all the inputs to the function (FoN), as illustrated in Figure 3.1.

The effect of node perturbation on the output is evaluated by comparing it with the output in the absence of perturbation (WT) using similarity metrics like correlation coefficient and Euclidean distance. The steady-state values/pattern of output for the WT and perturbed network are calculated before and after function perturbation using equations to determine the correlation and distance between them.

3.3 Methodology

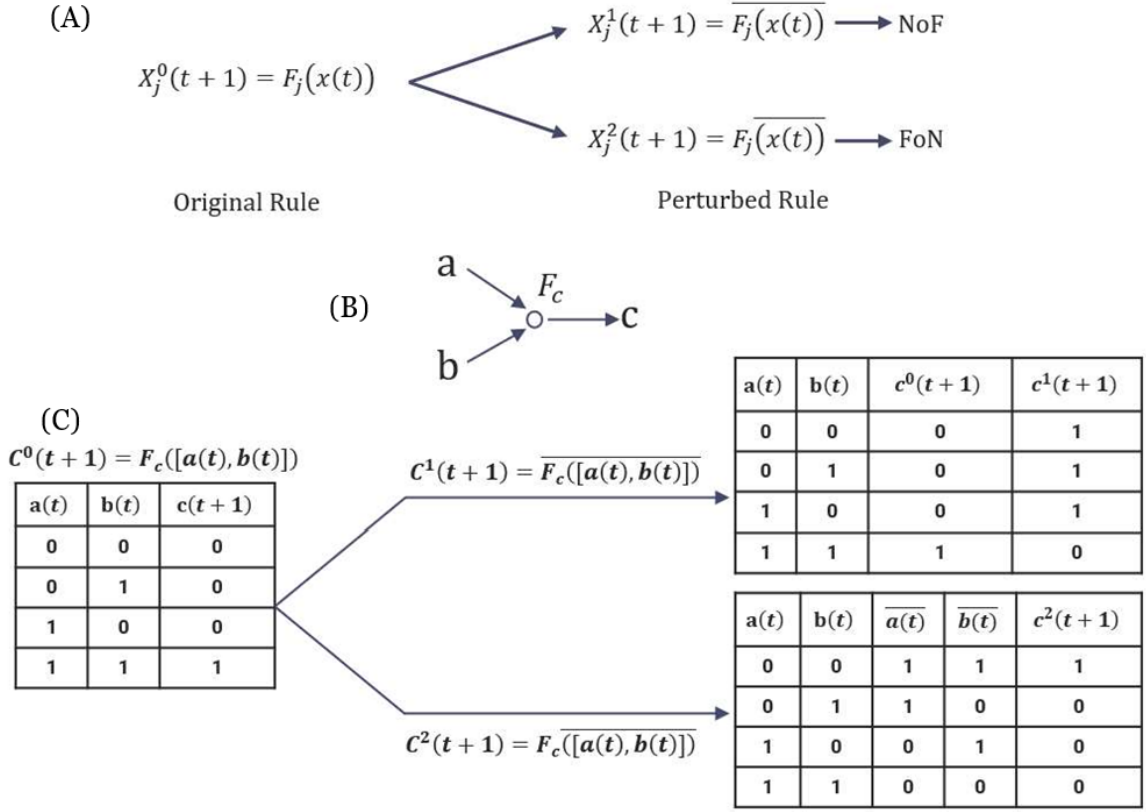


Figure 3.1: Methods of function perturbation with an example :(A) FoN and NoF Equations (B) Example model, (C) Both a and b are required to activate c but ‘NoF’ perturbation (c^1) will result in inhibition of c, i.e. not of output. Similarly, with ‘FoN’ perturbation (c^2) only inputs are flipped

$$R_{i,j}^k = correlation(\underline{S}_{i,j}^k, \underline{S}_i^0)$$

$$D_{i,j}^k = distance(\underline{S}_{i,j}^k, \underline{S}_i^0)$$

$$AvgD_{i,j}^k = distance(\underline{S}_{i,j}^k, \underline{S}_i^0)/n$$

Here nature of perturbation is denoted by $k \in \{0, 1, 2\}$, $i \in \{output\ nodes\}$ and $j \in \{all\ nodes\}$ respectively. R is the correlation coefficient, D is Euclidean distance and $AvgD$ is the average distance across all the n levels of UV or in general over the length of the vector \underline{S}_i^0 . $\underline{S}_{i,j}^k$, represents this activity at steady-state vector of output node i for all levels of UVB input when node j is subjected to a perturbation of type k , where $k = 0, 1, 2$ represents no perturbation (WT), NoF perturbation and FoN perturbation, respectively. \underline{S}_i^0 denotes the steady-state activity of output node i for WT condition ($k = 0$) for all levels of inputs. We apply these perturbations to two existing Boolean models. The identified sensitive nodes were then compared with those given in previous studies for constitutive state perturbation.

For the newly developed boolean model, we focused on nodes related to pigmentation and

cell survival in melanocytes and keratinocytes, which were the same nodes used in a previous study by Lee et. al. Two types of perturbation methods were used: constitutive activation and inhibition. The goal was to identify targets in the network that could reduce pigmentation while ensuring safety. Lee et. al. had previously developed these methods. The researchers simulated constitutive activation and inhibition of each node by setting the node state to 1 and 0, respectively. The UV input was varied from 0% to 100%. They obtained a "wild-type" profile of the average state of each node at each UV level in the absence of any perturbation. The sensitivity of each node was estimated by calculating the post-perturbation change in the profile of four output nodes: BCL2 in keratinocyte (BCL2K), BCL2 in melanocyte (BCL2M), eumelanin, and pheomelanin.

3.4 Results

3.4.1 New model for melanogenesis captures the response of the system to UV

Despite the vast size of the state space in the melanogenesis network, steady-state was observed within 1000 updating steps after running simulations for 2000 updating steps. We conducted simulations using 10, 50, 100, and 150 initial conditions and found that mean and standard deviation values remained largely constant when using 100 or more initial conditions. We calculated the attractor mean value as the average of the last 100 updating steps. The UV input's likelihood of being on or off was allocated at random for each simulation run, and the intensity of UVA and UVB was set to 0%, 25%, 50%, 75%, and 100%. Every iteration included randomization of the initial states of every node (50% '0' and 50% '1'), and the mean value presented is an average of 100 initial conditions. By monitoring the steady-state activities of the output nodes eumelanin, pheomelanin, and BCL2-kerat, the pigmentation state and apoptotic balance of the cells were identified. The findings (Figure 3.2) show that the melanogenesis network model accurately reflects the qualitative characteristics of the known biochemical processes of the species in the system. According to studies in the literature, exposure to UV radiation increases skin pigmentation. Our simulations demonstrate that both models anticipate a drop in BCL2-K levels with UV, which is in line with experimental findings (Tadokoro et al., 2005; Gillardon et al., 1994).

In addition to eumelanin and pheomelanin, there are 7 other terminal nodes in the graphical network of Raghunath et. al., and our model successfully captured the qualitative response of these target nodes to changing UV levels (Figure 3.3). A study by Gillardon et. al. showed that UV irradiation of mammalian skin cells causes growth arrest and cell death followed by hyperpro-

3.4 Results

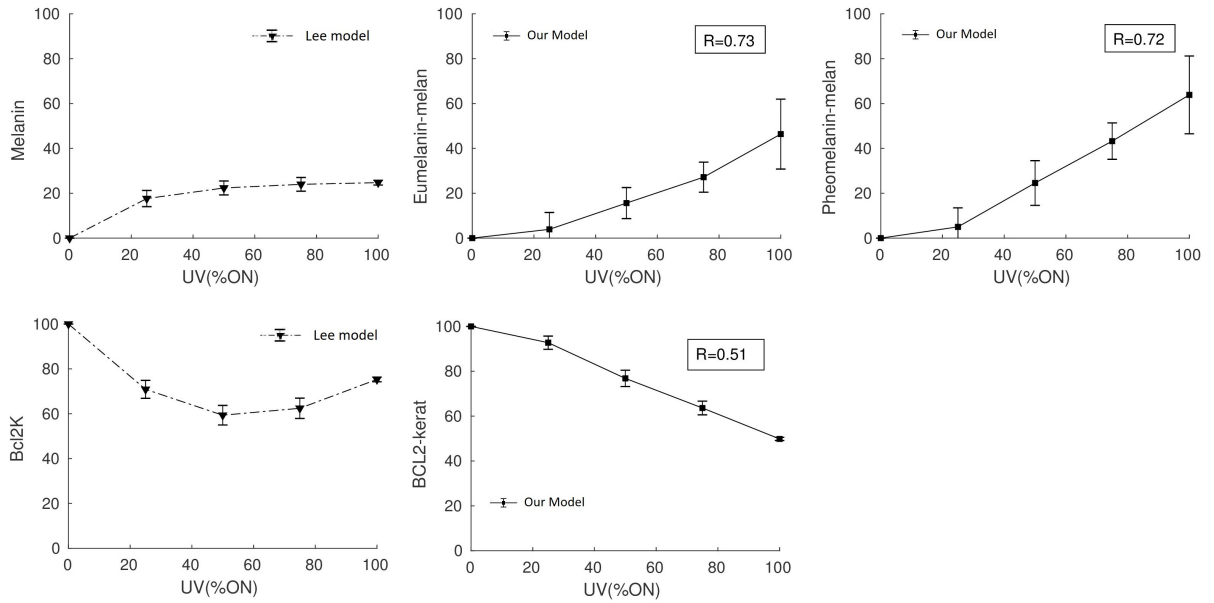


Figure 3.2: Qualitative, individual input–output relationships in the Boolean model of melanogenesis network. The nodes for keratinocytes and melanocytes are denoted by ‘kerat/K’ and ‘melan/M’, respectively. The activity at steady-state of each output node is represented by a single point, which reflects the average value. The standard deviation is represented by error bars, while the correlation coefficient is denoted by R . Error bars represent the dispersion of results obtained from 100 distinct initial conditions. Row (A) shows the comparison between melanin from the Lee model and eumelanin and pheomelanin from the new model. (B) Comparison of BCL2 activity between both models.

liferation of epidermal cells (Gillardon et al., 1994). According to Scott and Cassidy’s research, hormones and exposure to ultraviolet light can stimulate dendrite formation in melanocytes (Scott and Cassidy, 1998). Bessou et al discovered during their investigation of pigmentation physiology that UV irradiation speeds up melanosome transfer from dendritic melanocytes to keratinocytes (Bessou et al., 1995). Another study by Bivik et. al. demonstrated that UV radiation causes anti-apoptotic factors such as BCL2 to be transported to the mitochondria, where they prevent the release of cytochrome C in the cytoplasm, ultimately safeguarding the cell from apoptosis (Bivik et al., 2006). Despite the construction of Boolean rules for each node in the extensive network, the model’s predictions for the output response to varying UV exposure are consistent with these experimental findings.

3.4.2 Comparison with the Lee model

We compared our results with the output of the Lee model by quantifying the similarity between the nodes using the correlation coefficient. To do this, we calculated the correlation between a

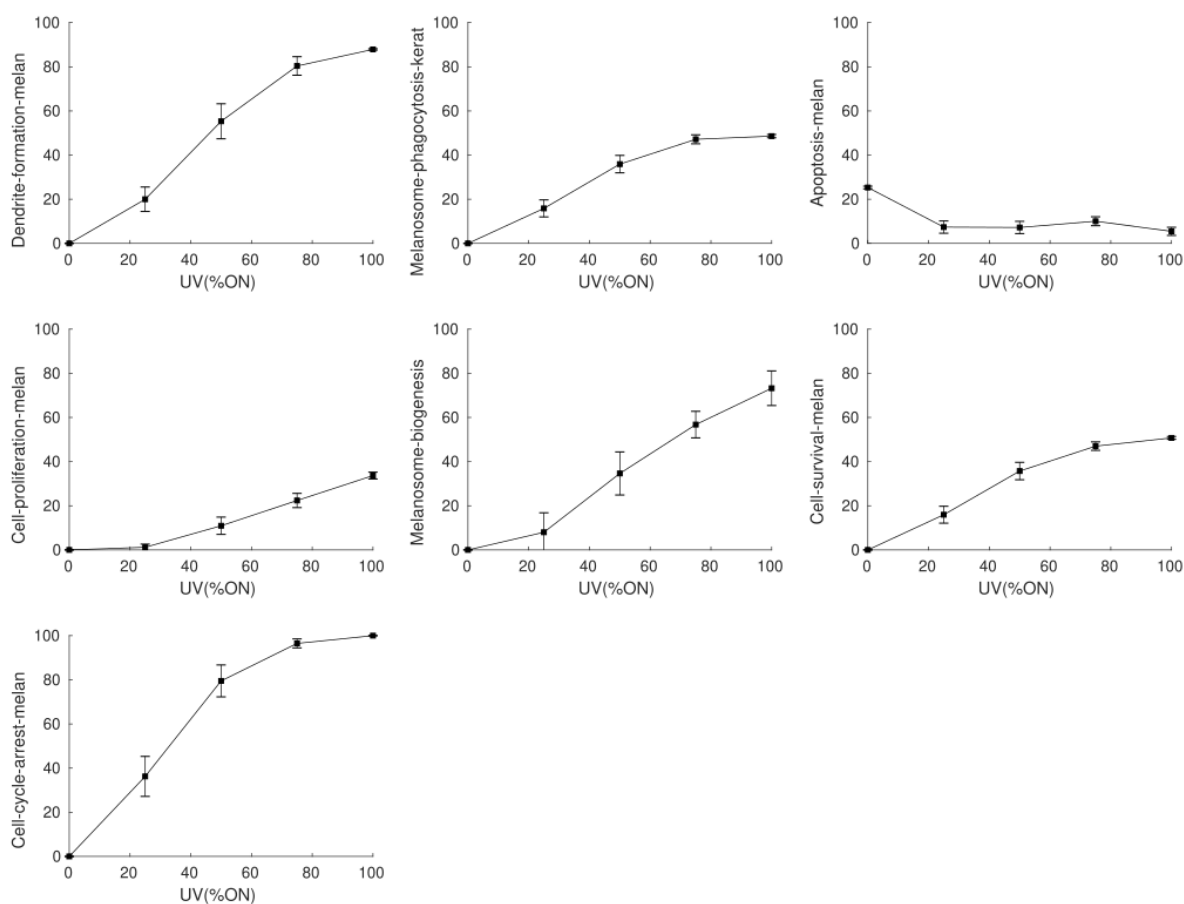


Figure 3.3: The qualitative relationships between individual inputs-outputs in the melanogenesis network. The term 'kerat' refers to the nodes of keratinocytes, while 'melan' refers to the nodes of melanocytes. Each data point represents the average activity at steady-state of the output node at five different UV exposure levels (0%, 25%, 50%, 75%, and 100%). The error bars represent the standard deviation. The following relationships were observed: (A) A positive correlation was found between UV exposure and cell-cycle-arrest-melan. (B) A positive correlation was found between UV exposure and cell-survival-melan. (C) A positive correlation was found between UV exposure and cell-proliferation-melan. (D) A positive correlation was found between UV exposure and dendrite-formation-melan. (E) A positive correlation was found between UV exposure and melanosome-biogenesis activation. (F) A positive correlation was found between UV exposure and melanosome-phagocytosis. (G) A negative correlation was found between UV exposure and apoptosis-melan.

node in our model and its corresponding node in the Lee model, specifically for steady-state values/output, using the equation described in the methods section. Figure 3.4 displays a selection of nodes and their corresponding correlation coefficients.

Of the 56 common nodes between the models, 46 were positively correlated ($R_i > 0.3$, see Figure 3.5). These nodes included critical nodes, such as eumelanin, pheomelanin, and BCL2 in keratinocytes and melanocytes, as defined by Lee et. al. On the other hand, the list of negatively

3.4 Results

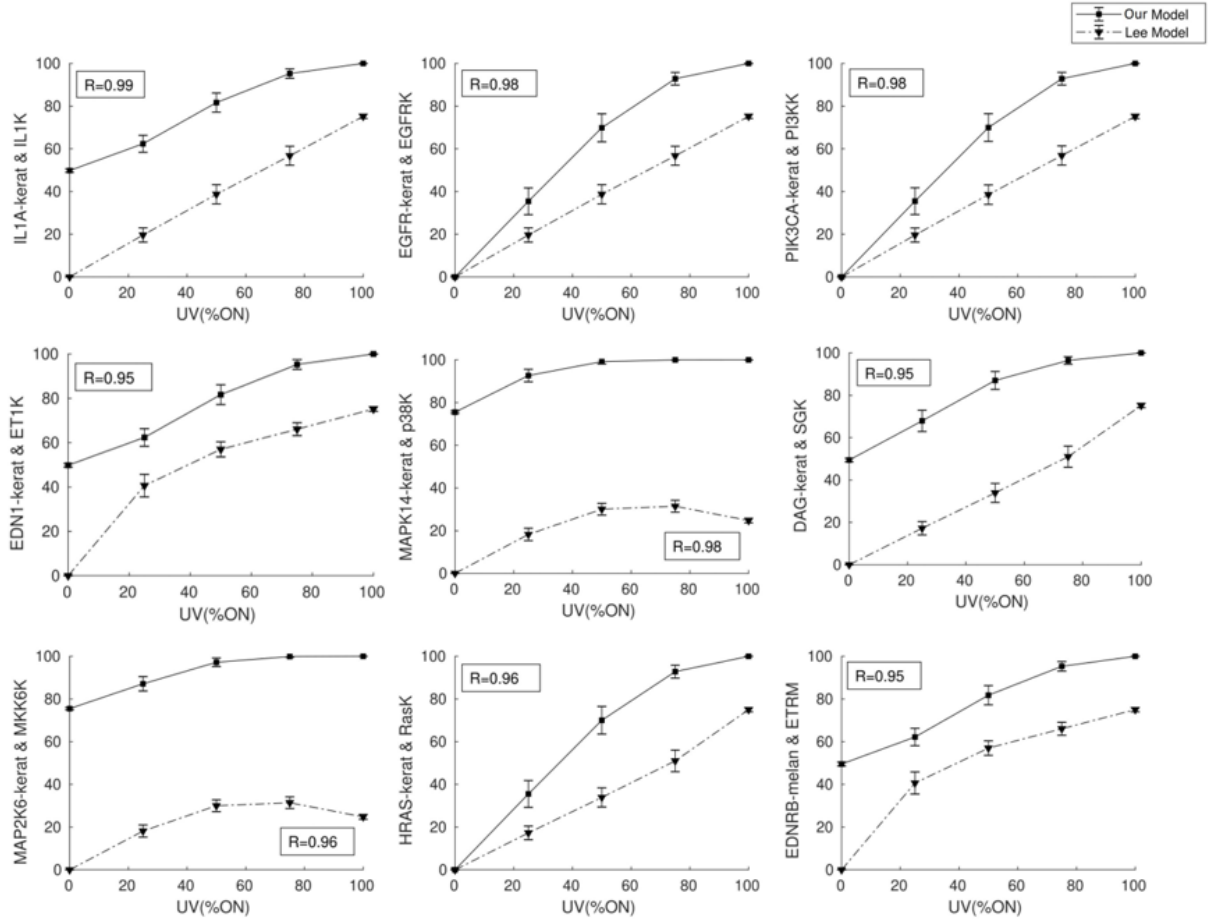


Figure 3.4: Comparing the effect of UV radiation on the few selected nodes in the existing model and the newly developed Boolean model. The activity at steady-state of the output node was measured at five different UVB levels (0%, 25%, 50%, 75%, and 100%). The standard deviation was represented by error bars, and the correlation coefficient was denoted by R . In the new model, the keratinocyte and melanocyte modules were equivalent to K and M in the Lee et al model.

correlated nodes included kinases, as well as a few other nodes like adenylate cyclase and CREB.

A comparison of the Boolean rule between the two models revealed that while some nodes had identical rules and regulating nodes, several others had different participating nodes. This outcome was expected due to the presence of additional nodes in the new network.

3.4.3 Identification of sensitive nodes in the new model

We determined the impact of perturbation in the melanogenesis network by comparing the activity profiles of output nodes, including eumelanin, pheomelanin, BCL2_melan, and BCL2_kerat, with their unperturbed profiles under 0%, 25%, 50%, 75%, and 100% levels of UVB exposure. The perturbations were designed to mimic knockouts and continuous activation of certain nodes,

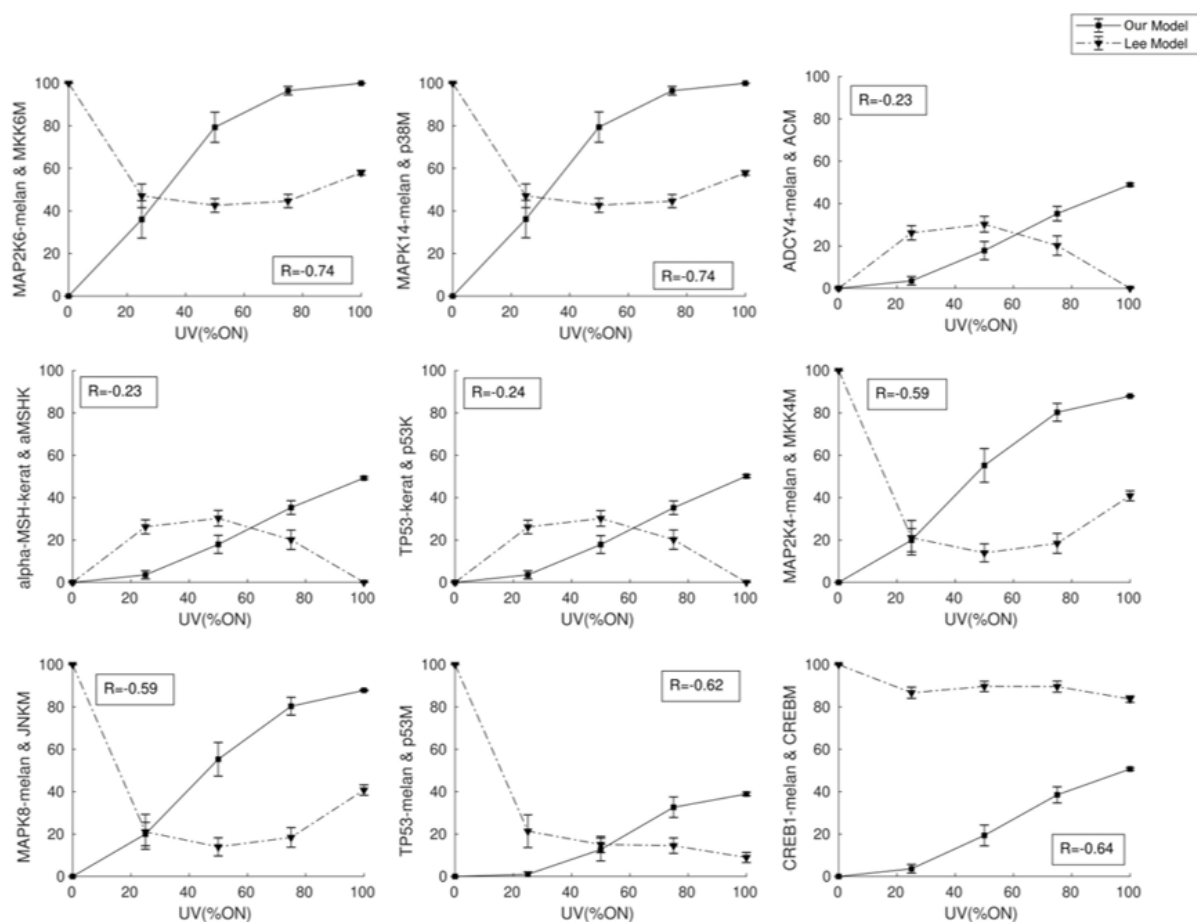


Figure 3.5: Comparing the effect of UV radiation on the few negatively correlated nodes in the existing model and the newly developed Boolean model. The activity at steady-state of the output node was measured at five different UVB levels (0%, 25%, 50%, 75%, and 100%). The standard deviation was represented by error bars, and the correlation coefficient was denoted by R . In the new model, the keratinocyte and melanocyte modules were equivalent to K and M in the Lee et al model.

and nodes that caused constant activation or inactivation of output nodes were deemed "sensitive" and marked as such in Table 3.5. Nodes were considered sensitive if their activation/inactivation represented a qualitative departure from the unperturbed system dynamics. The comparison between the new and previous models revealed that the new model had a greater number of sensitive nodes, as expected given its larger size and complexity. Fewer sensitive nodes were consistently identified in both models, including MITF and CREB, the key transcription factors involved in melanogenesis regulation.

The new model identifies nodes that are not part of the Lee et. al. model as sensitive, including dopachrome and tyrosinase, both of which have experimental support for their importance in the melanogenesis process. Dopachrome reacts with cysteine or glutathione to produce

3.4 Results

the benzothiazine derivatives of pheomelanin, while tyrosinase catalyzes the tautomerization of dopachrome to 5, 6-dihydroxyindole-2-carboxylic acid (DHICA), which is later oxidized to eumelanin (Ebanks et al., 2009). By inhibiting lipid peroxidation, protocatechuic acid decreases melanin production in α -MSH induced B16 cells (Chou et al., 2010). 4-HNE is a highly reactive molecule made from lipid peroxidation reactions caused by ultraviolet radiation exposure. PLC is responsible for producing secondary messengers called IP3 and DAG. DAG activates PKC, which then activates other proteins in the cytosol like NF κ B (HUANG et al., 2011; Adams et al., 2007). KIT is a growth factor produced by keratinocytes that stimulates Ras phosphorylation by activating a signaling pathway composed of KIT receptor, SHC protein, GRB2 and SOS. As a result, Raf1 and MAPK pathways are activated (Imokawa and Ishida, 2014). This chain reaction of activation results in MITF phosphorylation, which allows the transcriptional coactivator CREB to be recruited. This, in turn, leads to the transcription of melanogenic enzymes TYR, TYRP1, and TYRP2 (Hemesath et al., 1998; Rönstrand, 2004; Buscà et al., 2000). The new model has 429 connections between 265 nodes making it difficult to apply function perturbations. However, we applied our newly developed function perturbation methods to existing smaller models and found that it is successful in identifying previously unreported sensitive nodes.

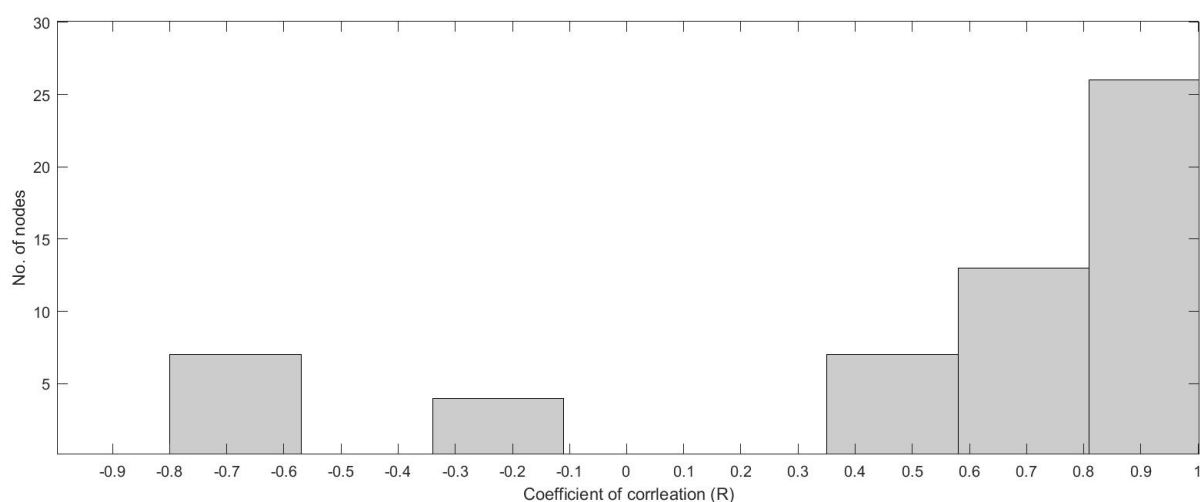


Figure 3.6: Distribution of coefficient correlation (R) values in the new model. R values are obtained by comparing the response of common node to varying UV levels

Boolean modeling of melanogenesis pathway

	Sensitive nodes (Lee model)	Insensitive nodes (Lee model)
Sensitive Nodes (new model)	MITF_melan, CREB1_melan, cAMP_melan, RAF1_melan	FourHNE_kerat, ADCY4_melan, α _MSH_kerat, Calcium_cyt_kerat, CASP3_kerat, Ceramide_kerat, DFFB_DFFA_kerat, DFFB_kerat, DNA_Damage_kerat, DOPA_melan, dopachrome_melan, Dopaquinone_melan, IKBKA_kerat, IP3_kerat, Lipid_Peroxidation_kerat, MITF_EP300_melan, NFKB1_kerat, PKC_kerat, PLC_kerat, PRKCB_melan, PRKCZ_kerat, RYR1_kerat, TNF_kerat, TYR_melan, HRAS_melan, SOS1_GRB2_SHC1_melan, ACTH_kerat, Indole_5_6_quinone_carboxylic_acid_melan, Indole_5_6_quinone_melan, PRKACA_melan, TP53_kerat, MAP2K1_melan, MAP2K2_melan, MAPK1_melan, MAPK3_melan, RPS6KA1_melan, Cysteinyl_DOPA_melan, Glutathionyl_DOPA_melan, NGF_kerat
Insensitive Nodes (new model)	ASK1M, MKK6M, p38M, GSK3bM, ERKM, AktM, PI3KM, PDK1M, MEKM, bcateninM, ASK1K, MKK6K, p38K, AktK, EGFRK, PI3KK, PDK1K, BCL2K, MITFproteinM, MKK4M, JNKM, p53M	30 common insensitive nodes in both models

Table 3.5: Sensitive nodes identified in both models. A sensitive node is one that is identified as sensitive when constitutively activated or inhibited, but does not belong to the other model

3.4.4 Effect of function perturbations in the Lee model

By comparing the activity profiles of the output nodes melanin, BCL2M, and BCL2K to their respective unperturbed output profiles for the inputs of 0%, 25%, 50%, 75%, and 100% UVB, the effect of function perturbations in the melanogenesis network was calculated. The change in the output's activity profile was determined using the metrics mentioned in the methodology

3.4 Results

section. Nodes with correlation coefficient values less than 0.8 or the top five Euclidean distance scores were chosen as sensitive nodes (Table 3.6). Figure 3.7 shows sensitive nodes with a correlation coefficient of 0.8. The network's nodes were also subjected to constitutive activation and inhibition perturbations, as described by Lee et. al., and their effects on the outputs were evaluated using the same metrics. The sensitive nodes were subjected to function perturbation, which produced a Euclidean distance score for melanin between 126 and 180. This is the same as $AvgD \geq 25$. Likewise, the $AvgD$ scores for BCL2M and BCL2K were in the range of 21–24 and 20–30, respectively. For constitutive activation and inhibition, the average D values for melanin, BCL2M, and BCL2K are respectively 30–36 and 7–9, 30–32 and 12–20. With a few exceptions, the comparison revealed that the majority of the nodes classified as sensitive by function perturbations coincide with the findings of state perturbation analysis (non-underlined nodes in Table 3.6). There are reports in the literature that point to the significance of these nodes. For instance, an experimental work by Jost et. al. demonstrated that down-regulation of BCL2 expression and higher vulnerability to cell death induction are both related to the suppression of MAPK/ERK kinase (MEK) enzymatic activity in keratinocytes (Jost et al., 2001). Moreover, nodes identified as sensitive by the new techniques and perturbations caused by constitutive activation/inhibition are supported by published data. For instance, it is known that activation of the MITF promoter, which encourages melanogenesis, activates the cAMP response element-binding protein (CREB) (Saha et al., 2006).

3.4.5 Effect of function perturbations in *D. melanogaster* segment polarity network

The way in which the *D. melanogaster* segment polarity gene is expressed and maintained involves interactions between different gene products such as secreted proteins, receptors, and transcription factors that are expressed by cells in a particular area. Von Dassow developed a continuous state model for predicting patterning and concluded that it was robust to the choice of reaction rate constants. (von Dassow et al., 2000). Albert and Othmer took this idea further by creating a Boolean model of the regulatory network, which did not require any rate parameter (Albert and Othmer, 2003). This model consisted of 14 cells across four parasegments, with each cell having 15 nodes. Simulations were performed using Boolean updating rules and initial conditions specified by Albert and Othmer (Albert and Othmer, 2003). The simulations were carried out until the system reached an attractor state and then perturbations were applied to individual nodes by subjecting them to constitutive activation or inhibition. The sensitivity of nodes was identified by a qualitative difference in the attractor state or by a 20% difference in node states compared to the wild-type. The simulations

were conducted using MATLAB 2015b. For each node in all the cells in all the parasegments, the Boolean function was perturbed in order to find sensitive nodes in the segment polarity network. For a selected few nodes, it was found that when the logic function was disturbed, the system tended to move closer to a cyclic attractor. This circumstance greatly contrasts with the WT pattern, in which the system approaches a point attractor. It suggests a dynamic behaviour in the system, possibly indicating a periodic or oscillatory response under certain conditions of perturbation. As a result, these nodes were considered sensitive (Table 3.7). The Euclidean distance was determined for the remaining nodes (node perturbations resulting in point attractors), and if the distance was more than 3.35, the node was classified as sensitive. This is comparable to the requirement that when a given node is perturbed, the expression value for at least 20% other nodes (11 out of 56) should change. Previous constitutive inhibition investigation has demonstrated that null mutations of specific genes in the segment polarity network produce various steady-state patterns, such as "no segmentation pattern" and "wide stripes pattern" (Albert and Othmer, 2003). Similar to how critical and benign nodes are recognized by transient perturbation, these are nodes where a disturbance results in an alternate steady state or the "wide stripes pattern" (Subramanian and Gadgil, 2010). Using the new function perturbation techniques, we were able to successfully identify the majority of the nodes that had been previously classified as sensitive. There are also some rare cases in which previously recognized sensitive nodes are not revealed to be so by FoN or NoF perturbations, and new nodes are discovered to be sensitive (Table 3.7). Our data show that patterning is responsive to cubitus interruptus disruption. The findings of Albert and Othmer are in contrast with this. Curiously, the experimental literature also appears to be mixed, with one report claiming that cubitus interruptus (CI) is not necessary before embryonic stage 11 (Gallet et al., 2000) and another claiming that CI is "absolutely required" for hedgehog signaling (Méthot and Basler, 2001). Several perturbation approaches can be used to evaluate sensitivity because it appears likely that the node sensitivity varies under various circumstances.

3.4 Results

	Constitutive activation	Inhibition	NoF	FoN
Melanin	<u>MITFproteinM</u> , <u>PKCM</u> , <u>RasM</u> , <u>ET1K</u> , <u>ETRM</u> , <u>SGM</u> , <u>IL1K</u>	ERKM, AktM, PI3KM, RafM, PDK1M, MEKM, <u>MITFproteinM</u> , <u>bcateninM</u> , CREBM, <u>IL1K</u> , ASK1M, MITFmRNAM, p38M, MKK6M	<u>MITFproteinM</u> , <u>SGM</u> , <u>IL1K</u> , <u>RasM</u> , <u>ET1K</u> , <u>ETRM</u> , <u>PKCM</u>	<u>RasM</u> , <u>ET1K</u> , <u>MITFproteinM</u> , <u>ETRM</u> , <u>PKCM</u>
BCL2M	<u>AktM</u> , <u>PI3KM</u> , <u>PDK1M</u> , <u>PKCM</u> , <u>ET1K</u> , <u>ETRM</u> , <u>RasM</u> , <u>SGM</u> , <u>IL1K</u>	<u>ASK1M</u> , <u>p38M</u> , <u>MKK6M</u> , <u>AktM</u> , <u>PI3KM</u> , <u>PDK1M</u> , <u>CREBM</u>	<u>SGM</u> , <u>IL1K</u> , <u>AktM</u> , <u>RasM</u> , <u>ET1K</u> , <u>ETRM</u> , <u>PDK1M</u> , <u>PI3KM</u>	<u>RasM</u> , <u>ET1K</u> , <u>ETRM</u> , <u>PKCM</u> , <u>PDK1M</u> , <u>AktM</u>
BCL2K	<u>ASK1K</u> , <u>MKK6K</u> , <u>p38K</u> , <u>MKK4K</u> , <u>JNKK</u> , p53K, <u>RasK</u> , ERKK, RafK, <u>SGK</u>	<u>PDK1K</u> , <u>PI3KK</u> , <u>EGFRK</u> , <u>AktK</u> , <u>ASK1K</u>	<u>MKK6K</u> , <u>p38K</u> , <u>ASK1K</u> , <u>JNKK</u> , <u>MKK4K</u> , <u>RasK</u> , <u>SGK</u>	<u>MKK6K</u> , <u>p38K</u> , <u>JNKK</u> , <u>MEKK</u> , <u>RasK</u>

Table 3.6: The table displays the nodes that have a significant impact on melanin, BCL2M and BCL2K activities when subjected to different methods of perturbation such as activation, inhibition, NoF and FoN. The nodes with the highest Euclidean distance scores and correlation coefficient values less than negative 0.8 are presented for each perturbation method. Nodes that are sensitive to at least one method of function perturbation and one of constitutive activation or inhibition are underlined

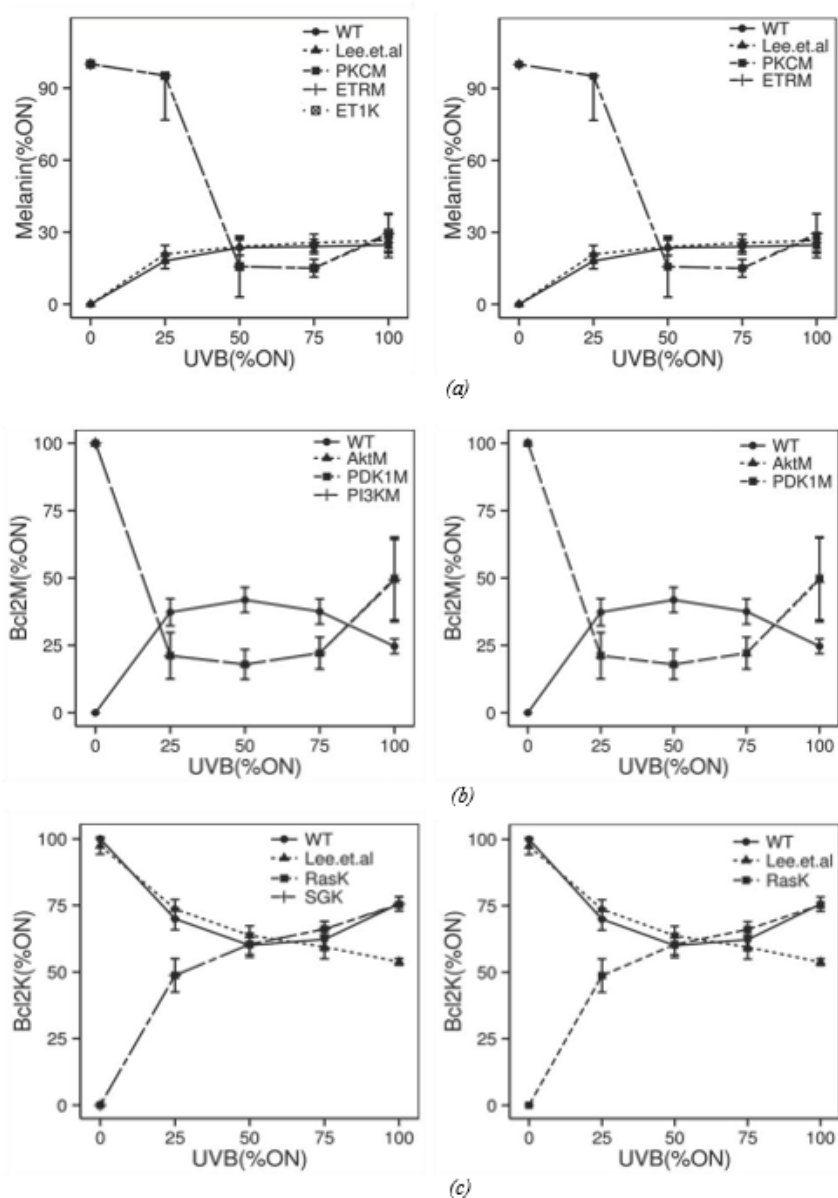


Figure 3.7: Effect of function perturbation (left column – NoF and right column – FoN) of selected nodes on UVB-induced skin pigmentation and BCL-2 expressions. Each data point represents the average steady-state activity of the output node at 0, 25, 50, 75 and 100% of UVB. The error bar represents the standard deviation. Steady-state value of WT and Lee et. al. WT fall under each other's standard deviation. (a) A positive relationship between UVB and melanin synthesis (WT) is seen for $k=0$. A negative relationship is observed when function perturbations are applied to certain nodes, implying a large average distance and negative correlation. Effect of perturbing PKCM, ETRM and ET1K on melanin are quantitatively identical, (b) Nodes that greatly affect WT activity of BCL2M on 'NoF' perturbations. Lee et. al. WT values are not available for BCL2M, (c) A negative relation between UVB and BCL2K activations. Perturbation in the GRB) and SOS complex, SG, and RAS in keratinocytes result in a quantitatively overlapping positive relationship.

3.5 Discussion

	NoF	FoN	Transient perturbation	Gene mutation (knockout)
Nodes with cyclic attractor	$\overline{\text{en}(1)}, \overline{\text{en}(2)}, \overline{\text{EN}(1)}, \overline{\text{EN}(2)}, \overline{\text{wg}(2)}, \overline{\text{wg}(3)}, \overline{\text{wg}(4)}, \overline{\text{WG}(3)}, \overline{\text{WG}(4)}, \overline{\text{PTC}(1)}, \overline{\text{hh}(1)}, \overline{\text{hh}(2)}, \overline{\text{HH}(1)}, \overline{\text{SMO}(4)}$	$\overline{\text{EN}(1)}, \overline{\text{EN}(2)}, \overline{\text{wg}(3)}, \overline{\text{wg}(4)}, \overline{\text{WG}(3)}, \overline{\text{WG}(4)}, \overline{\text{hh}(1)}, \overline{\text{HH}(1)}$	$\overline{\text{wg}(1)}, \overline{\text{wg}(3)}, \overline{\text{wg}(2)}, \overline{\text{WG}(1)}, \overline{\text{WG}(3)}, \overline{\text{en}(2)}, \overline{\text{en}(4)}, \overline{\text{EN}(2)}, \overline{\text{EN}(4)}, \overline{\text{hh}(2)}, \overline{\text{hh}(4)}, \overline{\text{HH}(2)}, \overline{\text{HH}(4)}, \overline{\text{ptc}(1)}, \overline{\text{PTC}(1)}, \overline{\text{PTC}(3)}, \overline{\text{SMO}(3)}$	$\overline{\text{wg}(1)}, \overline{\text{wg}(2)}, \overline{\text{wg}(3)}, \overline{\text{wg}(4)}, \overline{\text{en}(1)}, \overline{\text{en}(4)}, \overline{\text{en}(2)}, \overline{\text{en}(3)}, \overline{\text{hh}(1)}, \overline{\text{hh}(2)}, \overline{\text{hh}(3)}, \overline{\text{hh}(4)}, \overline{\text{ptc}(1)}, \overline{\text{ptc}(2)}, \overline{\text{ptc}(3)}, \overline{\text{ptc}(4)}$
Nodes with point attractor	$\overline{\text{en}(4)}, \overline{\text{EN}(4)}, \overline{\text{wg}(1)}, \overline{\text{WG}(1)}, \overline{\text{PTC}(3)}, \overline{\text{CI}(1)}, \overline{\text{hh}(4)}, \overline{\text{HH}(2)}, \overline{\text{HH}(4)}, \overline{\text{CIR}(1)}, \overline{\text{CIR}(4)}, \overline{\text{SMO}(3)}$	$\overline{\text{en}(1)}, \overline{\text{en}(4)}, \overline{\text{EN}(4)}, \overline{\text{WG}(1)}, \overline{\text{PTC}(3)}, \overline{\text{CI}(1)}, \overline{\text{HH}(2)}, \overline{\text{HH}(4)}, \overline{\text{SMO}(3)}$		

Table 3.7: Comparison of nodes identified as sensitive using the "NoF" and "FoN" methods with those identified as critical using transient perturbation and gene mutation methods. The cells they belong to in relation to the parasegment are indicated by numbers in parenthesis (1-4). Both the function perturbation method and the transient perturbation/gene mutation method identify the underlined nodes as sensitive.

3.5 Discussion

We developed a new 265-node Boolean model for melanogenesis, compared it to the existing model, and found the network's sensitive nodes. The interaction network created by Raghunath et. al. and the Boolean model created by Lee et. al. are two solid foundations around which the model is built. The pioneering 62-node Lee et. al. model for skin pigmentation is the dynamic model that comes closest to this research. It is the only publicly accessible Boolean model of melanogenesis. The model is, however, more simplified and does not depict minute aspects of the melanogenesis procedure. Tyrosine, L-DOPA, cysteinyl L-DOPA, Dopaquinone, and TYRP1, for instance, are intermediate components that link MITF to the formation of melanin but are not included in the Lee model (Fang and Setaluri, 1999; Simon et al., 2009). The transfer of melanin to the upper layer of skin is explained by biological processes like melanosome biogenesis, dendrite formation, and melanosome phagocytosis, and information about these processes is included in the network built by Raghunath et. al., which serves as the foundation for the nodes in this model.

We discover that the majority of common nodes respond to UV stimulation in a manner that is consistent with Lee et al's descriptions. MITF, BCL2, β -catenin, and melanin are examples

of output nodes that exhibit a correlation value of > 0.5 despite the presence of numerous more intermediary nodes between the UV input and the output nodes. As a result, we can show that the extension of the network has no significant impact on the predictions of the smaller Lee model. We believe that our study is an improvement over the Lee model because it contains more information about molecular interactions than the Lee model and because it allows one to examine the impacts of numerous components that are lumped together in the Lee model.

In the two models, a few nodes react to rising UV levels differently. We have done a thorough analysis of all 11 anti-correlated nodes, including their UV response in both the Lee model and this model. The new larger model is more in line with the experimental literature, despite the fact that some nodes exhibit clearly distinct behavior (increasing with UV in one model and reducing in the other). This is evident from our review of the literature. There are other responses that appear to be non-monotonic, including (α _MSH_kerat, MC1R_melan, TP53_kerat, and TP53_melan). In the Lee et. al. model, these compounds exhibit an early rise in expression followed by a slow decline, whereas, in the new model, their expression rises steadily with increasing UV exposure. Also, we have found experimental research that confirms the hypothesis that UV stimulation does boost the expression of these substances. While investigating the pigmentary responses in mouse melanoma cells, Chakraborty et. al. discovered that epidermal melanocytes and keratinocytes respond to UVR by boosting their expression of α _MSH and ACTH, which up-regulate the expression of MC1R (Chakraborty et al., 1995).

After subjecting the system to constitutive activation and inhibition, we found numerous sensitive nodes that significantly alter the activity of the output nodes eumelanin, pheomelanin, and BCL2. Among the few nodes that are frequently designated as sensitive in both models are MITF, cAMP, and CREB (Table 3.5). According to various studies, MITF is a crucial regulator of melanogenesis, and its blockage results in the process' cessation (Park et al., 2004; Chung et al., 2009). Moreover, it is known that tyrosinase and MITF are situated upstream of cAMP and CREB in the pathway (Lee et al., 2015; Kim et al., 2008). So, a change in their activity will undoubtedly have an impact on the amount of melanin in the skin (Lehraiki et al., 2014). A few nodes are identified as being crucial for the BCL2 activity in keratinocytes and melanocytes despite not being sensitive in the Lee model. A few of these include NFKB1, ADCY4, TP53, PKC, and PRKCZ. The experimental data and their outcomes agree. For instance, while examining the function of NFKB in skin biology, Fullard et. al. discovered that knocking down NFKB or activating it constitutively causes epidermal hyperplasia in mice (Fullard et al., 2013). According to the study, NFKB is the principal regulator of epidermal homeostasis. In keratinocyte-melanocyte signaling, TP53 is crucial. Wei et. al. demonstrated through a binding site analysis of TP53 that the majority of the key paracrine factors released

3.5 Discussion

from keratinocytes after UV exposure are possibly regulated by p53 and that p53 disruption may lead to the dysregulation of cytokine signaling in keratinocytes (Wei et al., 2006). Li et. al. examined the function of PKC and its isoforms in another study. Their findings suggested that overexpression of PKC and its isoform modulates cell survival pathways in response to external stimuli and negatively regulates Akt phosphorylation and kinase activity in mouse keratinocytes Li et al. (2006a).

To thoroughly map the number of attractors and their basins of attraction, it would be interesting to conduct a comparative investigation of the dynamics of both the Lee model and this model. In all scenarios, the system reaches a number of cyclic attractors for 100% UV. Just a small percentage of these states have melanin-related nodes that are active. This is the cause of the simulation results for both models showing that melanin does not reach 100% when the UV is always on ($UV = 100\%$). In the 100 initial states sampled for our model, we find 16 distinct cyclic attractors ranging in size from fixed points to 16 nodes. Eumelanin and/or pheomelanin is active in about 8 of the 16 states comprising each of the large attractors.

The model presented here is the largest Boolean model for melanogenesis reported to date, with about four-fold more nodes compared to Lee model. We believe it will provide a tool for the simulation and analysis of the complex interplay between keratinocytes and melanocytes that results in melanogenesis.

We used the existing smaller melanogenesis signaling network and the segment polarity network models to test our newly developed dynamic function perturbation methods, namely FoN and NoF. To our knowledge, the SIF and SIN perturbation methods formulated by Garg et. al. are the closest to FoN and NoF. However, there are significant differences between these two methods. NoF changes the state of the output node when it is implemented, and when that node has a flaw, it is comparable to SIN for a specific update period. As opposed to SIN, which allows different nodes to be defective at various points throughout a single simulation instance, the NoF method has a "permanent" flaw that lasts the duration of the simulation. We also find that predictions using NoF are consistent with other perturbation studies in contrast to the 'implausible' results obtained using SIN (Garg et al., 2009). SIF perturbations take the unlikelihood of transcription without activation as an example and make the assumption that defects only occur in active nodes. Nevertheless, switch-on defects and leaky transcription are also known to occur. Switch-on and switch-off defects are both a part of our FoN disturbance. Conceptually, we view such a disturbance as a defect in our ability to correctly interpret each input signal. Consideration of a fault in how a multi-input node interprets one of its inputs might make for an intriguing follow-up study. Unfortunately, this would make it more difficult to compare nodes with different numbers of inputs. Each of the two perturbations has been applied to two different

models, varying in size and complexity (the segment polarity network with 13 nodes each in 4 cells and the melanogenesis network with 64 nodes in two cell types). Implementation was not straightforward, as neither method calls for new node inputs and only modifies the ones that already exist in the truth tables. Also, we have confirmed that it is feasible to perturb a bigger network (about 100 nodes; results are not shown) using these methods. We have just examined the perturbed networks in terms of identifying vulnerable nodes. A better understanding of the stability of the phenotype can result from the impact of minor perturbations on attractor states and trajectories (Yao et al., 2017). Further analysis of the effects of such perturbations on the attractors and their basins of attraction would be desirable but very challenging for large networks. It would be useful to conduct more investigation of how such perturbations affect the attractors and their basins of attraction, but doing so would be extremely difficult for large networks, even ones of the size of the network involved in melanogenesis. Signaling pathways and cancer pathways have been studied using larger Boolean networks (Fumiã and Martins, 2013; Ryll et al., 2011). But it might be difficult, particularly for networks with asynchronous updating, to analyze the attractor states of vast unperturbed networks (Saadatpour et al., 2010). We have focused on the identification of node sensitivity and have not conducted an examination of the state space of the perturbed networks in this work, despite the existence of methods (Neff et al., 2013; Choo and Cho, 2016) for identifying attractors for large networks, such as the cancer pathways network. The approaches are equally relevant to asynchronous updating even if we have only employed synchronous updating because they both entail a time-invariant change to the truth table. The adjusted truth table corresponding to NoF and FoN perturbations can be updated in the order and frequency specified by a specific asynchronous updating technique.

We compared the outcomes of our methods with those of other approaches in order to determine if FoN and NoF perturbations could successfully locate sensitive nodes in the network. Sensitivity is anticipated to depend on the type of perturbation introduced into the network. The melanin activity was discovered to be sensitive to MITFproteinM, while PDK1M and AktM were revealed to be crucial for sustaining BCL2M level. However, in the case of melanogenesis, a few nodes were robustly identified as sensitive regardless of the perturbation method applied to them. According to a published experimental finding, MEKK is identified as a sensitive node that is crucial for BCL2K activity as a result of FoN perturbation. In the segment polarity network, nodes were labelled as "sensitive" if a perturbation caused a deviation from the WT pattern. We were able to pinpoint a few new nodes that are crucial for maintaining the WT steady-state pattern, such as the posterior cells of the parasegment, where an imbalance between the cubitus interruptus transcriptional activator (CIA) and cubitus interruptus transcriptional repressor (CIR) results in the mutant state (Chaves et al., 2005). We were able to recognize CI as

3.6 Conclusion

a sensitive node, which is consistent with some experimental reports (but not all of them). The data suggest that several perturbation methods may capture different biological conditions since conflicting reports are likely to indicate that the sensitivity varies depending on the experimental environment investigated. Hence applying several perturbation techniques to the network may be necessary for a thorough determination of node sensitivity.

The majority of the nodes identified by our methods as sensitive are likewise characterized by constitutive activation/inhibition as sensitive. This implies that our approach is stricter than constitutive activation/repression and that lowering the Euclidean distance cut-off criteria will enable the identification of more sensitive nodes (inclusion of non-underlined nodes in Tables 3.6 and 3.7). To our knowledge, there is no theoretical conclusion that suggests an optimal perturbation method. Individual cells and growing organisms do experience many stochastic disturbances that come from both internal and external sources. Hence, based on the question that needs to be answered, either a specific perturbation corresponding to a specific experiment (for example, gene knockout) is applied to evaluate the effect on the network output, or a variety of perturbation methods are applied to study node and network robustness. Two methods that we think might be good additions to this group of perturbation methods for Boolean networks are provided in this thesis. The nodes that were previously identified as sensitive by other perturbation methods are further supported by these methods. More intriguingly, though, they also result in the discovery of sensitive nodes that previous perturbation methods evaluated here had missed. This implies that these novel methods query into system dynamics and responses in a manner distinct from those of earlier methods. The collection of perturbations used to evaluate the sensitivity of nodes and networks should therefore benefit from the addition of these methods.

3.6 Conclusion

In our investigation of melanogenesis, the newly developed model, with its expansive network capturing the intricacies of UV-induced responses, has exhibited substantial qualitative agreement with known biological activities. Despite the considerable complexity of the system, simulations revealed that steady states were reached within 1000 updating steps, validating the efficiency. The model successfully replicated the impact of UV radiation on melanin levels, aligning with experimental findings that indicate increased skin pigmentation upon UV exposure. Furthermore, the model captured the qualitative responses of various target nodes, including those associated with cell cycle, survival, apoptosis, dendrite formation, and melanosome processes, corroborating existing physiological knowledge.

A direct comparison with the Lee et al. model demonstrated a noteworthy positive correlation between the nodes, particularly in crucial elements such as eumelanin, pheomelanin, and Bcl-2. While some differences in Boolean rules and regulating nodes were expected due to the increased complexity of the new network, the overarching agreement supports the consistency of our model with established melanogenesis dynamics.

Exploring the sensitivity of the new model, we identified a significant number of sensitive nodes, reflecting its larger size and complexity. Notably, some nodes crucial for melanin production, such as DOPAchrome and tyrosinase, were identified as sensitive in our model, demonstrating experimental validation for their importance. The nuanced understanding of melanogenesis provided by this comprehensive model serves as a valuable resource for unraveling the intricate regulatory mechanisms governing skin pigmentation.

CHAPTER 4

A systems model for vitiligo

4.1 Introduction

4.1.1 About vitiligo

Vitiligo is a skin disorder characterized by the formation of amelanotic, non-scaly, chalky-white macules with a clear border. These discolored areas of skin typically grow over time. The prevalence of vitiligo is estimated to be between 0.08 and 2%, with higher rates (about 8.8%) reported in India (Sehgal and Srivastava, 2007). Despite its classification as a cosmetic issue, the consequences of vitiligo can be mentally distressing and can have a significant impact on daily life (Grimes and Miller, 2018; Joge et al., 2022). Different cultural attitudes towards skin integrity affect how the disease is perceived by patients and society. The extent and location of skin affected by vitiligo can determine its impact on quality of life, with white patches on the face and hands being particularly distressing. Additionally, vitiligo can be particularly prominent in individuals with dark skin, while it may go unnoticed and undiagnosed in fair-skinned individuals.

Vitiligo typically appears as a number of skin spots, most frequently in a symmetric pattern, on both sides of the body. So, if a spot is present on one side of the face, it is frequently matched by a spot on the opposite side. A spot will spread across the center and involve the other side if it is discovered close to the body's center. When the patches are limited to mucosal body regions such as the lips, inner nose, or genital regions, the condition is known as mucosal vitiligo. Acrofacial vitiligo is the term used when the hands and/or feet are involved along with the lips or other facial features. When the lips and fingertips are affected, it is called lip-tip vitiligo. When the spots are confined to a small area, it is referred to as focal vitiligo. However, if the patches of discoloration spread to involve larger areas of the body, it is known as generalized vitiligo. In cases where most of the body is affected, typically more than 80%, it is classified as universal vitiligo (noa, 2020). The age at which individuals present with this condition varies from country to country. However, it is observed that most patients develop this condition before they turn 40 years old. This means that individuals who are below 40 years of age are more likely to develop vitiligo than those who are older. Another important risk factor for developing vitiligo is a family history of the disorder. Individuals who have one or more family members with vitiligo are at a higher risk of developing the condition than those without a family history. This suggests that there may be a genetic component to the development of vitiligo. It is also worth noting that vitiligo affects both men and women equally. There is no significant difference in the prevalence of vitiligo between the two genders (Picardo et al., 2015; Mahajan et al., 2019).

4.1 Introduction

4.1.2 Theories of vitiligo pathogenesis

The etiopathogenesis of vitiligo is not entirely known, despite its old history and clinical importance. The majority of the currently available data is in favor of individual phenomena such as autoimmunity, oxidative stress, local neural injury, chemical exposure, and or genetic predisposition. Nonetheless, with further study and progress, newer insights into its etiopathogenesis are still developing. An in-depth description of how each of these factors contributes to melanocyte loss in vitiligo is given below.

The biochemical theory

The earliest circumstances that can cause vitiligo are not fully understood. Yet, multiple studies suggest that exposure to specific environmental factors and a combination of intrinsic melanocyte abnormalities may play a significant role in the development of the disease. One such important environmental factor was identified back in 1939 when a group of factory workers developed vitiligo. These factory workers made leather and wore rubber gloves to protect their hands from the chemicals used in the process. It was discovered that the rubber gloves contained a chemical called monobenzyl ether of hydroquinone (or monobenzene), which induced vitiligo. This same phenomenon was observed in other industries, such as tanneries, plating works, and electrical apparatus manufactories that used the same type of gloves (Oliver et al., 1939). These incidents strongly suggested that chemicals can cause vitiligo and raised concerns about other potentially harmful chemicals in everyday products. After this incidence, a number of products—the majority of which contain phenols—have been claimed to cause vitiligo. The cause of vitiligo has also been linked to other chemicals, including 4-tertiary-butyl phenol (4-TBP), which is present in adhesives, and 4-tertiary-butyl catechol (4-TBC), which is present in rubber and other items. In India in 2009, a variety of commercial products that have been claimed to cause vitiligo were identified by Ghosh and Mukhopadhyay. This includes cosmetic dyes that are occasionally applied to the skin, detergents, and permanent hair dyes (Ghosh and Mukhopadhyay, 2009). These chemicals are similar in structure to the amino acid tyrosine, which melanocytes use to produce the pigment melanin. When these chemicals enter the body, they are mistaken for tyrosine and taken up by melanocytes, which can lead to inflammation and autoimmunity that can result in vitiligo (Figure 4.1).

A recent example of this occurred in Japan in 2013, where a highly effective skin-lightening cream containing rhododendrol, a phenol that resembles tyrosine, induced vitiligo in over 18,000 consumers who had used the product. Rhododendrol is found to compete with tyrosine for hydroxylation by tyrosinase and interfere with melanin synthesis as do derivatives of phenols and

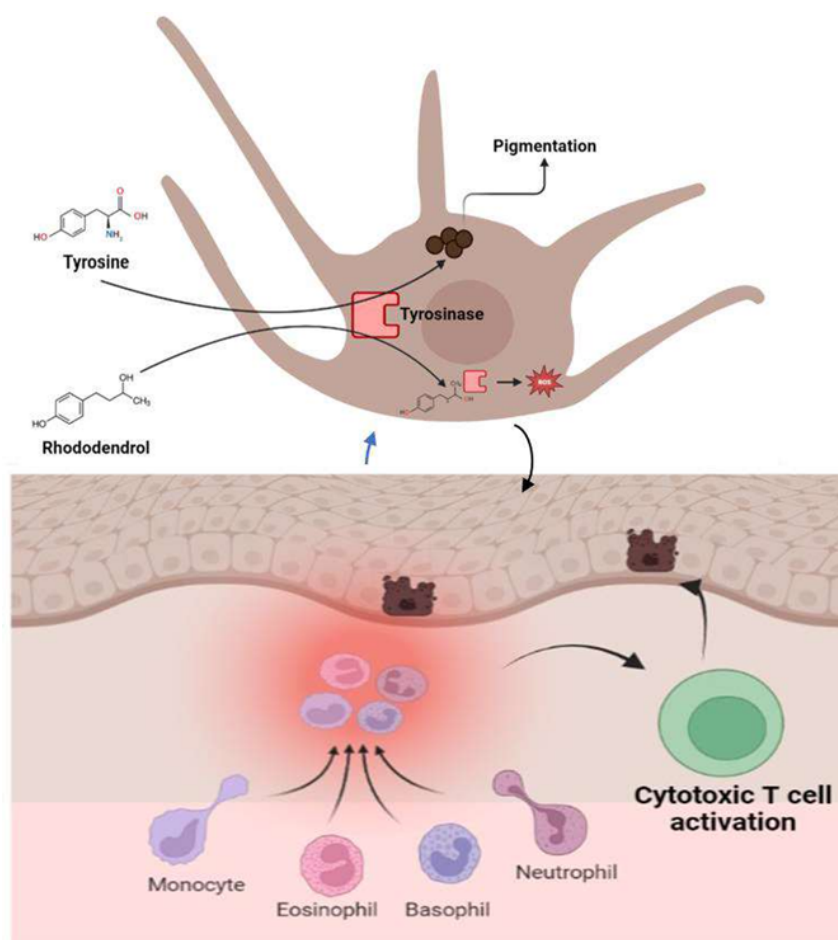


Figure 4.1: Illustration of the development of chemical-induced vitiligo. Rhododendrol interferes with tyrosinase. Consequently, this disruption triggers the cellular stress response, resulting in inflammation and autoimmunity, leading to melanocyte destruction (Harris, 2017)

catechols, resulting in the effective prevention of melanin biosynthesis (Tokura et al., 2015). In another study, Van den Boorn et al. found that when exposed to a monobenzene, the tyrosinase enzyme undergoes a modification process known as quinone haptenation. This process involves the formation of a new protein by covalently linking the enzyme and the chemical, which then acts as a foreign antigen that could trigger an immune response. The modified protein is then packaged into small particles called exosomes and secreted from the cells. These exosomes are then absorbed by dendritic cells, which present the modified protein to autoreactive T cells (van den Boorn et al., 2011).

The neuronal theory

The neural theory, initially introduced by Lerner in 1959, suggests that neuropeptides are released by nerve endings in response to local neuronal injury. In individuals with a genetic susceptibility, the release of these peptides can initiate a series of events that ultimately result

4.1 Introduction

in the immune system attacking and destroying melanocytes (Figure 4.2). The theoretical claim and several clinical observations served as the major foundation for the theory. On rare occasions, vitiligo has been documented in a specific dermatomal region, such as the distribution of the trigeminal nerve i.e. the nerve that provides sensory information and motor functions to the face. An important proof of neuronal involvement is provided by the symmetrical distribution of the lesions (Al'Abadie et al., 1994). A case study described a patient with transverse

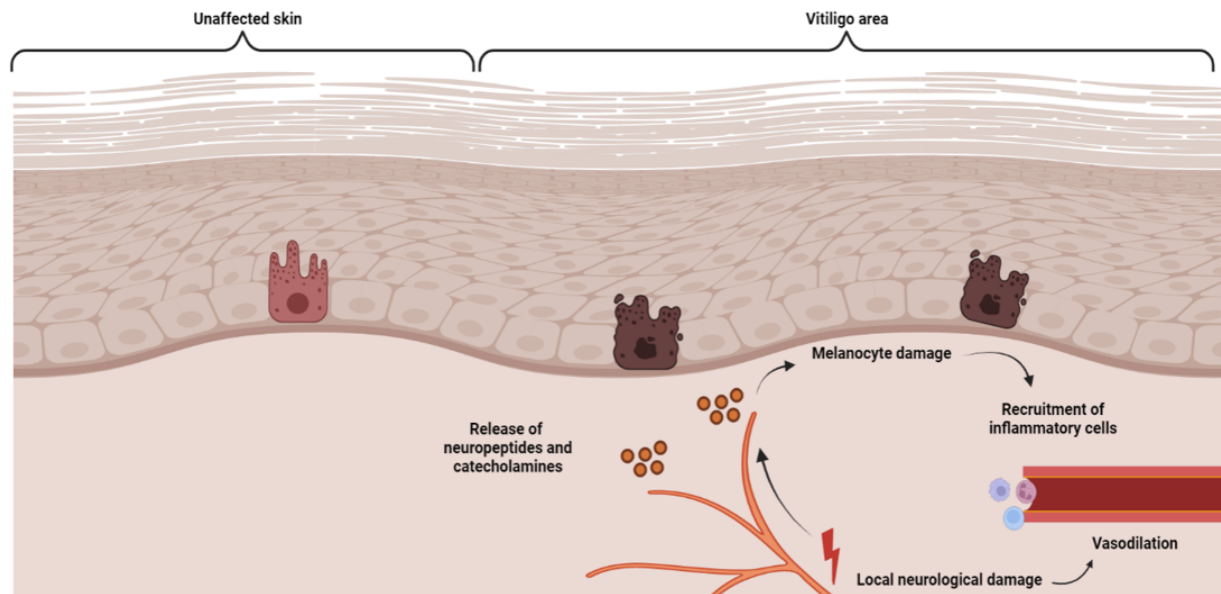


Figure 4.2: Neuronal hypothesis for segmental vitiligo (van Geel et al., 2012)

myelitis who experienced paralysis from the waist down. Interestingly, this patient only developed vitiligo lesions on specific areas of the body, including the face, upper body (neck, axillae, arms, and hands) (Abadie et al., 2019). Such distribution of vitiligo lesions is uncommon in patients with generalized vitiligo. Furthermore, there have been reports linking vitiligo to viral encephalitis in toddler and multiple sclerosis patients who had Horner's syndrome (Stolar, 1963; BREATHNACH and WYLLIE, 1965). A diabetic patient who experienced severe diabetic neuropathy experienced spontaneous re-pigmentation of their significant vitiligo (Breathnach et al., 1966). A patient who experienced severe damage to the right brachial plexus, a collection of nerves that govern the arm and hand, as well as the development of white patches of skin on the same side of their body, is another case that supports this claim. Their upper arm, chest, buttock, lower back, and scrotum all had these white patches (Chanco-Turner and Lerner, 1965). The neurological explanation of vitiligo has gained support from studies on surgical transplants. Haxthausen transplanted skin from a pigmented area to a non-pigmented area and vice versa. He showed that, once the local signaling has been reestablished, transplant skin always takes on

the characteristics of the area into which the graft is implanted (Chu et al., 2006). Melanocytes are thought to move in the third trimester towards the epidermis, according to Hsin-Su Yu. The neural crest is the source of both melanocytes and nerve cells (Yu, 2002). Melanoblast migrates from the dorsal portion of the neural tube to the basal layer of the epidermis, the hair bulb, the inner ear, and the meninges. According to a study, segmental vitiligo and malfunction of the sympathetic nervous system, which controls "fight-or-flight" reactions, may be related. According to research on vitiligo lesions, sympathetic adrenergic innervation is more active than normal. This may have an impact on the production of melanin and the growth of melanocytic cells (Kaur and Sarin, 1988). More recently, it was shown that nerve growth factors and neuropeptides are essential as emotional response regulators in the development of vitiligo in some vulnerable people. Neurogenic factors include substances like neuropeptide Y (NPY), CGRP (Calcitonin Gene-Related Peptide), catecholamines, NGFs (Nerve Growth Factors), and NGF receptors that can directly harm melanocytes as well as trigger and spread local and widespread immune or inflammatory responses. These neurogenic stimuli can also cause melanocytes to be killed by a particular adaptive immune response (S Al Abadie, 2021).

The impaired redox status theory

In healthy skin, energy is efficiently produced by mitochondria, and metabolic pathways, including those for bipterin metabolism, are balanced and controlled in response to demand. Reactive oxygen species (ROS) are formed in a closely controlled manner after external stress, such as UV radiation exposure or chemical damage, and they are valuable intracellular messengers. Melanocytes respond to these challenges by triggering physiological changes such as melanin synthesis or kinase activation; they do not activate immune cells, and their survival is unaffected. One of the potential pathogenic mechanisms responsible for the loss of melanocytes is oxidative stress. Melanocytes in vitiligo exhibit metabolic defects that disrupt the steady-state equilibrium and make it challenging to handle further stress. Elevated ROS levels damage essential enzymes and further jeopardize crucial metabolic processes, such as those in the mitochondrion, which are a marker of the dysregulation of energy pathways. Further oxidative stress and cell damage result from the synthesis and recycling of bipterin. Also, increased levels of catecholamines inhibit the uptake of calcium by mitochondria, while UV radiation triggers the production of quinones in melanocytes, both of which result in the generation of free radicals. The accumulation of free radicals causes oxidative stress due to an imbalance in the antioxidant system and ROS production (Laddha et al., 2013; Picardo et al., 2015). These changes in the context of susceptible genetic background activate the unfolded protein response (which recognizes and reacts to the accumulation of unfolded or misfolded proteins), causing

4.1 Introduction

DNA damage, and membrane disintegration. Membrane debris and damage-associated molecular patterns (DAMPs) are produced, activating macrophages and dendritic cells. Thereafter, T

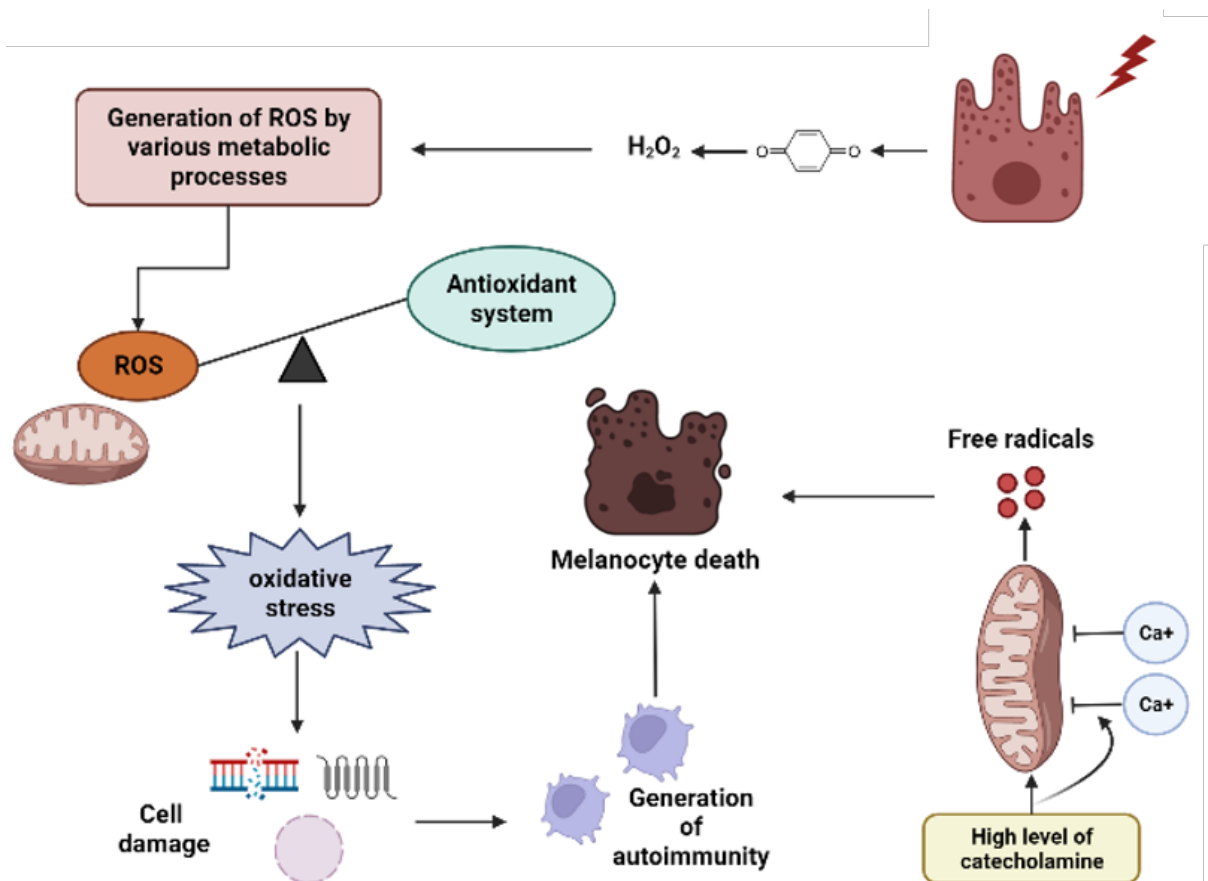


Figure 4.3: Different pathways triggered by oxidative stress in vitiligo

helper 17 (Th17) cells are activated by cytokines and chemokines, and T regulatory (T_{reg}) cells become dysfunctional. Furthermore, elevated ROS levels in melanocytes may result in defective apoptosis, which produces aberrated proteins that could act as autoantigens and trigger autoimmunity (Figure 4.3) (Kuhreber et al., 2003). Additionally, in response to cytokines like $TNF\alpha$ (tumor necrosis factor-alpha) and $TGFb1$ (transforming growth factor b1), which are powerful inhibitors of melanogenesis, the intracellular levels of H_2O_2 and ROS rise. The expression of the anti-apoptotic protein Bcl-2 (B-cell lymphoma-2) is upregulated in response to high amounts of cytokines, such as IL-2 (interleukin-2), making T cells resistant to apoptosis (Laddha et al., 2013; ?; Clemens et al., 2000).

The autoimmune theory

Early clinicians observed that vitiligo frequently affected people and members of their families who had other autoimmune disorders, including thyroid disease and juvenile diabetes, indicating that it was also an autoimmune disease (Kemp et al., 2001). The patient's blood was found to have antibodies to melanocytes, which appeared to confirm this theory. When damaged skin was examined under a microscope, it was discovered that T cells were present immediately next to dying melanocytes (Wańkiewicz-Kalińska et al., 2003), further indicating that immune cells were important in the development of the illness. Others discovered that vitiligo patients' blood and skin included more melanocyte-specific CD8+ T cells, which can directly destroy melanocytes, than did healthy controls (Lang et al., 2001; Andersen et al., 2006). An experiment revealed that immune T cells could be isolated from white skin and combined with unaffected, pigmented skin from the same patient. The T cells then crawled into this skin and killed melanocytes, proving that T cells were both necessary and sufficient to cause vitiligo in the patient (Palermo et al., 2001). This suggested that abnormal melanocytes cause skin inflammation, which leads to T cells mediated destruction of melanocytes.

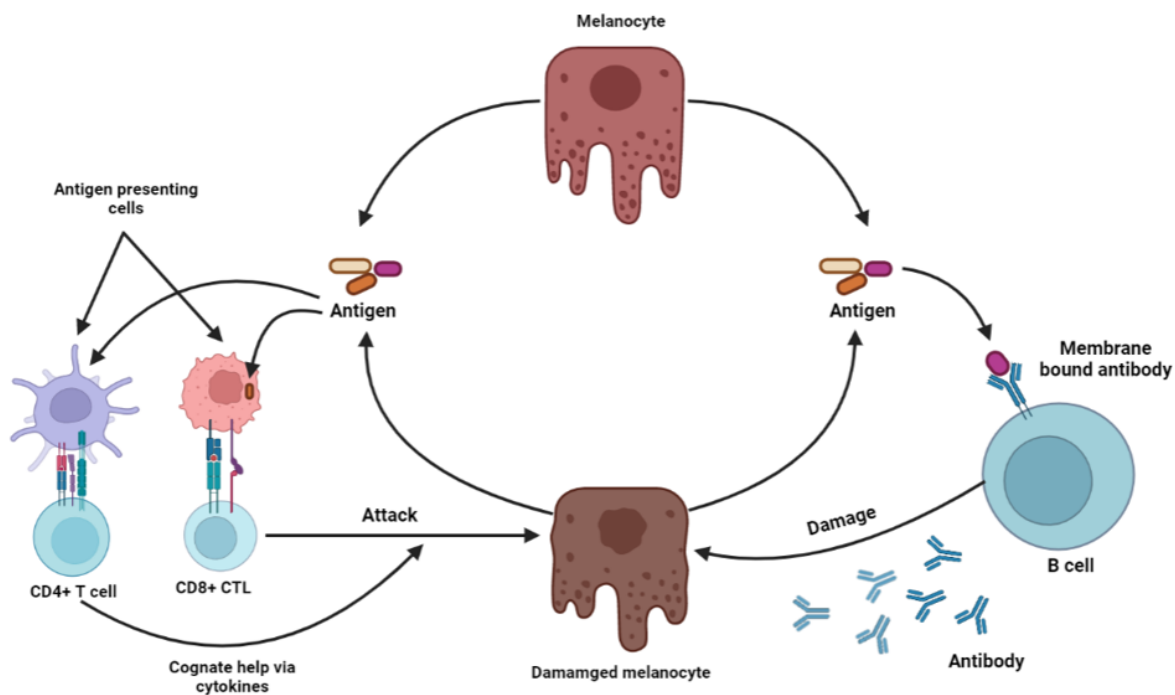


Figure 4.4: Autoimmune theory of vitiligo showing both cell-mediated and humoral autoimmune responses Laddha et al. (2013)

Genetic studies have identified numerous innate immune genes associated with an increased

4.2 About this study

risk for vitiligo, suggesting a critical role for this pathway in the development of the condition. Innate immunity involves various cell types that use pattern recognition receptors (PRRs) to identify foreign patterns and respond to tissue damage. In vitiligo, melanocytes may be initially abnormal and release damage-associated molecular patterns (DAMPs) that activate innate immunity. One recent review examines the potential involvement of innate immunity in vitiligo (Richmond et al., 2013).

Immune effector cells, including cytotoxic T cells, T helper cells, and B cells, may recognize melanocyte-produced antigens, which can be released from injured melanocytes or cross-react with other cell types or pathogens. In cell-mediated immunity, antigenic peptides are presented to cytotoxic T lymphocytes (CTLs) by antigen-presenting cells in the context of major histocompatibility complex (MHC) class I molecules. Antigen-specific T helper cells cooperate by producing cytokines, displayed on MHC class II molecules, to sustain a cytotoxic T-cell response against melanocytes, resulting in their destruction. During humoral immunity, B cells use antigen-specific membrane immunoglobulins to bind to antigens and produce antigen-specific antibodies. However, B cells require support from antigen-specific T helper cells through cytokine synthesis to secrete these antibodies. Anti-melanocyte antibodies can then kill pigment cells through antibody-dependent cell-mediated cytotoxicity or antibody-dependent complement-mediated damage (Figure 4.4) (Kemp et al., 2001).

4.2 About this study

We have integrated multiple mechanisms responsible for melanocyte death in our model. Many patients find the treatment choices for vitiligo to be unsatisfying since they are costly, time-consuming, and not effective. In order to develop optimal treatment protocols, an integrated understanding of drug distribution kinetics and disease kinetics is required. Despite the clinical significance of vitiligo, there is currently no systems model available to understand skin pigmentation-related disorders. There are many theories that have been put out to explain the loss of melanocytes in vitiligo, including local neuronal injury, exposure to toxic substances, intrinsic melanocyte abnormalities, oxidative stress, and immunological responses. The gradual loss of melanocytes may be caused by a number of processes, some of which may entail immunological attack, cell deterioration and detachment. There are theories that explain the overall contribution of each of these processes but no study to our knowledge has considered multiple mechanisms. Here, we report the formulation of the first systems model for vitiligo. We developed a model that incorporates multiple mechanisms responsible for melanocyte death in vitiligo, along with their correlation to clinical outcomes. Moreover, we also simulated drug

effects through parameter variations.

4.3 The first disease model for vitiligo

We assume that melanocytes exist in two states, stressed and unstressed, with the interconversion depending on the level of cellular stress (Figure 4.5). When the skin comes in contact with environmental stressors such as reactive oxygen species (ROS), UV radiation, or chemicals (phenolic and catecholic compounds - found in dyes), keratinocytes and melanocytes become stressed (K_{str} and M_{str}), which then releases inflammatory cytokines (IL1 β , CXCL9) and antigens. These cytokines activate the dendritic cells (DCs) which leads to the priming of naïve T cells (T_{naive}). The activated T_{naive} cells are differentiated into Th1, Th17, T_{reg} and CD8. Activated T cells are recruited by chemokines and further activate keratinocytes (K) by producing inflammatory cytokines. The CD8 and Effector Memory (T_{EM}) T cells eventually kill melanocytes and cause skin depigmentation.

4.3.1 Model construction and simulation

We have modeled each step of vitiligo pathogenesis as a chemical reaction and constructed mass balance equations for each species involved. For instance, the equation for stressed keratinocytes (K_{str}) is expressed as follows:

$$\frac{dK_{str}}{dt} = \frac{ROS^n}{ROS^n + Ka^n} \cdot k_{1K} \cdot K(t) - d_{K_s} \cdot K_{str}(t)$$

Here, ROS represents a stress/input that triggers the conversion of normal keratinocytes (K) to stressed keratinocytes at a rate of k_{1K} . The hill coefficient n and association constant Ka govern the strength of the stressor. Meanwhile, d_{K_s} denotes the death rate of K_{str} . Ordinary Differential Equations (ODEs) given below from 4.1 to 4.11 are for skin cells and immune cells, and from 4.12 to 4.16 for cytokines. Some of the rate parameters used in this model are derived from the literature (see Table 4.1), while the rest were fixed based on the steady-state concentrations of species found in the literature (Table 4.2). The ODE solver (ode23s) in MATLAB was used to simulate the system. Initially, we exposed the system to 0.1 ROS for 10,000 hours, and we used these variable concentrations as the initial conditions to vary ROS again from 0.1 to 10 for 2 to 300 hours with an interval of 24 hours. Additionally, we adapted the Vitiligo Area Severity Index (VASI) to evaluate the impact of stress on clinical outcomes (4.17).

4.3 The first disease model for vitiligo

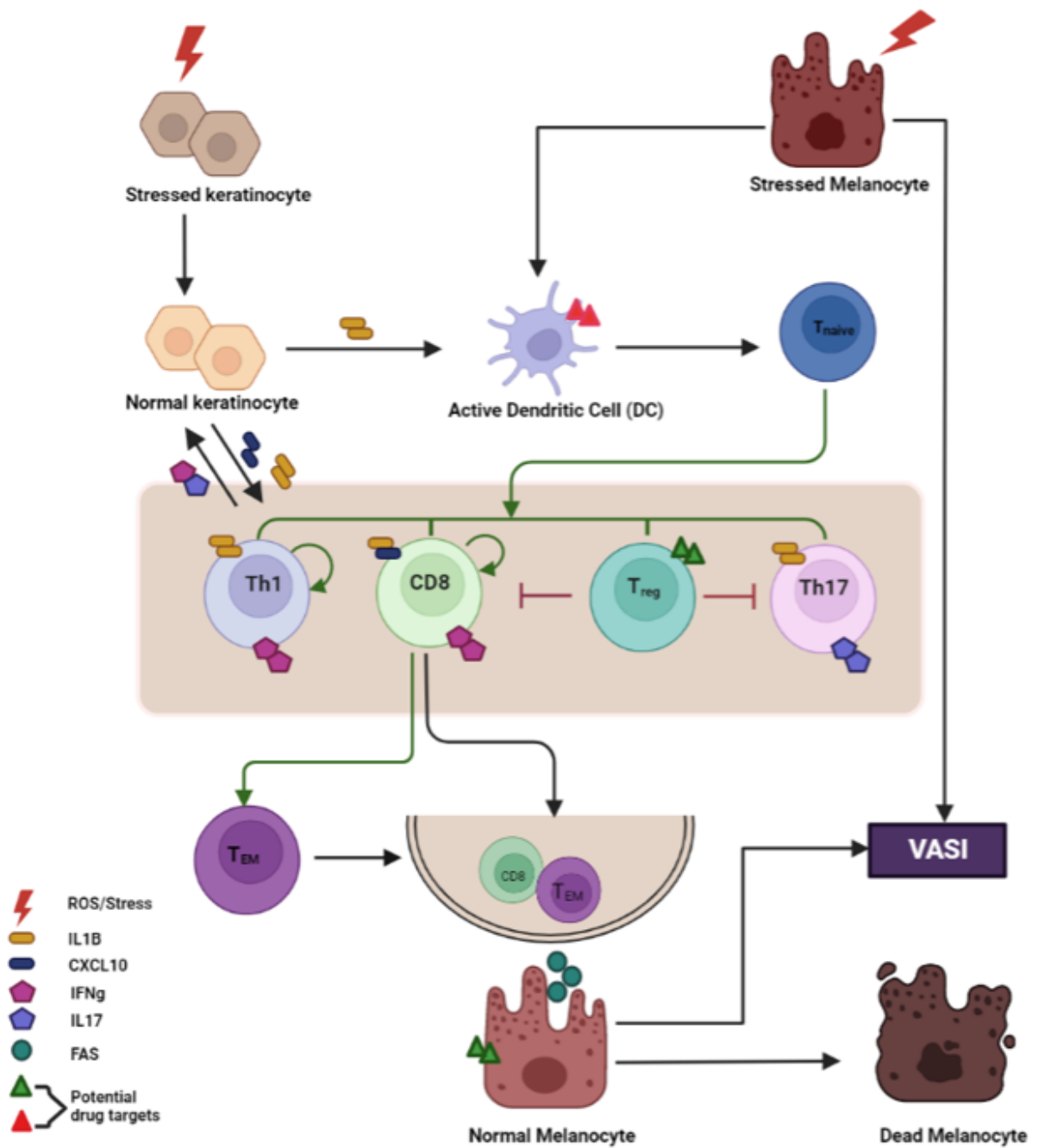


Figure 4.5: A systems model for vitiligo

4.3.2 Equations for cells and cytokines

$$\frac{dK_{str}}{dt} = \frac{ROS^n}{ROS^n + K a^n} \cdot k_{1K} \cdot K(t) - d_{K_s} \cdot K_{str}(t) \quad (4.1)$$

$$\frac{dK}{dt} = k_K - d_k \cdot K(t) - \frac{ROS^n}{ROS^n + Ka^n} \cdot k_{1K} \cdot K(t) \quad (4.2)$$

$$\frac{dM_{str}}{dt} = \frac{ROS^n}{ROS^n + Ka^n} \cdot k_{2K} \cdot K(t) - d_{M_s} \cdot M_{str}(t) \quad (4.3)$$

$$\frac{dDC}{dt} = k_{DC} \cdot (1 + k_{3_{dc}} \cdot IL1\beta(t) + k_{4_{dc}} \cdot M_{str}(t)) - d_{dc} \cdot DC(t) \quad (4.4)$$

$$\begin{aligned} \frac{dT_n}{dt} = & k_{T_n} \cdot (1 + k_{5_{T_n}} \cdot M_{str}(t) + k_{6_{T_n}} \cdot DC(t) - k_{tn1} \cdot T_n(t) + k_{tn2} \cdot T_n(t) \\ & + k_{tn3} \cdot T_n(t) + k_{tn4} \cdot T_n(t) \end{aligned} \quad (4.5)$$

$$\frac{dTh1}{dt} = k_{tn1} \cdot T_n(t) \cdot (1 + K_{3_{th1}} \cdot IL1B(t)) + (k_{p_{th1}} \cdot Th1(t)) - d_{th1} \cdot Th1(t) \quad (4.6)$$

$$\frac{dTh17}{dt} = k_{tn2} \cdot T_n(t) + (1 + k_{3_{th17}} \cdot IL1\beta(t)) - d_{th1} \cdot Th1(t) \cdot (1 + d_{t_{reg_{th17}}} \cdot T_{reg}(t)) \quad (4.7)$$

$$\frac{dT_{reg}}{dt} = k_{tn3} \cdot T_n(t) - d_{t_{reg}} \cdot T_{reg}(t) \quad (4.8)$$

$$\begin{aligned} \frac{dCD8}{dt} = & k_{tn4} \cdot T_n(t) \cdot (1 + k_{3_{cd8}} \cdot IL1\beta(t) + k_{7_{cd8}} \cdot CXCL10(t)) + k_{p_{cd8}} \cdot CD8(t) \\ & - d_{cd8} \cdot CD8(t) \cdot (1 + d_{t_{reg_{cd8}}} \cdot T_{reg}(t)) - k_{T_{EM}} \cdot CD8(t) \end{aligned} \quad (4.9)$$

$$\frac{dT_{EM}}{dt} = k_{T_{EM}} \cdot CD8(t) - d_{tem} \cdot T_{EM}(t) \quad (4.10)$$

$$\frac{dM}{dt} = k_M - d_m \cdot k_{8_M} \cdot FAS(t) \cdot M(t) - \frac{ROS^n}{ROS^n + Ka^n} \cdot k_{2K} \cdot M(t) \quad (4.11)$$

$$\frac{dIL1\beta}{dt} = k_1 \cdot K(t) \cdot (1 + k_{1_{il17}} \cdot IL17(t)) - d_1 \cdot IL1\beta(t) \quad (4.12)$$

$$\frac{dCXCL10}{dt} = k_2 \cdot K(t) \cdot IFN\gamma(t) \cdot (1 + k_{2_{tem}} \cdot T_{EM}(t)) - d_2 \cdot CXCL10(t) \quad (4.13)$$

4.3 The first disease model for vitiligo

Species	Steady State Conc.	Source
K_{str}	10E+3 cells/ mm^2	-
K	60E+03 cells/ mm^2	1 melanocyte contacts up to 40 keratinocytes (Fitzpatrick and Breathnach, 1963) hence, K=1500*40 cell/ mm^2
M_{str}	1 cells/ mm^2	-
DC	40E+03 cells /ml	(Kim et al., 2007)
T_{naive}	400E+04 cells/ml	-
Th1	100E+04 cells/ml	(Kim et al., 2007)
Th17	100E+04 cells/ml	(Kim et al., 2007)
T_{reg}	500E+03 cells/ml	-
CD8	600E+03 cells/ml	(Kim et al., 2007)
T_{EM}	150E+03 cells/ml	-
M	1500 cells/ mm^2	(Sun et al., 2021)
IL1 β	0.5 pg/ml	(Raam et al., 2018)
CXCL10	50 pg/ml	(Raam et al., 2018)
IFN γ	6 pg/ml	(Tembhre et al., 2013)
IL17	5 pg/ml	(Tembhre et al., 2013)
FAS	70 pg/ml	(Yazicioglu et al., 2020)

Table 4.1: Steady state level of species at healthy state

$$\frac{dIFN\gamma}{dt} = k_3 \cdot Th1(t) \cdot k_{3_{cd8}} \cdot CD8(t) \cdot (1 + k_{3_{tem}} \cdot T_{EM}(t)) - d_3 \cdot IFN\gamma(t) \quad (4.14)$$

$$\frac{dIL17}{dt} = k_4 \cdot Th17(t) - d_4 \cdot IL17(t) \quad (4.15)$$

$$\frac{dFAS}{dt} = k_{5_{cd8}} \cdot CD8(t) \cdot k_{5_{tem}} \cdot T_{EM}(t) - d_5 \cdot FAS(t) \quad (4.16)$$

$$VASI = \frac{\frac{M_{str}}{M+M_{str}}}{\left(\frac{M_{str}}{M+M_{str}} + 0.1\right) \cdot \left(1 + \frac{M}{1500}\right)} \quad (4.17)$$

Parameter	Description	Value
d_5	Elimination rate of FAS	0.15/hr
k_4	Secretion rate of IL17	1.6E-06 pg/cell/hr
d_3	Elimination rate of IFN γ	0.03/hr
k_2	Secretion rate of CXCL10 by K	9.0E-07 pg/cell/hr
k_1	Secretion rate of IL1 β by K	1.4E-06 pg/cell/hr
k_{8M}	Enhancement in elimination of melanocytes by FAS	0.4

k_{1K}	Rate of conversion of K to K_{str}	0.02
k_K	Formation rate of K	115.68 cells/mm ² /hr
k_{2K}	Rate of conversion of M to M_{str}	3E-3 /hr
d_{tem}	Elimination rate of T_{EM}	6.9E-3/hr
$d_{treg_{cd8}}$	Inhibition rate of CD8 by T_{reg}	1.20E-05
d_{treg}	Elimination rate of T_{reg}	0.05/hr
$d_{treg_{th17}}$	Inhibition rate of Th17 by T_{reg}	1.30E-05
d_{th1}	Elimination rate of Th1	1.7E-2/hr
k_{T_n}	Formation rate of T_{naive}	0.08 cells/ml/hr
k_{DC}	Formation rate of DC	3.28 cells/ml/hr
$k_{5_{tem}}$	Secretion rate of FAS by T_{EM}	1.4e-5 pg/cell/hr
$k_{5_{cd8}}$	Secretion rate of FAS by CD8	1.4e-5 pg/cell/hr
d_4	Elimination rate of FAS	0.33/hr
$k_{3_{tem}}$	Enhancement in the secretion of IFN γ by T_{EM}	1.10E-07
$k_{3_{cd8}}$	Secretion rate of IFN γ by CD8	1.1E-07 pg/cell/hr
k_3	Secretion rate of IFN γ by Th1	1.1E-07 pg/cell/hr
$k_{2_{tem}}$	Enhancement in the secretion of CXCL10 by T_{EM}	1.00E-04
d_2	Elimination rate of CXCL10	0.1/hr
$k_{1_{il17}}$	Enhancement in the secretion of IL1 β by IL17	1.00E-04
d_1	Elimination rate of IL1 β	0.17/hr
d_m	Elimination rate of M	4.7E-05/hr
k_M	Formation rate of M	22 cells/mm ² /hr
d_{ms}	Elimination rate of M_{str}	0.2/hr
d_k	Elimination rate of K	4.2E-4/hr
d_{ks}	Elimination rate of K_{str}	9E-3/hr
ROS	Stress	0.001:0.001:0.1
Ka	Association constant	0.01
n	Hill coefficient	2
$k_{T_{EM}}$	Formation rate of T_{EM}	1.7E-3cells/ml/hr
d_{cd8}	Elimination rate of CD8	6.6E-3/hr
$k_{p_{cd8}}$	Proliferation rate of CD8	1E-04 ml/cells
$k_{7_{cd8}}$	Activation of CD8 by CXCL10	1.00E-03
$k_{3_{cd8}}$	Activation of CD8 by IL1 β	1.00E-03
$k_{3_{th17}}$	Activation of Th17 by IL1 β	1.00E-03

4.4 Results

d_{th17}	Elimination rate of Th17	1.9E-3/hr
kp_{th1}	Proliferation rate of Th1	2E-04 ml/cells
$k_{3_{th1}}$	Activation of Th1 by IL1 β	5.00E-05
k_{tn1}	Differentiation rate of T_{naive} to Th1	4.2E-3 ml/cells
$k_{5_{T_n}}$	Activation of T_{naive} by M_{str}	25
$k_{6_{T_n}}$	Activation of T_{naive} by DC	25
d_{dc}	Elimination rate of DC	4.2E-3 /hr
$k_{3_{dc}}$	Activation of DC by IL1 β	0.5
$k_{4_{dc}}$	Activation rate of DC by M_{str}	0.5
k_{tn2}	Differentiation rate of T_{naive} to Th17	3.7E-3 ml/cells
k_{tn3}	Differentiation rate of T_{naive} to T_{reg}	6.4E-3 ml/cells
k_{tn4}	Differentiation rate of T_{naive} to CD8	6.9E-3 ml/cells

Table 4.2: Parameter description and values

4.4 Results

4.4.1 Vitiligo model captures the system response to varying levels of stress

The VASI scoring system is used to evaluate the severity of vitiligo by taking into account the percentage of the body surface area affected by vitiligo and the degree of depigmentation in those areas. However, we adapted this score to align the output with clinically observed trends. On the other hand, ROS is a stress input that can harm cells and tissues and initiate a downstream pathogenesis response. Preliminary findings indicate that low ROS exposure for prolonged periods does not affect VASI scores (Figure 4.6). VASI remains minimal or close to zero when ROS is below 0.5, but it begins to increase as ROS increases. The score reaches a maximum of 5% when exposed to 0.5 ROS for 12 days. For the same level of exposure, VASI reaches 15% at ROS 1 and 30% at ROS 2. This suggests that as ROS levels increase, the severity of vitiligo (as measured by VASI) also increases.

However, the precise shape and trend of the plot depend on various other factors. Few studies qualitatively support this finding. Zhang et al. discovered that when vitiligo melanocytes were exposed to oxidative stress, the total CRT levels went up in a time-dependent manner. They carried out this study to determine the function of calreticulin (CRT) in hydrogen peroxide (H_2O_2)-induced apoptosis in melanocytes. Additionally, CRT levels were favorably linked

($R=0.7$) with lesion extent and duration of vitiligo in patients in an in vivo model (Zhang et al., 2014). Malondialdehyde (MDA), a sign of oxidative damage, as well as superoxide dismutase (SOD) and reduced glutathione (rGSH), both antioxidants, were examined by Mathachan et al. in vitiligo patients. These three parameters pertain to the oxidative stress pathway. SOD and rGSH are antioxidants, but MDA is a sign of oxidative damage. In comparison to the control group, the patient group showed significantly higher levels of MDA and significantly lower levels of SOD and rGSH (Mathachan et al., 2021). By analyzing the levels of the antioxidant enzymes SOD and CAT, some studies have demonstrated that active vitiligo cases had higher levels of antioxidant activity than stable vitiligo cases and healthy controls (Pv et al., 2009; Chang and Ko, 2023). The serum oxidative stress markers total antioxidant capacity (TAC), MDA, and 8-hydroxy-2-deoxyguanosine (8-OHdG) have been shown by Li et al. to be able to predict the severity and activity in individuals with non-segmental vitiligo (Li et al., 2021).

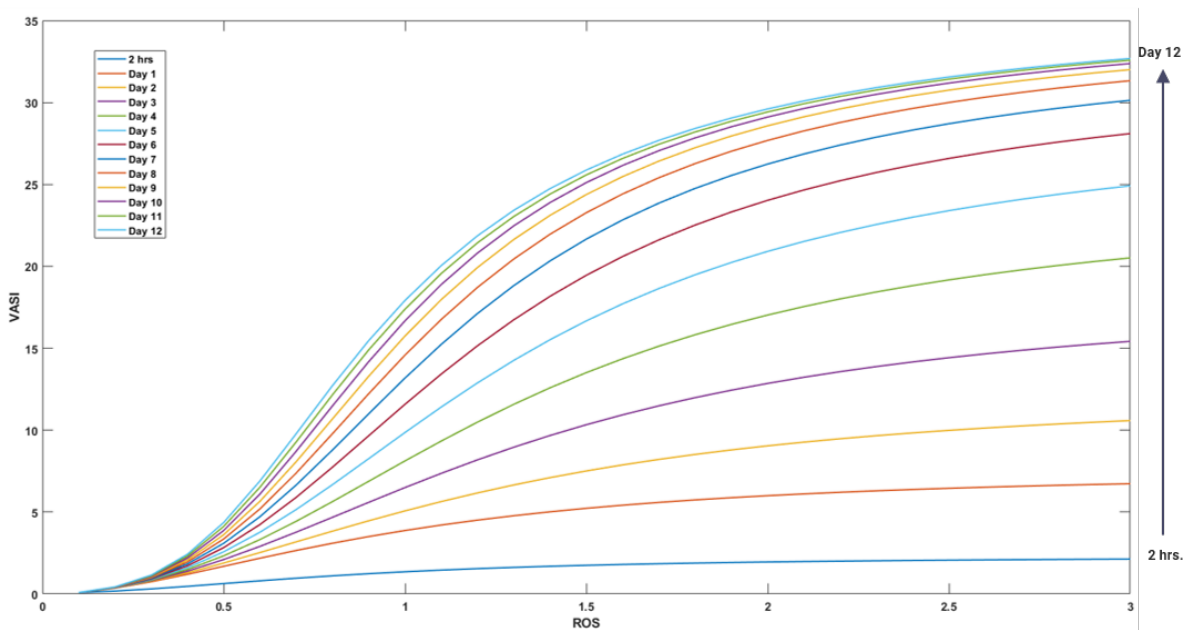


Figure 4.6: Change in Vitiligo Area Severity Index (VASI) in response to increasing ROS for different days of exposure

4.4.2 Effect of stress on skin cells, immune cells and cytokines

The gradual increase in ROS has a negative effect on keratinocyte levels, while stressed keratinocytes (K_{str}) demonstrate the opposite trend. In contrast, normal melanocytes (M) and stressed melanocytes (M_{str}) exhibit a similar relationship as K_{str} , but M_{str} levels decrease earlier than K_{str} due to the reduction in M levels (Figure 4.7). The levels of DC increase until day

4.4 Results

4 and then start to decline because of a drop in M_{str} and $IL1\beta$ level. T_{naive} , Th1, and T_{reg} show a similar pattern as DC. Inhibition by T_{reg} causes a further decrease in Th17 and CD8 levels. The cytokine levels display similar behavior to the cells that produce them. Low-stress exposure for a more extended period leads to a steep increase in CXCL10 due to additional activation through T_{EM} and $IFN\gamma$. FAS, which is a death signal produced by CD8 and T_{EM} , decreases after day 4 because of the reduction in CD8 levels (Figure 4.8).

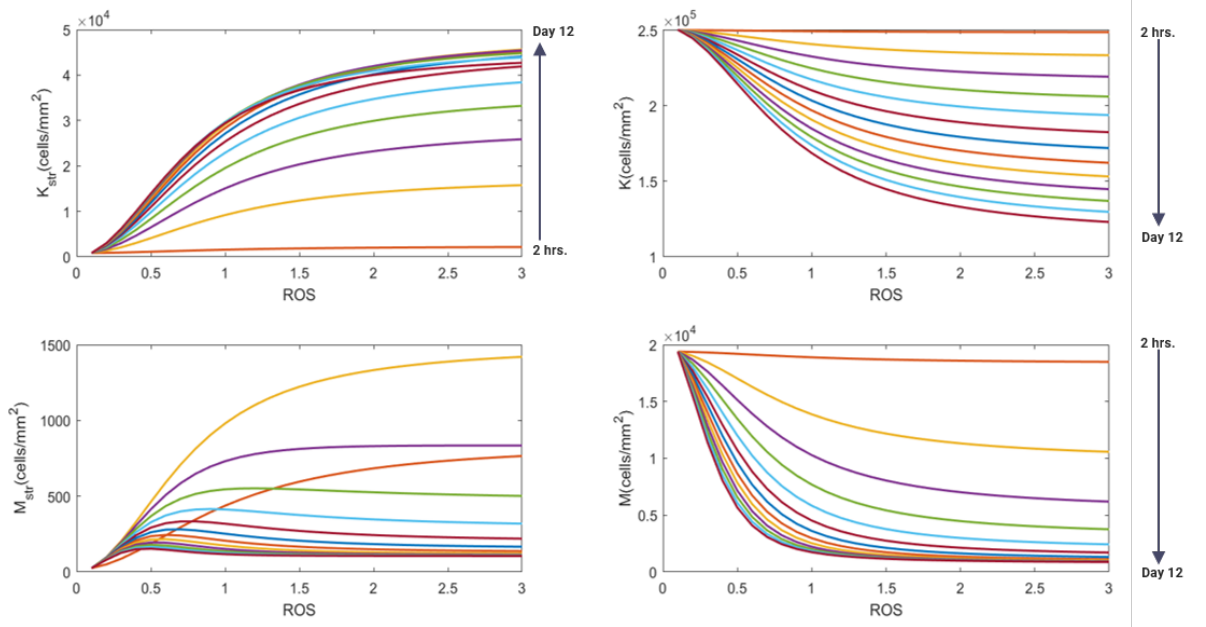


Figure 4.7: Change in the level of skin cells in response to increasing ROS for different days of exposure

According to the theory that autoreactive T cells infiltrate the skin and cause vitiligo, a team used flow cytometry to count the T cells in a mouse model's ear skin. They discovered that accumulation of these cells starts between the first and third week after transfer, peaks at the fifth week, when depigmentation becomes apparent, and then starts to diminish (Harris et al., 2012). A melanoma mouse model with CD4+ T cell depletion similarly produced hair coat depigmentation (Byrne and Turk, 2011; Zhang et al., 2007). To our knowledge, there is no literature that measured the levels of stressed melanocytes and keratinocytes in vitiligo. However, HMGB1 levels were shown to increase up to 3 fold within 48 hours under oxidative stress in a study conducted by Cui et al (Cui et al., 2019). HMGB1 is a Damage-associated molecular pattern molecule released by ferroptotic cells (in this case M_{str} and K_{str}) in an autophagy-dependent manner. Similarly, other skin cell-secreted cytokines such as CXCL10, and $IL1\beta$ show an increase in vitiligo (Cui et al., 2019; Rashighi et al., 2014). Another significant cytokine released by T cells during an immunogenic response is $IFN\gamma$. Its expression was shown to be

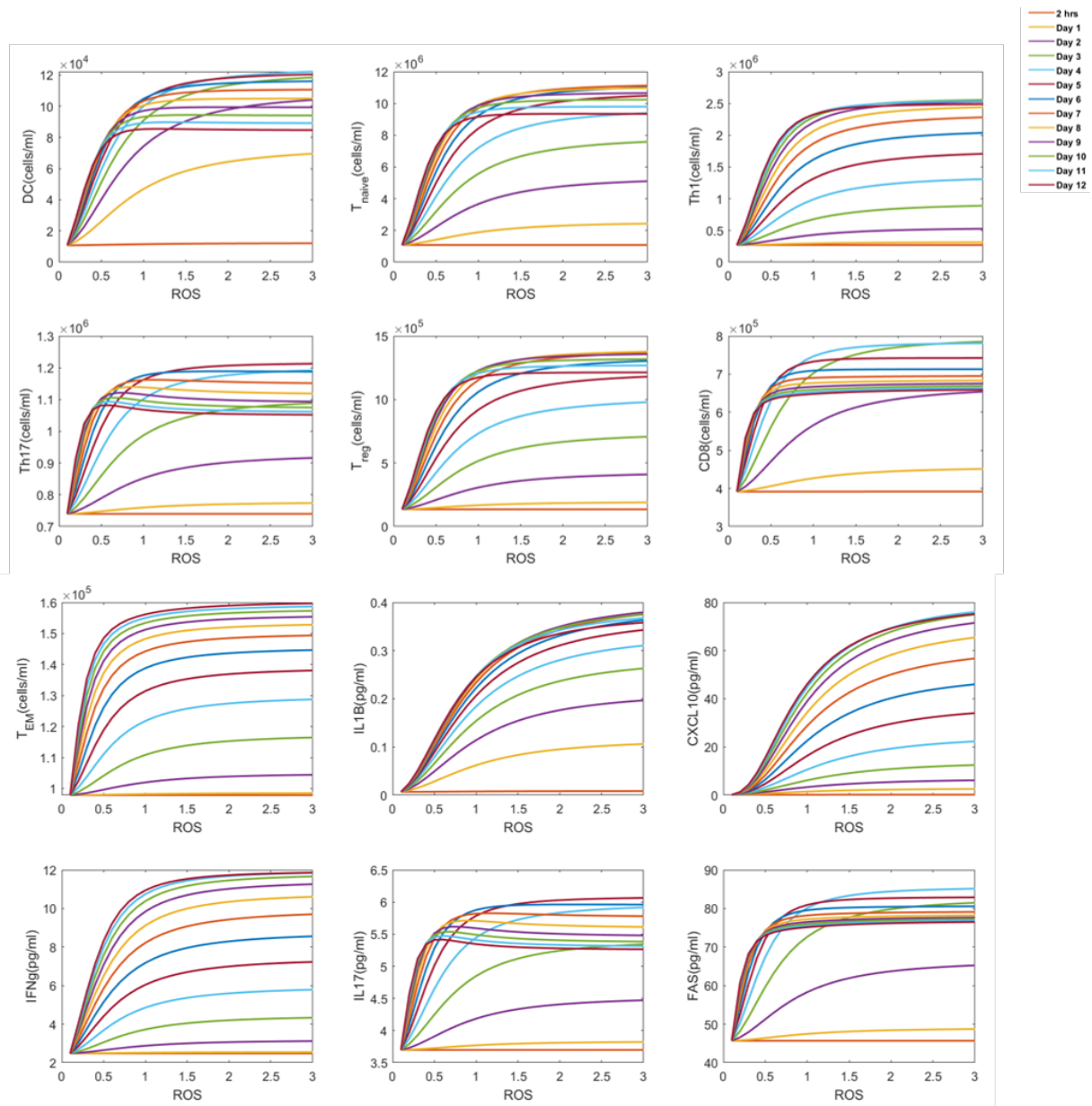


Figure 4.8: Change in the level of immune cells and cytokines in response to increasing ROS for different days of exposure

higher in the depigmenting skin of vitiligo mice. This expression dramatically increased two weeks after transfer and remained high throughout the disease (Harris et al., 2012).

4.4.3 Simulating the drug effect

As shown in Figure 4.5, normal melanocytes, DC and T_{reg} are some of the known therapeutic targets in vitiligo. Topical application of an active form of vitamin D increases T_{reg} in the skin,

4.4 Results

resulting in suppressed immunity and particularly reduced contact hypersensitivity responses (AlGhamdi et al., 2013). Afamelanotide is an analog of α -MSH that stimulates melanocytes. Combination therapy with afamelanotide showed improved repigmentation on the face and upper extremities relative to narrow-band UVB alone (Lim et al., 2015). We simulated the effect of these drugs in 2 different ways: 1) by increasing the formation rate of melanocytes (K_m), 2) by increasing the rate of differentiation of T_{naive} to T_{reg} (k_{tn3}). In both cases, we increased the rate up to ten fold. When the system was pre-exposed to maximum ROS for a short duration, increasing K_m up to ten-fold for 2 days did not reduce VASI. However, when VASI was max., increasing K_m up to five-folds for 12 days reduced the score to 20; when K_m increased ten-fold, the score continued to decline. As for k_{tn3} , a fold increase in the rate for 12 days could only lower the score by one unit (Figure 4.9). This suggests that melanocyte-specific drugs might be

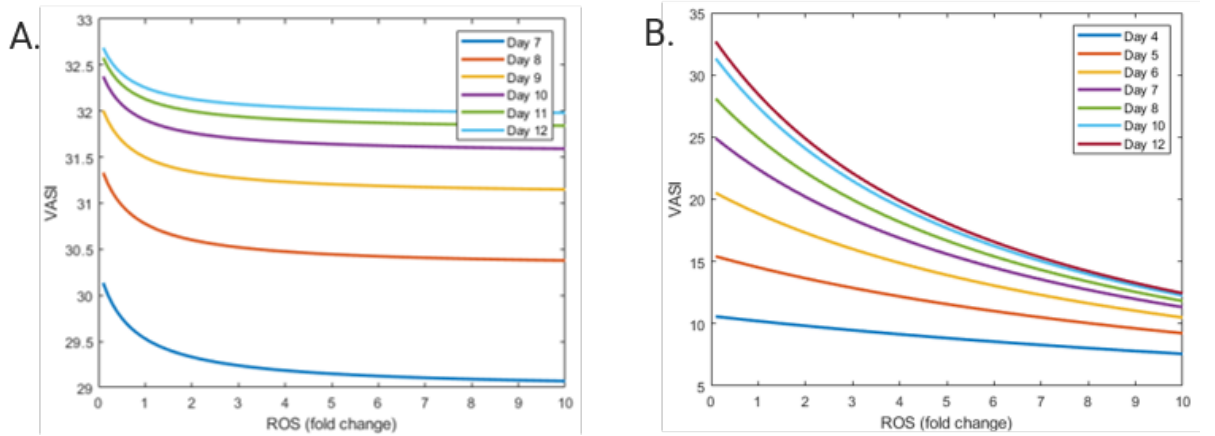


Figure 4.9: Changes in VASI during drug treatment (A) change in VASI in response to k_m fold increase (afamelanotide treatment) (B) change in VASI in response k_{tn3} fold increase (Vitamin D, helin treatment)

more effective than immune cell modulators in treating vitiligo. Here, we focused on simulating the effect of drugs by specifically examining changes in target activity, without incorporating the pharmacokinetics and pharmacodynamic properties of the drugs. It is important to note that during the treatment of vitiligo, multiple drugs are often given, which can potentially interact with one another, resulting in adverse reactions. While we have not directly investigated drug-drug interactions (DDIs) in the context of vitiligo, we have developed a separate model that comprehensively considers all possible DDIs when two drugs are administered simultaneously. Details of which can be found in the Appendix.

4.5 Discussion

In summary, the model presented here is the first disease model for vitiligo. The model provides insights into the response of the system to varying levels of stress. The particulars of all the molecular changes occurring in the vitiligo skin compared to healthy exposure are well documented. However, the time-dependent change in the cellular dynamics upon stress is hardly documented. Here, by using a systems biology approach, we showed that as ROS levels increase, the severity of vitiligo also increases gradually over time. This result is in line with other research that showed oxidative stress to be a factor in the aetiology of vitiligo. In addition, we have also managed to connect the output of the model to a modified clinical score which enables the measurement of disease severity for different levels of stress, which has never been achieved before.

Moreover, we examined the impact of stress on skin cells, immune cells, and cytokines. Our findings indicate that gradual increases in ROS have a negative effect on keratinocyte and melanocyte levels. However, K_{str} and M_{str} show an opposite trend, with M_{str} levels decreasing earlier than K_{str} due to a reduction in M levels. Research shows that the levels of DC initially increase but then decline due to a drop in M_{str} and $IL1\beta$ levels. T_{naive} , Th1, and T_{reg} exhibit a similar pattern as DC. Qing Nie's group conducted a study that revealed the enrichment of stressed keratinocytes and immune cells in vitiligo skin. Stressed keratinocytes increased from 6% to 13%, while immune cells increased from 2 to 4% (Shiu et al.). This indicates that a subset of keratinocytes is involved in establishing and maintaining vitiligo lesions in the skin. Previous studies acknowledge the role of stressed melanocytes in initiating pathogenesis (Cui et al., 2019; Richmond et al., 2013). However, changes in their dynamics have not yet been studied. Dwivedi et al. discovered a significant increase in CD8+ T-cell number and a decrease in CD4+ T-cell number in the circulation of vitiligo patients. This suggests that reduced numbers and impaired function of T cells such as T_{reg} fail to control the widespread activation of CD8+ T-cells, which may lead to the destruction of melanocytes (Dwivedi et al., 2013). The population of dendritic cells, other T cells, and cytokines were also reported to be enhanced during vitiligo (Wang et al., 2011). However, there is no evidence that suggests their decline after prolonged exposure to stress. In our model, the normal melanocyte serves as the source of antigen/signal that initiates vitiligo. Therefore, when its population declines after prolonged exposure to stress, other cells and cytokines also tend to decrease.

The sensitivity of the predictions to the parameters (in Table 4.2) was systematically explored by perturbing the level of ROS. Specifically, variations were tested by adjusting ROS levels from 0.005 to 0.01 and subsequently from 1 to 3. The observed outcomes indicated that with a

4.6 Conclusion

ROS level of 0.005, there was a gradual increase in VASI until day 6, followed by a plateau or saturation of VASI levels. On the other hand, for ROS levels of 0.02 and 0.01, the behaviour of the system remained unaltered. Additionally, changes in the time duration of the simulation by a few steps did not introduce any visible impact on the predictions.

In Figure 4.5, we have shown known therapeutic targets for treating vitiligo, including normal melanocytes, DC, and T_{reg} . Vitamin D is a topical drug while afamelanotide is a systemic drug that is known to target these cells. Here, we have simulated the effect of these drugs in two ways: increasing the formation rate of melanocytes and increasing the rate of differentiation of T_{naive} to T_{reg} . The simulations showed that increasing the rate of melanocyte formation was more effective in reducing VASI than increasing the rate of T_{reg} differentiation. This suggests that melanocyte-specific drugs may be more effective in treating vitiligo than immune cell modulators. However, the effectiveness of these drugs is dependent on the degree of pre-exposure to maximum ROS and the duration and intensity of treatment. Further research is needed to explore the full potential of these therapeutic targets for treating vitiligo.

Overall, the disease model presented in this study provides a framework for understanding the pathogenesis of vitiligo and may help in developing effective treatment strategies. The study highlights the importance of oxidative stress in the development and progression of vitiligo and provides a deeper understanding of the cellular and molecular mechanisms underlying the disease. Future studies can build on this model to identify new therapeutic targets and develop more effective treatments for vitiligo.

4.6 Conclusion

Our comprehensive systems modeling exploration of vitiligo has highlighted the intricate dynamics underlying this skin disorder, unraveling the complex interplay between stress, immune response, and therapeutic interventions. The adapted Vitiligo Area Severity Index (VASI) scoring system, aligning with clinical trends, serves as a relevant metric in our model. The positive correlation between increased levels of reactive oxygen species (ROS) and heightened vitiligo severity, substantiated by existing studies, reinforces the model's accuracy in capturing oxidative stress effects. Validation from literature, notably Zhang et al. and Mathachan et al., further supports the fidelity of our model in replicating oxidative stress impacts on vitiligo. The model extends its reach to elucidate the repercussions of stress on skin and immune cells, unraveling a nuanced relationship that mirrors experimental findings.

Within this framework, the simulation of drug effects provides crucial insights. Identified therapeutic targets, including normal melanocytes, dendritic cells (DC), and regulatory T cells

(Treg), resonates with established treatments like vitamin D and afamelanotide. Simulation outcomes hint at the potential efficacy of melanocyte-specific drugs in significantly reducing VASI compared to immune cell modulators. This study, while emphasizing the importance of further investigations into the pharmacokinetics and pharmacodynamics of vitiligo drugs, has opened the door to a more targeted and effective approach to vitiligo treatment. As we progress, understanding the intricate details of drug interactions becomes important for precise therapeutic predictions. In summary, our systems model not only enriches our comprehension of vitiligo dynamics but also lays a robust foundation for refining therapeutic strategies tailored to the complexities of this skin disorder.

CHAPTER 5

Summary and Future Perspective

The epidermis is the human skin's outermost, stratified lining. It is mostly made up of keratinocytes and pigment-producing melanocytes. Keratinocytes divide at the basal epidermal layer and differentiate further as they move up toward the skin's surface. The outermost epidermal layer, which contains a dense network of keratin filaments and melanin globules, sheds off from the skin's surface every 28 days. Keratinocytes, Melanocytes, and other immune cells work together in a highly coordinated manner to maintain skin pigmentation. Any disturbance in this regulatory mechanism can lead to skin depigmentation disorders such as vitiligo. In this thesis, we have developed models and adapted existing models to study skin pigmentation at multiple biological scales as well as how the disturbance could lead to pigmentation-related disorders.

The first work in this thesis sheds light on the importance of metabolic rewiring in melanocytes during the process of pigmentation. By analyzing transcriptomic data of a B16 cell pigmentation model, we identified the involvement of SREBF1-mediated fatty acid metabolism in melanogenesis. The study also highlighted the key role of MITF in triggering the uptake of glucose and channeling it toward anabolic pathways that support melanosome biogenesis. However, this heightened bioenergetic activity impairs mitochondria, shifting metabolism to glycolysis, which is recovered through NRF2 detoxication pathways. The study's findings have implications for understanding cutaneous pigmentary diseases and developing effective treatments for them. The use of topical formulations targeting fatty acid metabolism, such as Orlistat, has shown promise in resolving hyperpigmentary conditions. Overall, this study provides a valuable framework for understanding melanogenesis programming and cellular responses to external stimuli in melanocytes.

The second study of this thesis focuses on understanding the keratinocyte-melanocyte interaction, metabolism and signaling. There are existing models that include intracellular interaction in melanocytes as well as intercellular interaction among skin cells. However, these models are either too small and do not include important elements or are presented in the form of a static network graph. In order to gain a detailed understanding of systems dynamics to different levels of input/UV, we converted this static network graph into a dynamic Boolean model and compared it to the existing Lee et al. model. The new model contains more information about molecular interactions and components that were lumped together in the Lee model. The majority of common nodes in both models respond to UV stimulation consistently, and the extension of the network has no significant impact on the predictions of the smaller Lee model. However, some nodes react to rising UV levels differently in both models. The study found numerous sensitive nodes that significantly alter the activity of the output nodes eumelanin, pheomelanin, and Bcl-2 after subjecting the system to constitutive activation and inhibition. Some nodes were identified as being crucial for the Bcl-2 activity in keratinocytes and melanocytes despite not

being sensitive in the Lee model. The experimental data and outcomes agree with the study’s findings.

In the next section (of the second study), we explain the formulation of two new methods of dynamic function perturbation, FoN and NoF, and their application to two existing Boolean models, the melanogenesis signaling network and segment polarity network. The results showed that both methods were able to identify sensitive nodes in the network and that the nodes identified as sensitive by the new methods were consistent with those identified by constitutive activation/inhibition. Furthermore, it was found that multiple perturbation methods may capture differing biological situations, and hence a comprehensive determination of node sensitivity may require different perturbation methods to be applied to the network. We suggest that these two methods are useful additions to the suite of perturbation methods for Boolean networks.

The final study in this thesis presents the first disease model for skin depigmentation disorder i.e. vitiligo. Many theories have been proposed to cause melanocyte destruction in vitiligo including autoimmunity, oxidative stress, chemical exposure, and local neural injury. However, no one has considered the combined effect of these factors. We formulated the first disease model for vitiligo that simulate the combined effect of all the proposed theories and connected it to the clinical score VASI. Results show that gradual increases in ROS have a negative effect on keratinocyte and melanocyte levels and that the severity of vitiligo increases gradually over time as ROS levels increase. We also examined the impact of stress on skin cells, immune cells, and cytokines and showed that stressed keratinocytes and immune cells are enriched in vitiligo skin, suggesting their role in establishing and maintaining vitiligo lesions in the skin. Our study identifies known therapeutic targets for treating vitiligo, including normal melanocytes, DC, and T_{reg} and shows that increasing the rate of melanocyte formation is more effective in reducing VASI than increasing the rate of T_{reg} differentiation. Our study highlights the importance of oxidative stress in the development and progression of vitiligo and provides a deeper understanding of the cellular and molecular mechanisms underlying the disease.

The third study (Chapter 4) is a systems pharmacology model without a detailed pharmacokinetic model. Though there are several PK models, they for the most part ignore drug-drug-interactions beyond the effect on efficacy. However, it is known that drugs compete for metabolizing enzymes in the liver, and in general may influence the uptake and distribution through such effects. The next section (Appendix A) presents a model for such interactions and simulations that suggest that in some circumstances, this effect may be nonintuitive and severe. While it is impossible to exhaustively list all possible interactions, studies have developed mathematical models to analyze specific drug combinations. In this work, we adopted a more general approach to modeling DDIs and focused on pharmacokinetic interactions, specifically

the alteration in the clearance of a drug due to an effect exerted by another or the same drug. We model the potential interactions of drugs with each other and themselves as different motifs. Through mathematical simulation, we found that the infusion rates of two drugs are important in dictating the system's behavior, and certain infusion rates can lead to undesirable characteristics in a clinical setting, such as periodic oscillations or bistability. The system displays dynamic behavior dependent on the intrinsic properties of the drug-drug pair as well as on external factors such as the infusion rate of one drug relative to the other.

The second work in this thesis can be furthered by adding an immune cell module in a melanogenesis network. This way we will have a boolean model for vitiligo with three types of cell modules i.e. 2 for skin cells and 1 for immune cells. We can simulate the intrinsic defect in melanocytes by perturbing key genes/nodes associated with melanin formation. Spritz and co-workers identified variants of FOXD3 in vitiligo patients that reduce melanoblast differentiation. Melanoblasts are neural crest-derived specific precursors of melanocytes that are unable to synthesize melanin because of the absence of tyrosinase (TYR)-related protein. We can mimic the effect of reduced melanoblast differentiation in the existing model by flipping the output (NoF) or input (FoN) of the tyrosinase (TYR)-related protein. Apart from FOXD3, CTLA4 and PTPN22 variants have been identified in vitiligo. CTLA4 encodes a T-cell co-receptor involved in the regulation of T-cell activation (Spritz and Andersen, 2017). Perturbations in these and other immune components can help to transform the normal melanogenesis model into a vitiligo disease model. Overall, the inclusion of an immune cell module in the melanogenesis network can enhance the model's relevance by accounting for immune-mediated mechanisms in vitiligo. By investigating these mechanisms, we can gain insights into the disease's pathophysiology and potentially identify new therapeutic targets.

To gain a more comprehensive understanding of the pathogenesis of vitiligo, the last chapter can be further extended by integrating components from the molecular and cellular models into the disease model. By doing so, a multiscale understanding of the disease process can be achieved. Furthermore, the disease model can be extended into a QSP model by incorporating a physiology-based pharmacokinetic (PBPK) model. This model would account for skin, lymph, and blood compartments based on the availability of parameters (Figure 5.1). The PBPK model would be useful in simulating the transport and metabolism of drugs between these compartments using mass balance equations. These equations describe organ and tissue-specific blood flow into and out of each compartment. The combination of the skin disease model and the PBPK model will provide a unique framework for evaluating the effectiveness of multiple drugs used to treat vitiligo and optimizing treatment protocols. By using this model, the impact of different drug doses, administration routes, and schedules on the outcome of treatment can be assessed.

Overall, this model has the potential to provide valuable insights into the pharmacodynamics and pharmacokinetics of drugs used to treat vitiligo and other skin diseases.

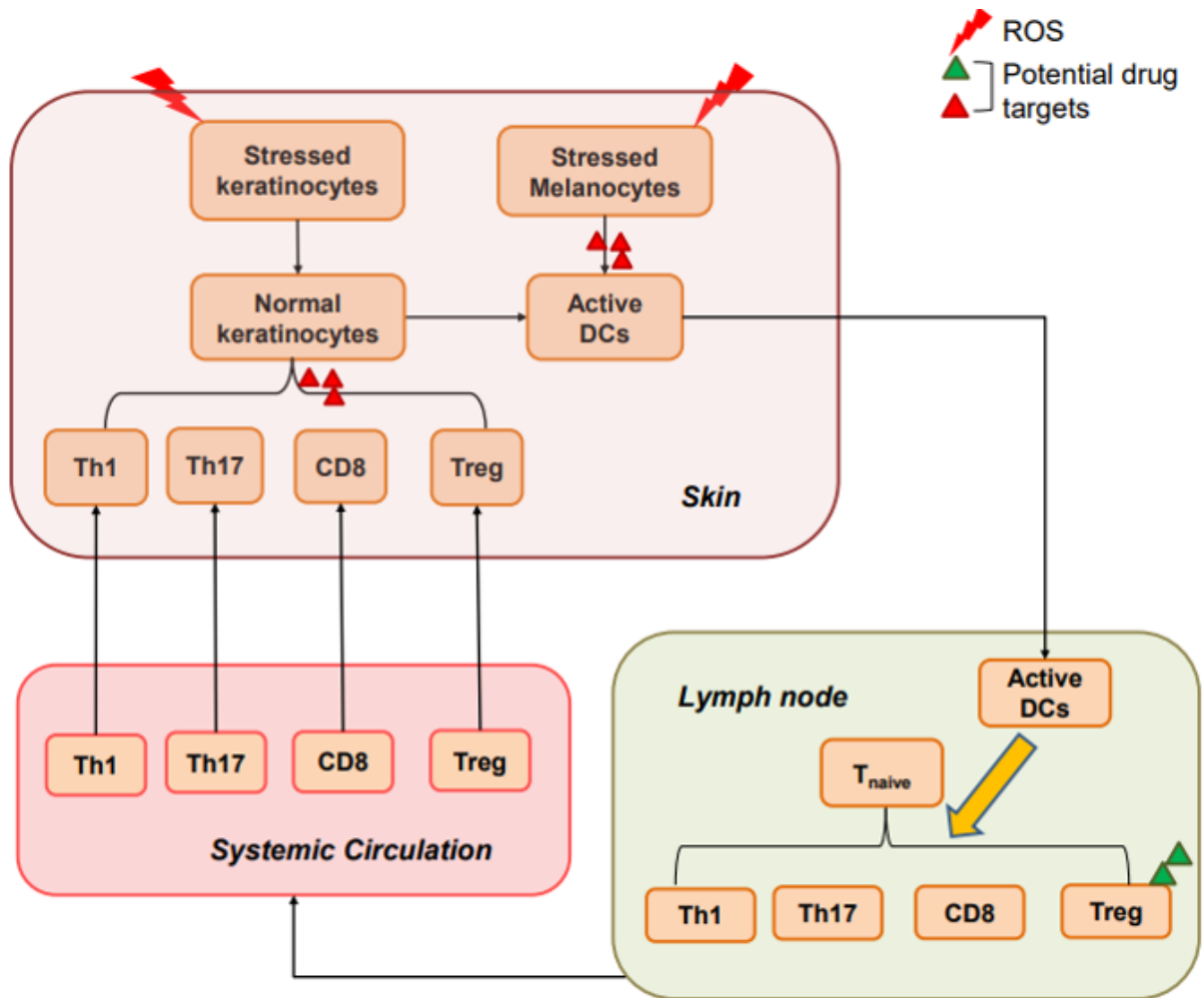


Figure 5.1: Concept diagram of Physiology Based Pharmacokinetic Model for Vitiligo

Drug-Drug Interaction

1

A.1 Understanding drug-drug interactions: mechanisms, risk factors, and existing models

DDIs occur when one drug affects the effectiveness of another concurrently administered drug, often resulting in unwelcome side effects (Hines and Murphy, 2011). Combination therapy, commonly used in conditions like vitiligo (Travis and Silverberg, 2004), HIV treatment (de Maat et al., 2003), and cancer (van Leeuwen et al., 2013), contributes to the rise in DDIs. Concurrent use of psoralen-containing topical treatments and NSAIDs, such as methoxsalen and ibuprofen, respectively, may increase the risk of phototoxicity and skin irritation due to their photosensitivity properties. Risk factors for DDIs include age (very young and advanced age), polypharmacy, multiple prescribers, changed hepatic/renal activity, altered metabolism/endocrine problems, and coexisting illnesses (Dechanont et al., 2014; Grattagliano et al., 2010).

DDIs are categorized into two groups: pharmacodynamic and pharmacokinetic interactions. Pharmacodynamic interactions alter the physiological effect of a drug, such as the additive effects of nonsteroidal anti-inflammatory drugs and phenprocoumon, or the synergistic or antagonistic effects of aspirin and ibuprofen (van Leeuwen et al., 2014; Cascorbi, 2012). Pharmacokinetic interactions occur when one drug affects the absorption, distribution, metabolism, or excretion of another drug taken simultaneously (van Leeuwen et al., 2014).

Metabolic enzymes in the liver can be activated or inhibited by drugs, leading to clinically severe DDIs and unexpected adverse drug reactions (ADRs). Around 20% of ADRs are associated with DDIs (van Leeuwen et al., 2013; Magro et al., 2012). Certain drugs, like mibefradil, terfenadine, astemizole, and cisapride, were withdrawn from the market due to their potential to cause harmful levels of other drugs or deadly arrhythmias through metabolic inhibition by other pharmaceuticals (Mullins, 1998). The use of statins and CYP3A4 inhibitors carry a risk of rhabdomyolysis (Dresser et al., 2000).

¹This is a joint work with Aparna Ramachandran (manuscript under preparation)

Mathematical models have been developed to understand enzyme-mediated DDIs. For example, the enzyme turnover model explains rifampicin autoinduction, where increased rifampicin plasma concentration nonlinearly raises enzyme levels and increases rifampicin clearance (Smythe et al., 2012). Models simulating the DDIs of lopinavir, ritonavir, and rifampicin in HIV-infected individuals showed that ritonavir hindered lopinavir clearance, while rifampicin increased clearance of both drugs (Zhang et al., 2012a). Another model studied the DDI between clopidogrel and omeprazole, where omeprazole’s inhibitory effect on CYP2C19 led to increased plasma concentrations of clopidogrel (Tangamornsuksan et al., 2017). The Loewe additivity model and Bliss independence model use pharmacodynamic interactions to theoretically describe DDIs (Vakil and Trappe, 2019). While there is currently no dedicated research investigating DDIs in vitiligo, we have developed a comprehensive model that primarily examines the impact of co-administered drugs on drug clearance. Our model explores pharmacokinetic interactions as network motifs, specifically emphasizing alterations in drug clearance caused by the presence of other drugs.

A.2 Model for drug-drug interaction

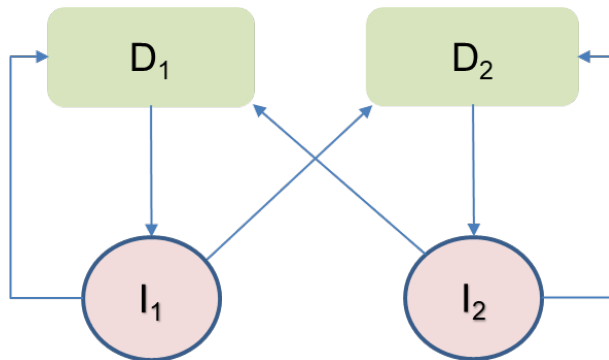


Figure A.1: Schematic presentation of drug-drug interaction model

The model depicted in Figure A.1 describes drug-drug interactions in our studies. It contains two drugs, D_1 and D_2 , as well as their intermediary factors/enzymes, I_1 and I_2 . The drug concentration is represented by a one-compartment pharmacokinetic model with constant drug infusion and elimination. D_1 and D_2 induce the production of intermediate components I_1 and I_2 . The intermediary factors then influence the other drug’s metabolism by altering its elimination. Hill kinetics is used to describe the activation/repression of elimination by intermediates, as well as the induction of intermediates by drug concentrations. The following equations are used to calculate time-dependent drug and intermediate concentrations:

$$\frac{d\widehat{D}_i}{dt} = \widehat{k}_{in} - \widehat{D}_i \cdot \left(1 + \frac{\widehat{I}_j^{n_{ji}} \cdot k_{ji}}{\widehat{K}_{ji}^{n_{ji}} + \widehat{I}_j^{n_{ji}}} + \frac{\widehat{I}_i^{n_{ii}} \cdot k_{ii}}{\widehat{K}_{ii}^{n_{ii}} + \widehat{I}_i^{n_{ii}}} \right) \quad (\text{A.1})$$

$$\frac{d\widehat{I}_j}{dt} = \widehat{\alpha}_j \cdot \left(\frac{\widehat{D}_j^{n_j}}{\widehat{D}_j^{n_j} + \widehat{K}_j^{n_j}} \right) - \widehat{\beta}_j \cdot \widehat{I}_j \quad (\text{A.2})$$

When k_{ji} is negative, the regulatory term changes, elimination decreases, and D levels rise. Similarly, as k_{ji} increases, D decreases. $k_{ji}=0$ denotes that there is no regulation.

A.2 Model for drug-drug interaction

Symbol	Parameter	Values
$\widehat{k_{in}}$	Infusion rates of the drugs are given as the ratio $\frac{kin_1}{kin_2}$ where kin_1 and kin_2 are the infusion rates of drug 1 and 2 respectively	$kin_1 = 0.4, kin_2 = 1$
$\widehat{kel_i}$	Basal elimination rates of the drugs	$kel_1 = 1, kel_2 = 1$
$\widehat{\alpha_i}$	Synthesis of intermediates, given as $\frac{\alpha_1}{kin_2}$ and $\frac{\alpha_2}{kin_2}$ for I_1 and I_2 respectively, where α_1 and α_1 are the synthesis rates of I_1 and I_2 respectively	$\alpha_1 = 1, \alpha_2 = 1$
$\widehat{\beta_i}$	Decay of intermediate factors, given as ratios $\frac{\beta_1}{kel_1}$ and $\frac{\beta_2}{kel_1}$ for I_1 and I_2 respectively, where α_1 and α_1 are the decay rates of I_1 and I_2 respectively	$\beta_1 = 1, \beta_2 = 1$
n_{ij}	Hill coefficient	$n_{ij} = 8$
k_{ji}	Magnitude of influence of I_j on elimination of D_i	$-1 \leq k_{ji} < 0$ when D_i inhibits clearance of D_j , $0 < k_{ji} \leq 10$ when D_i induces clearance of D_j (Values in Table A.2)
$\widehat{K_{ji}}$	Concentrations of the intermediates I_1 and I_2 respectively, producing 50% of the maximum effect (induction or inhibition) on drugs clearance is given as a ratio $K_{ji} \cdot \frac{kel_1}{kin_2}$	$K_{ji} = 0.5$
$\widehat{K_j}$	Concentrations of drugs D_1 and D_2 resulting in 50% of the maximum yield of intermediates I_1 and I_2 resp. given as a ratio $K_j \cdot \frac{kel_1}{kin_2}$	$K_j = 0.5$

Table A.1: Parameter definitions and values

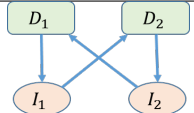
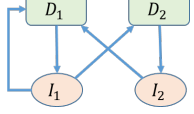
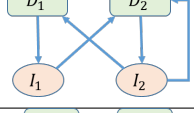
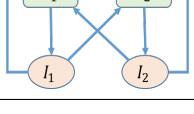
	Motifs	k_{21}	k_{12}	k_{11}	k_{22}	$\widehat{k_{in}}$
1		-1 to 10	-1 to 10	0	0	0.1 to 5
2		-1 to 10	-1 to 10	-1 to 10	0	0.4
3		-1 to 10	-1 to 10	0	-1 to 10	0.4
4		-1 to 10	-1 to 10	-1 to 10	-1 to 10	0.1 to 0.8

Table A.2: Various interaction scenarios and their corresponding regulatory parameter values used during simulation

A.2.1 Simulation Methodology

The goal of this study is to investigate the scenarios in which continuous drug infusion may result in unanticipated systemic concentrations. We performed simulations on 48 drug-drug interaction motifs that involved incoherent and coherent (particularly double negative) regulation since these types of regulation frequently contribute to abnormal behavior in biological systems. The numbers n , K_{ji} , and K_j were obtained through a literature review (Ferrell et al., 2011). The remaining constants were picked at random (Table A.1 and A.2). Using ode23s, time-dependent concentrations were calculated in MATLAB 2020b.

By determining stability borders as functions of a system parameter, bifurcation analysis aids in calculating regions of stable and unstable solutions. We used bifurcation analysis to determine value ranges for important parameters where the system (particularly, drug concentrations) exhibits periodic behavior or bistability rather than the expected monostability. XPPAUT (Ermentrout and Mahajan, 2003) was used for the analysis.

A.3 Continual drug infusions may alter the system's behavior

A.3.1 Incoherent regulation may lead to oscillations

We simulated the administration of two drugs, D_1 and D_2 , which can influence each other's or their own elimination via intermediates I_1 and I_2 . Continuous infusion of drugs may result in the oscillation of their systemic concentrations for positive-negative regulation (Figure A.2). This periodic activity, however, is limited to a specific range of parameter values. We varied k_{12} and k_{21} at different values of \widehat{k}_{in} to determine these parameter ranges.

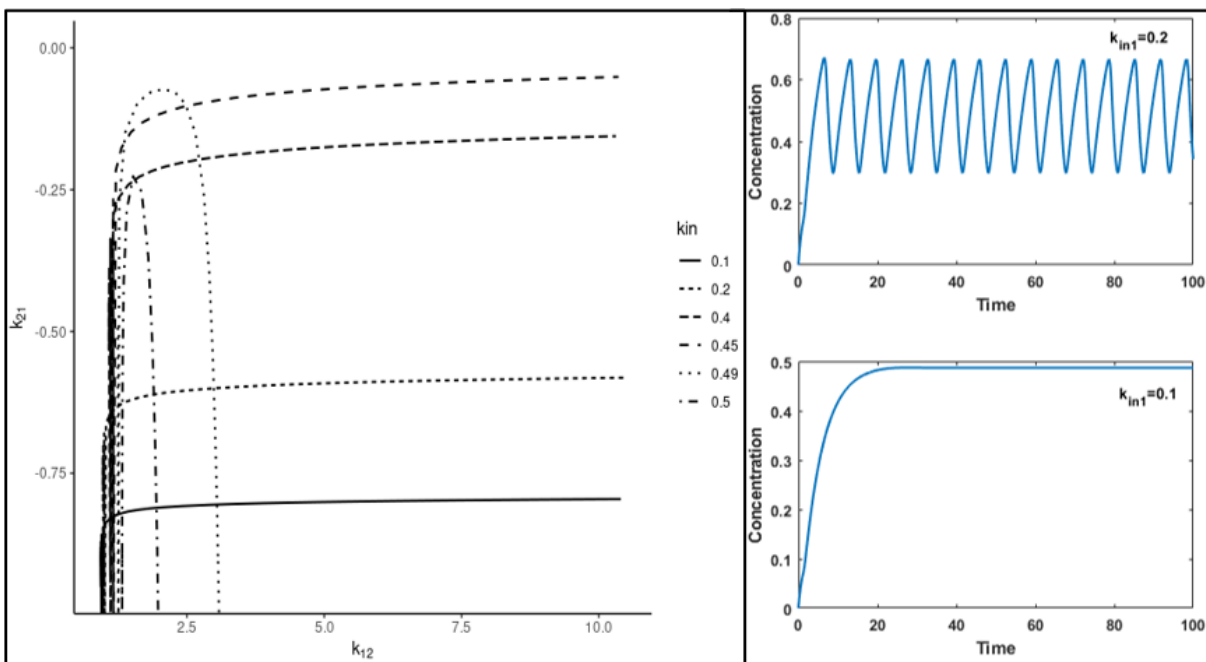


Figure A.2: Left: Bifurcation diagram for oscillatory behavior with respect to the parameters k_{12} , k_{21} and k_{in} . Parameter values are the same as described in Table A.2, except \widehat{k}_{in} which is varied as shown. Right: For the same values of k_{12} , k_{21} , change in \widehat{k}_{in} from 0.1 to 0.2 results in oscillations

A.4 Codimension-two bifurcation analysis of motif 2 and 3

A.3.2 Double negative regulation may lead to bistability

In the case of coherent regulation, a change in the initial condition may result in a difference in the steady-state systemic drug concentration. At $\widehat{k}_{in} = 0.5$, the system exhibits oscillations as well as bistability. An increase in $\widehat{k}_{in} = 0.5$ broadens the set of parameter values that result in bistability. However, this region appears to be migrating to the left. Gradual increases in $\widehat{k}_{in} = 0.5$ from 0.5 to 1 are also observed. When $\widehat{k}_{in} = 1$, the region begins to shrink rapidly in an upward direction, which continues until $\widehat{k}_{in} = 0.5$. Figure A.3 depicts this behavior. This could affect the order of drug administration based on pre-existing amounts of metabolizing enzymes.

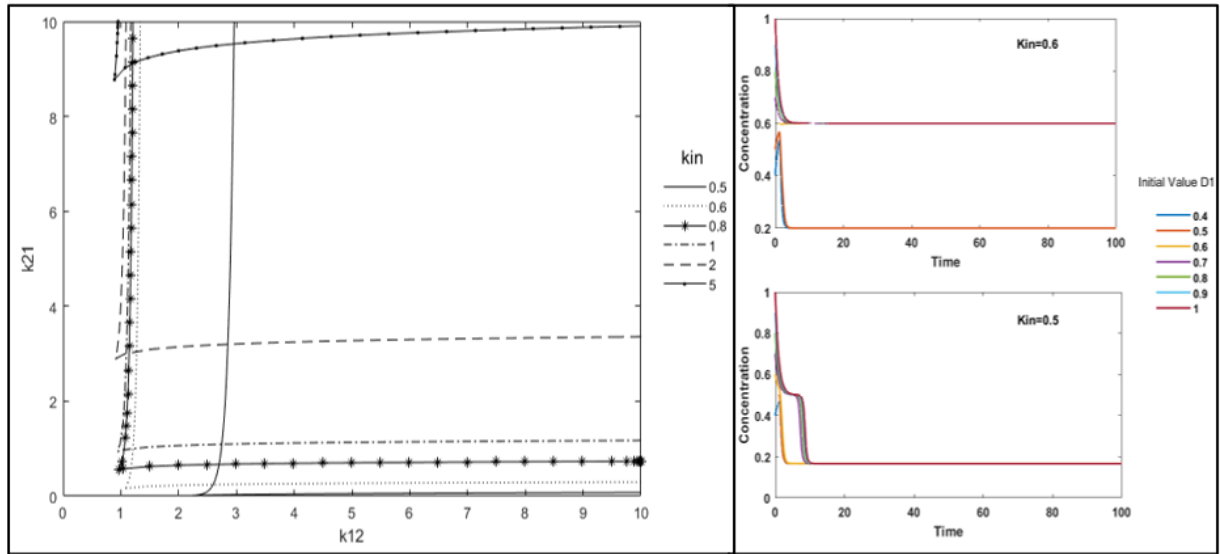


Figure A.3: Left: Bifurcation diagram for bistability with respect to the parameters k_{12} , k_{21} and \widehat{k}_{in} . Parameter values are the same as described in Table A.2, except \widehat{k}_{in} which is varied as shown. Right: For the same values of k_{12} , k_{21} , change in \widehat{k}_{in} from 0.5 to 0.6 results in bistability

A.4 Codimension-two bifurcation analysis of motif 2 and 3

To acquire a more thorough understanding of the system dynamics regulated by k_{11} and k_{22} in motifs 2 and 3 in Table A.2, codimension-two bifurcation analysis of these two parameters is performed in Figure A.4 for different values of k_{12} and k_{21} , respectively. When k_{12} is less than equal to 1 for motif 2, we observed only bistability, as illustrated in Figure A.4A. Then, when the k_{12} values increase, periodic behavior is introduced. This separates the parameter plane (k_{11} , k_{21}) into different regions with differing dynamics, as seen in Figure A.4(B-D): either one stable steady state, two stable steady states, or periodic behavior. Unstable steady states are neglected since they have no biological relevance in this context. As illustrated in Figure A.5, Motif 3 has a periodic character for certain parameter values. The parameter plane (k_{12} , k_{22}) depicts the k_{12} and k_{22} ranges (values under the curve) for which the systemic concentrations oscillate. The system exhibits this behavior for specified values of k_{21} . The area bound appears to decrease as k_{12} grows.

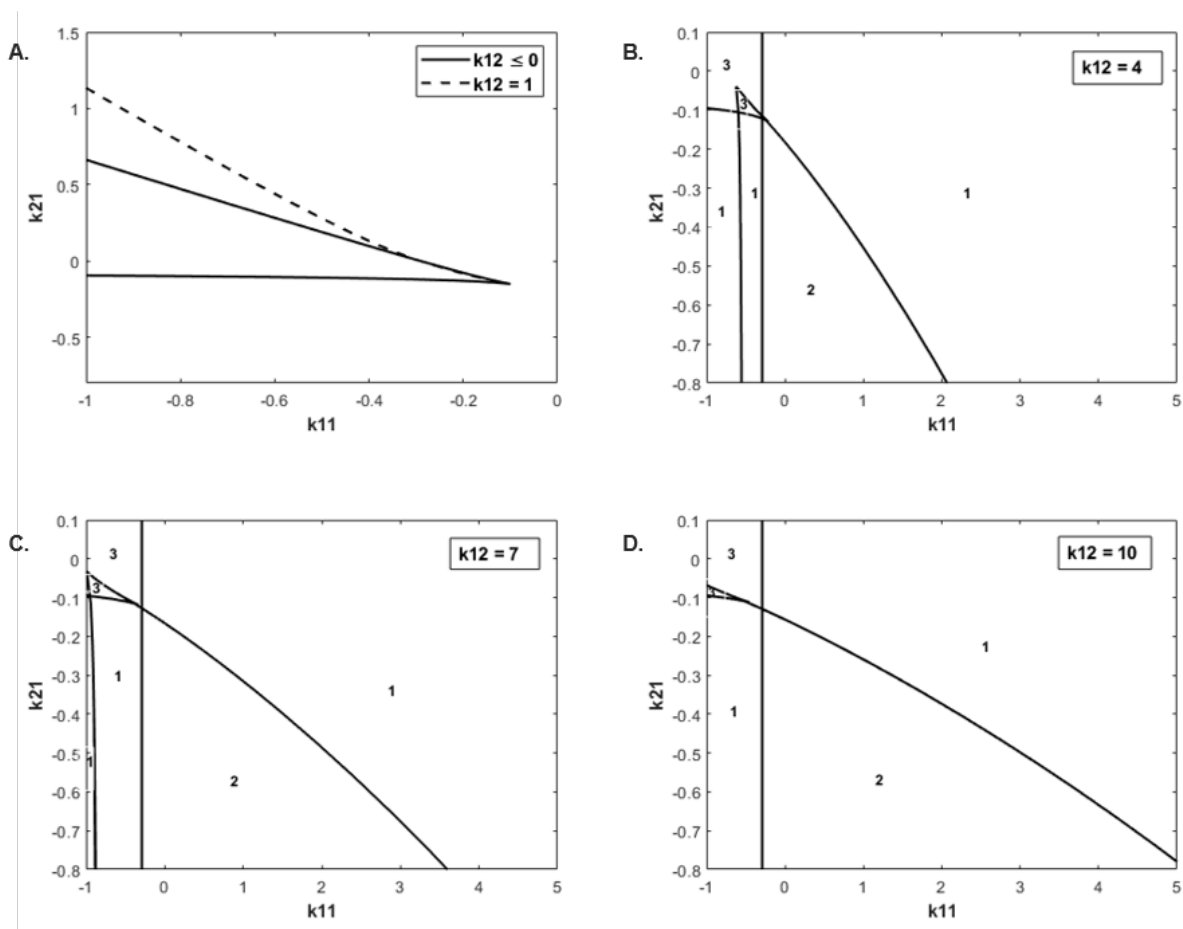


Figure A.4: Codimension-two bifurcation plots with respect to parameters k_{11} , k_{21} , for various values of k_{12} . A) Only bistability is observed. B-D) Bistability and periodicity are observed. The following labels are used to demarcate the behaviors. 1: One stable steady state; 2: Stable oscillations; 3: Two stable steady states

A.5 Codimension-two bifurcation analysis of motif 4

Bifurcation analysis of motif 4 is performed to acquire a better understanding of the systemic dynamics driven by cross-regulation (k_{12} and k_{21}) and self-regulation (k_{11} and k_{22}). We then adjusted the values of k_{12} and k_{21} while keeping k_{11} and k_{22} constant (Figure A.6A). In this scenario, increasing the drug infusion rate resulted in the extension of the oscillatory zone. This design is monotonous and distinct from motif 1 (Figure A.2). The bistability area on the left for incoherent cross-regulation increased as the drug infusion rate rose (Figure A.6B). Furthermore, there is a minor upward shift. This design is comparable to motif 1. Then we changed the values of k_{11} and k_{22} while keeping k_{12} and k_{21} constant. It is observed that when the drug infusion rate is below 0.5, the system exhibits oscillations for both positive and negative self-regulation (Figure A.6C). Additionally, if the infusion rate is higher than 0.5, the system exhibits bistability for both negative and positive self-regulation (Figure A.6D)

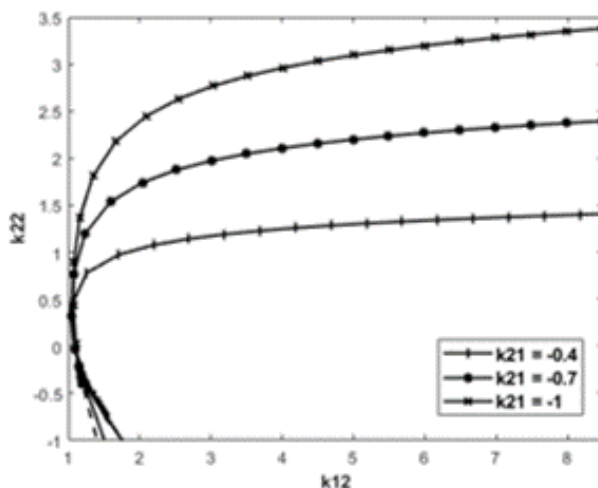


Figure A.5: Codimension-two bifurcation plots with respect to parameters k_{11} , k_{21} , for various values of k_{12} . Oscillating concentrations are seen when parameter values lie within the curve region

A.6 Conclusion

Drug-drug interactions (DDIs) are a common problem when multiple drugs are administered simultaneously to a patient, affecting a drug’s therapeutic efficacy and often causing adverse drug reactions (ADRs). While it is impossible to exhaustively list all possible interactions, there is a need to improve the prediction of potential DDIs. In our study, we focus on pharmacokinetic interactions, specifically changes in drug clearance caused by the impact of another drug. We use ordinary differential equations (ODEs) to represent the system of interactions, analyzing the continuous infusion of two drugs that act through intermediates.

Previous research has mathematically analyzed DDIs for specific drug combinations, such as cyclophosphamide and saquinavir with itraconazole (Hassan et al., 1999; Lohitnavy et al., 2015). However, our approach is broader, simulating interactions between drugs and themselves as different motifs. We investigated feedback effects caused by metabolic enzymes, which can either reduce or increase drug clearance, leading to abnormal drug concentrations. Through our simulations, we identified circumstances where the system exhibits bistability or periodic oscillations instead of converging to a single steady state.

We observed in motif 1 that the infusion rates of the two drugs play a critical role in determining the system’s behavior. Changes in the ratio of infusion rates result in oscillating systemic concentrations and two stable steady-state equilibriums. Incoherent regulation, where the drugs antagonize each other’s effects, leads to periodic behavior, while coherent regulatory motifs result in two stable steady states. Both of these characteristics are undesirable in a clinical setting as they can hinder effective therapy, highlighting the need to avoid infusion rates that lead to such behaviors.

By introducing more interactivity, model complexity increases, and periodicity and bistability coexist in motifs 2 and 3. These motifs depict interactions between two drugs, with one drug influencing its own clearance. Varying interaction factors and infusion rate values lead to different system behaviors. The dynamic behavior of the system depends on the intrinsic qualities of the drug-drug pair and external influences such as the infusion rate.

In natural systems, nonlinear feedback is associated with emergent dynamics, as seen in gene regulatory networks. Biological systems exhibit oscillatory behavior due to negative feedback

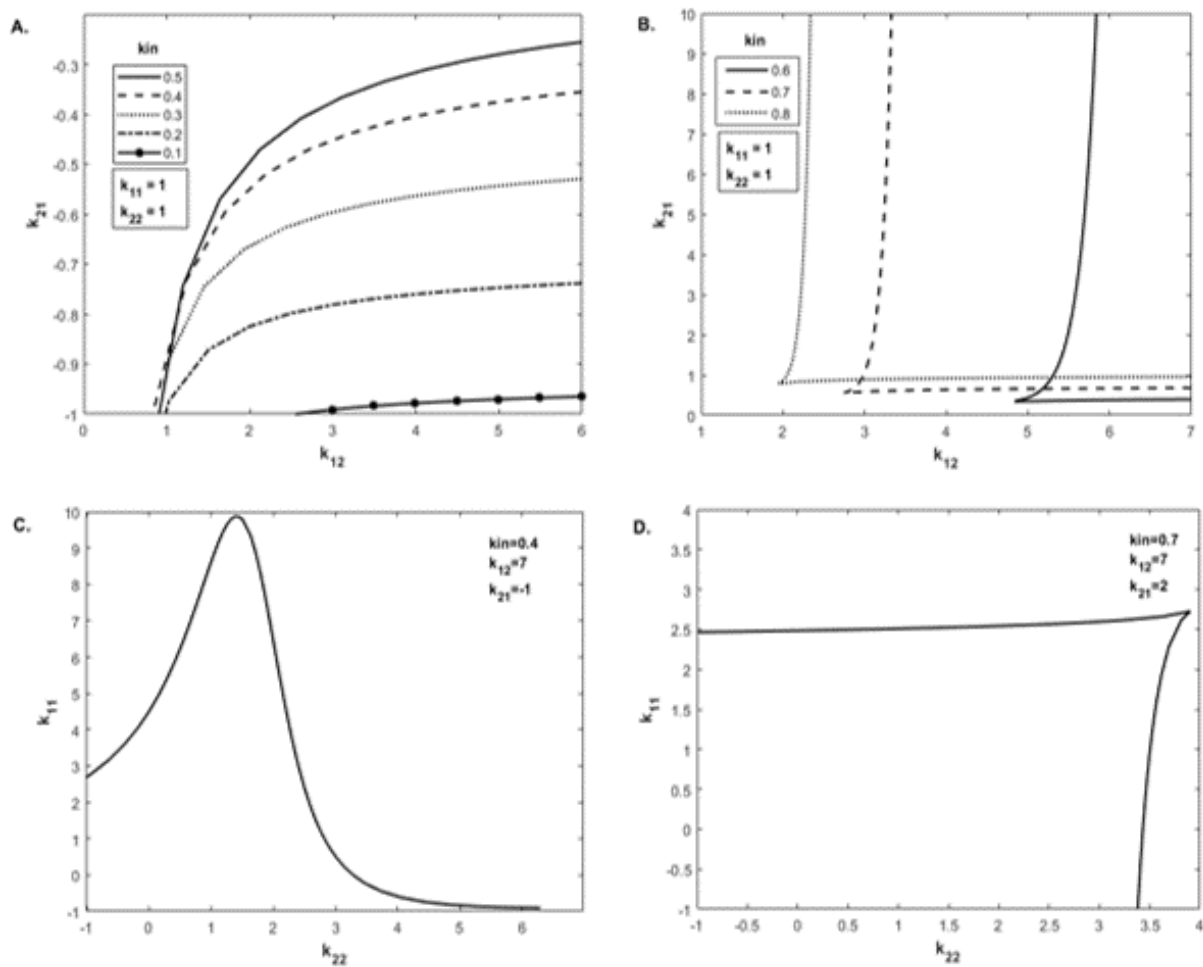


Figure A.6: Codimension-two bifurcation plots with respect to parameters k_{11} , k_{21} , k_{11} , k_{22} and \widehat{k}_{in} . Oscillations are seen in A and D, while the parameter plane exhibits bistable behavior in B and C.

and self-regulation (Goldbeter, 2018; Gérard and Goldbeter, 2009). Bistable behavior has also been observed in various biological systems, including disease models (Goldbeter et al., 2007; Ha et al., 2016; Rapin et al., 2011). Understanding these dynamics can help predict and mitigate potential DDIs.

It is important to acknowledge that not all potential DDIs are known, and they can significantly impact a drug's therapeutic value and patient safety. Developing methods to identify probable DDIs can aid in treatment decision-making. Our research aims to identify one possible cause of drug interactions—decreased drug clearance—and anticipate potential interactions. The ultimate goal is to reduce the potency of such interactions by modifying external parameters such as drug combinations or doses.

Bibliography

- Severity scoring of atopic dermatitis: the SCORAD index. Consensus Report of the European Task Force on Atopic Dermatitis. *Dermatology (Basel, Switzerland)*, 186(1):23–31, 1993. ISSN 1018-8665. doi: 10.1159/000247298.
- Patterns of Vitiligo. *UMass Chan Medical School*, May 2020. URL <https://www.umassmed.edu/vitiligo/blog/blog-posts1/2020/05/patterns-of-vitiligo/>. Section: Blog.
- M. A. Abadie, F. Asharaff, and D. A. Abadie. Impact of Childhood Vitiligo on Self Esteem and Quality of Life in Adulthood. *Archives of Dermatology and Skin Care*, 2(2):1–6, 2019. ISSN 2638-4914. doi: 10.22259/2638-4914.0202001. URL <https://www.sryahwapublications.com/archives-of-dermatology-and-skin-care/pdf/v2-i2/1.pdf>.
- S. Adams, S. Pankow, S. Werner, and B. Munz. Regulation of NF-B Activity and Keratinocyte Differentiation by the RIP4 Protein: Implications for Cutaneous Wound Repair. *Journal of Investigative Dermatology*, 127(3):538–544, Mar. 2007. ISSN 0022-202X. doi: 10.1038/sj.jid.5700588. URL <http://www.sciencedirect.com/science/article/pii/S0022202X15332760>.
- K. Aishwarya, P. V. Bhagwat, and N. John. Current concepts in melasma - A review article. *Journal of Skin and Sexually Transmitted Diseases*, 2(1):13–17, Apr. 2020. ISSN 2582-3175. doi: 10.25259/JSSTD_34_2019. URL <https://jsstd.org/current-concepts-in-melasma-a-review-article/>. Publisher: Scientific Scholar.
- R. L. C. Akkermans and P. B. Warren. Multiscale modelling of human hair. *Philosophical Transactions. Series A, Mathematical, Physical, and Engineering Sciences*, 362(1821):1783–1793, Aug. 2004. ISSN 1364-503X. doi: 10.1098/rsta.2004.1395.
- M. S. Al’Abadie, H. J. Senior, S. S. Bleehen, and D. J. Gawkrödger. Neuropeptide and neuronal marker studies in vitiligo. *The British Journal of Dermatology*, 131(2):160–165, Aug. 1994. ISSN 0007-0963. doi: 10.1111/j.1365-2133.1994.tb08486.x.
- S. Alaluf, K. Barrett, M. Blount, and N. Carter. Ethnic variation in tyrosinase and TYRP1 expression in photoexposed and photoprotected human skin. *Pigment Cell Research*, 16(1):35–42, Feb. 2003. ISSN 0893-5785. doi: 10.1034/j.1600-0749.2003.00005.x.
- R. Albert and H. G. Othmer. The topology of the regulatory interactions predicts the expression pattern of the segment polarity genes in *Drosophila melanogaster*. *Journal of Theoretical Biology*, 223(1):1–18, July 2003. ISSN 0022-5193. doi: 10.1016/s0022-5193(03)00035-3.
- M. Aldana and P. Cluzel. A natural class of robust networks. *Proceedings of the National Academy of Sciences of the United States of America*, 100(15):8710–4, July 2003. doi: 10.1073/pnas.1536783100. URL <http://www.ncbi.nlm.nih.gov/pubmed/12853565>.

- K. AlGhamdi, A. Kumar, and N. Moussa. The role of vitamin D in melanogenesis with an emphasis on vitiligo. *Indian Journal of Dermatology, Venereology and Leprology*, 79(6):750–758, 2013. ISSN 0973-3922. doi: 10.4103/0378-6323.120720.
- A. K. Alhowaish, N. Dietrich, M. Onder, and K. Fritz. Effectiveness of a 308-nm excimer laser in treatment of vitiligo: a review. *Lasers in Medical Science*, 28(3):1035–1041, May 2013. ISSN 1435-604X. doi: 10.1007/s10103-012-1185-1.
- T. S. Anbar, T. S. El-Ammawi, A. T. Abdel-Rahman, and M. R. Hanna. The effect of latanoprost on vitiligo: a preliminary comparative study. *International Journal of Dermatology*, 54(5): 587–593, 2015. ISSN 1365-4632. doi: 10.1111/ijd.12631.
- S. Anders, P. T. Pyl, and W. Huber. HTSeq—a Python framework to work with high-throughput sequencing data. *Bioinformatics*, 31(2):166–169, Jan. 2015. ISSN 1367-4803. doi: 10.1093/bioinformatics/btu638. URL <https://doi.org/10.1093/bioinformatics/btu638>.
- M. H. Andersen, D. Schrama, P. Thor Straten, and J. C. Becker. Cytotoxic T cells. *The Journal of Investigative Dermatology*, 126(1):32–41, Jan. 2006. ISSN 0022-202X. doi: 10.1038/sj.jid.5700001.
- H. Aoki and O. Moro. Involvement of microphthalmia-associated transcription factor (MITF) in expression of human melanocortin-1 receptor (MC1R). *Life sciences*, 71(18):2171–9, Sept. 2002. doi: 10.1016/s0024-3205(02)01996-3. URL <http://www.ncbi.nlm.nih.gov/pubmed/12204775>.
- M. S. Atkins, M. M. McKay, S. L. Frazier, L. J. Jakobsons, P. Arvanitis, T. Cunningham, C. Brown, and L. Lambrecht. Suspensions and detentions in an urban, low-income school: punishment or reward? *Journal of Abnormal Child Psychology*, 30(4):361–371, Aug. 2002. ISSN 0091-0627. doi: 10.1023/a:1015765924135.
- J. M. Bae, H. M. Jung, B. Y. Hong, J. H. Lee, W. J. Choi, J. H. Lee, and G. M. Kim. Phototherapy for Vitiligo: A Systematic Review and Meta-analysis. *JAMA Dermatology*, 153(7):666–674, July 2017. ISSN 2168-6068. doi: 10.1001/jamadermatol.2017.0002. URL <https://doi.org/10.1001/jamadermatol.2017.0002>.
- L. Bansal, T. Wilde, A. Gupta, G. Kang, S. Frey, B. Hussey, and V. Damian-Iordache. A Quantitative Systems Pharmacology (QSP) Approach to Understand the Pathogenesis of Acne and to Evaluate New Acne Therapies. In *JOURNAL OF PHARMACOKINETICS AND PHARMACODYNAMICS*, volume 41, pages S22–S23. SPRINGER/PLENUM PUBLISHERS 233 SPRING ST, NEW YORK, NY 10013 USA, 2014.
- L. Bansal, T. Wilde, G. Kang, R. Baillie, C. Friedrich, and V. Damian. Development of a Quantitative Systems Pharmacology (QSP) Model of Psoriasis: Overview and Challenges. *Journal of Pharmacokinetics and Pharmacodynamics*, 42:S103–S104, Oct. 2015.
- C. R. Beals, C. M. Sheridan, C. W. Turck, P. Gardner, and G. R. Crabtree. Nuclear export of NF-ATc enhanced by glycogen synthase kinase-3. *Science (New York, N.Y.)*, 275(5308): 1930–1934, Mar. 1997. ISSN 0036-8075. doi: 10.1126/science.275.5308.1930.
- C. Bergqvist and K. Ezzedine. Vitiligo: A Review. *Dermatology*, 236(6):571–592, 2020. ISSN 1018-8665, 1421-9832. doi: 10.1159/000506103. URL <https://www.karger.com/Article/FullText/506103>. Publisher: Karger Publishers.

BIBLIOGRAPHY

- P. R. Bergstresser and J. Richard Taylor. Epidermal 'turnover time'—a new examination. *British Journal of Dermatology*, 96(5):503–506, May 1977. ISSN 0007-0963, 1365-2133. doi: 10.1111/j.1365-2133.1977.tb07152.x. URL <https://academic.oup.com/bjd/article/96/5/503/6669757>.
- P. R. Bergstresser, R. J. Pariser, and J. R. Taylor. Counting and Sizing of Epidermal Cells in Normal Human Skin. *Journal of Investigative Dermatology*, 70(5):280–284, May 1978. ISSN 0022-202X. doi: 10.1111/1523-1747.ep12541516. URL <https://www.sciencedirect.com/science/article/pii/S0022202X15452534>.
- L. Berod, C. Friedrich, A. Nandan, J. Freitag, S. Hagemann, K. Harmrolfs, A. Sandouk, C. Hesse, C. N. Castro, H. Bähre, S. K. Tschirner, N. Gorinski, M. Gohmert, C. T. Mayer, J. Huehn, E. Ponimaskin, W.-R. Abraham, R. Müller, M. Lochner, and T. Sparwasser. De novo fatty acid synthesis controls the fate between regulatory T and T helper 17 cells. *Nature Medicine*, 20(11):1327–1333, Nov. 2014. ISSN 1546-170X. doi: 10.1038/nm.3704.
- A. S. Berthon, E. Szarek, and C. A. Stratakis. PRKACA: the catalytic subunit of protein kinase A and adrenocortical tumors. *Frontiers in Cell and Developmental Biology*, 3, May 2015. ISSN 2296-634X. doi: 10.3389/fcell.2015.00026. URL <https://www.ncbi.nlm.nih.gov/pmc/articles/PMC4438593/>.
- S. Bessou, J. E. Surlève-Bazeille, E. Sorbier, and A. Taïeb. Ex vivo reconstruction of the epidermis with melanocytes and the influence of UVB. *Pigment Cell Research*, 8(5):241–249, Oct. 1995. ISSN 0893-5785. doi: 10.1111/j.1600-0749.1995.tb00670.x.
- U. Bhor and S. Pande. Scoring systems in dermatology. *Indian Journal of Dermatology, Venereology, and Leprology*, 72(4):315, July 2006. ISSN 0378-6323. doi: 10.4103/0378-6323.26722. URL <http://www.ijdvl.com/article.asp?issn=0378-6323;year=2006;volume=72;issue=4;spage=315;epage=321;aulast=Bhor;type=0>. Publisher: Medknow Publications.
- C. A. Bivik, P. K. Larsson, K. M. Kågedal, I. K. Rosdahl, and K. M. Ollinger. UVA/B-induced apoptosis in human melanocytes involves translocation of cathepsins and Bcl-2 family members. *The Journal of Investigative Dermatology*, 126(5):1119–1127, May 2006. ISSN 0022-202X. doi: 10.1038/sj.jid.5700124.
- E. L. Bradshaw, M. E. Spilker, R. Zang, L. Bansal, H. He, R. D. Jones, K. Le, M. Penney, E. Schuck, B. Topp, A. Tsai, C. Xu, M. J. Nijsen, and J. R. Chan. Applications of Quantitative Systems Pharmacology in Model-Informed Drug Discovery: Perspective on Impact and Opportunities. *CPT: Pharmacometrics & Systems Pharmacology*, 8(11):777–791, Nov. 2019. ISSN 2163-8306. doi: 10.1002/psp4.12463. URL <https://www.ncbi.nlm.nih.gov/pmc/articles/PMC6875708/>.
- A. S. BREATHNACH and L. M. WYLLIE. ELECTRON MICROSCOPY OF MELANOCYTES AND LANGERHANS CELLS IN HUMAN FETAL EPIDERMIS AT FOURTEEN WEEKS. *The Journal of investigative dermatology*, 44:51–60, Jan. 1965. ISSN 1523-1747. doi: 10.1038/jid.1965.11. URL <https://doi.org/10.1038/jid.1965.11>.
- A. S. Breathnach, S. Bor, and L. M.-A. Wyllie. Electron Microscopy of Peripheral Nerve Terminals and Marginal Melanocytes in Vitiligo**From the Departments of Anatomy and Dermatology, St. Mary's Hospital Medical School, (University of London), London, W.2., England. *Journal of Investigative Dermatology*, 47(2):125–140, Aug. 1966. ISSN

- 0022202X. doi: 10.1038/jid.1966.117. URL <https://linkinghub.elsevier.com/retrieve/pii/S0022202X15471593>.
- M. Brenner and V. J. Hearing. Modifying skin pigmentation - approaches through intrinsic biochemistry and exogenous agents. *Drug Discovery Today. Disease Mechanisms*, 5(2):e189–e199, 2008. ISSN 1740-6765. doi: 10.1016/j.ddmec.2008.02.001.
- R. Buscà, P. Abbe, F. Mantoux, E. Aberdam, C. Peyssonnaud, A. Eychène, J. P. Ortonne, and R. Ballotti. Ras mediates the cAMP-dependent activation of extracellular signal-regulated kinases (ERKs) in melanocytes. *The EMBO journal*, 19(12):2900–10, June 2000. doi: 10.1093/emboj/19.12.2900. URL <http://www.ncbi.nlm.nih.gov/pubmed/10856235>.
- K. T. Byrne and M. J. Turk. New perspectives on the role of vitiligo in immune responses to melanoma. *Oncotarget*, 2(9):684–694, Sept. 2011. ISSN 1949-2553. doi: 10.18632/oncotarget.323.
- I. Cascorbi. Drug interactions—principles, examples and clinical consequences. *Deutsches Arzteblatt International*, 109(33-34):546–555; quiz 556, Aug. 2012. ISSN 1866-0452. doi: 10.3238/arztebl.2012.0546.
- A. Chakraborty, A. Slominski, G. Ermak, J. Hwang, and J. Pawelek. Ultraviolet B and melanocyte-stimulating hormone (MSH) stimulate mRNA production for alpha MSH receptors and proopiomelanocortin-derived peptides in mouse melanoma cells and transformed keratinocytes. *The Journal of Investigative Dermatology*, 105(5):655–659, Nov. 1995. ISSN 0022-202X. doi: 10.1111/1523-1747.ep12324134.
- M. L. Chanco-Turner and A. B. Lerner. PHYSIOLOGIC CHANGES IN VITILIGO. *Archives of Dermatology*, 91:390–396, Apr. 1965. ISSN 0003-987X.
- W.-L. Chang and C.-H. Ko. The Role of Oxidative Stress in Vitiligo: An Update on Its Pathogenesis and Therapeutic Implications. *Cells*, 12(6):936, Mar. 2023. ISSN 2073-4409. doi: 10.3390/cells12060936. URL <https://www.ncbi.nlm.nih.gov/pmc/articles/PMC10047323/>.
- C. Charman and H. Williams. Outcome measures of disease severity in atopic eczema. *Archives of Dermatology*, 136(6):763–769, June 2000. ISSN 0003-987X. doi: 10.1001/archderm.136.6.763.
- M. Chaves, R. Albert, and E. D. Sontag. Robustness and fragility of Boolean models for genetic regulatory networks. *Journal of Theoretical Biology*, 235(3):431–449, 2005. ISSN 0022-5193 (Print)\n0022-5193 (Linking). doi: 10.1016/j.jtbi.2005.01.023.
- Y.-F. Chen, P.-Y. Yang, D.-N. Hu, F.-S. Kuo, C.-S. Hung, and C.-M. Hung. Treatment of vitiligo by transplantation of cultured pure melanocyte suspension: analysis of 120 cases. *Journal of the American Academy of Dermatology*, 51(1):68–74, July 2004. ISSN 1097-6787. doi: 10.1016/j.jaad.2003.12.013.
- S.-M. Choo and K.-H. Cho. An efficient algorithm for identifying primary phenotype attractors of a large-scale Boolean network. *BMC systems biology*, 10(1):95, Oct. 2016. ISSN 1752-0509. doi: 10.1186/s12918-016-0338-4.
- T.-H. Chou, H.-Y. Ding, R.-J. Lin, J.-Y. Liang, and C.-H. Liang. Inhibition of Melanogenesis and Oxidation by Protocatechuic Acid from *Origanum vulgare* (Oregano). *Journal of Natural Products*, 73(11):1767–1774, Nov. 2010. ISSN 0163-3864. doi: 10.1021/np100281g. URL <https://doi.org/10.1021/np100281g>. Publisher: American Chemical Society.

BIBLIOGRAPHY

- C.-Y. Chu, Y.-L. Liu, H.-C. Chiu, and S.-H. Jee. Dopamine-induced apoptosis in human melanocytes involves generation of reactive oxygen species. *British Journal of Dermatology*, 154(6):1071–1079, 2006. ISSN 1365-2133. doi: 10.1111/j.1365-2133.2006.07293.x. URL <https://onlinelibrary.wiley.com/doi/abs/10.1111/j.1365-2133.2006.07293.x>. _eprint: <https://onlinelibrary.wiley.com/doi/pdf/10.1111/j.1365-2133.2006.07293.x>.
- S.-Y. Chung, Y.-K. Seo, J.-M. Park, M.-J. Seo, J.-K. Park, J.-W. Kim, and C.-S. Park. Fermented rice bran downregulates MITF expression and leads to inhibition of alpha-MSH-induced melanogenesis in B16F1 melanoma. *Bioscience, Biotechnology, and Biochemistry*, 73(8):1704–1710, Aug. 2009. ISSN 1347-6947. doi: 10.1271/bbb.80766.
- M. J. Clemens, W. J. van Venrooij, and L. B. A. van de Putte. Apoptosis and Autoimmunity. *Cell Death & Differentiation*, 7(1):131–133, Jan. 2000. ISSN 1476-5403. doi: 10.1038/sj.cdd.4400633. URL <https://www.nature.com/articles/4400633>. Number: 1 Publisher: Nature Publishing Group.
- S. G. Coelho, S. A. Miller, B. Z. Zmudzka, and J. Z. Beer. Quantification of UV-induced erythema and pigmentation using computer-assisted digital image evaluation. *Photochemistry and Photobiology*, 82(3):651–655, 2006. ISSN 0031-8655. doi: 10.1562/2005-08-02-TSN-635.
- S. Corre, A. Primot, E. Sviderskaya, D. C. Bennett, S. Vaultont, C. R. Goding, and M.-D. Galibert. UV-induced expression of key component of the tanning process, the POMC and MC1R genes, is dependent on the p-38-activated upstream stimulating factor-1 (USF-1). *The Journal of biological chemistry*, 279(49):51226–33, Dec. 2004. doi: 10.1074/jbc.M409768200. URL <http://www.ncbi.nlm.nih.gov/pubmed/15358786>.
- G.-E. Costin and V. J. Hearing. Human skin pigmentation: melanocytes modulate skin color in response to stress. *FASEB journal: official publication of the Federation of American Societies for Experimental Biology*, 21(4):976–994, Apr. 2007. ISSN 1530-6860. doi: 10.1096/fj.06-6649rev.
- T. Cui, W. Zhang, S. Li, X. Chen, Y. Chang, X. Yi, P. Kang, Y. Yang, J. Chen, L. Liu, Z. Jian, K. Li, G. Wang, T. Gao, P. Song, and C. Li. Oxidative Stress-Induced HMGB1 Release from Melanocytes: A Paracrine Mechanism Underlying the Cutaneous Inflammation in Vitiligo. *Journal of Investigative Dermatology*, 139(10):2174–2184.e4, Oct. 2019. ISSN 0022-202X. doi: 10.1016/j.jid.2019.03.1148. URL <https://www.sciencedirect.com/science/article/pii/S0022202X19314794>.
- T. Daniele, I. Hurbain, R. Vago, G. Casari, G. Raposo, C. Tacchetti, and M. V. Schiaffino. Mitochondria and melanosomes establish physical contacts modulated by Mfn2 and involved in organelle biogenesis. *Current biology: CB*, 24(4):393–403, Feb. 2014. ISSN 1879-0445. doi: 10.1016/j.cub.2014.01.007.
- M. M. R. de Maat, G. C. Ekhart, A. D. R. Huitema, C. H. W. Koks, J. W. Mulder, and J. H. Beijnen. Drug interactions between antiretroviral drugs and comedicated agents. *Clinical Pharmacokinetics*, 42(3):223–282, 2003. ISSN 0312-5963. doi: 10.2165/00003088-200342030-00002.
- S. Dechanont, S. Maphanta, B. Butthum, and C. Kongkaew. Hospital admissions/visits associated with drug-drug interactions: a systematic review and meta-analysis. *Pharmacoepidemiology and Drug Safety*, 23(5):489–497, May 2014. ISSN 1099-1557. doi: 10.1002/pds.3592.

- S. A. N. D’Mello, G. J. Finlay, B. C. Baguley, and M. E. Askarian-Amiri. Signaling Pathways in Melanogenesis. *International Journal of Molecular Sciences*, 17(7), July 2016. ISSN 1422-0067. doi: 10.3390/ijms17071144.
- J. A. D’Orazio, T. Nobuhisa, R. Cui, M. Arya, M. Spry, K. Wakamatsu, V. Igras, T. Kunisada, S. R. Granter, E. K. Nishimura, S. Ito, and D. E. Fisher. Topical drug rescue strategy and skin protection based on the role of Mc1r in UV-induced tanning. *Nature*, 443(7109):340–344, Sept. 2006. ISSN 1476-4687. doi: 10.1038/nature05098.
- G. K. Dresser, J. D. Spence, and D. G. Bailey. Pharmacokinetic-Pharmacodynamic Consequences and Clinical Relevance of Cytochrome P450 3A4 Inhibition. *Clinical Pharmacokinetics*, 38(1):41–57, Jan. 2000. ISSN 1179-1926. doi: 10.2165/00003088-200038010-00003. URL <https://doi.org/10.2165/00003088-200038010-00003>.
- A. Duran, M. T. Diaz-Meco, and J. Moscat. Essential role of RelA Ser311 phosphorylation by PKC in NF- κ B transcriptional activation. *The EMBO Journal*, 22(15):3910–3910, Aug. 2003. doi: 10.1093/EMBOJ/CDG370. URL <http://www.ncbi.nlm.nih.gov/pubmed/12881425>.
- M. Dwivedi, N. C. Laddha, P. Arora, Y. S. Marfatia, and R. Begum. Decreased regulatory T-cells and CD4+/CD8+ ratio correlate with disease onset and progression in patients with generalized vitiligo. *Pigment Cell & Melanoma Research*, 26(4):586–591, 2013. ISSN 1755-148X. doi: 10.1111/pcmr.12105. URL <https://onlinelibrary.wiley.com/doi/abs/10.1111/pcmr.12105>. _eprint: <https://onlinelibrary.wiley.com/doi/pdf/10.1111/pcmr.12105>.
- J. P. Ebanks, R. R. Wickett, and R. E. Boissy. Mechanisms regulating skin pigmentation: the rise and fall of complexion coloration. *International Journal of Molecular Sciences*, 10(9):4066–4087, Sept. 2009. ISSN 1422-0067. doi: 10.3390/ijms10094066.
- U. E. Emir and I. A. Kurnaz. An integrated model for melanocyte-specific gene expression and melanogenesis. *Signal Transduction*, 3(5-6):209–217, 2003. ISSN 1615-4061. doi: 10.1002/sita.200300026. URL <https://onlinelibrary.wiley.com/doi/abs/10.1002/sita.200300026>.
- A. Ermentrout, B and R. Mahajan, A. Simulating, Analyzing, and Animating Dynamical Systems: A Guide to XPPAUT for Researchers and Students. *Applied Mechanics Reviews*, 56(4):B53, July 2003. ISSN 0003-6900. doi: 10.1115/1.1579454. URL <https://doi.org/10.1115/1.1579454>.
- K. Ezzedine, V. Eleftheriadou, M. Whitton, and N. van Geel. Vitiligo. *Lancet (London, England)*, 386(9988):74–84, July 2015. ISSN 1474-547X. doi: 10.1016/S0140-6736(14)60763-7.
- D. Fang and V. Setaluri. Role of microphthalmia transcription factor in regulation of melanocyte differentiation marker TRP-1. *Biochemical and Biophysical Research Communications*, 256(3):657–663, Mar. 1999. ISSN 0006-291X. doi: 10.1006/bbrc.1999.0400.
- A. Fauré, A. Naldi, C. Chaouiya, and D. Thieffry. Dynamical analysis of a generic Boolean model for the control of the mammalian cell cycle. *Bioinformatics*, 22(14):124–131, 2006. ISSN 1460-2059 (Electronic). doi: 10.1093/bioinformatics/btl210.
- A. Feily. Vitiligo Extent Tensity Index (VETI) score: a new definition, assessment and treatment evaluation criteria in vitiligo. *Dermatology Practical & Conceptual*, 4(4):81–84, Oct. 2014. ISSN 2160-9381. doi: 10.5826/dpc.0404a18.

BIBLIOGRAPHY

- L. M. Felsten, A. Alikhan, and V. Petronic-Rosic. Vitiligo: a comprehensive overview Part II: treatment options and approach to treatment. *Journal of the American Academy of Dermatology*, 65(3):493–514, Sept. 2011. ISSN 1097-6787. doi: 10.1016/j.jaad.2010.10.043.
- J. E. Ferrell, T. Y.-C. Tsai, and Q. Yang. Modeling the Cell Cycle: Why Do Certain Circuits Oscillate? *Cell*, 144(6):874–885, Mar. 2011. ISSN 0092-8674, 1097-4172. doi: 10.1016/j.cell.2011.03.006. URL [https://www.cell.com/cell/abstract/S0092-8674\(11\)00243-1](https://www.cell.com/cell/abstract/S0092-8674(11)00243-1). Publisher: Elsevier.
- T. B. Fitzpatrick. Ultraviolet-induced pigmentary changes: benefits and hazards. *Current Problems in Dermatology*, 15:25–38, 1986. ISSN 1421-5721. doi: 10.1159/000412090.
- T. B. Fitzpatrick. The validity and practicality of sun-reactive skin types I through VI. *Archives of Dermatology*, 124(6):869–871, June 1988. ISSN 0003-987X. doi: 10.1001/archderm.124.6.869.
- T. B. Fitzpatrick and A. S. Breathnach. [THE EPIDERMAL MELANIN UNIT SYSTEM]. *Dermatologische Wochenschrift*, 147:481–489, May 1963. ISSN 0366-8940.
- T. Fredriksson and U. Pettersson. Severe psoriasis—oral therapy with a new retinoid. *Dermatologica*, 157(4):238–244, 1978. ISSN 0011-9075. doi: 10.1159/000250839.
- N. Fullard, A. Moles, S. O’Reilly, J. M. van Laar, D. Faini, J. Diboll, N. J. Reynolds, D. A. Mann, J. Reichelt, and F. Oakley. The c-Rel Subunit of NF- κ B Regulates Epidermal Homeostasis and Promotes Skin Fibrosis in Mice. *The American Journal of Pathology*, 182(6):2109–2120, June 2013. ISSN 0002-9440. doi: 10.1016/j.ajpath.2013.02.016. URL <http://www.sciencedirect.com/science/article/pii/S0002944013001946>.
- H. F. Fumiã and M. L. Martins. Boolean Network Model for Cancer Pathways: Predicting Carcinogenesis and Targeted Therapy Outcomes. *PLoS ONE*, 8(7):e69008, July 2013. ISSN 1932-6203. doi: 10.1371/journal.pone.0069008. URL <https://www.ncbi.nlm.nih.gov/pmc/articles/PMC3724878/>.
- A. Gallet, C. Angelats, S. Kerridge, and P. P. Thérond. Cubitus interruptus-independent transduction of the Hedgehog signal in Drosophila. *Development (Cambridge, England)*, 127(24):5509–5522, Dec. 2000. ISSN 0950-1991. doi: 10.1242/dev.127.24.5509.
- G. Garcin, L. Le Gallic, P.-E. Stoebner, A. Guezennec, J. Guesnet, T. Lavabre-Bertrand, J. Martinez, and L. Meunier. Constitutive Expression of MC1R in HaCaT Keratinocytes Inhibits Basal and UVB-induced TNF- Production. *Photochemistry and Photobiology*, 85(6):1440–1450, Nov. 2009. doi: 10.1111/j.1751-1097.2009.00598.x. URL <http://doi.wiley.com/10.1111/j.1751-1097.2009.00598.x>.
- A. Garg, K. Mohanram, A. Di Cara, G. De Micheli, and I. Xenarios. Modeling stochasticity and robustness in gene regulatory networks. *Bioinformatics*, 25(12):101–109, 2009. ISSN 1367-4811 (Electronic)\n1367-4803 (Linking). doi: 10.1093/bioinformatics/btp214.
- S. Ghosh and S. Mukhopadhyay. Chemical leucoderma: a clinico-aetiological study of 864 cases in the perspective of a developing country. *British Journal of Dermatology*, 160(1):40–47, Jan. 2009. ISSN 0007-0963. doi: 10.1111/j.1365-2133.2008.08815.x. URL <https://doi.org/10.1111/j.1365-2133.2008.08815.x>.
- P. U. Giacomoni and G. Rein. A mechanistic model for the aging of human skin. *Micron (Oxford, England: 1993)*, 35(3):179–184, 2004. ISSN 0968-4328. doi: 10.1016/j.micron.2003.11.004.

- F. Gillardon, C. Eschenfelder, E. Uhlmann, W. Hartschuh, and M. Zimmermann. Differential regulation of c-fos, fosB, c-jun, junB, bcl-2 and bax expression in rat skin following single or chronic ultraviolet irradiation and in vivo modulation by antisense oligodeoxynucleotide superfusion. *Oncogene*, 9(11):3219–3225, Nov. 1994. ISSN 0950-9232.
- L. Glass and S. A. Kauffman. The logical analysis of continuous, non-linear biochemical control networks. *Journal of Theoretical Biology*, 39(1):103–129, Apr. 1973. ISSN 0022-5193. doi: 10.1016/0022-5193(73)90208-7. URL <https://www.sciencedirect.com/science/article/pii/0022519373902087>.
- A. Goldbeter. Dissipative structures in biological systems: bistability, oscillations, spatial patterns and waves. *Philosophical Transactions of the Royal Society A: Mathematical, Physical and Engineering Sciences*, 376(2124):20170376, July 2018. doi: 10.1098/rsta.2017.0376. URL <https://royalsocietypublishing.org/doi/10.1098/rsta.2017.0376>. Publisher: Royal Society.
- A. Goldbeter, D. Gonze, and O. Pourquié. Sharp developmental thresholds defined through bistability by antagonistic gradients of retinoic acid and FGF signaling. *Developmental Dynamics*, 236(6):1495–1508, 2007. ISSN 1097-0177. doi: 10.1002/dvdy.21193. URL <https://anatomypubs.onlinelibrary.wiley.com/doi/abs/10.1002/dvdy.21193>. _eprint: <https://anatomypubs.onlinelibrary.wiley.com/doi/pdf/10.1002/dvdy.21193>.
- H. Goldschmidt and J. Z. Raymond. Quantitative analysis of skin color from melanin content of superficial skin cells. *Journal of Forensic Sciences*, 17(1):124–131, Jan. 1972. ISSN 0022-1198.
- F. Goon Goh, C. M. Sloss, M. R. Cunningham, M. Nilsson, L. Cadalbert, and R. Plevin. G-protein-dependent and -independent pathways regulate proteinase-activated receptor-2 mediated p65 NFkappaB serine 536 phosphorylation in human keratinocytes. *Cellular Signalling*, 20(7):1267–1274, July 2008. ISSN 0898-6568. doi: 10.1016/j.cellsig.2008.02.015.
- N. Grabe and K. Neuber. A multicellular systems biology model predicts epidermal morphology, kinetics and Ca²⁺ flow. *Bioinformatics (Oxford, England)*, 21(17):3541–3547, Sept. 2005. ISSN 1367-4803. doi: 10.1093/bioinformatics/bti585.
- I. Grattagliano, P. Portincasa, G. D’Ambrosio, V. O. Palmieri, and G. Palasciano. Avoiding drug interactions: here’s help. *The Journal of Family Practice*, 59(6):322–329, June 2010. ISSN 1533-7294.
- P. Grimes and M. Miller. Vitiligo: Patient stories, self-esteem, and the psychological burden of disease. *International Journal of Women’s Dermatology*, 4(1):32–37, Jan. 2018. ISSN 2352-6475. doi: 10.1016/j.ijwd.2017.11.005. URL <https://www.ncbi.nlm.nih.gov/pmc/articles/PMC5986114/>.
- H. Guan, J. Jiao, and R. P. Ricciardi. Tumorigenic adenovirus type 12 E1A inhibits phosphorylation of NF-kappaB by PKAc, causing loss of DNA binding and transactivation. *Journal of virology*, 82(1):40–8, Jan. 2008. doi: 10.1128/JVI.01579-07. URL <http://www.ncbi.nlm.nih.gov/pubmed/17959673>.
- C. Gérard and A. Goldbeter. Temporal self-organization of the cyclin/Cdk network driving the mammalian cell cycle. *Proceedings of the National Academy of Sciences*, 106(51):21643–21648, Dec. 2009.

BIBLIOGRAPHY

- J. Ha, L. S. Satin, and A. S. Sherman. A Mathematical Model of the Pathogenesis, Prevention, and Reversal of Type 2 Diabetes. *Endocrinology*, 157(2):624–635, Feb. 2016. ISSN 0013-7227. doi: 10.1210/en.2015-1564. URL <https://doi.org/10.1210/en.2015-1564>.
- K. M. Halprin. Epidermal “Turnover Time”—a Re-Examination. *British Journal of Dermatology*, 86(1):14–19, 1972. ISSN 1365-2133. doi: 10.1111/j.1365-2133.1972.tb01886.x. URL <https://onlinelibrary.wiley.com/doi/abs/10.1111/j.1365-2133.1972.tb01886.x>. [_eprint: https://onlinelibrary.wiley.com/doi/pdf/10.1111/j.1365-2133.1972.tb01886.x](https://onlinelibrary.wiley.com/doi/pdf/10.1111/j.1365-2133.1972.tb01886.x).
- I. Hamzavi, H. Jain, D. McLean, J. Shapiro, H. Zeng, and H. Lui. Parametric modeling of narrowband UV-B phototherapy for vitiligo using a novel quantitative tool: the Vitiligo Area Scoring Index. *Archives of Dermatology*, 140(6):677–683, June 2004. ISSN 0003-987X. doi: 10.1001/archderm.140.6.677.
- J. Harris, T. Harris, W. Weninger, E. J. Wherry, C. Hunter, and L. Turka. A Mouse Model of Vitiligo with Focused Epidermal Depigmentation Requires IFN- for Autoreactive CD8+ T-Cell Accumulation in the Skin. *The Journal of investigative dermatology*, 132:1869–76, Feb. 2012. doi: 10.1038/jid.2011.463.
- J. E. Harris. Chemical-induced Vitiligo. *Dermatologic clinics*, 35(2):151–161, Apr. 2017. ISSN 0733-8635. doi: 10.1016/j.det.2016.11.006. URL <https://www.ncbi.nlm.nih.gov/pmc/articles/PMC5362111/>.
- M. Hassan, U. S. H. Svensson, P. Ljungman, B. Björkstrand, H. Olsson, M. Bielenstein, M. Abdel-Rehim, C. Nilsson, M. Johansson, and M. O. Karlsson. A mechanism-based pharmacokinetic-enzyme model for cyclophosphamide autoinduction in breast cancer patients. *British Journal of Clinical Pharmacology*, 48(5):669–677, Nov. 1999. ISSN 0306-5251. doi: 10.1046/j.1365-2125.1999.00090.x. URL <https://www.ncbi.nlm.nih.gov/pmc/articles/PMC2014348/>.
- V. Heissmeyer, D. Krappmann, F. G. Wulczyn, and C. Scheidereit. NF-kappaB p105 is a target of IkappaB kinases and controls signal induction of Bcl-3-p50 complexes. *The EMBO journal*, 18(17):4766–78, Sept. 1999. doi: 10.1093/emboj/18.17.4766. URL <http://www.ncbi.nlm.nih.gov/pubmed/10469655>.
- T. J. Hemesath, E. R. Price, C. Takemoto, T. Badalian, and D. E. Fisher. MAP kinase links the transcription factor Microphthalmia to c-Kit signalling in melanocytes. *Nature*, 391(6664):298–301, Jan. 1998. ISSN 1476-4687. doi: 10.1038/34681. URL <https://www.nature.com/articles/34681>. Number: 6664 Publisher: Nature Publishing Group.
- L. E. Hines and J. E. Murphy. Potentially harmful drug-drug interactions in the elderly: a review. *The American Journal of Geriatric Pharmacotherapy*, 9(6):364–377, Dec. 2011. ISSN 1876-7761. doi: 10.1016/j.amjopharm.2011.10.004.
- H. Hirovani, N. A. Tuohy, J.-T. Woo, P. H. Stern, and N. A. Clipstone. The calcineurin/nuclear factor of activated T cells signaling pathway regulates osteoclastogenesis in RAW264.7 cells. *The Journal of biological chemistry*, 279(14):13984–92, Apr. 2004. doi: 10.1074/jbc.M213067200. URL <http://www.ncbi.nlm.nih.gov/pubmed/14722106>.
- H.-C. HUANG, S.-H. CHIU, and T.-M. CHANG. Inhibitory Effect of [6]-Gingerol on Melanogenesis in B16F10 Melanoma Cells and a Possible Mechanism of Action. *Bioscience, Biotechnology, and Biochemistry*, 75(6):1067–1072, June 2011. ISSN 0916-8451. doi: 10.1271/bbb.

100851. URL <https://doi.org/10.1271/bbb.100851>. Publisher: Taylor & Francis _eprint: <https://doi.org/10.1271/bbb.100851>.
- Y. Hushcha, I. Blo, L. Oton-Gonzalez, G. D. Mauro, F. Martini, M. Tognon, and M. D. Mattei. microRNAs in the Regulation of Melanogenesis. *International Journal of Molecular Sciences*, 22(11):6104, June 2021. ISSN 1422-0067. doi: 10.3390/ijms22116104. URL <https://www.ncbi.nlm.nih.gov/pmc/articles/PMC8201055/>.
- H. Iizuka. Epidermal turnover time. *Journal of Dermatological Science*, 8(3):215–217, Dec. 1994. ISSN 0923-1811. doi: 10.1016/0923-1811(94)90057-4.
- G. Imokawa and K. Ishida. Inhibitors of intracellular signaling pathways that lead to stimulated epidermal pigmentation: perspective of anti-pigmenting agents. *International Journal of Molecular Sciences*, 15(5):8293–8315, May 2014. ISSN 1422-0067. doi: 10.3390/ijms15058293.
- A. K. Jha, S. C.-C. Huang, A. Sergushichev, V. Lampropoulou, Y. Ivanova, E. Loginicheva, K. Chmielewski, K. M. Stewart, J. Ashall, B. Everts, E. J. Pearce, E. M. Driggers, and M. N. Artyomov. Network Integration of Parallel Metabolic and Transcriptional Data Reveals Metabolic Modules that Regulate Macrophage Polarization. *Immunity*, 42(3):419–430, Mar. 2015. ISSN 1074-7613. doi: 10.1016/j.immuni.2015.02.005. URL <https://www.sciencedirect.com/science/article/pii/S1074761315000801>.
- R. R. Joge, P. U. Kathane, and S. H. Joshi. Vitiligo: A Narrative Review. *Cureus*, 14(9):e29307, Sept. 2022. ISSN 2168-8184. doi: 10.7759/cureus.29307.
- M. Jost, T. M. Huggett, C. Kari, L. H. Boise, and U. Rodeck. Epidermal Growth Factor Receptor-dependent Control of Keratinocyte Survival and Bcl-xL Expression through a MEK-dependent Pathway. *Journal of Biological Chemistry*, 276(9):6320–6326, 2001. doi: 10.1074/jbc.M008210200.
- D.-W. Jung, D. Williams, S. M. Khersonsky, T.-W. Kang, N. Heidary, Y.-T. Chang, and S. J. Orlow. Identification of the F1F0 mitochondrial ATPase as a target for modulating skin pigmentation by screening a tagged triazine library in zebrafish. *Molecular bioSystems*, 1(1):85–92, May 2005. ISSN 1742-206X. doi: 10.1039/b417765g.
- R. Kapoor, M. M. Piske, and H. R. Jerajani. Evaluation of safety and efficacy of topical prostaglandin E2 in treatment of vitiligo. *The British Journal of Dermatology*, 160(4):861–863, Apr. 2009. ISSN 1365-2133. doi: 10.1111/j.1365-2133.2008.08923.x.
- G. Karlebach and R. Shamir. Modelling and analysis of gene regulatory networks. *Nat Rev Mol Cell Biol*, 9(10):770–780, 2008. ISSN 1471-0080 (Electronic)\r1471-0072 (Linking). doi: 10.1038/nrm2503. URL <http://www.ncbi.nlm.nih.gov/pubmed/18797474>.
- S. A. Kauffman, C. Peterson, B. Samuelsson, and C. Troein. Genetic networks with canalizing Boolean rules are always stable. *Proceedings of the National Academy of Sciences of the United States of America*, 101(49):17102–7, 2004. ISSN 0027-8424 (Print). doi: 10.1073/pnas.0407783101. URL <http://www.ncbi.nlm.nih.gov/pubmed/15572453>.
- A. Kaur and R. C. Sarin. Study of neurotropic influences in vitiligo. *Indian Journal of Dermatology*, 33(3):33, July 1988. ISSN 0019-5154. URL <https://www.e-ijd.org/article.asp?issn=0019-5154;year=1988;volume=33;issue=3;spage=33;epage=36;aulast=Kaur;type=0>. Publisher: Medknow Publications.

BIBLIOGRAPHY

- E. H. Kemp, E. A. Waterman, and A. P. Weetman. Autoimmune Aspects of Vitiligo. *Autoimmunity*, 34(1):65–77, Jan. 2001. ISSN 0891-6934. doi: 10.3109/08916930108994127. URL <https://doi.org/10.3109/08916930108994127>. Publisher: Taylor & Francis _eprint: <https://doi.org/10.3109/08916930108994127>.
- N. Khunger, S. D. Kathuria, and V. Ramesh. TISSUE GRAFTS IN VITILIGO SURGERY – PAST, PRESENT, AND FUTURE. *Indian Journal of Dermatology*, 54(2):150–158, 2009. ISSN 0019-5154. doi: 10.4103/0019-5154.53196. URL <https://www.ncbi.nlm.nih.gov/pmc/articles/PMC2807155/>.
- A. Kim, Y. Yang, M.-S. Lee, Y. D. Yoo, H. G. Lee, and J.-S. Lim. NDRG2 gene expression in B16F10 melanoma cells restrains melanogenesis via inhibition of Mitf expression. *Pigment Cell & Melanoma Research*, 21(6):653–664, 2008. ISSN 1755-148X. doi: 10.1111/j.1755-148X.2008.00503.x. URL <https://onlinelibrary.wiley.com/doi/abs/10.1111/j.1755-148X.2008.00503.x>.
- D. Kim, B. Langmead, and S. L. Salzberg. HISAT: a fast spliced aligner with low memory requirements. *Nature methods*, 12(4):357–360, Apr. 2015. ISSN 1548-7091. doi: 10.1038/nmeth.3317. URL <https://www.ncbi.nlm.nih.gov/pmc/articles/PMC4655817/>.
- D.-S. Kim, Y.-M. Jeong, I.-K. Park, H.-G. Hahn, H.-K. Lee, S.-B. Kwon, J. H. Jeong, S. J. Yang, U. D. Sohn, and K.-C. Park. A new 2-imino-1,3-thiazoline derivative, KHG22394, inhibits melanin synthesis in mouse B16 melanoma cells. *Biological & pharmaceutical bulletin*, 30(1):180–3, 2007. ISSN 0918-6158 (Print)\r0918-6158 (Linking). URL <http://www.ncbi.nlm.nih.gov/pubmed/17202683>.
- E. S. Kim, S. J. Park, M.-J. Goh, Y.-J. Na, D. S. Jo, Y. K. Jo, J. H. Shin, E. S. Choi, H.-K. Lee, J.-Y. Kim, H. B. Jeon, J. C. Kim, and D.-H. Cho. Mitochondrial dynamics regulate melanogenesis through proteasomal degradation of MITF via ROS-ERK activation. *Pigment Cell & Melanoma Research*, 27(6):1051–1062, Nov. 2014. ISSN 1755-148X. doi: 10.1111/pcmr.12298.
- A. M. Klein, D. P. Doupé, P. H. Jones, and B. D. Simons. Kinetics of cell division in epidermal maintenance. *Physical Review. E, Statistical, Nonlinear, and Soft Matter Physics*, 76(2 Pt 1):021910, Aug. 2007. ISSN 1539-3755. doi: 10.1103/PhysRevE.76.021910.
- C. K. Koh and Z. Huang. A Simple Physics Model to Animate Human Hair Modeled in 2D Strips in Real Time. In N. Magnenat-Thalmann and D. Thalmann, editors, *Computer Animation and Simulation 2001*, Eurographics, pages 127–138, Vienna, 2001. Springer. ISBN 978-3-7091-6240-8. doi: 10.1007/978-3-7091-6240-8_12.
- V. Kolinko and C. M. Littler. Mathematical modeling for the prediction and optimization of laser hair removal. *Lasers in Surgery and Medicine*, 26(2):164–176, 2000. ISSN 1096-9101. doi: 10.1002/(SICI)1096-9101(2000)26:2<164::AID-LSM7>3.0.CO;2-W. URL <https://onlinelibrary.wiley.com/doi/abs/10.1002/%28SICI%291096-9101%282000%2926%3A2%3C164%3A%3AAID-LSM7%3E3.0.CO%3B2-W>. _eprint: <https://onlinelibrary.wiley.com/doi/pdf/10.1002/%28SICI%291096-9101%282000%2926%3A2%3C164%3A%3AAID-LSM7%3E3.0.CO%3B2-W>.
- W. M. Kuhlreiber, T. Hayashi, E. A. Dale, and D. L. Faustman. Central role of defective apoptosis in autoimmunity. *Journal of Molecular Endocrinology*, 31(3):373–399, Dec. 2003. ISSN 1479-6813, 0952-5041. doi: 10.1677/jme.0.0310373. URL <https://jme.bioscientifica>.

- com/view/journals/jme/31/3/373.xml. Publisher: BioScientifica Section: Journal of Molecular Endocrinology.
- Y. K. Kwon and K. H. Cho. Quantitative analysis of robustness and fragility in biological networks based on feedback dynamics. *Bioinformatics*, 24(7):987–994, 2008. doi: 10.1093/bioinformatics/btn060.
- N. C. Laddha, M. Dwivedi, M. S. Mansuri, A. R. Gani, M. Ansarullah, A. V. Ramachandran, S. Dalai, and R. Begum. Vitiligo: interplay between oxidative stress and immune system. *Experimental Dermatology*, 22(4):245–250, 2013. ISSN 1600-0625. doi: 10.1111/exd.12103. URL <https://onlinelibrary.wiley.com/doi/abs/10.1111/exd.12103>. __eprint: <https://onlinelibrary.wiley.com/doi/pdf/10.1111/exd.12103>.
- K. S. Lang, C. C. Caroli, A. Muhm, D. Wernet, A. Moris, B. Schitteck, E. Knauss-Scherwitz, S. Stevanovic, H. G. Rammensee, and C. Garbe. HLA-A2 restricted, melanocyte-specific CD8(+) T lymphocytes detected in vitiligo patients are related to disease activity and are predominantly directed against MelanA/MART1. *The Journal of Investigative Dermatology*, 116(6):891–897, June 2001. ISSN 0022-202X. doi: 10.1046/j.1523-1747.2001.01363.x.
- H.-S. Lee, M.-J. Goh, J. Kim, T.-J. Choi, H. Kwang Lee, Y. Joo Na, and K.-H. Cho. A systems-biological study on the identification of safe and effective molecular targets for the reduction of ultraviolet B-induced skin pigmentation. *Scientific Reports*, 5, May 2015. ISSN 2045-2322. doi: 10.1038/srep10305. URL <https://www.ncbi.nlm.nih.gov/pmc/articles/PMC4434836/>.
- A. Lehraiki, P. Abbe, M. Cerezo, F. Rouaud, C. Regazzetti, B. Chignon-Sicard, T. Passeron, C. Bertolotto, R. Ballotti, and S. Rocchi. Inhibition of Melanogenesis by the Antidiabetic Metformin. *Journal of Investigative Dermatology*, 134(10):2589–2597, Oct. 2014. ISSN 0022-202X. doi: 10.1038/jid.2014.202. URL <http://www.sciencedirect.com/science/article/pii/S0022202X15365052>.
- L. Li, K. Sampat, N. Hu, J. Zakari, and S. H. Yuspa. Protein kinase C negatively regulates Akt activity and modifies UVC-induced apoptosis in mouse keratinocytes. *The Journal of Biological Chemistry*, 281(6):3237–3243, Feb. 2006a. ISSN 0021-9258. doi: 10.1074/jbc.M512167200.
- S. Li, S. M. Assmann, and R. Albert. Predicting essential components of signal transduction networks: A dynamic model of guard cell abscisic acid signaling. *PLoS Biology*, 4(10):1732–1748, 2006b. ISSN 1545-7885. doi: 10.1371/journal.pbio.0040312.
- S. Li, W. Dai, S. Wang, P. Kang, Z. Ye, P. Han, K. Zeng, and C. Li. Clinical Significance of Serum Oxidative Stress Markers to Assess Disease Activity and Severity in Patients With Non-Segmental Vitiligo. *Frontiers in Cell and Developmental Biology*, 9, 2021. ISSN 2296-634X. URL <https://www.frontiersin.org/articles/10.3389/fcell.2021.739413>.
- H. W. Lim, P. E. Grimes, O. Agbai, I. Hamzavi, M. Henderson, M. Haddican, R. V. Linkner, and M. Lebwohl. Afamelanotide and narrowband UV-B phototherapy for the treatment of vitiligo: a randomized multicenter trial. *JAMA dermatology*, 151(1):42–50, Jan. 2015. ISSN 2168-6084. doi: 10.1001/jamadermatol.2014.1875.
- J. Lock-Andersen, P. Therkildsen, F. F. d. Olivarius, M. Gniadecka, K. Dahlstrom, T. Poulsen, and H.-C. Wulf. Epidermal thickness, skin pigmentation and constitutive photosensitivity. *Photodermatology, Photoimmunology & Photomedicine*, 13(4):153–158, Aug. 1997. ISSN 1600-0781. doi: 10.1111/j.1600-0781.1997.tb00220.x. URL <https://onlinelibrary.wiley.com/doi/10.1111/j.1600-0781.1997.tb00220.x>. Publisher: John Wiley & Sons, Ltd.

BIBLIOGRAPHY

- M. Lohitnavy, J. Methaneethorn, T. Sriarwut, A. Pankaew, A. Jenjob, and K. Phuphuak. A semi-mechanistic pharmacokinetic model of saquinavir combined with itraconazole in HIV-1-positive patients. In *2015 37th Annual International Conference of the IEEE Engineering in Medicine and Biology Society (EMBC)*, pages 3242–3245, Aug. 2015. doi: 10.1109/EMBC.2015.7319083. ISSN: 1558-4615.
- C. Loy and R. Govindarajan. Biology of Skin Pigmentation and Cosmetic Skin Color Control. In *Dermatologic, Cosmeceutic, and Cosmetic Development: Therapeutic and Novel Approaches*, pages 61–95. Dec. 2007. ISBN 978-0-8493-7589-7. doi: 10.3109/9780849375903-6. Journal Abbreviation: Dermatologic, Cosmeceutic, and Cosmetic Development: Therapeutic and Novel Approaches.
- L. J. Lubaki, G. Ghanem, P. Vereecken, E. Fouty, L. Benammar, J. Vadoud-Seyedi, M. L. Dell’Anna, S. Briganti, M. Picardo, and M. Heenen. Time-kinetic study of repigmentation in vitiligo patients by tacrolimus or pimecrolimus. *Archives of Dermatological Research*, 302(2): 131–137, Mar. 2010. ISSN 1432-069X. doi: 10.1007/s00403-009-0973-3.
- F. Luciani, D. Champeval, A. Herbette, L. Denat, B. Aylaj, S. Martinozzi, R. Ballotti, R. Kemler, C. R. Goding, F. De Vuyst, L. Larue, and V. Delmas. Biological and mathematical modeling of melanocyte development. *Development*, 138(18):3943–3954, Sept. 2011. ISSN 0950-1991. doi: 10.1242/dev.067447. URL <https://doi.org/10.1242/dev.067447>.
- M. Madarkar, B. S. Ankad, and R. Manjula. Comparative study of safety and efficacy of oral betamethasone pulse therapy and azathioprine in vitiligo. *Clinical Dermatology Review*, 3(2):121, July 2019. ISSN 2542-551X. doi: 10.4103/CDR.CDR_13_18. URL <https://www.cdriadvlkn.org/article.asp?issn=2542-551X;year=2019;volume=3;issue=2;spage=121;epage=125;aulast=Madarkar;type=0>. Publisher: Medknow Publications.
- S. A. Maggelakis. A mathematical model of tissue replacement during epidermal wound healing. *Applied Mathematical Modelling*, 27(3):189–196, Mar. 2003. ISSN 0307-904X. doi: 10.1016/S0307-904X(02)00100-2. URL <https://www.sciencedirect.com/science/article/pii/S0307904X02001002>.
- L. Magro, U. Moretti, and R. Leone. Epidemiology and characteristics of adverse drug reactions caused by drug-drug interactions. *Expert Opinion on Drug Safety*, 11(1):83–94, Jan. 2012. ISSN 1744-764X. doi: 10.1517/14740338.2012.631910.
- V. K. Mahajan, S. Vashist, P. S. Chauhan, K. I. S. Mehta, V. Sharma, and A. Sharma. Clinico-Epidemiological Profile of Patients with Vitiligo: A Retrospective Study from a Tertiary Care Center of North India. *Indian Dermatology Online Journal*, 10(1):38, Feb. 2019. ISSN 2229-5178. doi: 10.4103/idoj.IDOJ_124_18. URL https://journals.lww.com/idoj/Fulltext/2019/10010/Clinico_Epidemiological_Profile_of_Patients_with.6.aspx.
- I. Majid and S. Imran. Relapse After Methylprednisolone Oral Minipulse Therapy in Childhood Vitiligo: A 12-Month Follow-Up Study. *Indian Journal of Dermatology*, 58(2):113–116, 2013. ISSN 0019-5154. doi: 10.4103/0019-5154.108040. URL <https://www.ncbi.nlm.nih.gov/pmc/articles/PMC3657209/>.
- C. R. Marçon and M. Maia. Albinism: epidemiology, genetics, cutaneous characterization, psychosocial factors. *Anais Brasileiros de Dermatologia*, 94(5):503–520, Sept. 2019. ISSN 0365-0596. doi: 10.1016/j.abd.2019.09.023. URL <https://www.sciencedirect.com/science/article/pii/S0365059619300583>.

- S. R. Mathachan, A. Khurana, R. K. Gautam, A. Kulhari, L. Sharma, and K. Sardana. Does oxidative stress correlate with disease activity and severity in vitiligo? An analytical study. *Journal of Cosmetic Dermatology*, 20(1):352–359, Jan. 2021. ISSN 1473-2165. doi: 10.1111/jocd.13499. URL <https://onlinelibrary.wiley.com/doi/10.1111/jocd.13499>. Publisher: John Wiley & Sons, Ltd.
- S. Mcelwain, B. Cumming, and Z. Upton. A mathematical model of wound healing and subsequent scarring. *Journal of The Royal Society Interface*, 7, Apr. 2009. doi: 10.1098/rsif.2008.0536.
- J. McKesey, A. Tovar-Garza, and A. G. Pandya. Melasma Treatment: An Evidence-Based Review. *American Journal of Clinical Dermatology*, 21(2):173–225, Apr. 2020. ISSN 1179-1888. doi: 10.1007/s40257-019-00488-w.
- W. V. Meira, T. A. Heinrich, S. M. S. C. Cadena, and G. R. Martinez. Melanogenesis inhibits respiration in B16-F10 melanoma cells whereas enhances mitochondrial cell content. *Experimental Cell Research*, 350(1):62–72, Jan. 2017. ISSN 1090-2422. doi: 10.1016/j.yexcr.2016.11.006.
- M. E. Mullins. Life-Threatening Interaction of Mibefradil and -Blockers With Dihydropyridine Calcium Channel Blockers. *JAMA*, 280(2):157, July 1998. ISSN 0098-7484. doi: 10.1001/jama.280.2.157. URL <http://jama.jamanetwork.com/article.aspx?doi=10.1001/jama.280.2.157>.
- M. Martínez-García and L. Montoliu. Albinism in Europe. *The Journal of Dermatology*, 40(5):319–324, 2013. ISSN 1346-8138. doi: 10.1111/1346-8138.12170. URL <https://onlinelibrary.wiley.com/doi/abs/10.1111/1346-8138.12170>. _eprint: <https://onlinelibrary.wiley.com/doi/pdf/10.1111/1346-8138.12170>.
- N. Méthot and K. Basler. An absolute requirement for Cubitus interruptus in Hedgehog signaling. *Development (Cambridge, England)*, 128(5):733–742, Mar. 2001. ISSN 0950-1991. doi: 10.1242/dev.128.5.733.
- F. F. Naini, A. V. Shooshtari, B. Ebrahimi, and R. Molaei. The effect of pseudocatalase/superoxide dismutase in the treatment of vitiligo: A pilot study. *Journal of Research in Pharmacy Practice*, 1(2):77–80, 2012. ISSN 2319-9644. doi: 10.4103/2279-042X.108375. URL <https://www.ncbi.nlm.nih.gov/pmc/articles/PMC4076862/>.
- V. T. Natarajan, P. Ganju, A. Singh, V. Vijayan, K. Kirty, S. Yadav, S. Puntambekar, S. Bajaj, P. P. Dani, H. K. Kar, C. J. Gadgil, K. Natarajan, R. Rani, and R. S. Gokhale. IFN- signaling maintains skin pigmentation homeostasis through regulation of melanosome maturation. *Proceedings of the National Academy of Sciences*, 111(6):2301–2306, Feb. 2014. ISSN 0027-8424, 1091-6490. doi: 10.1073/pnas.1304988111. URL <https://www.pnas.org/content/111/6/2301>. Publisher: National Academy of Sciences Section: Biological Sciences.
- K. L. Neff, D. P. Argue, A. C. Ma, H. B. Lee, K. J. Clark, and S. C. Ekker. Mojo Hand, a TALEN design tool for genome editing applications. *BMC bioinformatics*, 14:1, Jan. 2013. ISSN 1471-2105. doi: 10.1186/1471-2105-14-1.
- M. D. Njoo, P. K. Das, J. D. Bos, and W. Westerhof. Association of the Köbner phenomenon with disease activity and therapeutic responsiveness in vitiligo vulgaris. *Archives of Dermatology*, 135(4):407–413, Apr. 1999. ISSN 0003-987X. doi: 10.1001/archderm.135.4.407.

BIBLIOGRAPHY

- H. Nugroho, A. F. Mohd Hani, V. Yap, N. Shamsudin, and H. Suraiya. Determination of Skin Repigmentation Progression. *Conference proceedings : ... Annual International Conference of the IEEE Engineering in Medicine and Biology Society. IEEE Engineering in Medicine and Biology Society. Conference*, 2007:3442–5, Feb. 2007. doi: 10.1109/IEMBS.2007.4353071.
- O. A. Ogbechie-Godec and N. Elbuluk. Melasma: an Up-to-Date Comprehensive Review. *Dermatology and Therapy*, 7(3):305–318, July 2017. ISSN 2193-8210. doi: 10.1007/s13555-017-0194-1. URL <https://www.ncbi.nlm.nih.gov/pmc/articles/PMC5574745/>.
- E. A. Oliver, L. Schwartz, and L. H. Warren. OCCUPATIONAL LEUKODERMA: PRELIMINARY REPORT. *Journal of the American Medical Association*, 113(10):927–928, Sept. 1939. ISSN 0002-9955. doi: 10.1001/jama.1939.72800350003010a. URL <https://doi.org/10.1001/jama.1939.72800350003010a>.
- D. O’Sullivan, G. J. W. van der Windt, S. C.-C. Huang, J. D. Curtis, C.-H. Chang, M. D. Buck, J. Qiu, A. M. Smith, W. Y. Lam, L. M. DiPlato, F.-F. Hsu, M. J. Birnbaum, E. J. Pearce, and E. L. Pearce. Memory CD8(+) T cells use cell-intrinsic lipolysis to support the metabolic programming necessary for development. *Immunity*, 41(1):75–88, July 2014. ISSN 1097-4180. doi: 10.1016/j.immuni.2014.06.005.
- B. Palermo, R. Campanelli, S. Garbelli, S. Mantovani, E. Lantelme, V. Brazzelli, M. Ardigó, G. Borroni, M. Martinetti, C. Badulli, A. Necker, and C. Giachino. Specific Cytotoxic T Lymphocyte Responses Against Melan-A/MART1, Tyrosinase and Gp100 in Vitiligo by the Use of Major Histocompatibility Complex/Peptide Tetramers: the Role of Cellular Immunity in the Etiopathogenesis of Vitiligo. *Journal of Investigative Dermatology*, 117(2):326–332, Aug. 2001. ISSN 0022-202X. doi: 10.1046/j.1523-1747.2001.01408.x. URL <https://www.sciencedirect.com/science/article/pii/S0022202X15413314>.
- Y. Pan, T. Tian, C. O. Park, S. Y. Lofftus, S. Mei, X. Liu, C. Luo, J. T. O’Malley, A. Gehad, J. E. Teague, S. J. Divito, R. Fuhlbrigge, P. Puigserver, J. G. Krueger, G. S. Hotamisligil, R. A. Clark, and T. S. Kupper. Survival of tissue-resident memory T cells requires exogenous lipid uptake and metabolism. *Nature*, 543(7644):252–256, Mar. 2017. ISSN 1476-4687. doi: 10.1038/nature21379.
- S.-H. Park, D.-S. Kim, W.-G. Kim, I.-J. Ryoo, D.-H. Lee, C.-H. Huh, S.-W. Youn, I.-D. Yoo, and K.-C. Park. Terrein: a new melanogenesis inhibitor and its mechanism. *Cellular and molecular life sciences: CMLS*, 61(22):2878–2885, Nov. 2004. ISSN 1420-682X. doi: 10.1007/s00018-004-4341-3.
- D. Parsad, R. Saini, and R. Nagpal. Calcipotriol in vitiligo: a preliminary study. *Pediatric Dermatology*, 16(4):317–320, 1999. ISSN 0736-8046. doi: 10.1046/j.1525-1470.1999.00083.x.
- N. D. Perkins. Integrating cell-signalling pathways with NF-B and IKK function. *Nature Reviews Molecular Cell Biology*, 8(1):49–62, Jan. 2007. doi: 10.1038/nrm2083. URL <http://www.nature.com/articles/nrm2083>.
- S. Phung, D. Chai, and A. Bouzerdoum. *A universal and robust human skin color model using neural networks*, volume 4. Feb. 2001. ISBN 978-0-7803-7044-9. doi: 10.1109/IJCNN.2001.938827. Pages: 2849 vol.4.
- M. Picardo, M. L. Dell’Anna, K. Ezzedine, I. Hamzavi, J. E. Harris, D. Parsad, and A. Taieb. Vitiligo. *Nature Reviews Disease Primers*, 1(1):1–16, June 2015. ISSN 2056-676X. doi:

- 10.1038/nrdp.2015.11. URL <https://www.nature.com/articles/nrdp201511>. Number: 1
Publisher: Nature Publishing Group.
- G. Prota. Progress in the chemistry of melanins and related metabolites. *Medicinal Research Reviews*, 8(4):525–556, 1988. ISSN 0198-6325. doi: 10.1002/med.2610080405.
- S. Pugazhenthii, A. Nesterova, C. Sable, K. A. Heidenreich, L. M. Boxer, L. E. Heasley, and J. E. Reusch. Akt/protein kinase B up-regulates Bcl-2 expression through cAMP-response element-binding protein. *The Journal of biological chemistry*, 275(15):10761–6, Apr. 2000. doi: 10.1074/jbc.275.15.10761. URL <http://www.ncbi.nlm.nih.gov/pubmed/10753867>.
- S. Pv, B. Nk, G. Kv, R. Gr, R. Ar, M. B, and R. Tr. Determination of oxidative stress in vitiligo by measuring superoxide dismutase and catalase levels in vitiliginous and non-vitiliginous skin. *Indian journal of dermatology, venereology and leprology*, 75(3), June 2009. ISSN 0973-3922. doi: 10.4103/0378-6323.48427. URL <https://pubmed.ncbi.nlm.nih.gov/19439879/>.
Publisher: Indian J Dermatol Venereol Leprol.
- X. Qian and E. R. Dougherty. Effect of function perturbation on the steady-state distribution of genetic regulatory networks: Optimal structural intervention. *IEEE Transactions on Signal Processing*, 56(10 I):4966–4976, 2008. ISSN 1053-587X. doi: 10.1109/TSP.2008.928089.
- X. Qian and E. R. Dougherty. On the long-run sensitivity of probabilistic Boolean networks. *Journal of Theoretical Biology*, 257(4):560–577, 2009. ISSN 1095-8541. doi: 10.1016/j.jtbi.2008.12.023.
- L. Raam, E. Kaleviste, M. Šunina, H. Vaher, M. Saare, E. Prans, M. Pihlap, K. Abram, M. Karelson, P. Peterson, A. Rebane, K. Kisand, and K. Kingo. Lymphoid Stress Surveillance Response Contributes to Vitiligo Pathogenesis. *Frontiers in Immunology*, 9:2707, 2018. ISSN 1664-3224. doi: 10.3389/fimmu.2018.02707. URL <https://www.frontiersin.org/article/10.3389/fimmu.2018.02707>.
- A. Raghunath, A. Sambarey, N. Sharma, U. Mahadevan, and N. Chandra. A molecular systems approach to modelling human skin pigmentation: identifying underlying pathways and critical components. *BMC research notes*, 8:170–170, 2015. doi: 10.1186/s13104-015-1128-6. URL <http://www.pubmedcentral.nih.gov/articlerender.fcgi?artid=4424494&tool=pmcentrez&rendertype=abstract>.
- N. Rapin, E. Mosekilde, and O. Lund. Bistability in autoimmune diseases. *Autoimmunity*, 44(4):256–260, June 2011. ISSN 0891-6934. doi: 10.3109/08916934.2010.523233. URL <https://doi.org/10.3109/08916934.2010.523233>. Publisher: Taylor & Francis _eprint: <https://doi.org/10.3109/08916934.2010.523233>.
- M. Rashighi, P. Agarwal, J. M. Richmond, T. H. Harris, K. Dresser, M. Su, Y. Zhou, A. Deng, C. A. Hunter, A. D. Luster, and J. E. Harris. CXCL10 is critical for the progression and maintenance of depigmentation in a mouse model of vitiligo. *Science translational medicine*, 6(223):223ra23, Feb. 2014. ISSN 1946-6234. doi: 10.1126/scitranslmed.3007811. URL <https://www.ncbi.nlm.nih.gov/pmc/articles/PMC4086941/>.
- J. M. Richmond, M. L. Frisoli, and J. E. Harris. Innate immune mechanisms in vitiligo: Danger from within. *Current opinion in immunology*, 25(6):676–682, Dec. 2013. ISSN 0952-7915. doi: 10.1016/j.coi.2013.10.010. URL <https://www.ncbi.nlm.nih.gov/pmc/articles/PMC3935321/>.

BIBLIOGRAPHY

- J. N. Rodríguez-López, J. Tudela, R. Varón, F. García-Carmona, and F. García-Cánovas. Analysis of a kinetic model for melanin biosynthesis pathway. *Journal of Biological Chemistry*, 267(6):3801–3810, Feb. 1992. ISSN 0021-9258, 1083-351X. URL <http://www.jbc.org/content/267/6/3801>.
- A. Ryll, R. Samaga, F. Schaper, L. G. Alexopoulos, and S. Klamt. Large-scale network models of IL-1 and IL-6 signalling and their hepatocellular specification. *Molecular bioSystems*, 7(12):3253–3270, Dec. 2011. ISSN 1742-2051. doi: 10.1039/c1mb05261f.
- L. Rönstrand. Signal transduction via the stem cell factor receptor/c-Kit. *Cellular and molecular life sciences: CMLS*, 61(19-20):2535–2548, Oct. 2004. ISSN 1420-682X. doi: 10.1007/s00018-004-4189-6.
- M. S Al Abadie. The Neuronal Theory in the Pathogenesis of Vitiligo: Past and Present. *Dermatology and Dermatitis*, 6(3):01–06, Oct. 2021. ISSN 25788949. doi: 10.31579/2578-8949/082. URL <https://auctoresonline.org/article/the-neuronal-theory-in-the-pathogenesis-of-vitiligo-past-and-present>.
- A. Saadatpour, I. Albert, and R. Albert. Attractor analysis of asynchronous Boolean models of signal transduction networks. *Journal of Theoretical Biology*, 266(4):641–656, Oct. 2010. ISSN 1095-8541. doi: 10.1016/j.jtbi.2010.07.022.
- A. Saadatpour, R.-S. Wang, A. Liao, X. Liu, T. P. Loughran, I. Albert, and R. Albert. Dynamical and structural analysis of a T cell survival network identifies novel candidate therapeutic targets for large granular lymphocyte leukemia. *PLoS computational biology*, 7(11):e1002267–e1002267, 2011. ISSN 1553-7358. doi: 10.1371/journal.pcbi.1002267. URL <http://www.pubmedcentral.nih.gov/articlerender.fcgi?artid=3213185&tool=pmcentrez&rendertype=abstract>.
- J. Saez-Rodriguez, L. Simeoni, J. A. Lindquist, R. Hemenway, U. Bommhardt, B. Arndt, U. U. Haus, R. Weismantel, E. D. Gilles, S. Klamt, and B. Schraven. A logical model provides insights into T cell receptor signaling. *PLoS Computational Biology*, 3(8):1580–1590, 2007. ISSN 1553-7358 (Electronic)\n1553-734X (Linking). doi: 10.1371/journal.pcbi.0030163.
- B. Saha, S. K. Singh, C. Sarkar, R. Bera, J. Ratha, D. J. Tobin, and R. Bhadra. Activation of the Mitf promoter by lipid-stimulated activation of p38-stress signalling to CREB. *Pigment Cell Research*, 19(6):595–605, Dec. 2006. ISSN 0893-5785. doi: 10.1111/j.1600-0749.2006.00348.x.
- S. Said-Fernandez, C. Sanchez-Dominguez, M. Salinas-Santander, H. Martinez-Rodriguez, D. Kubelis-Lopez, N. A. Salazar, O. Vázquez-Martínez, U. Wollina, T. Lotti, and J. Ocampo-Candiani. Novel immunological and genetic factors associated with vitiligo: A review. *Experimental and Therapeutic Medicine*, 21, Feb. 2021. doi: 10.3892/etm.2021.9743.
- J. Sandby-Møller, T. Poulsen, and H. C. Wulf. Epidermal thickness at different body sites: relationship to age, gender, pigmentation, blood content, skin type and smoking habits. *Acta Dermato-Venereologica*, 83(6):410–413, 2003. ISSN 0001-5555. doi: 10.1080/00015550310015419.
- G. A. Scott and L. Cassidy. Rac1 mediates dendrite formation in response to melanocyte stimulating hormone and ultraviolet light in a murine melanoma model. *The Journal of Investigative Dermatology*, 111(2):243–250, Aug. 1998. ISSN 0022-202X. doi: 10.1046/j.1523-1747.1998.00276.x.

- V. N. Sehgal and G. Srivastava. Vitiligo: compendium of clinico-epidemiological features. *Indian Journal of Dermatology, Venereology and Leprology*, 73(3):149–156, 2007. ISSN 0973-3922. doi: 10.4103/0378-6323.32708.
- S.-H. Seo, J. K. Jo, E.-J. Kim, S.-E. Park, S. Y. Shin, K. M. Park, and H.-S. Son. Metabolomics Reveals the Alteration of Metabolic Pathway by Alpha-Melanocyte-Stimulating Hormone in B16F10 Melanoma Cells. *Molecules*, 25(15):3384, Jan. 2020. ISSN 1420-3049. doi: 10.3390/molecules25153384. URL <https://www.mdpi.com/1420-3049/25/15/3384>. Number: 15 Publisher: Multidisciplinary Digital Publishing Institute.
- Q.-B. She, W.-Y. Ma, S. Zhong, and Z. Dong. Activation of JNK1, RSK2, and MSK1 is involved in serine 112 phosphorylation of Bad by ultraviolet B radiation. *The Journal of biological chemistry*, 277(27):24039–48, July 2002. doi: 10.1074/jbc.M109907200. URL <http://www.ncbi.nlm.nih.gov/pubmed/11983683>.
- S. D. Shenoi and S. Prabhu. Photochemotherapy (PUVA) in psoriasis and vitiligo. *Indian Journal of Dermatology, Venereology and Leprology*, 80:497, Nov. 2014. ISSN 0378-6323. doi: 10.4103/0378-6323.144143. URL <https://ijdvl.com/photochemotherapy-puva-in-psoriasis-and-vitiligo/>. Publisher: scientific scholar.
- J. A. Sherratt and J. C. Dallon. Theoretical models of wound healing: past successes and future challenges. *Comptes Rendus Biologies*, 325(5):557–564, May 2002. ISSN 1631-0691. doi: 10.1016/s1631-0691(02)01464-6.
- J. A. Sherratt and J. D. Murray. Mathematical analysis of a basic model for epidermal wound healing. *Journal of Mathematical Biology*, 29(5):389–404, 1991. ISSN 0303-6812. doi: 10.1007/BF00160468.
- M. Shimada, Y. Yamada, M. Itoh, and T. Yatagai. Melanin and blood concentration in a human skin model studied by multiple regression analysis: assessment by Monte Carlo simulation. *Physics in Medicine and Biology*, 46(9):2397–2406, Sept. 2001. ISSN 0031-9155. doi: 10.1088/0031-9155/46/9/309.
- J. Shiu, L. Zhang, G. Lentsch, J. L. Flesher, S. Jin, C. Polleys, S. J. Jo, C. Mizzoni, P. Mobasher, J. Kwan, F. Rius-Diaz, B. J. Tromberg, I. Georgakoudi, Q. Nie, M. Balu, and A. K. Ganesan. Multimodal analyses of vitiligo skin identify tissue characteristics of stable disease. *JCI Insight*, 7(13):e154585. ISSN 2379-3708. doi: 10.1172/jci.insight.154585. URL <https://www.ncbi.nlm.nih.gov/pmc/articles/PMC9310536/>.
- I. Shmulevich, E. R. Dougherty, and W. Zhang. Gene perturbation and intervention in probabilistic Boolean networks. *Bioinformatics*, 18(10):1319–1331, 2002. ISSN 1367-4803 (Print)\n1367-4803 (Linking). doi: 10.1093/bioinformatics/18.10.1319.
- J. D. Simon, D. Peles, K. Wakamatsu, and S. Ito. Current challenges in understanding melanogenesis: bridging chemistry, biological control, morphology, and function. *Pigment Cell & Melanoma Research*, 22(5):563–579, Oct. 2009. ISSN 1755-1471. doi: 10.1111/j.1755-148X.2009.00610.x.
- S. K. Singh, R. Kurfurst, C. Nizard, S. Schnebert, E. Perrier, and D. J. Tobin. Melanin transfer in human skin cells is mediated by filopodia—a model for homotypic and heterotypic lysosome-related organelle transfer. *The FASEB Journal*, 24(10):3756–3769, 2010. ISSN 1530-6860. doi: 10.1096/fj.10-159046. URL <https://onlinelibrary.wiley.com/doi/abs/10.1096/fj.10-159046>. _eprint: <https://onlinelibrary.wiley.com/doi/pdf/10.1096/fj.10-159046>.

BIBLIOGRAPHY

- R. Smallwood, S. Adra, and G. Khodabakhshi. Multiscale, multi-paradigm modelling of tissues: embedding development in tissue behaviour. Aug. 2010.
- W. Smythe, A. Khandelwal, C. Merle, R. Rustomjee, M. Gninafon, M. Bocar Lo, O. B. Sow, P. L. Olliaro, C. Lienhardt, J. Horton, P. Smith, H. McIlleron, and U. S. H. Simonsson. A Semimechanistic Pharmacokinetic-Enzyme Turnover Model for Rifampin Autoinduction in Adult Tuberculosis Patients. *Antimicrobial Agents and Chemotherapy*, 56(4):2091–2098, Apr. 2012. ISSN 0066-4804. doi: 10.1128/AAC.05792-11. URL <https://www.ncbi.nlm.nih.gov/pmc/articles/PMC3318330/>.
- D. Spies, P. F. Renz, T. A. Beyer, and C. Ciaudo. Comparative analysis of differential gene expression tools for RNA sequencing time course data. *Briefings in Bioinformatics*, 20(1): 288–298, Oct. 2017. ISSN 1467-5463. doi: 10.1093/bib/bbx115. URL <https://www.ncbi.nlm.nih.gov/pmc/articles/PMC6357553/>.
- R. Spritz and G. Andersen. Genetics of Vitiligo. *Dermatologic clinics*, 35(2):245–255, Apr. 2017. ISSN 0733-8635. doi: 10.1016/j.det.2016.11.013. URL <https://www.ncbi.nlm.nih.gov/pmc/articles/PMC5362127/>.
- R. Stolar. Induced Alterations of Vitiliginous Skin. *Annals of the New York Academy of Sciences*, 100(1):58–75, 1963. ISSN 1749-6632. doi: 10.1111/j.1749-6632.1963.tb57113.x. URL <https://onlinelibrary.wiley.com/doi/abs/10.1111/j.1749-6632.1963.tb57113.x>. [__eprint: https://onlinelibrary.wiley.com/doi/pdf/10.1111/j.1749-6632.1963.tb57113.x](https://onlinelibrary.wiley.com/doi/pdf/10.1111/j.1749-6632.1963.tb57113.x).
- I. Subramanian, V. K. Singh, and A. Jere. Elucidating mechanistic insights into drug action for atopic dermatitis: a systems biology approach. *BMC Dermatology*, 18, Feb. 2018. ISSN 1471-5945. doi: 10.1186/s12895-018-0070-4. URL <https://www.ncbi.nlm.nih.gov/pmc/articles/PMC5803917/>.
- K. Subramanian and C. Gadgil. Robustness of the Drosophila segment polarity network to transient perturbations. *IET systems biology*, 4(2):169–76, 2010. ISSN 1751-8849. doi: 10.1049/iet-syb.2009.0036. URL <http://www.ncbi.nlm.nih.gov/pubmed/20232996>.
- K.-L. Sun, W. Liu, X.-M. Gao, M. Yang, and J.-M. Chang. A Study of Normal Epidermal Melanocyte Distribution. *International Journal of Dermatology and Venereology*, 4(1):32–35, Mar. 2021. ISSN 2641-8746
ISSN (print): 2096-5540
CN: 32-1880/R. doi: 10.1097/JD9.000000000000125. URL https://journals.lww.com/ijdv/Fulltext/2021/03000/A_Study_of_Normal_Epidermal_Melanocyte.5.aspx.
- T. Tadokoro, N. Kobayashi, B. Z. Zmudzka, S. Ito, K. Wakamatsu, Y. Yamaguchi, K. S. Korossy, S. A. Miller, J. Z. Beer, and V. J. Hearing. UV-induced DNA damage and melanin content in human skin differing in racial/ethnic origin. *FASEB journal: official publication of the Federation of American Societies for Experimental Biology*, 17(9):1177–1179, June 2003. ISSN 1530-6860. doi: 10.1096/fj.02-0865fje.
- T. Tadokoro, Y. Yamaguchi, J. Batzer, S. G. Coelho, B. Z. Zmudzka, S. A. Miller, R. Wolber, J. Z. Beer, and V. J. Hearing. Mechanisms of skin tanning in different racial/ethnic groups in response to ultraviolet radiation. *The Journal of Investigative Dermatology*, 124(6):1326–1332, June 2005. ISSN 0022-202X. doi: 10.1111/j.0022-202X.2005.23760.x.

- A. Taieb, A. Alomar, M. Böhm, M. Dell'anna, A. De Pase, V. Eleftheriadou, K. Ezzedine, Y. Gauthier, D. Gawkrödger, T. Jouary, and others. Vitiligo European Task Force (VETF); European Academy of Dermatology and Venereology (EADV); Union Européenne des Médecins Spécialistes (UEMS). Guidelines for the management of vitiligo: the European Dermatology Forum consensus. *Br J Dermatol*, 168(1):5–19, 2013.
- W. Tangamornsuksan, P. Thiansupornpong, T. Morasuk, O. Lohitnavy, and M. Lohitnavy. A pharmacokinetic model of drug-drug interaction between clopidogrel and omeprazole at CYP2C19 in humans. In *2017 39th Annual International Conference of the IEEE Engineering in Medicine and Biology Society (EMBC)*, pages 2704–2707, July 2017. doi: 10.1109/EMBC.2017.8037415. ISSN: 1558-4615.
- J. Tanwar, S. Saurav, R. Basu, J. B. Singh, A. Priya, M. Dutta, U. Santhanam, M. Joshi, S. Madison, A. Singh, N. Nair, R. S. Gokhale, and R. K. Motiani. Mitofusin-2 Negatively Regulates Melanogenesis by Modulating Mitochondrial ROS Generation. *Cells*, 11(4):701, Feb. 2022. ISSN 2073-4409. doi: 10.3390/cells11040701.
- M. K. Tembhre, V. K. Sharma, A. Sharma, P. Chattopadhyay, and S. Gupta. T helper and regulatory T cell cytokine profile in active, stable and narrow band ultraviolet B treated generalized vitiligo. *Clinica Chimica Acta; International Journal of Clinical Chemistry*, 424: 27–32, Sept. 2013. ISSN 1873-3492. doi: 10.1016/j.cca.2013.05.005.
- J. Thingnes, L. Oyehaug, E. Hovig, and S. W. Omholt. The mathematics of tanning. *BMC systems biology*, 3:60, June 2009. ISSN 1752-0509. doi: 10.1186/1752-0509-3-60.
- R. Thomas. Boolean formalization of genetic control circuits. *Journal of Theoretical Biology*, 42 (3):563–585, Dec. 1973. ISSN 0022-5193. doi: 10.1016/0022-5193(73)90247-6. URL <https://www.sciencedirect.com/science/article/pii/0022519373902476>.
- H.-Y. Thong, S.-H. Jee, C.-C. Sun, and R. E. Boissy. The patterns of melanosome distribution in keratinocytes of human skin as one determining factor of skin colour. *The British Journal of Dermatology*, 149(3):498–505, Sept. 2003. ISSN 0007-0963. doi: 10.1046/j.1365-2133.2003.05473.x.
- Y. Tokura, T. Fujiyama, S. Ikeya, K. Tatsuno, M. Aoshima, A. Kasuya, and T. Ito. Biochemical, cytological, and immunological mechanisms of rhododendrol-induced leukoderma. *Journal of Dermatological Science*, 77(3):146–149, Mar. 2015. ISSN 0923-1811. doi: 10.1016/j.jdermsci.2015.02.001. URL <https://www.sciencedirect.com/science/article/pii/S0923181115000432>.
- L. Travis and N. Silverberg. Calcipotriene and Corticosteroid Combination Therapy for Vitiligo. *Pediatric dermatology*, 21:495–8, July 2004. doi: 10.1111/j.0736-8046.2004.21418.x.
- N. Tsumura, N. Ojima, K. Sato, M. Shiraishi, H. Shimizu, H. Nabeshima, S. Akazaki, K. Hori, and Y. Miyake. Image-based skin color and texture analysis/synthesis by extracting hemoglobin and melanin information in the skin. *ACM Transactions on Graphics (TOG)*, 22: 770–779, July 2003. ISSN 1-58113-709-5. doi: 10.1145/882262.882344.
- V. Vakil and W. Trappe. Drug Combinations: Mathematical Modeling and Networking Methods. *Pharmaceutics*, 11(5):208, May 2019. ISSN 1999-4923. doi: 10.3390/pharmaceutics11050208.
- J. G. van den Boorn, D. I. Picavet, P. F. van Swieten, H. A. van Veen, D. Konijnenberg, P. A. van Veelen, T. van Capel, E. C. de Jong, E. A. Reits, J. W. Drijfhout, J. D. Bos,

BIBLIOGRAPHY

- C. J. M. Melief, and R. M. Luiten. Skin-Depigmenting Agent Monobenzone Induces Potent T-Cell Autoimmunity toward Pigmented Cells by Tyrosinase Haptenation and Melanosome Autophagy. *Journal of Investigative Dermatology*, 131(6):1240–1251, June 2011. ISSN 0022-202X. doi: 10.1038/jid.2011.16. URL <https://www.sciencedirect.com/science/article/pii/S0022202X15352866>.
- K. Van Den Bossche, J.-M. Naeyaert, and J. Lambert. The quest for the mechanism of melanin transfer. *Traffic (Copenhagen, Denmark)*, 7(7):769–778, July 2006. ISSN 1398-9219. doi: 10.1111/j.1600-0854.2006.00425.x.
- N. van Geel, I. Mollet, L. Brochez, M. Dutré, S. De Schepper, E. Verhaeghe, J. Lambert, and R. Speeckaert. New insights in segmental vitiligo: case report and review of theories. *British Journal of Dermatology*, 166(2):240–246, 2012. ISSN 1365-2133. doi: 10.1111/j.1365-2133.2011.10650.x. URL <https://onlinelibrary.wiley.com/doi/abs/10.1111/j.1365-2133.2011.10650.x>. _eprint: <https://onlinelibrary.wiley.com/doi/pdf/10.1111/j.1365-2133.2011.10650.x>.
- R. W. van Leeuwen, F. G. A. Jansman, P. M. L. A. v. d. Bemt, F. De Man, F. Piran, I. Vincenten, A. Jager, A. W. Rijneveld, R. H. J. Mathijssen, and T. van Gelder. 484P - Drug-Drug Interactions in Patients Treated for Cancer: a Prospective Study on Clinical Interventions. *Annals of Oncology*, 25:iv162, Sept. 2014. ISSN 0923-7534. doi: 10.1093/annonc/mdu331.44. URL <https://www.sciencedirect.com/science/article/pii/S0923753419519044>.
- R. W. F. van Leeuwen, D. H. S. Brundel, C. Neef, T. van Gelder, R. H. J. Mathijssen, D. M. Burger, and F. G. A. Jansman. Prevalence of potential drug–drug interactions in cancer patients treated with oral anticancer drugs. *British Journal of Cancer*, 108(5):1071–1078, Mar. 2013. ISSN 0007-0920. doi: 10.1038/bjc.2013.48. URL <https://www.ncbi.nlm.nih.gov/pmc/articles/PMC3619066/>.
- I. F. d. S. Videira, D. F. L. Moura, and S. Magina. Mechanisms regulating melanogenesis*. *Anais Brasileiros de Dermatologia*, 88:76–83, Feb. 2013. ISSN 0365-0596, 1806-4841. doi: 10.1590/S0365-05962013000100009. URL <http://www.scielo.br/j/abd/a/gQQNYKcbCcD5mYKCTDpBRYm/?lang=en>. Publisher: Sociedade Brasileira de Dermatologia.
- G. von Dassow, E. Meir, E. M. Munro, and G. M. Odell. The segment polarity network is a robust developmental module. *Nature*, 406(6792):188–192, July 2000. ISSN 0028-0836. doi: 10.1038/35018085.
- T. L. Wachtel, C. C. Berry, E. E. Wachtel, and H. A. Frank. The inter-rater reliability of estimating the size of burns from various burn area chart drawings. *Burns: Journal of the International Society for Burn Injuries*, 26(2):156–170, Mar. 2000. ISSN 0305-4179. doi: 10.1016/s0305-4179(99)00047-9.
- K. WAKAMATSU, A. GRAHAM, D. COOK, and A. J. THODY. Characterisation of ACTH Peptides in Human Skin and Their Activation of the Melanocortin-1 Receptor. *Pigment Cell Research*, 10(5):288–297, Oct. 1997. doi: 10.1111/j.1600-0749.1997.tb00688.x. URL <http://doi.wiley.com/10.1111/j.1600-0749.1997.tb00688.x>.
- Q.-F. Wang, A. Cruz-Inigo, J. Fuentes-Duculan, D. Moussai, N. Gulati, M. Sullivan-Whalen, P. Gilleaudeau, J. Cohen, and J. Krueger. Th17 Cells and Activated Dendritic Cells Are Increased in Vitiligo Lesions. *PloS one*, 6:e18907, Apr. 2011. doi: 10.1371/journal.pone.0018907.

- R.-S. Wang and R. Albert. Elementary signaling modes predict the essentiality of signal transduction network components. *BMC Systems Biology*, 5(1):44–44, 2011. ISSN 1752-0509 (Electronic)\n1752-0509 (Linking). doi: 10.1186/1752-0509-5-44. URL <http://eutils.ncbi.nlm.nih.gov/entrez/eutils/elink.fcgi?dbfrom=pubmed&id=21426566&retmode=ref&cmd=prlinks%5Cnpapers2://publication/doi/10.1186/1752-0509-5-44>.
- R.-S. Wang, A. Saadatpour, and R. Albert. Boolean modeling in systems biology: an overview of methodology and applications. *Physical Biology*, 9(5):055001–055001, Oct. 2012. doi: 10.1088/1478-3975/9/5/055001. URL <http://www.ncbi.nlm.nih.gov/pubmed/23011283>.
- A. Wańkiewicz-Kalińska, R. M. J. G. J. van den Wijngaard, B. J. Tigges, W. Westerhof, G. S. Ogg, V. Cerundolo, W. J. Storkus, and P. K. Das. Immunopolarization of CD4+ and CD8+ T cells to Type-1-like is associated with melanocyte loss in human vitiligo. *Laboratory Investigation; a Journal of Technical Methods and Pathology*, 83(5):683–695, May 2003. ISSN 0023-6837. doi: 10.1097/01.lab.0000069521.42488.1b.
- H. J. Wearing and J. A. Sherratt. Keratinocyte growth factor signalling: a mathematical model of dermal–epidermal interaction in epidermal wound healing. *Mathematical Biosciences*, 165(1):41–62, May 2000. ISSN 00255564. doi: 10.1016/S0025-5564(00)00008-0. URL <https://linkinghub.elsevier.com/retrieve/pii/S0025556400000080>.
- C.-L. Wei, Q. Wu, V. B. Vega, K. P. Chiu, P. Ng, T. Zhang, A. Shahab, H. C. Yong, Y. Fu, Z. Weng, J. Liu, X. D. Zhao, J.-L. Chew, Y. L. Lee, V. A. Kuznetsov, W.-K. Sung, L. D. Miller, B. Lim, E. T. Liu, Q. Yu, H.-H. Ng, and Y. Ruan. A global map of p53 transcription-factor binding sites in the human genome. *Cell*, 124(1):207–219, Jan. 2006. ISSN 0092-8674. doi: 10.1016/j.cell.2005.10.043.
- C.-S. Wu, S. C.-S. Hu, C.-C. E. Lan, G.-S. Chen, W.-H. Chuo, and H.-S. Yu. Low-energy helium-neon laser therapy induces repigmentation and improves the abnormalities of cutaneous microcirculation in segmental-type vitiligo lesions. *The Kaohsiung Journal of Medical Sciences*, 24(4):180–189, Apr. 2008. ISSN 1607-551X. doi: 10.1016/S1607-551X(08)70115-3.
- C. Xing and A. Xu. The effect of combined calcipotriol and betamethasone dipropionate ointment in the treatment of vitiligo: an open, uncontrolled trial. *Journal of drugs in dermatology: JDD*, 11(10):e52–54, Oct. 2012. ISSN 1545-9616.
- Y. Yamaguchi, M. Brenner, and V. J. Hearing. The Regulation of Skin Pigmentation*. *Journal of Biological Chemistry*, 282(38):27557–27561, Sept. 2007. ISSN 0021-9258. doi: 10.1074/jbc.R700026200. URL <https://www.sciencedirect.com/science/article/pii/S0021925820586493>.
- Y. Yao, C. Ma, H. Deng, Q. Liu, W. Cao, R. Gui, T. Feng, and M. Yi. Dynamics and robustness of the cardiac progenitor cell induced pluripotent stem cell network during cell phenotypes transition. *IET systems biology*, 11(1):1–7, Feb. 2017. ISSN 1751-8849. doi: 10.1049/iet-syb.2015.0051.
- M. Yazicioglu, P. Gokmirza Ozdemir, B. Turgut, and N. Sut. Serum soluble Fas ligand levels and peripheral blood lymphocyte subsets in patients with drug-induced maculopapular rashes, dress, and viral exanthemas. *Allergologia et Immunopathologia*, 48(4):339–347, July 2020. ISSN 0301-0546. doi: 10.1016/j.aller.2019.02.003. URL <https://www.elsevier.es/en-revista-allergologia-et-immunopathologia-105-articulo-serum-soluble-fas-ligand-levels-S0301054620301003>. Publisher: Elsevier.

BIBLIOGRAPHY

- H.-S. Yu. Melanocyte destruction and repigmentation in vitiligo: A model for nerve cell damage and regrowth. *Journal of Biomedical Science*, 9(6):564–573, Sept. 2002. ISSN 1423-0127. doi: 10.1007/BF02254984. URL <https://doi.org/10.1007/BF02254984>.
- C. Zhang, P. Denti, E. Decloedt, G. Maartens, M. O. Karlsson, U. S. H. Simonsson, and H. McIlleron. Model-based approach to dose optimization of lopinavir/ritonavir when co-administered with rifampicin. *British Journal of Clinical Pharmacology*, 73(5):758–767, May 2012a. ISSN 1365-2125. doi: 10.1111/j.1365-2125.2011.04154.x.
- X. Zhang, G. Yan, J. Ji, J. Wu, X. Sun, J. Shen, H. Jiang, and H. Wang. PDE5 inhibitor promotes melanin synthesis through the PKG pathway in B16 melanoma cells. *Journal of Cellular Biochemistry*, 113(8):2738–2743, Aug. 2012b. ISSN 1097-4644. doi: 10.1002/jcb.24147.
- Y. Zhang, D. L. Wallace, C. M. de Lara, H. Ghattas, B. Asquith, A. Worth, G. E. Griffin, G. P. Taylor, D. F. Tough, P. C. L. Beverley, and D. C. Macallan. In vivo kinetics of human natural killer cells: the effects of ageing and acute and chronic viral infection. *Immunology*, 121(2): 258–265, June 2007. ISSN 0019-2805. doi: 10.1111/j.1365-2567.2007.02573.x.
- Y. Zhang, L. Liu, L. Jin, X. Yi, E. Dang, Y. Yang, C. Li, and T. Gao. Oxidative Stress-Induced Calreticulin Expression and Translocation: New Insights into the Destruction of Melanocytes. *Journal of Investigative Dermatology*, 134(1):183–191, Jan. 2014. ISSN 0022-202X. doi: 10.1038/jid.2013.268. URL <https://www.sciencedirect.com/science/article/pii/S0022202X15364824>.
- L. Øyehaug, E. Plahte, D. I. Våge, and S. W. Omholt. The Regulatory Basis of Melanogenic Switching. *Journal of Theoretical Biology*, 215(4):449–468, Apr. 2002. ISSN 0022-5193. doi: 10.1006/jtbi.2001.2521. URL <http://www.sciencedirect.com/science/article/pii/S0022519301925214>.

ABSTRACT

Student: Pooja Avinash Dnyane	Registration No. : 10BB18A26028
Faculty of Study: Biological Science	Year of Submission: 2023
CSIR Lab: National Chemical Laboratory	Supervisor: Dr.Chetan Gadgil
Title of the thesis: Towards the development of a systems pharmacology model for vitiligo	

The human skin is a complex organ made up of many different cell types which proliferate, differentiate, get eliminated, and interact with each other in a highly coordinated manner to maintain homeostasis of skin thickness, composition, and pigmentation. Any disturbance in the molecular events that regulate the molecular pathway that governs this interaction could result in pigmentation disorders such as Vitiligo. According to recent data, the worldwide occurrence of vitiligo is estimated to be between 1-2 %. The disorder can be psychologically and emotionally damaging. Unfortunately, it is incurable and the underlying pathogenesis mechanism is still unclear. The available therapeutic options for vitiligo are unsatisfactory for many patients as they are complex, time-consuming, and ineffective. In order to develop optimal treatment protocols, an integrated understanding of drug distribution kinetics and disease kinetics is required. This implies understanding the molecular network underlying melanogenesis and the effects leading to loss of pigmentation. To this end, I developed models, and adapted existing models, at molecular, cellular, and organ level to achieve an integrated perspective on skin depigmentation and treatment.

We began by understanding melanogenesis at the molecular level using transcriptomic data. B16 melanoma pigment cells were plated at low density for 6 days. The total RNA was isolated on days 3-6 and sequenced using Illumina Novaseq. I analyzed the sequenced raw data to identify differentially expressed genes and key pathways linked to melanogenesis. The study unraveled metabolic rewiring during pigmentation. It was found that fatty acid metabolism and glycolysis/gluconeogenesis are enhanced to maintain the bioenergetic requirements of cells during the pigmentation state.

I developed a Boolean model based on the nodes included in the Raghunath et al network. The interactions of the 265 nodes in that network were described using 23 different terms (activation, phosphorylation etc). Through additional manual curation of the reported interactions, I converted this description/network graph into a set of Boolean rules. This will provide a tool for simulation and analysis of the complex interplay between keratinocytes and melanocytes that results in skin pigmentation. In addition, I also carried out a perturbation analysis of the network through node deletion and constitutive activation to identify the sensitivity of outcomes such as melanin to individual nodes and compared the nodes identified as important to previous reports for smaller melanogenesis networks. Multiple theories have been proposed for melanocyte destruction in vitiligo. It is possible that several processes work simultaneously to cause progressive loss of melanocytes and they either involve immune attack, or cell degradation and detachment. I built a model that incorporates multiple mechanisms responsible for melanocyte death in vitiligo, along with their correlation to clinical outcomes. The model captured the dynamic responses of skin cells, immune cells and cytokines to varying levels of stress. Moreover, I also simulated drug effects through parameter variations.

There are very few models even at one scale, and none to our knowledge spanning scales in the public domain. Through this work, I have tried to provide a qualitative interpretation of disease dynamics at various levels. As a step further, the disease model can be extended to a quantitative system pharmacology (QSP) model by including a physiology-based pharmacokinetic (PBPK) model. I believe that this combination of the skin disease model and the PBPK model will serve as a unique framework for checking the effect of multiple drugs used in treating vitiligo and optimizing treatment protocols.

List of publications in SCI Journals

1. Sultan, F.; Basu, R.; Murthy, D.; Kochar, M.; Attri, K. S.; Aggarwal, A.; Kumari, P.; Dnyane, P.; Tanwar, J.; Motiani, R. K.; Singh, A.; Gadgil, C.; Bhavesh, N. S.; Singh, P. K.; Natarajan, V. T.; Gokhale, R. S. “Temporal Analysis of Melanogenesis Identifies Fatty Acid Metabolism as Key Skin Pigment Regulator”. *PLOS Biology*. 2022, 20 (5), e3001634.
2. Dnyane, P.; Gadgil, C. Boolean Model for Melanogenesis. *IOP Physical Biology* 2021, 18 (2), 026004. <https://doi.org/10.1088/1478-3975/abd3dd>
3. Dnyane, P. A.; Puntambekar, S. S.; Gadgil, C. J. Method for Identification of Sensitive Nodes in Boolean Models of Biological Networks. *IET Systems Biology* 2017, 12 (1), 1–6. <https://doi.org/10.1049/iet-syb.2017.0039>.



Conference poster presentations

1. **Poster presentation: Dnyane, P** and Gadgil, C. (May 11th. 2022), Towards the development of a systems pharmacology model for vitiligo, Virtual Student symposium organized by International Society of Pharmacometrics Quantitative Systems Pharmacology Group

Abstract: Vitiligo is an acquired, chronic skin depigmentation disorder that affects 0.5 to 2% of the world population. The disorder can be psychologically devastating and stigmatizing. In order to develop an optimal treatment protocol, an integrated understanding of disease kinetics and drug distribution kinetics is required, which can be achieved using a quantitative system pharmacology (QSP) model. To our knowledge, there is no QSP model available to understand skin pigmentation related disorders. Here, we report the formulation of the first disease model for vitiligo. Multiple mechanisms responsible for melanocyte destruction in vitiligo are integrated in our model. It includes processes related to exposure of skin to stress, production of cytokines by skin cells upon stress, elimination of melanocytes by immune cells as well as correlation of these processes to clinical outcomes. Preliminary simulations show that the predicted response to varying stress levels for most of the cells is similar to the outcomes of the existing experiments. The pharmacology aspect of this QSP model is being developed to target various components of the system. It would be helpful in determining the plasma concentration of drug.

2. **Poster presentation: Dnyane, P***, Ramachandran A*., and Gadgil, C. (June 13th. 2021 - June 17th. 2021), Network motifs in drug-drug interaction, Society for mathematical Biology Virtual Annual Meeting

Abstract: Combination therapy/multiple drug treatment is useful in some cases and necessary for the successful treatment of diseases such as leprosy, HIV/AIDS, tuberculosis and various cancers. During the treatment, drugs interact with each other and alter the medication's effect on body. The effect could be less or more potent than intended. Drugs could also have potential antagonistic effect on each other's systemic properties. When two drugs for different diseases are administered simultaneously, it is possible that one of them could decrease the concentration of other by increasing its elimination. This could lead to increased disease severity. There are models that study autoinduction where the drug upregulates enzyme that promote its own clearance. But very few models to our knowledge include drug-drug interaction wherein they modulate each other's concentration by regulating absorption and elimination rate. We present 4 network motifs that explains the positive and negative effect a drug could have on its own elimination, or on elimination of other drug administered simultaneously. We define 32 structures that represents these network motifs. Finally, we study the sensitivity of maximum drug concentration and variation in drug concentration to different parameters. This would help in optimizing the dosing protocol that involves multiple drugs.

3. **Poster presentation: Dnyane, P** and Gadgil, C. (August 17th. 2020 – August 20 2020), Boolean model for melanogenesis, Society for mathematical Biology Virtual Annual Meeting

Abstract: Melanogenesis is a highly regulated process through which the pigment melanin is produced in the skin cells. Irregularities in the molecular events that govern the process of skin pigmentation can cause disorders like vitiligo. In order to understand the biology of disease progression, it is important to have an in depth understanding of intracellular events. There are very few models to date that incorporate intracellular processes relevant to melanogenesis and only one to our knowledge that simulates the dynamics of response to varying levels of input. Here, we report the formulation of the largest Boolean model (265 nodes) for melanogenesis to date. The model was built on the basis of a detailed interaction network graph published by Raghunath et al. Through additional manual curation of the reported interactions, we converted the graph into a set of Boolean rules, following the procedure of the first Boolean model (61 nodes) for melanogenesis published by Lee et al. Simulations show that the predicted response to varying UV levels for most of the nodes is similar to the predictions of the existing model.

4.

4. **Poster presentation: Dnyane, P** and Gadgil, C. (February 5th. 2019 – February 7th 2019), Method for identification of sensitive nodes in the boolean models of biological networks, Accelerating Biology Symposium, CDAC, Pune

Abstract: Biological systems are often represented as networks, nodes being the molecules and edges being the connections. They are analyzed to identify the sensitive nodes which upon perturbation disproportionately change a predefined output. Nodes may have defects in reading the input from other nodes and calculation of the node output. To simulate these defects and assess their effect on the system output, two new function perturbations, referred to as 'not of function' and 'function of not', are introduced. These and previously used perturbation methods were applied to two existing Boolean models, namely the human melanogenesis signaling network and the fly segment polarity network. Through mathematical simulations, it was found that these methods successfully identified nodes earlier found to be sensitive using other methods, and were also able to identify sensitive nodes which were previously unreported.

Copy of all SCI publications

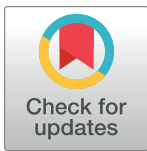
RESEARCH ARTICLE

Temporal analysis of melanogenesis identifies fatty acid metabolism as key skin pigment regulator

Farina Sultan^{1,2}, Reelina Basu¹, Divya Murthy¹, Manisha Kochar³, Kuldeep S. Attri⁴, Ayush Aggarwal^{1,2}, Pooja Kumari⁵, Pooja Dnyane^{2,6}, Jyoti Tanwar^{1,2,7}, Rajender K. Motiani⁷, Archana Singh^{1,2}, Chetan Gadgil^{1,2,6}, Neel Sarovar Bhavesh⁵, Pankaj K. Singh⁴, Vivek T. Natarajan^{1,2*}, Rajesh S. Gokhale^{3**}

1 CSIR-Institute of Genomics and Integrative Biology, New Delhi, India, **2** Academy of Scientific and Innovative Research, Ghaziabad, UP, India, **3** Immunometabolism Laboratory, National Institute of Immunology, New Delhi, India, **4** Eppley Institute for Research in Cancer and Allied Diseases, University of Nebraska Medical Center, Omaha, Nebraska, United States of America, **5** International Centre for Genetic Engineering and Biotechnology, New Delhi, India, **6** CSIR-National Chemical Laboratory, Pune, Maharashtra, India, **7** Laboratory of Calciomics and Systemic Pathophysiology, Regional Centre of Biotechnology (RCB), Faridabad, Haryana, India

* Current address: Indian Institute of Science Education and Research, Pune, Maharashtra, India
* tnvivek@igib.in (VTN); rsg@nii.ac.in (RSG)



OPEN ACCESS

Citation: Sultan F, Basu R, Murthy D, Kochar M, Attri KS, Aggarwal A, et al. (2022) Temporal analysis of melanogenesis identifies fatty acid metabolism as key skin pigment regulator. *PLoS Biol* 20(5): e3001634. <https://doi.org/10.1371/journal.pbio.3001634>

Academic Editor: Heather Christofk, University of California Los Angeles, UNITED STATES

Received: November 23, 2021

Accepted: April 19, 2022

Published: May 18, 2022

Peer Review History: PLOS recognizes the benefits of transparency in the peer review process; therefore, we enable the publication of all of the content of peer review and author responses alongside final, published articles. The editorial history of this article is available here: <https://doi.org/10.1371/journal.pbio.3001634>

Copyright: This is an open access article, free of all copyright, and may be freely reproduced, distributed, transmitted, modified, built upon, or otherwise used by anyone for any lawful purpose. The work is made available under the [Creative Commons CC0](https://creativecommons.org/licenses/by/4.0/) public domain dedication.

Data Availability Statement: The accession number for the RNA sequencing data reported in this paper is GSE164375 (<https://www.ncbi.nlm.nih.gov/geo/query/acc.cgi?acc=GSE164375>).

Abstract

Therapeutic methods to modulate skin pigmentation has important implications for skin cancer prevention and for treating cutaneous hyperpigmentary conditions. Towards defining new potential targets, we followed temporal dynamics of melanogenesis using a cell-autonomous pigmentation model. Our study elucidates 3 dominant phases of synchronized metabolic and transcriptional reprogramming. The melanogenic trigger is associated with high MITF levels along with rapid uptake of glucose. The transition to pigmented state is accompanied by increased glucose channelisation to anabolic pathways that support melanosome biogenesis. SREBF1-mediated up-regulation of fatty acid synthesis results in a transient accumulation of lipid droplets and enhancement of fatty acids oxidation through mitochondrial respiration. While this heightened bioenergetic activity is important to sustain melanogenesis, it impairs mitochondria lately, shifting the metabolism towards glycolysis. This recovery phase is accompanied by activation of the NRF2 detoxication pathway. Finally, we show that inhibitors of lipid metabolism can resolve hyperpigmentary conditions in a guinea pig UV-tanning model. Our study reveals rewiring of the metabolic circuit during melanogenesis, and fatty acid metabolism as a potential therapeutic target in a variety of cutaneous diseases manifesting hyperpigmentary phenotype.

Introduction

Despite significant progress in understanding the physiology and biochemistry of human skin pigmentation, the strategies to manipulate this phenomenon for clinical benefit has met with

Further, the authors declare that all other data supporting the findings of this study are available within the paper and Source Data files.

Funding: R.S.G. acknowledges support from J.C. Bose fellowship and Department of Biotechnology (DBT) for providing funds to National Institute of Immunology (SB/S2/JCB-038/2015). R.S.G., T.N. V. & C.G. acknowledge the support of Council for Scientific and Industrial Research (CSIR) project TOUCH (BSC0302). R.K.M. acknowledges support of Department of Biotechnology/Wellcome Trust India Alliance Intermediate Fellowship (IA/19/2/504651). F.S. acknowledges UGC JRF/SRF fellowship. D.M. and K.S.A. were CSIR JRF/SRF Fellows. M.K. was supported by funds from SERB project. P.K., P.D. & A.A. are recipients of the CSIR JRF/SRF fellowship. The funders had no role in study design, data collection and analysis, decision to publish, or preparation of the manuscript.

Competing interests: I have read the journal's policy and the authors of this manuscript have the following competing interests: R.S.G. is a Co-founder of Vyome Biosciences Pvt. Ltd., a biopharmaceutical company working in the Dermatology area. Part of the study is patented under the Indian Patent Act. CSIR-IGIB and NII jointly applied for the patent titled "Compositions having application against hyper-pigmentation". Inventors are listed as Farina Sultan, Manisha Kochar, Rashmi Sanjay Bhosale, Vivek T. Natarajan and Rajesh S. Gokhale. Indian Patent Application No. 202011047316. Filing Date: 29.10.2020. Other authors do not have any conflict of interest.

Abbreviations: BCA, bichinchonic acid; BSA, bovine serum albumin; BMRB, Biological Magnetic Resonance Bank; CIP, calf intestinal phosphatase; DAG, diacylglycerol; DEG, differentially expressed gene; ER, endoplasmic reticulum; ETC, electron transport chain; HBP, hexosamine biosynthesis pathway; HMDB, Human Metabolome Database; HSL, hormone-sensitive lipase; LRT, likelihood-ratio test; MC1R, melanocortin 1 receptor; MiNA, Mitochondrial Network Analysis; NMR, nuclear magnetic resonance; O-GlcNAc, O-linked β -N-acetylglucosamine; PCA, principal component analysis; PDH, pyruvate dehydrogenase; PDK1, pyruvate dehydrogenase kinase; PPP, pentose phosphate pathway; PTU, 1-phenyl-2-thiourea; qRT-PCR, quantitative real-time polymerase chain reaction; ROS, reactive oxygen species; siRNA, small interfering RNA; TAG, triacylglycerol; TCA, tricarboxylic acid cycle; TEM, transmission electron microscopy; TF, transcription factor; TG, target gene; UDP-GlcNAc, uridine diphosphate- β -N-acetylglucosamine; VST, variance-stabilizing transformation; 25-HC, 25-hydroxycholesterol.

minimal success. To counter the deleterious effects of UV radiations, human skin activates melanisation that protects skin from cancer and photoaging [1]. On the other hand, pathological hyperpigmentation response of skin occurs due to inflammatory conditions [2]. Patchy cutaneous hyperpigmentation is an associated comorbidity in more than 30% of patients with diabetes and obesity [3]. Skin pigmentation is due to the presence of melanocyte cells in the epidermis, which possesses biosynthetic machinery to produce melanin within melanosomes [4]. These specialized membrane-bound organelles are then transferred to neighbouring keratinocytes imparting photoprotection [5,6]. Melanogenesis thus can be considered to be a conglomeration of many interacting components wherein individual components, as well as the interaction networks, manifest spatiotemporal coherence. Perturbations within any of these events result in homeostatic imbalance leading to a disease phenotype. The challenge is to elucidate dynamic temporal interactions between constituent molecules of various cellular processes.

MITF, the central transcription regulator of melanocyte lineage, connect array of gene networks pertaining to melanogenesis, proliferation, and survival [7]. MITF regulates the expression of numerous pigmentation-associated genes such as PMEL17 and MART1 and melanin synthesis enzymes TYR, DCT, and TYRP1 to promote melanocyte differentiation [8–10]. UV-mediated activation of pigmentation proceeds through secretion of α -MSH by keratinocytes, which binds to epidermal melanocytes receptor, the melanocortin 1 receptor (MC1R), triggering cAMP production and CREB-mediated MITF transcription [11–13]. Further, coactivators like SOX10 activate MITF, while suppressors like TCF4 and ATF4 down-regulate MITF transcriptional response [14–16]. Melanocytes thus possess the ability to respond to environmental signals and assume a wide variety of distinct functional fates. These specialized cells of the epidermis return to a resting state, where they are known to persist, potentially prepared for another round of activation. These distinct phases of melanocytes can be anticipated to be dependent on dynamic changes in cellular metabolism to cater cellular energy demands and biomolecule requirements.

Several lines of evidence suggest the alteration of mitochondrial function during melanogenesis, some of which are rather paradoxical. For example, induction of melanin synthesis in B16F10 melanoma cells reduces the oxygen consumption after 48 hours of stimulation, without changes in mitochondrial membrane potential [17]. However, mitochondrial mass is reported to be higher in cells with melanogenesis stimulation [17]. A fraction of these mitochondria is shown to be in direct contact with melanosomes, where the interorganelle connections mediated by fibrillar bridges are proposed to facilitate the exchange of small molecules between the 2 organelles [18]. Remodelling mitochondria towards increased fission enhances reactive oxygen species (ROS) levels that can have contradictory effect on melanogenesis [19,20]. While targeting F_1F_0 -ATP synthase that should also result in ROS accumulation, induces hyperpigmentation [21]. In a recent study, untargeted metabolomics of α -MSH-induced B16F10 cells analysed at 1, 24, and 48 hours showed minimal changes in the metabolite profile, when compared with their respective controls [22]. While it is surprising, a possibility is that the time points used in this study do not capture the dynamics of metabolite concentrations and metabolic fluxes. Another distinct possibility is the heterogeneity within cellular populations and cell surface receptors, which could obscure the interpretation of the results. Cellular heterogeneity has been reported for primary melanocyte cultures, where the cells could be transiting between precursor cells and their descendants at different stages of pigmentation [23]. For the identification of transient regulatory events during melanogenesis, it is pertinent to resolve melanocyte function over time in a synchronized model system that can capture a full array of events.

As metabolic reprogramming is emerging as a hallmark of cellular effector functions, it is important to leverage metabolic dependencies as a possible target for modulating skin pigmentation. In this study, we have employed a previously developed B16 cell-autonomous pigmentation model where cells transit from basal depigmented to the pigmented state over a period of 6 days [24]. Transcriptomic and metabolomic studies allowed us to identify dynamically changing key transcriptional network modules and corresponding metabolic configuration in a time-dependent manner. Along with defining a framework for understanding melanogenesis programming, our studies identify the transient, yet the key role of SREBF1-mediated fatty acid metabolism during the melanogenic phase. Based on the guinea pig tanning model, we show that inhibitors of fatty acid metabolism can resolve hyperpigmentary conditions, thus revealing new targets for modulating skin pigmentation.

Results

Melanogenesis is coupled to transcriptional activation of metabolic genes

To understand the differentiation programming of melanocytes from depigmented to pigmented state, we perform a global transcriptomic analysis of B16 cell-autonomous pigmentation model [24]. B16 pigmentation model is a density-dependent model, wherein cells are seeded at a very low density of 100 cells/cm² and transition from basal depigmented to the pigmented state of cells occurs over a period of 6 days as shown in the schematic (Fig 1A). In this model, melanogenesis is probably triggered by the fine balance between the intrinsic needs of the cells and the constraints imposed by the extrinsic conditions. A series of coordinated processes encompassing transcriptional activation, melanosome biogenesis and melanin synthesis can be captured at the phenotypic and molecular level. The phenotypic changes in the melanin are best observed and quantitated from days 3 to 6 (Fig 1A) [25]. At the molecular level, we observe a higher MITF protein expression on days 3 and 4. The classical MITF-mediated pigmentation targets show different trajectories of expressions during this period. PMEL17, a marker of early-stage melanosomes, is found to peak around days 4 and 5, indicating new melanosomes formation as an early event that diminishes by day 6. This is followed by increased expression of tyrosinase, the rate-limiting enzyme in melanin synthesis, on days 5 and 6 (Fig 1B and 1C).

To study temporal events during melanogenesis, genome-wide transcriptome analysis was performed from days 3 to 6. Principal component analysis (PCA) of the transcriptome data showed separation of different samples on the major PC axis (PC1) (S1A Fig). The correlation coefficient “r” between the biological replicates of the same sample were in the range of 0.98 to 0.99 (S1B Fig), suggesting overall high concordance between the 2 replicates. Time-course analysis was performed using the LRT (likelihood-ratio test), and genes with adjusted *p*-value < 0.001 were taken as significant differentially expressed genes (DEGs) from days 3 to 6 using DESeq2. Heatmap was plotted for these 1,493 DEGs obtained in time-course analysis (Fig 1D). As expected, several key pigmentation-related genes like *Mitf*, *Pmel*, and *Tyr* could be observed among the DEGs. Hierarchical clustering was performed on the expression data of 1,493 DEGs, and the data were divided into 7 clusters. In general, genes on days 3 and 4 show substantially similar gene expression values as compared to days 5 and 6. Pathway enrichment analysis using the KEGG database, illustrated as Bubble Plot (Fig 1E), for these gene clusters revealed pathways like RNA transport, ribosome biogenesis, and spliceosome enriched on days 3 and 4, indicative of transcriptional activation during early pigmentation phases. Day 5 showed up-regulation of metabolic pathways like steroid biosynthesis, unsaturated fatty acid synthesis, and fatty acid metabolism. Enrichment of fatty acid metabolism

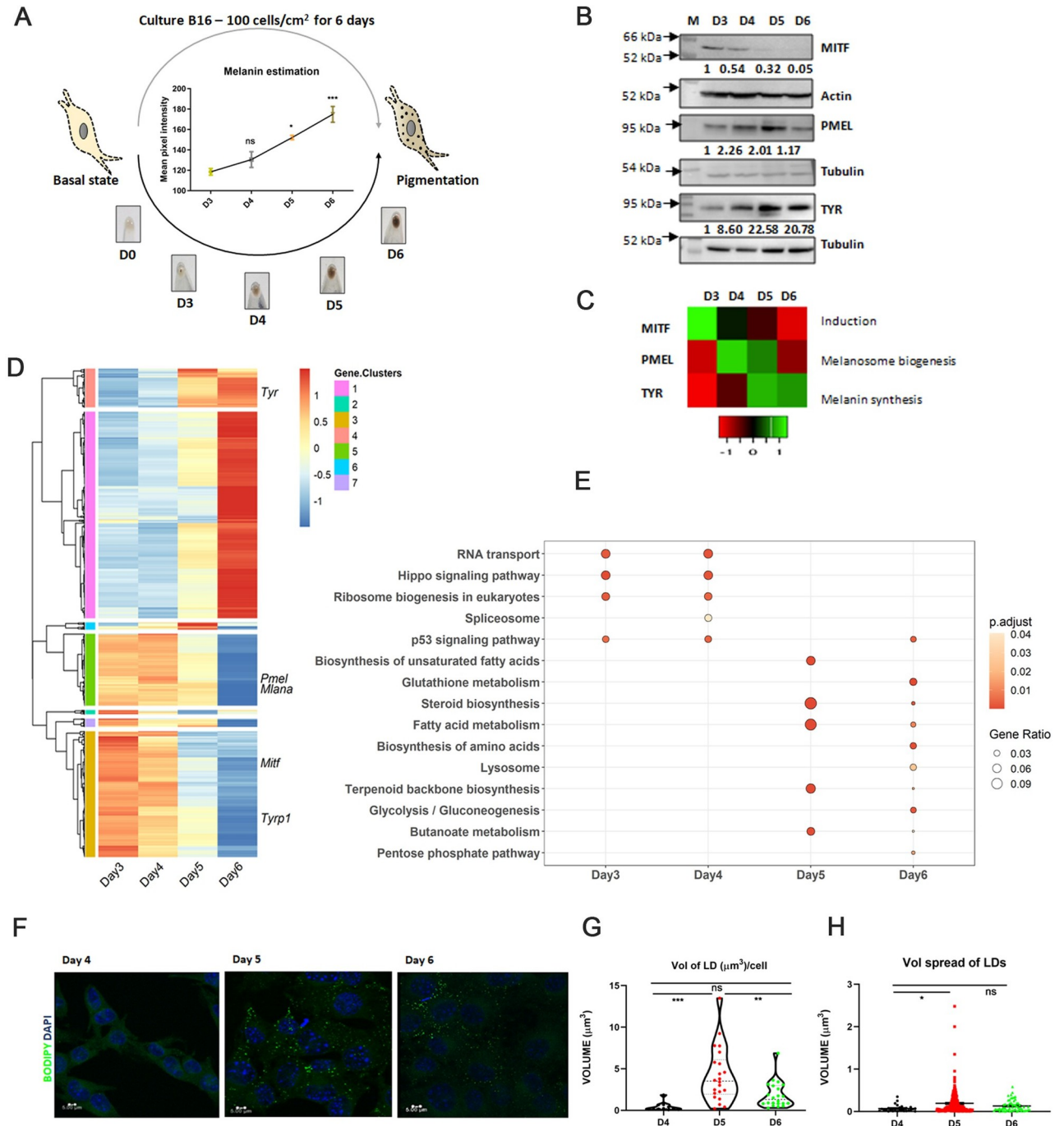


Fig 1. Melanogenesis is coupled to transcriptional activation of metabolic genes. (A) Schematic diagram illustrating the assay setup where culturing B16 cells at low density of 100 cells/cm² (Top) results in the transition of melanocyte from depigmented (day 0) to pigmented state (day 6) as shown in the pellet images (N = 3) (Bottom). Quantitative analysis of melanin intensity of the pellets is shown in the line graph (Between). Mean ± SEM is plotted for 3 biological replicates. One-way ANOVA is applied, F(3,8) = 18.28. p-Value = 0.0006. Turkey's test is performed for pairwise comparison. (B) Representative western blot of key pigmentation proteins, MITF, PMEL, TYR, and DCT on days 3 to 6 (D3 to D6) (N = 3). Arrows mark the sizes of molecular weight markers written in kDa. Numerical values show average fold change for 3 biological replicates. (C) Heatmap depicting relative mean expression levels of pigmentation proteins wrt D3 for 3 independent experiments. Scale from red to green represents the z-scores of fold change (below). (D) Heatmap represents 1,493 DEGs with an adjusted p-value < 0.001 obtained from time-course analysis performed using the LRT test for 2 independent biological replicates. Scale from blue to red represents z-score from -1 to +1. Hierarchical clustering was performed on the expression data of 1,493 DEGs into 7 clusters. (E) KEGG pathway enrichment analysis was done for DEGs with adjusted p-value < 0.001 up-regulated on days 3, 4, 5, and 6. Bubble plot depicts the enrichment of pathways on different days, where the size of bubble represents the gene ratio and colour represents the p-value. (F) Representative confocal microscopy images show lipid droplet accumulation in B16 cells during pigmentation. Images were taken at

63×. Scale is 5 μm. (G) Violin plot depicting the quantitation of total volume of lipid droplets per cell using VOLOCITY software. Approximately 25 to 30 cells are taken in each replicate. Mean ± SEM is plotted in 3 independent biological replicates. One-way ANOVA is applied, $F(2,52) = 11.45$. p -Value < 0.0001. Turkey's test is performed for pairwise comparison. *** p -Value = 0.0001, ** p -value = 0.034. ns is not significant. (H) Dot plot depicting the quantitation of size of individual lipid droplets (as volume spread of lipid droplets) using VOLOCITY software. Approximately 25 to 30 cells are taken in each replicate. Mean ± SEM is plotted in 3 independent biological replicates. One-way ANOVA is applied, $F(2,262) = 3.54$. p -Value = 0.0303. Turkey's test is performed for pairwise comparison. Quantitative data are provided in [S1 Data](#) for Panels A, C, G, and H. Quantitative data for Panels D and E are provided in [S3 Data](#). DEG, differentially expressed gene; LRT, likelihood-ratio test.

<https://doi.org/10.1371/journal.pbio.3001634.g001>

along with the up-regulation of glycolysis and glutathione metabolism could be noted on day 6.

An important facet of lipid metabolism is the assimilation of free fatty acids in the form of neutral lipids (triacylglycerols (TAGs)) within lipid droplets, which are otherwise toxic to cells. We analysed the expression of fatty acid synthesis genes and TAG synthesis genes from RNA sequencing data ([S1C and S1D Fig](#)). Analysis showed a concordant increased expression of several of the genes in both fatty acid and TAG synthesis pathways with pigmentation. This may result in increased lipid droplets formation during pigmentation. We, therefore, traced lipid droplets during pigmentation using BODIPY dye ([Fig 1F](#)). Quantitative analysis of the volume of lipid droplets per cell and volume of individual lipid droplets revealed the formation of these lipid aggregates significantly increases on D5 ([Fig 1G and 1H](#)). Further, a significant and rapid depletion in the volume of lipid droplets per cell was observed on D6. These results suggest that B16 cells assimilate and utilise fatty acids synthesized by cells as lipid droplets.

To demonstrate that these metabolic changes are a consequence of pigmentation, we treated the B16 cells grown at low density with 1-phenyl-2-thiourea (PTU), which inhibits the formation of melanin pigment. PTU-treated cells show depigmented phenotype and, in fact, exhibit enhanced proliferation, when compared with pigmented day 6 cells ([S1E and S1F Fig](#)). Examination of FASN in PTU-treated cells showed a significant decrease in protein expression, contrary to the increase observed for pigmenting B16 cells ([S1G–S1J Fig](#)). These studies provide credence to the hypothesis that the synchronized modulation of metabolic pathways identified during transcriptome studies is associated with cellular pigmentation.

Differential transcriptionally regulated metabolic networks emerge at different stages of melanogenesis

To identify prominent transcriptional networks on days 3 to 6, we performed transcription factor (TF) enrichment analysis for differentially regulated genes using the TRRUST database. We constructed TF-target gene (TG) network maps for the top 7 TFs identified on each day. This was overlaid with transcript expression changes observed for the TGs ([Fig 2](#)). Such a temporal representation of the TF-TG network maps revealed an interesting insight into the transcriptional programming during the course of pigmentation. On day 3, pigmentation regulators *Mitf* and *Egr1* networks are functional, both of which are known to induce pigmentation response in melanocytes [26,27]. Another melanogenesis-associated gene *Tcf4* could also be noted in the days 3 and 4 regulons, which is known to suppress *Mitf* levels [15]. The expression of *Myc* network, which is involved in proliferation [28], decreases with each day and this is congruent with our experimental observations. On day 5, completely new sets of TF-TG networks emerge, prominent of them are the *Sreb1* and *Sreb2* clusters, which are known to regulate lipid metabolism across different cell types [29]. Another significant cluster that becomes evident is the *Nfe2l2* (*Nrf2*) regulon. This TF is involved in the phase II detoxification pathway, and previous studies have shown that melanocytes resist oxidative detoxification through a robust expression of this pathway during pigmentation [30]. While the transcriptional analysis provides interesting insights into the temporal regulation of TF-TG

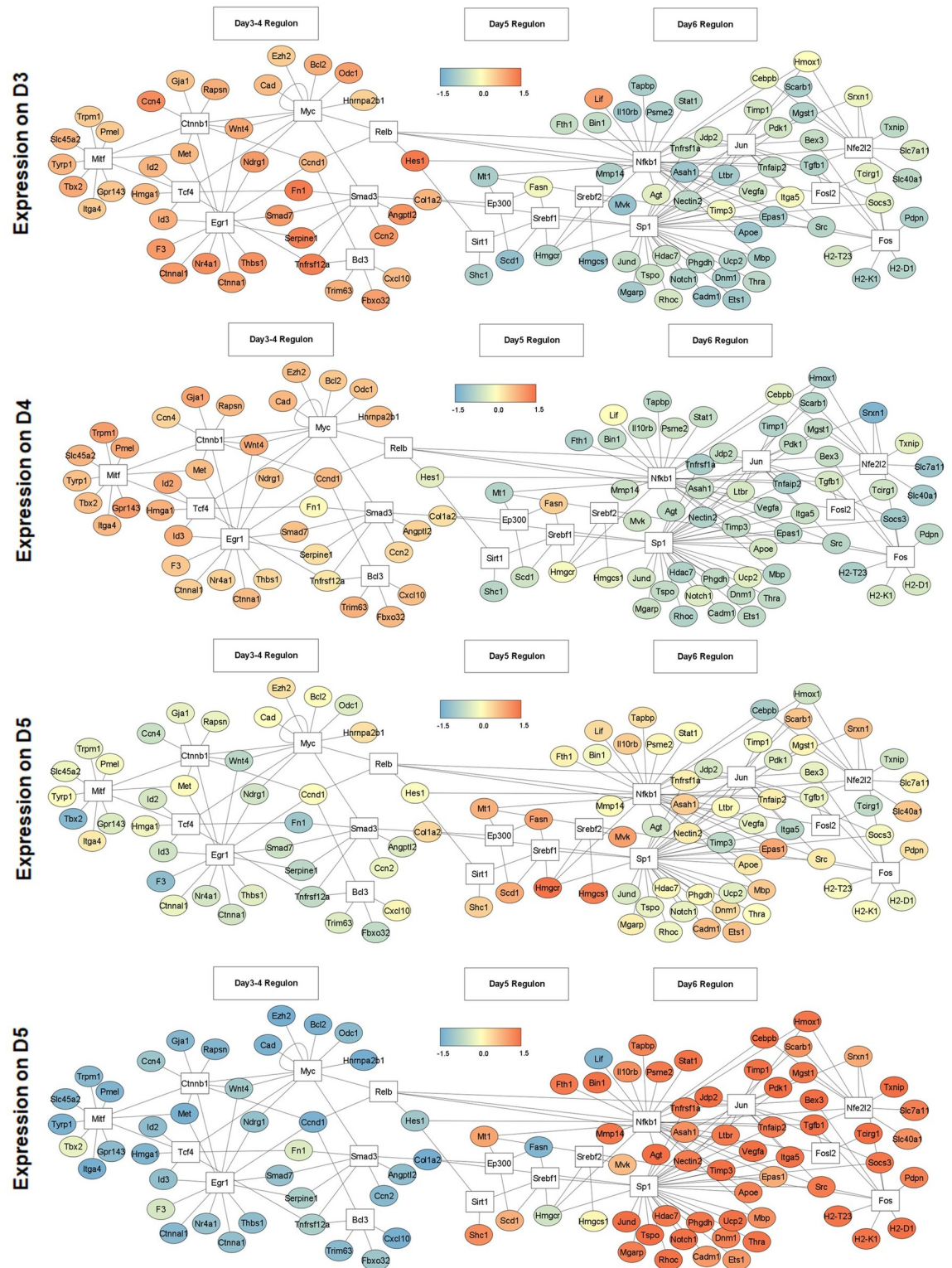


Fig 2. Transcriptionally regulated metabolic networks map for different stages of melanogenesis. DEGs were analysed for the TG enrichment of TF using the TRRUST database on metacscape (metacscape.org). TF-TG network analysis shows top 7 up-regulated TFs obtained in DEGs analysis on days 3 to 6, along with the expression profile of their TGs. TFs are enclosed in white box and the lines connect each TF to the set of genes regulated by them during pigmentation. TGs are enclosed in circle and colour gradient represents the scaled (row-wise) expression values from the RNA Seq data. Quantitative data are provided in [S3 Data](#). DEG, differentially expressed gene; TF, transcription factor; TG, target gene.

<https://doi.org/10.1371/journal.pbio.3001634.g002>

networks, we mainly focus on the metabolic programming of these cells during different phases of melanogenesis.

To validate key transcriptional networks that emerged on different days in TF-TG analysis, we analysed mRNA expression of *Mitf*, *Srebf1*, *Nrf2*, and their downstream TGs. Consistent with the TF-TG analysis, *Mitf* showed significant up-regulation on days 3 and 4, (S2A Fig), and *Tyr*, a rate-limiting enzyme in melanin synthesis, showed significantly higher expression on days 5 and 6 (S2B Fig). *Srebf1* emerges as a prominent metabolic network on day 5. *Srebf1* showed maximum up-regulation on day 5, followed by day 6 at mRNA level (S2C Fig). This is congruent with the observed induction up to 1.5- to 2-fold for key fatty acid synthesis genes, *Fasn*, *Acaca*, *Acacb*, and *Acy* on days 5 and 6, as analysed by quantitative real-time polymerase chain reaction (qRT-PCR) (S2D Fig). Another important network that emerged on day 6 is *Nrf2*. Examination of mRNA expression of *Nrf2* and its TGs, *Gsr* and *Gst*, showed a consistent up-regulation on day 6 (S2E and S2F Fig). Together, TF-TG analysis delineates diverse transcriptional networks regulating metabolism, mediating an important role during the transition from depigmented to pigmented state.

Steady-state analysis of polar metabolites using mass spectrometry during pigmentation

To understand how metabolic changes are linked with the process of melanogenesis, we measured the levels of polar metabolites from days 3 to 6 cells using liquid chromatography-coupled tandem mass spectrometry. A total of 306 peaks were obtained, out of which 175 were mapped to different metabolites with high confidence. The relatedness between all the data sets was compared using PCA. All replicates showed good clustering and clear day-wise segregation was observed (S3A Fig). Hierarchical clustering analysis based on the top 50 regulated metabolites showed an increased level of metabolites corresponding to nucleotide and amino acid metabolism during days 3 and 4. On days 5 and 6, a substantial number of cofactors and Krebs's cycle metabolites were seen to be up-regulated (S3B Fig). To understand the pathway-based connectivity, we overlaid the data on 4 major central carbon metabolic pathways—glycolysis, tricarboxylic acid cycle (TCA), pentose phosphate pathway (PPP), and hexosamine biosynthesis pathway (HBP) (Fig 3A). Analysis of glycolytic intermediates showed 2 distinct patterns of regulation. Metabolites in the upper half of the glycolysis (6-carbon metabolites) showed limited variations across all 4 days. The upper half of glycolysis is known to branch into the PPP and HBP. Indeed, analysis of metabolites from PPP and HBP indicated an increased accumulation on days 5 and 6. PPP generates NADPH to maintain a redox environment and provides intermediates for fatty acid and nucleotide synthesis. HBP forms uridine diphosphate- β -N-acetylglucosamine (UDP-GlcNAc) moiety required for O-linked β -N-acetylglucosamine (O-GlcNAc) posttranslational modification of melanogenic proteins [31,32]. The metabolites in the lower half of glycolysis (3-carbon metabolites) increased approximately 4-fold during the pigmentation phase. The lower half of the glycolysis produces lactate and feeds into the TCA cycle. Interestingly, the levels of both lactate and TCA metabolites show an increase with time. Melanogenesis trigger augments distribution of glucose into all the branches of central carbon metabolism during pigmentation, providing necessary metabolic pools, probably required for melanosome formation and maturation within melanocytes. Furthermore, increased HBP and PPP metabolic pathways suggest a supporting role for the synthesis of a variety of biomolecules.

[U-¹³C]-Palmitate incorporation in TCA metabolites during pigmentation phase

To understand how the glucose uptake during the pigmentation phase (days 5 and 6) is quantitatively apportioned between the lactate and TCA metabolites, we performed stable isotope

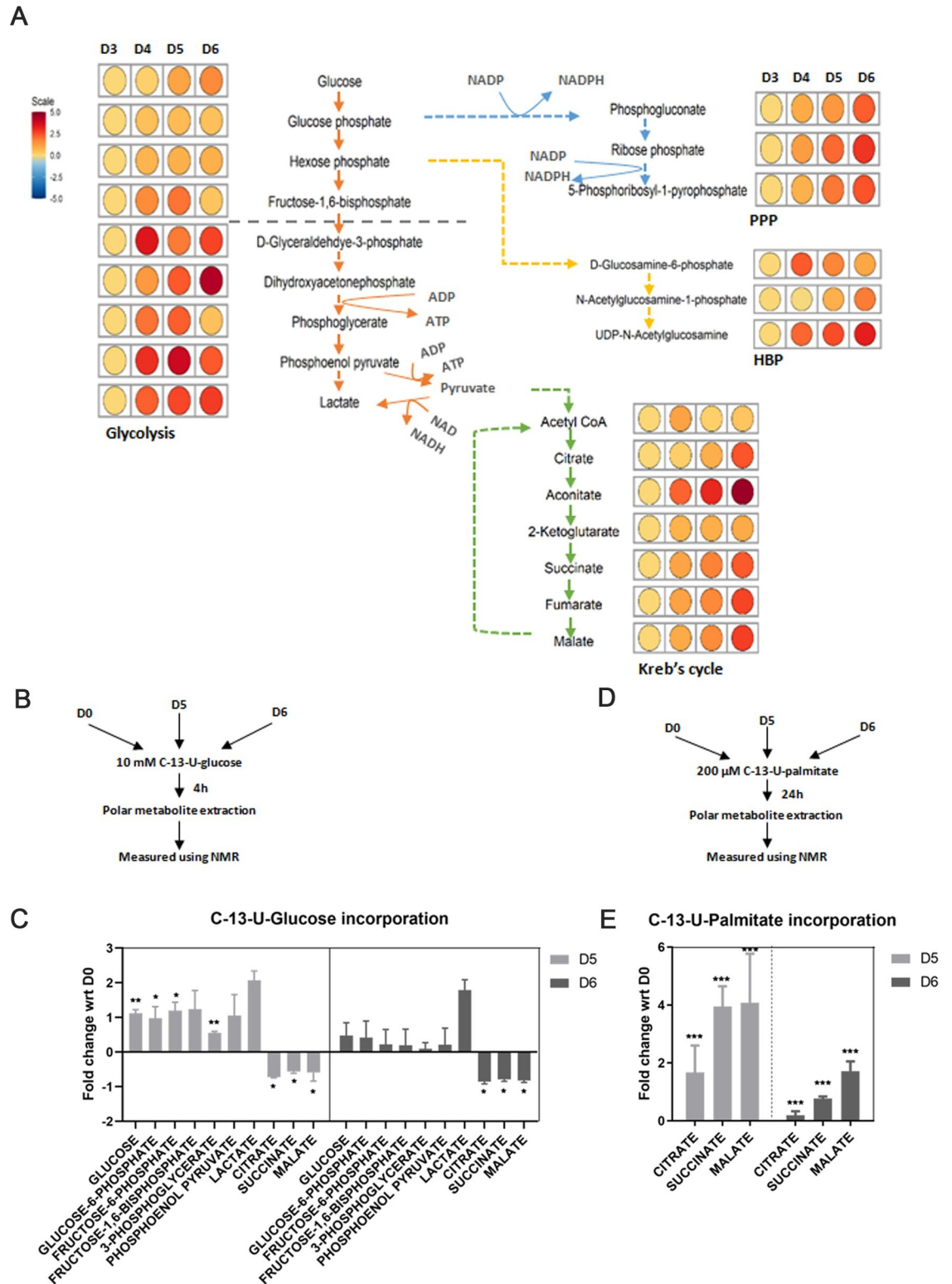


Fig 3. Partial uncoupling of glycolysis and TCA supports biosynthesis pathways (PPP, HBP) while FAO increases to sustain TCA. (A) Liquid chromatography-coupled tandem mass spectrometry-based metabolomic analysis is performed for polar metabolites extracted from D3 to D6 for 4 independent replicates. Metabolic network is drawn for glycolysis, Kreb's cycle, PPP, and HBP by comparing their metabolite levels across D3 to D6. Fold changes are plotted as heatmaps along each metabolite in the pathway with respect to D3. Scale bar ranges from blue to red corresponding to metabolite change from -5 to +5 fold. (B) Schematic

depicting study design for pulse-chase labelling of uniformly ^{13}C labeled glucose in glycolysis and TCA metabolites at D0, D5, and D6 using NMR. (C) NMR-based quantitation of $[\text{U-}^{13}\text{C}]$ -glucose incorporation in glycolysis and TCA metabolites at D5 and D6 with respect to D0. Mean \pm SEM is plotted for 3 independent replicates. Two-way ANOVA is applied, time factor, $F(1.667,33.33) = 33.95$, p -value < 0.0001 . Dunnett's test is performed for pairwise analysis. *** p -Value < 0.005 , ** p -value < 0.01 , * p -value < 0.05 . ns is not significant. (D) Schematic depicting study design for pulse-chase labelling of uniformly ^{13}C labeled palmitate in TCA metabolites at D5 and D6 with respect to D0 using NMR. (E) NMR-based quantitation of $[\text{U-}^{13}\text{C}]$ -palmitate incorporation in TCA metabolites at D5 and D6. Mean \pm SEM is plotted for 3 independent replicates. Two-way ANOVA is applied, time factor, $F(2,12) = 19.91$, p -value < 0.0002 . Dunnett's test is performed for pairwise analysis. *** p -Value < 0.005 , ** p -value < 0.01 , * p -value < 0.05 . ns is not significant. Quantitative data are provided in [S1 Data](#) for Panels C and E. Quantitative data for Panel A are provided in [S4 Data](#). FAO, fatty acid oxidation; HBP, hexosamine biosynthesis pathway; NMR, nuclear magnetic resonance; PPP, pentose phosphate pathway; TCA, tricarboxylic acid cycle.

<https://doi.org/10.1371/journal.pbio.3001634.g003>

tracing using labelled $[\text{U-}^{13}\text{C}]$ -Glucose. These pulse-labelling experiments were analyzed after 4 hours of addition of 10 mM $[\text{U-}^{13}\text{C}]$ -Glucose in the glucose-free medium ([Fig 3B](#)). The incorporation of ^{13}C isotope in different metabolites was followed by nuclear magnetic resonance (NMR)-based measurements and several metabolites could be identified with high confidence. We observed a 2-fold increase in the ^{13}C labelling of glycolytic metabolites on day 5 when compared with depigmented cells ([Fig 3C](#)). In contrast, the TCA metabolites—citrate, succinate, and malate showed a substantial decrease in the ^{13}C incorporation. This configuration of increased glycolytic metabolites and decrease in TCA metabolites is also observed for day 6, suggesting that the pigmentation phase is associated with decreased channelisation of pyruvate to acetyl CoA. Interestingly, incorporation of ^{13}C labelling on day 6 in glycolytic metabolites is lower than day 5, while relatively little variation is observed for TCA metabolites and lactate levels. This suggested an increased uncoupling of glycolysis and TCA. The enhancement in glycolytic flux on days 5 and 6 is majorly contributed by increased utilization of glucose from media ([S3C Fig](#)).

Earlier studies have shown the role of pyruvate dehydrogenase kinase (PDK1) in reducing the activity of pyruvate dehydrogenase (PDH), which is responsible for converting pyruvate to acetyl-CoA [[33,34](#)]. We observed increased expression of *Pdk1* during the late phase of pigmentation, which substantiates the quantitative increase in the level of lactate formed at day 6 ([S3D–S3F Fig](#)). Overall, this indicates the uncoupling of glycolysis and TCA in the late recovery phase of pigmentation. Incidentally, steady-state analysis had suggested an increase in the accumulation of TCA metabolites during day 6. We, therefore, reasoned that other pathways may be directly feeding into TCA metabolites.

Since up-regulation of fatty acid synthesis and metabolism was observed in transcriptional analysis, we evaluated the role of fatty acid oxidation in generating acetyl-CoA pools by following incorporation of $[\text{U-}^{13}\text{C}]$ -Palmitate into TCA metabolites during the pigmentation phase ([Fig 3D](#)). NMR measurements of ^{13}C label revealed a more than 2-fold increase in the incorporation on day 5 when compared with depigmented cells ([Fig 3E](#)). A subsequent decrease was observed on day 6, suggesting a restricted requirement of oxidative phosphorylation in maintaining the energy demands of the cells in the late phase of pigmentation. Such a dynamical metabolic adaptation during the pigmentation phase may be a crucial metabolic switch that shunts fatty acids to mitochondria to maintain ATP production and sustain PPP via glycolytic shunting to keep a balance between available nutrients and energy.

Fatty acid availability increases mitochondrial respiration during pigmentation

To determine how cellular bioenergetics is affected by the availability of carbon source, we measured oxygen consumption rate in either glucose- or oleate-supplemented media using the Seahorse Mito Stress Test assay ([Fig 4A](#)). We observed that the basal respiration rate, which

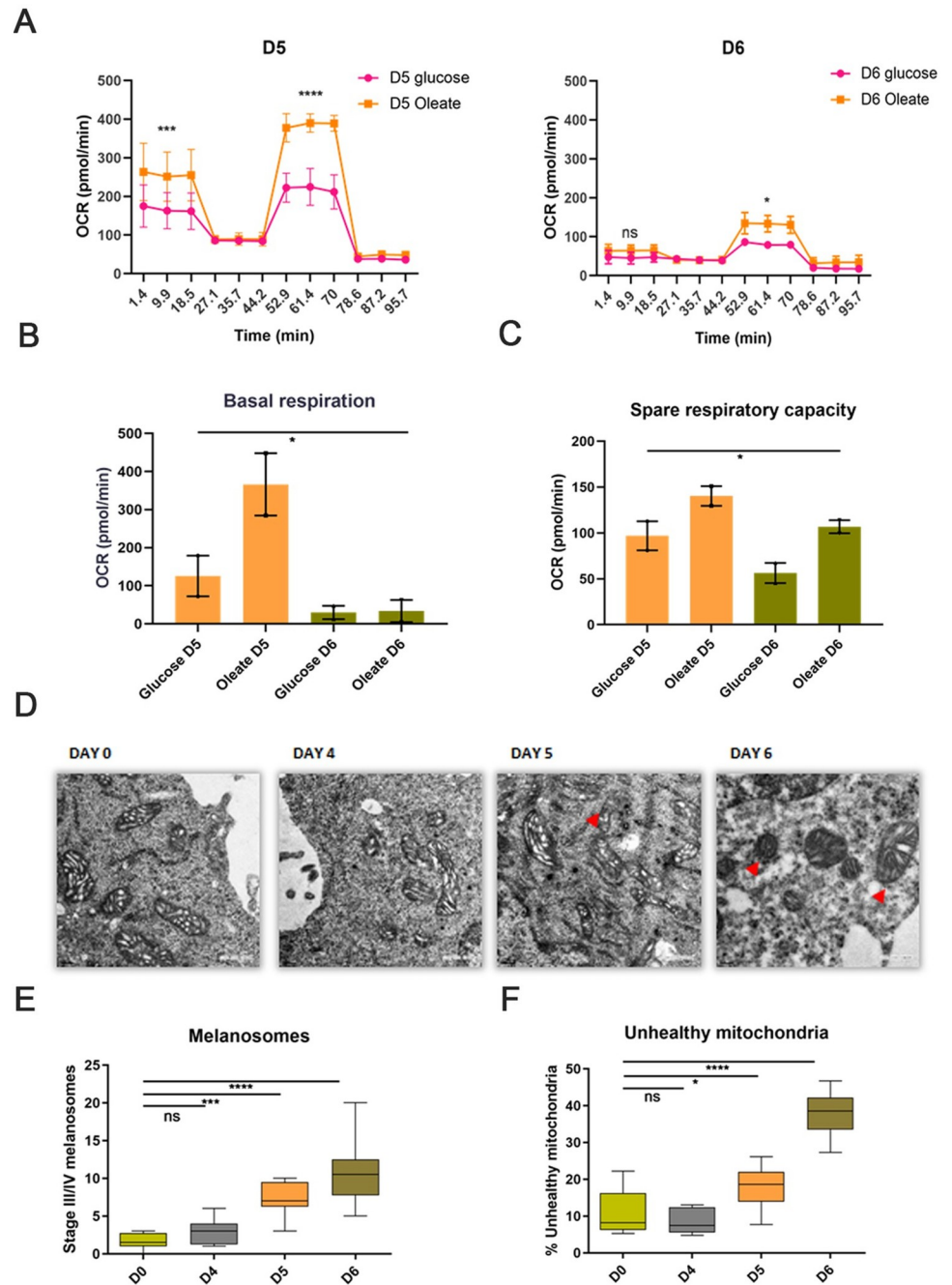


Fig 4. Fatty acids are preferred carbon source for mitochondrial respiration during pigmentation. (A) Comparative analysis of oxygen consumption rate in glucose or fatty acid supplemented media on D5 and D6 using Seahorse Mito Stress Test assay. Represented plot depicts Mean \pm SEM for 2 independent biological replicates with 3 technical replicates in each set. Two-way ANOVA is applied. Sidak's multiple comparison test is performed for pairwise analysis. *p*-Value. *****p*-value < 0.001, ****p*-value < 0.005, ***p*-value < 0.01, **p*-value < 0.05. ns is not significant. (B) Quantitative analysis of basal respiration in glucose or fatty acid supplemented media on D5 and D6. Mean \pm SEM is plotted for 2 biological replicates with 3 technical replicates for each set. One-way ANOVA is applied F (3,4) = 9.337, *p*-value = 0.028. (C) Quantitative analysis of spare respiratory capacity in glucose or fatty acid supplemented media on D5 and D6. Mean \pm SEM is plotted for 2 biological replicates with 3 technical replicates for each set. One-way ANOVA is applied F (3,4) = 8.915, *p*-value = 0.0303. (D) Representative TEM-based analysis showing mitochondrial cristae morphology change during pigmentation from D3 to D6 (Number of cells, *n* = 8). Images were taken at 3500 \times magnification. Scale is 0.2 μ m (Bottom left). (E) Box plot depicting quantitative analysis of stage III/IV melanosomes on different days (Number of cells, *n* = 8). Whiskers represent min and max range with

mean as centre line. One-way ANOVA is applied $F(3,28) = 19.60$, p -value < 0.0001 . Tukey's test is performed for pairwise comparison. **** p -Value < 0.0001 , *** p -value = 0.007. ns is not significant. (F) Box plot depicting quantitative analysis of unhealthy mitochondria on different days (Number of cells, $n = 8$). Whiskers represent min and max range with mean as centre line. One-way ANOVA is applied $F(3,28) = 47.08$, p -value < 0.0001 . Tukey's test is performed for pairwise comparison. **** p -Value < 0.0001 , * p -value = 0.027. ns is not significant. Quantitative data are provided in S1 Data for Panels A, B, C, E, and F. TEM, transmission electron microscopy.

<https://doi.org/10.1371/journal.pbio.3001634.g004>

accounts for total oxygen consumption by the cells, is higher on day 5 than on day 6 (Fig 4B). However, in the presence of oleate, cells show higher basal respiration on day 5 in comparison to glucose. Availability of oleate in the media also results in higher spare respiration capacity of

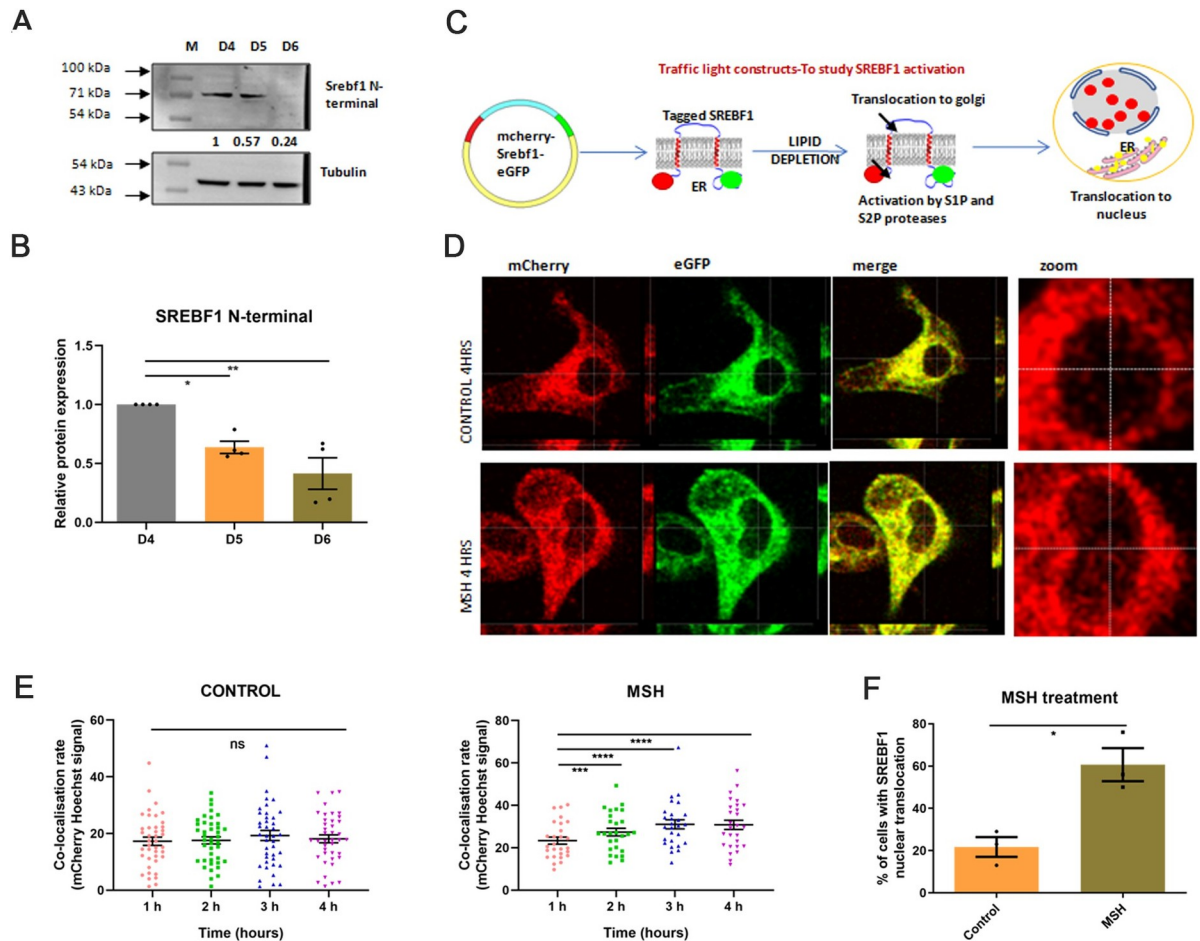


Fig 5. Melanogenesis induction causes activation of SREBF1. (A) Representative western blot showing SREBF1 N-terminal levels on different days of pigmentation, normalized to tubulin ($N = 4$). Numerical values show average fold change for 4 biological replicates. (B) Bar graph depicting quantitative fold change of SREBF1 N-terminal expression with respect to D4. Mean \pm SEM is plotted for 4 biological replicates. One-way ANOVA is applied, $F(2,9) = 12.71$, p -value = 0.0024. (C) Schematic design for studying SREBF1 activation using traffic light mCherry-SREBF1-eGFP vector and analyzing localization in different cellular compartments. Full-length protein localized in ER and gives yellow signal due to colocalization of mCherry and eGFP fluorescence. Cleaved SREBF1 N-terminal is transported to the nucleus along with mCherry tag, thus, accumulation of mCherry signal in the nucleus is indicative of SREBF1 activation. (D) Representative fluorescence images showing mCherry, eGFP, and merge signal. Magnified nuclear images were shown to focus on SREBF1 nuclear translocation after 4 hours of MSH treatment. DMSO is taken as vehicle control. (E) Dot plot depicts colocalization rate between mCherry and Hoechst signal analyzed for each cell at 1 to 4 hours, for control and MSH treatment. Around 20 to 30 cells were analyzed in each of the 3 biological replicates. One-way ANOVA is applied. For DMSO, $F(2,512,99.63) = 0.9264$, p -value = 0.4175, for MSH $F(2,668,39.36) = 15.14$, p -value < 0.0001 . Dunnett's multiple comparison test is performed for pairwise analysis. **** p -Value < 0.0001 , *** p -value < 0.0009 . ns is nonsignificant. (F) Bar graph depicting the quantitation of number of cells showing positive phenotype after MSH treatment, determined by increased colocalization rate of mCherry and Hoechst signal from 1 to 4 hours. Mean \pm SEM is plotted for combined analysis. Two-tailed Student t test is performed, $t = 4.267$, $df = 4$ p -value = 0.0130. Quantitative data are provided in S1 Data for Panels B, E, and F.

<https://doi.org/10.1371/journal.pbio.3001634.g005>

cells on both days, days 5 and 6 (Fig 4C). This indicates that fatty acids rapidly undergo β -oxidation resulting in increased electron flow through mitochondrial complexes on day 5. Together, these studies provide support to the hypothesis that glucose is partially uncoupled from TCA while fatty acid oxidation is the preferred pathway during the intermediate phase of pigmentation.

In order to understand whether decreased mitochondrial respiration is associated with altered mitochondrial morphology, which is essential to maintain an efficient electron transport chain (ETC) [35], we performed transmission electron microscopy (TEM)-based ultrastructural analysis of mitochondria during melanogenesis (Fig 4D). Our data showed the presence of a few stage III/IV (electron-dense) melanosomes on days 3 and 4, which dramatically increases up to 6 to 8 times on days 5 and 6, respectively (Fig 4E). At the same time, we also observed an increase in the number of unhealthy mitochondria during the late pigmentation phase, as determined by cristae stacking and the presence of vacuoles around mitochondria. The number of unhealthy mitochondria observed is about 40% on day 6, and thus substantially impact mitochondrial respiration (Fig 4F). To determine that the observed mitochondrial changes are attributed to pigmentation and not senescence, we analyze the mitochondrial fragmentation in D6 pigmented cells and PTU-treated D6 depigmented cells using Mitotracker RED dye (S4A Fig). Analysis of individual mitochondria using Image J macro tool for Mitochondrial Network Analysis (MiNA) [36] showed a significantly high round and punctate individual mitochondria in pigmented D6 cells (S4B Fig).

Altogether, from transcriptomic and metabolomics analysis, we propose that melanogenesis can be divided into 3 broad phases—preparatory, melanogenic, and recovery phase. Days 3 and 4 capture the preparatory phase where the MITF-mediated signalling networks are induced and anabolic pathways are activated. Following this, the melanogenic phase on day 5 has heightened pigmentation activity and associated metabolic changes with increased fatty acid utilization. Day 6 profile captures the recovery phase, where pigment inhibitory functions and recovery pathways are up-regulated.

Epidermal melanogenesis mediator α -MSH activates SREBF1

As fatty acid metabolism is important during pigmentation and the SREBF1 network was among the prominently regulated network in TF-TG analysis, we interrogated the role of SREBF1 during melanogenesis. SREBF1 is an endoplasmic reticulum (ER)-resident protein that is activated upon the cleavage and nuclear translocation of its N-terminal domain. To examine SREBF1 activation, we performed western blot analysis with SREBF1 N-terminal antibody (Fig 5A). Quantitation of cleaved SREBF1 N-terminal band showed increased levels on days 4 and 5, which then slowly declined on day 6 (Fig 5B). Next, we explored whether the classical inducer of melanogenesis, α -MSH, could activate SREBF1. To study this, we designed an activation assay for SREBF1 using a “traffic light construct,” wherein the mCherry tag was fused with the N-terminal of SREBF1 and eGFP was fused with C-terminal (S5 Fig). Upon SREBF1 activation, mCherry along with the N-terminal SREBF1 fragment would get translocated to the nucleus while the eGFP remains localized in ER (Fig 5C). Functional validation of this assay was assessed with insulin, which is a known activator of SREBF1 in hepatocytes [37] (S6A Fig). Insulin indeed activated SREBF1 in melanocytes within hours in about 65% of the cells (S6B and S6C Fig). We then carried out live-cell imaging for 4 to 6 hours after α -MSH treatment using confocal microscopy. Representative images show mCherry and eGFP signals in different channels after 4 hours of treatment (Fig 5D). Careful analysis for red signal in the nuclear region shows that the presence of mCherry increases after α -MSH treatment. Time-dependent changes in the colocalization rate of mCherry and Hoechst dye was analyzed after 1

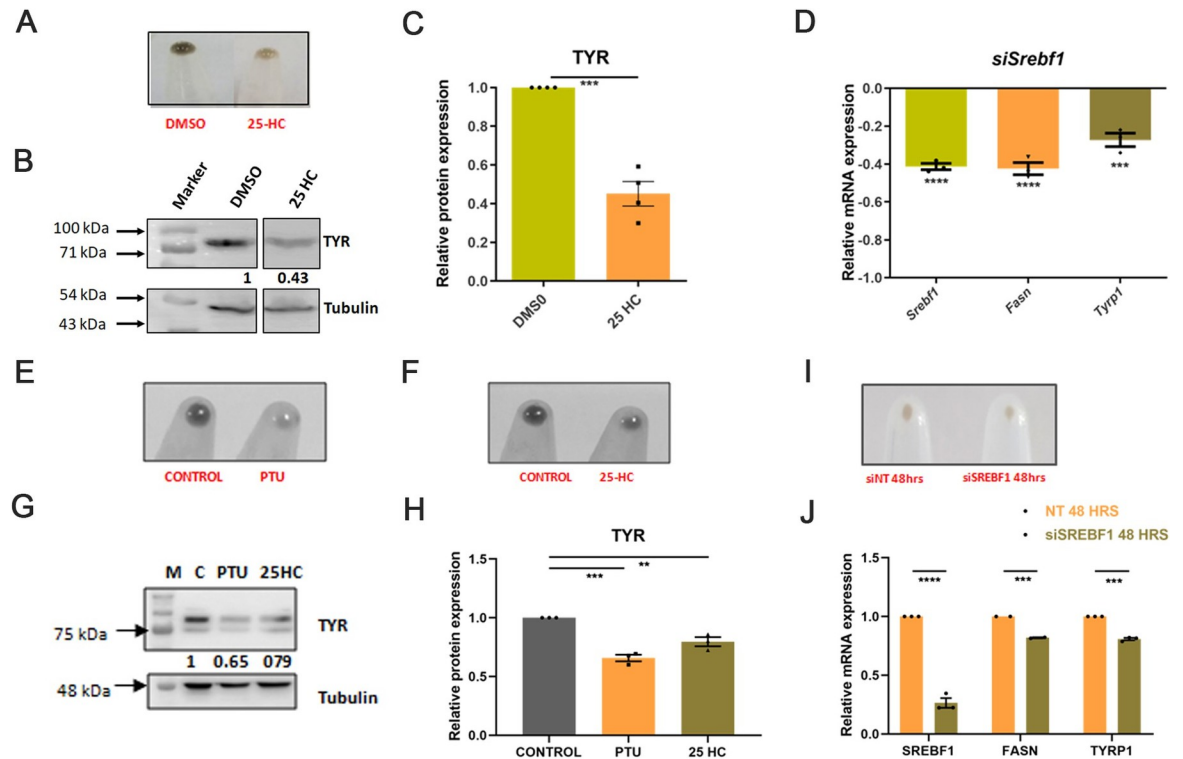


Fig 6. SREBF1 regulates pigmentation by altering fatty acid metabolism. (A) Representative B16 cell pellet images showing the phenotypic difference in melanin accumulation on day 6 upon inhibiting SREBF1 activation with 25-HC treatment. (B) Representative western blot showing TYR protein expression, normalized to tubulin, upon 25-HC treatment ($N = 4$). Numerical values show average fold change for 4 biological replicates. (C) Bar graph depicting quantitative fold change of TYR expression with respect to control. Mean \pm SEM is plotted for 4 independent biological replicates. Two-tailed unpaired t test is performed, $t = 8.663$, $df = 6$. *** p -value = 0.0001. (D) Bar graph representing qRT-PCR-based quantitation of *Srebf1*, *Fasn*, and *Tyrp1* genes on D5 upon silencing of *Srebf1* using smart pool siRNA. Mean \pm SEM is plotted for 3 biological replicates. One-way ANOVA is applied, $F(3,8) = 61.03$, p -value < 0.0001. Tukey's test is performed for pairwise analysis. **** p -Value < 0.001 *** p -value < 0.005, ** p -value < 0.01, * p -value < 0.05. (E) Representative primary melanocytes cell pellet images showing the phenotypic difference in melanin accumulation upon PTU treatment. (F) Representative primary melanocytes cell pellet images showing the phenotypic difference in melanin accumulation upon 25-HC treatment. (G) Representative western blot showing TYR protein expression, normalized to tubulin, upon PTU and 25-HC treatment in primary melanocytes ($N = 3$). Numerical values show average fold change for 3 biological replicates. (H) Bar graph depicting quantitative fold change of TYR expression with respect to control. Mean \pm SEM is plotted for 3 independent biological replicates. One-way ANOVA is applied, $F(2,6) = 37.61$, p -value = 0.0004. Dunnett's multiple comparison test is performed for pairwise analysis. **** p -Value < 0.0003, ** p -value < 0.0038. (I) Representative primary melanocytes cell pellet images showing the phenotypic difference in melanin accumulation upon down-regulating *Srebf1* with siRNA. (J) Bar graph representing qRT-PCR-based quantitation of *Srebf1*, *Fasn*, and *Tyrp1* genes upon down-regulating of *Srebf1* using smart pool siRNA. Mean \pm SEM is plotted for 3 biological replicates. Two-tailed unpaired t test is performed. For *Srebf1* **** p -value < 0.0001, for *Fasn* *** p -value = 0.0006, for *Tyrp1* *** p -value < 0.0001. Quantitative data are provided in S1 Data for Panels C, D, H, and J. PTU, 1-phenyl-2-thiourea; qRT-PCR, quantitative real-time polymerase chain reaction; siRNA, small interfering RNA; 25-HC, 25-hydroxycholesterol.

<https://doi.org/10.1371/journal.pbio.3001634.g006>

to 4 hours to follow kinetic activation (Fig 5E). In control cells (DMSO-treated), the colocalization rate of mCherry and Hoechst dye did not increase in a time-dependent manner, suggesting no activation of SREBF1. For α -MSH, we observed that the colocalization rate of mCherry and Hoechst significantly increases in 2 hours. Further, the number of cells showing positive phenotype considerably increases to 60% after α -MSH treatment (Fig 5F). These data suggest that α -MSH induces nuclear translocation of SREBF1 N-terminal in B16 cells. We thus propose the role of the activation of SREBF1 upon pigmentation induction for ensuring efficient fatty acid synthesis.

SREBF1 regulates pigmentation by altering fatty acid metabolism

After establishing the activation of SREBF1 during pigmentation, we argued whether SREBF1 activation is essential for pigmentation. Towards this, we utilised 25-hydroxycholesterol (25-HC), a pharmacological inhibitor of SREBF1 activation, and evaluated its effect on pigmentation. The inhibitor was added on day 3, and analysis was performed on day 6. Along with the phenotypic change in pigmentation (Fig 6A), quantitative analysis showed a 50% decrease in tyrosinase expression upon 25-HC treatment (Fig 6B and 6C). 25-HC shows broad specificity for both SREBF1 and SREBF2 [38,39]. Thus, we studied the effect of small interfering RNA (siRNA)-based down-regulation of *Srebf1* on pigmentation genes (Fig 6D). Transfections were carried out with Smart pool *Srebf1* siRNA on day 3 and transcriptional changes in pigmentation genes were monitored on day 5. qRT-PCR analysis revealed about 40% to 50% decrease in the *Srebf1* levels (Fig 6D). *Srebf1* down-regulation results in reduced expression of its target *Fasn* on day 5 (Fig 6D). Further, a significant decrease in expression of *Tyrp1* was seen, a gene involved in melanin synthesis, upon *Srebf1* down-regulation (Fig 6D). Next, we examine the effect of PPAR- $\alpha/\beta/\gamma$ involvement in melanogenesis. PPARs inhibitors (GW9662 for PPAR- γ , GW6471 for PPAR- α , and GSK3787 for PPAR- β) did not show significant changes in melanin content (S7A Fig). In our RNA-seq analysis, we could only capture expression for PPAR- α and PPAR- γ , but not PPAR- β . Thus, we performed siRNA-mediated down-regulation of PPAR- α and PPAR- γ during pigmentation. Here also, we could not observe a significant effect on pigmentation genes (S7B and S7C Fig). Thus, *Srebf1* could be the major transcriptional regulator of lipid metabolism during pigmentation in the B16 cells.

To further substantiate the effect of pharmacological inhibitor and siRNA-mediated down-regulation of *Srebf1* on pigmentation, we performed similar studies with pigmented primary human melanocytes. We treated primary human melanocytes with 25-HC and PTU for 96 hours and observed a phenotypic decrease in pigmentation in the pellet images of 25-HC and PTU as compared to control (Fig 6E and 6F). These changes are consistent with molecular changes observed in tyrosinase protein expression (Fig 6G and 6H). Next, we studied the effect of siRNA-based down-regulation of *Srebf1* in primary human melanocytes and observed a phenotypic decrease in pigmentation (Fig 6I). We noticed around 70% to 80% decrease in the *Srebf1* levels along with down-regulation of its TG, *Fasn*. Further, *Srebf1* down-regulation induced a significant decrease in the expression of *Tyrp1*, a gene involved in melanin synthesis (Fig 6J). Despite primary melanocytes being pigmented, modest decrease in the expression of pigmentation genes upon *Srebf1* down-regulation indicates that SREBF1 could be a potential target for regulating melanogenesis.

Fatty acid metabolism is the critical pathway in mediating pigment production

To evaluate the pertinent role of fatty acid metabolism for pigmentation, we performed an inhibitor screen for specific enzymes involved in de novo fatty acid synthesis, TAG synthesis, and lipolysis. We standardised the inhibitor dose using MTT assay and further observed that these standardised doses for different inhibitors do not significantly affect cell count or induce cells death in pigmentating B16 cells (S8A–S8C Fig). B16 cells were treated with FASN inhibitor (C75-20 μM), DGAT inhibitor (T863-10 μM), and lipase inhibitor/FASN inhibitor (Orlistat-50 μM) on day 3 and analysed for pigmentation differences on day 6 (Fig 7A). As expected, C75 and T863 decrease lipid droplet content of the cells on day 5, while Orlistat results in increased accumulation of lipid droplets suggesting that it acts as a lipase inhibitor (S8D Fig). We noted a substantial decrease in the melanin content for all 3 inhibitors, with 60% on Orlistat treatment, 40% on T863 treatment, and 50% on C75 treatment (Fig 7B and

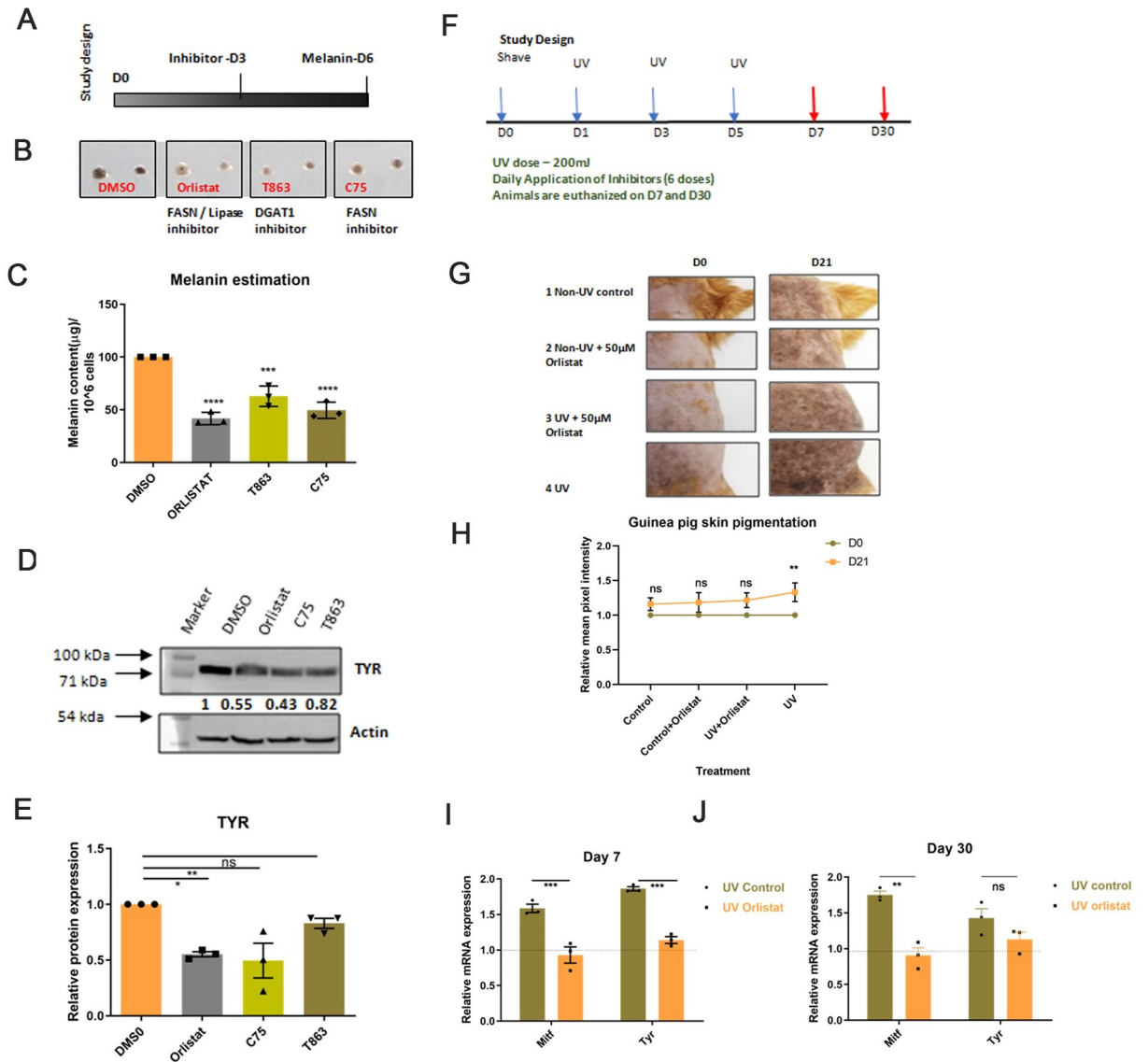


Fig 7. Fatty acid metabolism is a critical pathway in mediating pigment production. (A) Schematic showing experimental timeline for inhibitor addition and analysis of pigmentation in B16 cells. (B) Representative image showing phenotypic differences in melanin accumulation upon inhibitor treatment in 2 technical replicates of D6 cells. Two technical replicates are taken for 3 independent biological sets. (C) Bar graph depicting melanin estimation after different inhibitor treatments. Mean \pm SEM is plotted for 3 biological replicates. One-way ANOVA is applied, $F(3,8) = 43.13$, p -Value < 0.0001 . Dunnett's test for pairwise. (D) Representative western blot for TYR expression, wrt to Actin, on D6 upon Orlistat, C75 and T863 treatment. Numerical values show average fold change for 3 biological replicates. (E) Bar graph depicting quantitative analysis of tyrosinase expression upon Orlistat, C75, and T863 treatment with respect to Actin. Fold change is calculated relative to DMSO. Mean \pm SEM is plotted for 3 independent replicates. One-way ANOVA is applied, $F(3,8) = 8.438$, p -value = 0.0074. Dunnett's multiple comparison test is performed for pairwise analysis. *** p -Value < 0.005 , ** p -value < 0.01 , * p -value < 0.05 . ns is not significant. (F) Experimental timeline showing UV-mediated pigmentation induction in guinea pigs. Three doses of UVA+B were given on days 1, 3, and 5 (shown by the blue arrow). Six doses of inhibitor were applied for the first 6 days. Animals were euthanized on D7 and D30 (shown by the red arrow). (G) Representative photographs showing phenotypic differences in guinea pig skin pigmentation on D0 and D21. Four segments were marked based on different treatments and are followed temporally on the same animals in the groups of 3. Arrows represent the region showing maximum changes. (H) Line plot showing fold change of mean pixel intensity of images on D21 normalized to D0. Fold change was calculated by comparing each segment across days on the same animal. Mean \pm SEM is plotted for 3 independent biological replicates. Two-way ANOVA is applied. Sidak's multiple comparison test is performed for pairwise analysis. p -Value for Control D0–D21 = 0.1882, p -value for Control + Orlistat D0–D21 = 0.1104, p -value for UV + Orlistat D0–D21 = 0.0554, p -value for Control D0–D21 = 0.0055. (I) Bar graph depicting qRT-PCR-based analysis of *Mitf* and *Tyr* expression from epidermal cells on day 7. Mean \pm SEM is plotted for 3 individual guinea pigs. One-way ANOVA is applied, $F(3,8) = 36.64$, p -value < 0.0001 . Tukey's test is performed for pairwise analysis. *** p -Value < 0.005 , ** p -value < 0.01 , * p -value < 0.05 . (J) Bar graph depicting qRT-PCR-based analysis of *Mitf* and *Tyr* expression from epidermal cells on day 30. Mean \pm SEM is plotted for 3 individual guinea pigs. One-way ANOVA is applied, $F(3,8) = 12.87$, p -value = 0.002. Tukey's test is performed for pairwise analysis.

****p*-Value < 0.005, ***p*-value < 0.01, **p*-value < 0.05. Quantitative data are provided in [S1 Data](#) for Panels C, E, H, I, and J. qRT-PCR, quantitative real-time polymerase chain reaction.

<https://doi.org/10.1371/journal.pbio.3001634.g007>

7C). The melanin estimation data were recapitulated at the molecular level, as measured by tyrosinase protein levels (Fig 7D and 7E). As inhibition of lipases with Orlistat showed a decrease in pigmentation, we further analyzed the expression of lipase during pigmentation. We observed that the expression of one of the lipases, hormone-sensitive lipase (HSL), increases with pigmentation (S8E Fig). Moreover, a 60% to 70% knockdown of *Hsl* with siRNA showed a significant decrease in *Tyrp1* expression by 25% to 30% (S8F Fig). Altogether, inhibitor data suggest that both fatty acid synthesis and lipolysis arm are important during pigmentation for increasing availability of free fatty acids for further utilization.

To validate the formation of TAGs in pigmented primary human melanocytes, we inhibit DGAT1 enzyme that catalyses the rate-limiting step of diacylglycerol (DAG) to TAG formation using T863 (S8G Fig). To our surprise, pigmented primary human melanocytes have abundant lipid droplets. Treatment with T863 for 8 hours resulted in the complete disappearance of the lipid droplets indicating a high turnover of lipids in pigmented melanocytes (S8H Fig). The above studies highlight the importance of de novo lipogenesis, the storage of lipid droplets and lipolysis as an integral feature of melanogenesis.

Cells can de novo synthesize fatty acid from acetyl CoA or uptake fatty acid from media to accumulate as lipid droplets and utilize for β -oxidation. Thus, we measured the fatty acid uptake ability of cells during pigmentation using C12-Bodipy-labelled fluorescent fatty acids. We observed that in comparison to day 6 cells, days 4 and 5 showed significantly higher uptake (S9A Fig). We further examined the expression of FA transporters in RNA-seq data and found very few of them showing expression values. With qRT-PCR analysis, we observed that *Fabp5*, one of the regulated fatty acid transporter genes in RNA expression analysis showed marginal up-regulation on days 4 and 5 (S9B Fig) and may contribute to fatty acid uptake. Together, our data suggest that both the pathways, FA uptake and de novo fatty acid synthesis are likely to provide fatty acids for β -oxidation. Since fatty acid uptake is dependent on the availability of exogenous fatty acids, our focus was more on de novo fatty acid synthesis.

Orlistat prevents induction of UV-mediated pigmentation in a guinea pig model

Having established the important role of lipid metabolism in melanogenesis, we were next interested to investigate whether the pharmacological targeting of fatty acid metabolism could show a therapeutic effect in an animal model. We established the guinea pig model to induce skin pigmentation, wherein 200 mJ of UVA and UVB dose were given for 3 alternate days (Fig 7F), as also reported previously [40,41]. Since Orlistat is an FDA-approved drug, we examined whether topical application of Orlistat could be a safe alternative for depigmentation. Orlistat was formulated with PEG8000 and applied topically at 50 μ M for 6 days. As expected, we did not observe any toxicological effect of Orlistat on the skin. Anatomically one can observe the subtle level of pigmentation difference in the skin of guinea pigs for different parts of their body. To make our comparison robust, we have performed experiments on the same animals in groups of 3 and followed them temporally. In this study, brown patches on guinea pig skin were divided into 4 sections and subjected to different treatments due to better contrast for hyperpigmentation phenotype than the black patches. The first section corresponds to the non-UV-exposed control region, while the second section is the non-UV-exposed Orlistat treated region. The third section is the UV-exposed region with the application of the Orlistat,

and the fourth section is the UV-exposed control region. Phenotypic changes in the animals were captured on day 21 by taking photographs (Fig 7G). Enhanced induction of pigment was noted in section 4 due to UV exposure. Sections 1 and 2, where the skin is not exposed to UV, show no changes in the pigmentation phenotype. In contrast, the Orlistat-treated UV-exposed region 3 showed reduced pigmentation as compared to the fourth quadrant. Quantitative image analysis suggests a significant increase in pigmentation in the UV-treated section, while the UV + Orlistat-treated section did not show significant changes on day 21 (Fig 7H). These phenotypic changes were confirmed at the molecular level on days 7 and 30 when animals were euthanized. We observed that *Mitf* and *Tyr* expression increased upon UV treatment when compared with non-UV control patch of the skin. While UV Orlistat treatment did not show a similar increase when compared to the non-UV Orlistat skin patch on days 7 and 30 (Fig 7I and 7J). Together, these data suggest that the topical application of Orlistat can be repurposed to decrease hyperpigmentary responses and that modulators of metabolism may be an alternate mechanism to regulate skin pigmentation.

Discussion

Seminal studies with infiltrating immune cells have underscored the importance of metabolism and metabolites as a guiding force and a critical determinant of the quality and quantity of immune responses [42,43]. However, metabolic rewiring in parenchymal cells like melanocytes to maintain cellular functions is largely unknown. Melanocytes in the human skin epidermis mostly consist of differentiated and non-dividing cells [1]. These cells must rapidly and effectively respond to physiological cues like UV radiations and/or to the secreted factors like cytokines, growth factors, and hormones and regain physiological homeostasis [44,45]. In this study, we have mapped the dynamics associated with transcriptional and metabolic networks that dictate the efficient melanogenesis response of melanocytes. To avoid confounding variables arising from different cell populations, we employed a functionally defined B16 cell pigmentation model that autonomously transits from basal depigmented to the pigmented state over a period of 6 days. This model recapitulates a series of coordinated processes encompassing signalling, transcriptional activation, melanosome biogenesis, melanin synthesis and returns to a homeostatic state. Previous time-series analysis of this pigmentation model had resulted in the identification of interferon- γ signatures in dictating the depigmentation phase of melanogenesis [24]. Our studies here delineate the pivotal role of fatty acid metabolism in melanocyte effector function and also establish the potential therapeutic efficacy of this target.

MITF is the master regulator of melanocyte lineage regulating several genes associated with pigmentation and proliferation [7]. An interesting question is how MITF selectively and differentially activates these genes upon different cues? Some recent studies have provided interesting leads towards this understanding. Malcov-Brog and colleagues showed that MITF expression dynamics tightly control the temporal relationship between the stress response and pigmentation skin protection programs. It is proposed that pigmentation genes have a high affinity for MITF and only small amounts of MITF are required for their expression [26]. Louphrasitthiphol and colleagues suggest that MITF occupancy of promoters is modulated by acetylation [46]. Our group showed enhanced H3K27 histone acetylation at selected differentiation genes facilitate their amplified expression via MITF [47]. In the present study, pigmentation programming is temporally resolved to days (from days 3 to 6), and the above studies could probably explain our observation of different trajectories of protein expression for the classical MITF-mediated pigmentation targets.

Integrated analysis of transcriptomic and metabolomics studies resolved melanocyte pigmentation function into 3 intricately synchronized phases corresponding to preparatory,

melanogenic, and recovery, defined by distinct transcriptional and metabolic signatures. During the preparatory phase, cells start to accumulate precursors and reducing equivalents by increasing the flux of glycolysis towards anabolic pathways like PPP and HBP. The shunting of glycolytic intermediates to the hexosamine biosynthesis module generates substrates for N-glycosylation that will facilitate extensive glycosylation of pigment-producing enzymes, TYR and DCT [8,31,32] and protein components of the melanosome like PMEL17 [10], which are heavily glycosylated in functional form. The flux through PPP remains high during the melanogenic phase that produces NADPH to facilitate the fatty acid biosynthesis crucial in the next phase.

Induction of the melanogenic phase activates fatty acid biosynthesis and accumulation of lipid droplets, which are then rapidly utilised for increased energy requirements of the cell. The onset of melanogenesis triggers gene expression of the central lipid mediator, SREBF1, and its activation maximally around the melanogenic phase. This activation is likely to be triggered by various activators of pigmentation, and we demonstrate α -MSH-mediated cleavage and activation of SREBF1. Increased fatty acid synthesis results in the formation of TAGs. These lipid droplets are much smaller in size than those found in hepatocytes and are rapidly turned over during the continued melanogenic phase through β -oxidation [48]. The accumulation of lipid droplets has been reported earlier within melanocytes in the skin of individuals exposed to therapeutic UV radiations [49]. While lipid metabolism is governed by PPARs and SREBFs, only *Srebf1* knockdown displayed a reproducible modest depigmenting phenotype in melanocytes, in both B16 and primary melanocytes. Although the reasons for this phenotype are unclear, it may be noted that *Srebf1* protein is cleaved and translocated to the nucleus for transcriptional activation, and the transient decrease in its mRNA expression may not be sufficient to completely reverse the pigmentation phenotype. Indeed, the inhibitor 25-HC that targets the activation of SREBF1 shows a better depigmenting effect during the course of treatment. Another possibility is the compensation effect by 2 *Srebf1* isoforms, *Srebf1a* and *Srebf1c*. Several inhibitors targeting FASN, DGAT1, and lipase affect pigmentation phenotype, confirming that de novo fatty acid synthesis, storage, and lipolysis are integral in carrying out melanogenesis.

Seahorse-based mitochondrial respiration analysis of these cells during pigmentation show that melanocytes have higher spare respiration capacity for utilizing fatty acids and thus have the potential to make use of this pathway during increased energy requirements. Mitochondrial reliance on fatty acids could result in increased accumulation of free radicals, which is manifested as the accumulation of defective mitochondria in the recovery phase. This corroborates with previous reports suggesting decreased mitochondrial respiration in hyperpigmented cells [17]. The switch to glycolysis and depletion of stored lipid droplets indicates an almost complete reliance on anaerobic glycolysis for the cells' energy needs.

During pathological conditions, it is critical to selectively inhibit the pathways that dysregulate cellular functions such that treatment can restore homeostasis. Since the dynamic nature of metabolic programming among immune cells is linked with their plasticity and function, various inhibitors for metabolic pathways are being perused as a novel therapeutic approach to treat inflammation and autoimmunity [42,50,51]. However, one of the challenges is to generate selectivity during systemic administration for obtaining therapeutic benefits. In our study, by using inhibitors of fatty acid metabolism through a topical formulation, we are able to selectively target melanocyte function to treat hyperpigmentary diseases. We showed that the FDA-approved drug, Orlistat, can be a potential molecule to treat hyperpigmentary responses. In future studies, detailed screening of fatty acid synthesis and lipase inhibitors as depigmenting agents could provide a new class of pigmentation modulators. In conclusion, our study defines principles of cellular homeostasis during melanogenesis that reveals how melanocytes respond

to systemic cues to elicit a physiological response by balancing energetic and cellular stability by sensing the environment. This knowledge can benefit in determining how cutaneous pigmentary diseases develop as well as the means to treat them.

Material and methods

B16 pigmentation model and primary melanocyte cultures

B16 melanoma cells were cultured in Dulbecco's modified Eagle's Media (DMEM-high glucose, Sigma-Aldrich, Burlington, Massachusetts, USA, D5648) supplemented with 10% fetal bovine serum (FBS, Gibco, 10270106). Cells were maintained at 5% CO₂ levels at 37°C and grown till 60% to 80% confluency. For the pigmentation model, B16 cells were seeded at a low density of 100 cells/cm² in DMEM-high glucose media and allowed to gradually pigment for 6 days of the model. Pigmentation was quantitated from pellet images using ImageJ software. As a control, 200 μM PTU (Sigma-Aldrich, P7629) is added on day 2 to maintain depigmented state in the low-density model. B16 cells were treated with C75-20 μM (Sigma-Aldrich, C5490), T863-10 μM (Sigma-Aldrich, SML0539), and Orlistat-50 μM (Sigma-Aldrich, O4139), and 25-HC-500 nM (Sigma-Aldrich, H1015) on day 3 and analyzed for pigmentation differences on day 6.

Adult Human Melanocytes were purchased from Lonza (CC-2586) and cultured in Lonza MGM4 media (CC-3250). These are pigmented at the basal level. As a control, 200-μM PTU is added to induce depigmentation in these cells. Primary human melanocytes were treated with SREBF1 inhibitor (25-HC-100 nM) for 96 hours.

UV-induced guinea pig pigmentation model

The 3- to 4-month-old guinea pigs were housed for the experiment. Animals were shaved with depilating cream to expose the skin a day before starting the UV dose. Three doses of 200 mJ of UVA+UVB was given on alternate days to half body of the animal while the remaining half was covered with aluminum foil, which serves as non-UV control skin [40,41]. Both the regions were then applied topically with an equal volume of 50 μM of Orlistat dissolved in 50% of polyethylene glycol 8000 (PEG8000). PEG8000 was used as vehicle control. In each experimental set, a total of 6 doses of drugs were given for the first 6 days. The first drug application was done after first UV dose. Three animals were euthanized at each time point, days 7 and 30. The 1 × 1 cm² of skin was collected from both control and treated region. Epidermis and dermis were separated by treating with 0.25% dispase solution in HBSS for 2 hours at 37°C. Transcriptional analysis was done for pigmentation genes from RNA isolated from the epidermis. UV-exposed region was compared to the non-UV-exposed region. All animal procedures were performed with an approved protocol (IAEC #521/19) from the Institutional Animal Ethical Committee at the National Institute of Immunology (CPCSEA Registration No- 38/GO/ReBi/SL/99/CPCSEA dated 20.03.17).

RNA sequencing

RNA isolation was performed using the Triprep RNA isolation kit (Macherey Nagel, Duren Germany, 740966.250) according to the manufacturer's instructions. Briefly, B16 cells were cultured at low density on consecutive days such that days 6 and 3 time points would coincide on the same day. For RNA isolation, an equal number of cells (5×10^5) were counted for each time point and stored in the lysis buffer. To obtain high-quality RNA, purification was performed using triprep column. The quality of extracted RNA was assessed by visualizing bands on 1.5% agarose gel and monitoring 260/280 ratio. All the RNA samples were frozen together

Table 1. List of qRT-PCR primers.

Identifier	Gene name	Sequence	Species
RSG 1232	Gapdh F	AACTGCTTAGCACCCCTGGC	Mouse
RSG1233	Gapdh R	ATGACCTTGCCACAGCCTT	Mouse
IML 359	Pdk1 F	GGCGGCTTTGTGATTTGTAT	Mouse
IML 360	Pdk1 R	ACCTGAATCGGGGGATAAAC	Mouse
IML 335	Fasn F	CTGCGTGGCTATGATTATGG	Mouse
IML 336	Fasn R	AGGTTGCTGTCTGTAGT	Mouse
IML311	Acaca F	CCTCCGTCAGCTCAGATACA	Mouse
IML312	Acaca R	TTACTAGGTGCAAGCCAGACA	Mouse
IML 313	Acly F	CCAGTGAACAACAGACCTATGA	Mouse
IML 314	Acly R	AATGCTGCCTCCAATGATG	Mouse
RSG8994	Srebf1 F	GATCAAAGAGGAGCCAGTGC	Mouse
RSG8995	Srebf1 R	TAGATGGTGGCTGCTGAGTG	Mouse
RSG 5828	Typr1 F	GATCCGTTCTAGAAGCACCAAGA	Mouse
RSG 5829	Typr1 R	CCTCAGCATAGCGTTGATAGTGA	Mouse
RSG 1232	Gapdh F	AACTGCTTAGCACCCCTGGC	Guinea pig
RSG1233	Gapdh R	ATGACCTTGCCACAGCCTT	Guinea pig
IML 641	Tyr F	CAGCTTTCAGGCAGAGGTTTC	Guinea pig
IML 642	Tyr R	TCCCCAGTATCCAAACTTGC	Guinea pig
IML 643	Mitf F	GAAATTCTGGGCTTGATGGA	Guinea pig
IML 644	Mitf R	ACGCTGTGAGCTCCCTTTTA	Guinea pig
IML 1245	Srebf1 F	AGGTGGAGGACACACTGACC	Human
IML 1246	Srebf1 R	CAGGACAGGCAGAGGAAGAC	Human
IML 1247	Fasn F	AGTACACACCCAAGCCAAG	Human
IML 1248	Fasn R	GTGGATGATGCTGATGATGG	Human
IML 1249	Typr1	CCGAAACACAGTGGAAAGTT	Human
IML 1250	Typr1	TCTGTGAAGGTGTGCAGGAG	Human

<https://doi.org/10.1371/journal.pbio.3001634.t001>

at -80°C . RNA was precipitated with ethanol to preserve the quality during transportation. A total of 1- μg RNA sample was sent for 2 biological replicates of each time point for RNA sequencing. RNA samples were outsourced to the company, Bencos Research Solutions, for RNA sequencing. RNA with RIN > 8.5 was proceeded for library preparation using TruSeq RNA Sample Prep Kit v2. Sequencing was performed using Illumina NovaSeq 6000 platform. QC check was done using FastQC. Preprocessing to remove trim bases and adaptor was done using Cutadapt. Read alignment was done using HISAT2. GRCm38 was used as the reference genome. Read quantification was performed with HTSeq and normalized counts and differential regulation were obtained using the DESeq2 package in R Studio. Time-course analysis was done using the LRT test, and genes with adjusted p -value < 0.001 were taken as significantly differentially expressed from days 3 to 6. Raw counts were transformed using the variance-stabilizing transformation (VST) function, and DEGs were clustered and plotted using the pheatmap package. Genes enriched on the respective days were identified and KEGG pathway enrichment was done using the cluster Profiler package. Selected pathways were plotted using ggplot2 in R Studio. DEGs were analysed for the TG enrichment of TF using the TRRUST database on metascape (metascape.org). Top 7 TFs from each day (except Trp53 as it was enriched on all the days) were plotted as a TF-TG network using cytoscape. The colour gradient represents the scaled (row-wise) expression values from the RNA Seq data.

cDNA synthesis and real-time PCR

RNA was reverse transcribed using the Superscript III cDNA synthesis kit (Life Technologies, Carlsbad, California, USA, 18080–051) according to the manufacturer's protocol. Gene expression analysis by quantitative real-time PCR was performed on a Roche Light Cycler 480 II real-time cycler using the SYBR GREEN qPCR Master Mix (Kapa Biosystems, Massachusetts, USA, KM4101) to evaluate transcriptional regulations. Most of the primers were designed using Primer3 and checked by the NCBI Primer blast tool. List of primers used for qRT-PCR is provided in the [Table 1](#). Gene-specific primers were obtained from Sigma Aldrich. Either *Hgprt* or *Gapdh* was used as the normalizing control and quantification was done by the comparative Ct method.

Cell lysate preparation and western blotting

B16 melanoma cells were washed with ice-cold Dulbecco's phosphate buffer saline (DPBS-Gibco, Thermo Fisher Scientific, Waltham, Massachusetts, USA, 14190144) and lysed with NP40 cell lysis buffer (Invitrogen, Waltham, Massachusetts, USA, FNN0021) supplemented with protease inhibitor cocktail (Roche, Basel Switzerland, 04693132001). Cells were incubated with NP40 for 30 minutes on ice. The soluble fractions of cell lysates were isolated by centrifugation at 13,000 rpm in a refrigerated microcentrifuge for 30 minutes. The protein concentration in the soluble fraction was quantified using the bicinchoninic acid (BCA) protein estimation kit (Thermo Fisher Scientific, Waltham, Massachusetts, USA, 23227). Known concentrations of bovine serum albumin (BSA) was used to plot the standard curve. The 30 to 50 μ g of the protein was boiled in SDS dye and separated on 10% SDS PAGE gel. Tyrosinase antibody is synthesized from Genescript. PMEL17 (ab137078), MITF (ab12039), and FASN (ab22759) antibodies are procured from Abcam, while SREBF1 (04–469) is ordered from Millipore. HRP-conjugated Actin (ab8227) and Tubulin (ab6046) are used as a loading control. Horseradish peroxidase-conjugate Anti-Mouse (NA931) and Anti-Rabbit (NA934) antibodies are obtained from GE Healthcare. For western blot standard-enhanced chemiluminescence reagents (WBLUF0100) were used from Millipore. ImageJ software was used for quantification.

Polar metabolite extraction for mass spectrometry and NMR

For liquid chromatography-coupled tandem mass spectrometric analysis, polar metabolite extraction was performed using 80% Methanol-Water solvent (LC-MS grade Methanol-Merck 106035, LC-MS grade Water-Fluka 39252). Cells were grown in multiple flasks to obtain 10^6 cells per replicate. The 3 to 4 replicates were prepared for each time point. B16 cells were washed with cold DPBS and trypsinized with 0.1% trypsin (Gibco, 15090046 diluted in Versene, Gibco, 15040066). Cells were harvested in defined trypsin inhibitor (Gibco, R007100), and 1 million cells were counted for each sample and proceeded for metabolite extraction. Again, cells were washed with DPBS and pelleted down at 500 g for 5 minutes at 4°C. Approximately 500 μ L of chilled 80% methanol was added to the cell pellet. For extraction, samples were mixed well by vortexing and incubated on dry ice for 10 minutes. Penicillin (Gibco, 15140122) was added in 80% methanol as an internal control during extraction. Samples were spun at 13,000 rcf for 30 minutes at 4°C. The supernatant was collected in a chilled 1.5 ml microcentrifuge tube and samples were dried in a SpeedVac vacuum concentrator. Samples were further lyophilized and stored at -80°C till mass spectrometric run. The samples were run on a Waters Xevo-TQS tandem mass spectrometer coupled to Acquity UPLC. The analysis was performed using MassLynx software, followed by analysis with MetaboAnalyst 5.0 for pathway enrichment. Fold changes were plotted for each metabolite.

Pulse-chase labeling of glycolysis and TCA metabolites was performed using NMR. The 10 mM [$U-^{13}\text{C}$]-Glucose (Cambridge Isotope Laboratory, Andover and Tewksbury,

Massachusetts, USA, CLM-1396-10) was fed in glucose-free RPMI media (Himedia, Mumbai, Maharashtra India, AT150) for 4 hours at each time point. Due to the low sensitivity of NMR, extraction was done from 20 million cells per sample. The 200 μM [$U\text{-}^{13}\text{C}$]-palmitate (Cambridge Isotope Laboratory, CLM-409-0.5) was added for 24 hours in glucose-free RPMI at each time point. Metabolite extraction was done with the same protocol as mentioned above. Samples were dissolved in 160 μL of deuterated water (D_2O) and transferred in 3 mm NMR tubes. All NMR measurements were performed on a 500 MHz Bruker Avance III spectrometer equipped with 5-mm TCI cryo-probe. Topspin 3.6 pl7 (Bruker) was used for data acquisition, Fourier transformation and processing of data. Two-dimensional [$^{13}\text{C}, ^1\text{H}$] heteronuclear single quantum coherence [HSQC] experiments were measured at 310 K. The 2D [$^{13}\text{C}, ^1\text{H}$] HSQC spectra were measured with a spectral width of 7002.8 Hz along the ^1H dimension, and 22639.57 Hz along the ^{13}C dimension. A total of 16 dummy scans and 96 scans with a relaxation delay of 1.5 second was used for a total acquisition time of 146 ms ($t_{2\text{max}}$) along ^1H dimension and 2.8 ms ($t_{1\text{max}}$) along ^{13}C dimension. Processing was performed using 90° shifted sine-square bell window function for both dimensions. Peak correlation and peak intensity calculation were performed using Computer Aided Resonance Assignment (CARA) software [52]. Chemical shift values were assigned to specific metabolites using the Biological Magnetic Resonance Bank (BMRB) (<http://www.bmrblib.org/>) and Human Metabolome Database (HMDB) (<http://www.hmdb.ca/>). A chemical shift error tolerance of 0.05 ppm and 0.5 ppm was used for ^1H and ^{13}C chemical shifts, respectively. Fold change as compared with day 0 was plotted for each metabolite.

Glucose measurement

Glucose concentration in media was measured on COBAS INTEGRA 400 using a glucose detection kit. It is based on the principle of an enzymatic assay where glucose is first converted to glucose-6-phosphate by hexokinase, followed by oxidation of glucose-6-phosphate by G6PD, which is coupled to the reduction of NAD to NADH. NADH produced in the reaction reduces the colourless probe to a coloured product with strong absorbance at 450 nm. The amount of glucose is equivalent to NADH produced. A standard curve was generated using glucose standards ranging in between 0 to 10 g/L concentration. The instrument is highly accurate up to the range of 6 g/L. The 200 μL residual media was collected on each day from days 3 to 6 in specialized tubes and placed in the COBAS instrument. Reagents were mixed automatically and readings were recorded. Glucose concentration in the media on different days was calculated from the standard curve.

Lactate measurement

Lactate was measured in cell lysate with the Sigma Lactate assay kit (MAK064) using the manufacturer's protocol. Briefly, an equal number of cells (10^6) were harvested on days 5 and 6 and the cellular lysate was prepared using the given lysis buffer. Lactate standards were prepared in a range of 0 to 10 nmole in 50 μL of assay buffer. An equal volume of a master mix containing lactate assay buffer, lactate enzyme, and lactate probe were added to standards and samples. The plate was incubated for 30 minutes at room temperature and colorimetric measurement was recorded at 570 nm.

Mitochondrial oxygen consumption rate measurement

Oxygen consumption rate was measured using the Seahorse Mito Stress Kit (Agilent, Santa Clara, California, USA, 103015–100) according to the manufacturer's protocol. Briefly, B16 cells were grown in low density in DMEM high glucose media. The 3 separate cultures were

setup on consecutive days so as to terminate all the time points (D5 and D6) on the same day. One day before termination of the cultures, cells were trypsinized and 60,000 cells were seeded in a Seahorse culture plate and allowed to adhere overnight. Cell density was first standardized to get reading in an appropriate range. Seahorse media was freshly reconstituted by adding glutamine (2 mM), sodium pyruvate (1 mM), and glucose (10 mM) or oleate (200 μ M) and equilibrated to 37°C for each experiment. pH was set to 7.4 by adding NaOH solution. Once the media was prepared, cells were washed twice with DPBS. A total of 500 μ l of freshly prepared media was added to each well, from the wall. Cells were incubated in Seahorse media in a non-CO₂ incubator for 1 hour before the assay. Inhibitors were added as per the kit direction in different ports just before starting the assay. Assay run for 2 hours and data generated was analyzed using WAVE software.

Immunofluorescence measurements

Lipid droplets were measured using BODIPY 493/503 dye (Invitrogen, D3922). B16 cells were grown on 1 cm² coverslip in low density (1,000 cells per coverslip) for different days. Cells were fixed by adding 4% methanol-free formaldehyde (Thermo Fischer Scientific, 28906) on the coverslip and incubated at room temperature for 20 minutes. 3X DPBS washes were given to remove 4% methanol-free formaldehyde. Cells were stored in DPBS at 4°C till the last time point. Fixed cells were incubated with 10 μ M BODIPY dye in DPBS for 1 hour at room temperature. 3X DPBS washes were done to remove excess stain. Coverslip was mounted with Gold antifade DAPI solution (Thermo Fischer Scientific, P36931). Imaging was done on the Leica SP8 confocal microscope. Three biological replicates were imaged for each experiment, with 30 cells per set in the B16 model.

Mitochondrial morphology was measured using Mito Tracker Red dye. B16 cells were cultured in 2-well live imaging chamber dishes with an area of 1 cm² in low density (500 cells per coverslip) for different days. Live cells were incubated with 500 nM Mito Tracker Red dye for 30 minutes at 37°C in DMEM without FBS. Three DPBS washes were given. Imaging was done on the Leica SP8 confocal microscope. Three biological replicates were imaged for each experiment, with 100 cells per set.

B16 cells overexpressing pmCherry-Srebf1-eGFP (traffic light construct) were seeded in live imaging chambers (2 chambered live imaging chambers from Nunc). The nucleus was stained with Hoechst 33342 solution (Thermo Fischer Scientific, 62249). Approximately 3.5 μ M Insulin (Sigma-Aldrich, I6634) or 10 μ M α -MSH (Sigma-Aldrich, M4135) was added just before setting up the live imaging module in the Leica SP8 Confocal microscope. Transfected cells were selected at random using the “Mark & Find” feature, and 30 to 40 cells were imaged for a duration of 4 to 6 hours per replicate. The experiment was performed in triplicates.

siRNA transfection

siRNA transfections were performed in T75 flasks on day 3 of the pigmentation model. A total of 100 nM of siRNA was added per flask with a 1: 3 times V: V ratio of Dharmafect transfection reagent. siRNA was commercially procured from Qiagen ([FlexiTube GeneSolution GS20787 for Mouse Srebf1](https://www.qiagen.com/en/products/5010010/FlexiTube_GeneSolution_GS20787_for_Mouse_Srebf1), FlexiTube Gene Solution 1027281 for negative C siRNA). Other siRNAs were purchased for Dharmacon (ON-TARGETplus Mouse Lipe 16890 siRNA Smart pool for HSL, ON-TARGETplus Human SREBF1 (6720) siRNA Smart pool). The transfection was done in opti-MEM (Gibco 31985070) media for 6 hours. Post transfection, the opti-MEM media was removed and cells were washed with 1X DPBS and then the day 3 culture media was added back to the cells. siRNA transfection in primary melanocytes was done using

Table 2. List of cloning primers.

Identifier	Gene name	Sequence	Species
IML524	Srebf1c F XhoI	CTCGAGggatggattgcacattgaa	Mouse
IML581	Srebf1c middle R	Cgggccagagtgtggcctagt	Mouse
IML580	Srebf1c middle F	Gccaatggactactagtgttg	Mouse
IML587	Srebf1c R EcoRI	GAATTCgctggaagtgcggtggt	Mouse

<https://doi.org/10.1371/journal.pbio.3001634.t002>

Nucleofection Kit. Media is changed after 24 hours of transfection. Cells were harvested at 48 hours time point to capture transcriptional changes.

Melanin estimation

Melanin estimation was performed as described earlier [53]. Briefly, cells were lysed in 1 N NaOH by heating at 80°C for 2 hours, and then, absorbance was measured at 405 nm. Finally, the melanin content was estimated by interpolating the sample readings on the melanin standard curve obtained with synthetic melanin.

Live/Dead cell analysis

Live dead staining is performed using Propidium Iodide dye (493/636). Briefly, the cells were trypsinised and washed with DPBS and incubated with 2.5 µg/ml Propidium Iodide Dye at room temperature for 1 minute. As a positive control, cell death was induced by incubating cells at 55°C for 20 minutes. Samples were run on flow-cytometry. The percentage of PI-positive cells were plotted.

Fatty acid uptake assay

Fatty acid uptake assay was performed using BODIPY FL C12 Dye (505/511) (Invitrogen, D3822). Briefly, the cells were trypsinised, washed with DPBS and incubated with 1 µM BODIPY FL C12 Dye at 37°C for 30 minutes. Subsequently, cells were washed thrice with DPBS and run-on flow-cytometry. Medium fluorescent intensity was analysed for different days.

Cloning

To clone *Srebf1*, we amplified the common splice variant, *Srebf1c*, using PCR. List of primers used to amplify *Srebf1* is provided in Table 2. To get a complete 3.4 kb fragment, we amplified the first 1.6 kb separately and the last 1.7 kb sequence separately. The complete sequence was amplified with overlapping PCR by using 2 amplicons specific to the first and second half sequence of *Srebf1c*. The amplicon was phosphorylated with T4 polynucleotide kinase. The plasmid pBluescript (pBS-SK+) was digested with EcoRV and end were dephosphorylated with calf intestinal phosphatase (CIP). Amplified full-length sequence of *Srebf1c* was cloned in pBS-SK+ vector in EcoRV restriction digestion site. From *Srebf1*-pBS plasmid, *Srebf1c* fragment was removed by doing partial restriction digestion with XhoI and EcoRI enzymes. Complete digestion gives 2 fragments, from 1 to 493 bp and 494 to 3,410 bp, while partial digestion gives 3 bands corresponding full length 1 to 3,410 and 1 to 493 bp and 494 to 3,410 bp. We extracted the full-length fragment from agarose gel corresponding to 3,335 bp and subcloned it in the mCherry-C1 vector. In our lab, eGFP was already cloned in the mCherry-C1 vector and stored in lab repository as clone number pAK4.0. With XhoI and EcoRI restriction enzymes, we subcloned *Srebf1c* in mCherry-eGFP vector. NEB enzymes and reagents are used for cloning.

Transmission electron microscopy

Cells were fixed in fixative containing 2.5% glutaraldehyde and 4% paraformaldehyde in 0.1 M sodium cacodylate buffer (pH 7.2) at room temperature for 4 hours and then rinsed in PBS. Fixed cells were embedded in 2% agar and post-fixed in 1% osmium tetroxide for 1 hour. Samples were dehydrated in graded series of ethanol (50% to 100%) and then subjected to propylene-oxide for 30 minutes and infiltrated with increasing proportions of propylene-oxide: Epon (2:1, 1:1 and 1:2) for 2 hours and embedded in Epon resin and polymerized for 72 hours at 60°C. Ultrathin sections (63 nm) were cut on Leica Ultra-microtome, placed on copper grids and stained with uranyl acetate and lead citrate, and examined on a 200-KV Tecnai G2 Twin transmission electron microscope (FEI make).

Statistical analysis

All statistical analysis was performed using GraphPad Prism 8 software. Unpaired Student *t* test, one-way ANOVA, or two-way ANOVA was applied to compare the significant difference between the means of 2 or multiple groups respectively. Tukey's test was applied to compare the pairwise sample. Dunnett's test was applied to compare with the control group. The *p*-values obtained during analysis are indicated in the figure legends.

Supporting information

S1 Fig. Validation of RNA sequencing data. (A) PCA plot from data obtained from unbiased transcriptomic analysis from 2 independent biological replicates. PC1 is 80.33% and PC2 is 13.81%. (B) Correlation plot showing correlation value *R* obtained between 2 biological replicates in RNA sequencing data. *R* ranges from 0.99–0.1, with high *p*-value 2.2e-16. (C) Heatmap representing the expression of fatty acid synthesis genes from days 3 to 6 in RNA sequencing data. Scale from blue to red represents *z*-score for normalized expression values from -1 to +1. (D) Heatmap representing the expression of TAG synthesis genes from days 3 to 6 in RNA sequencing data. Scale from blue to red represents *z*-score for normalized expression values from -1 to +1. (E) Representative image showing pigmented cell pellet in the low-density B16 pigmentation model for days 3 to 6 vs. PTU-treated depigmented cells. (F) Bar graph depicting cell count from days 4 to 6 in control and PTU-treated low-density cells in 3 independent biological sets. One-way ANOVA is applied, $F(5,12) = 203.3$. Turkey's test is performed for pairwise comparison. **p*-Value < 0.0142. (G) Representative western blot for FASN expression on D3–D6 during melanogenesis with respect to Actin. Numerical values show average fold change for 3 biological replicates. (H) Bar graph depicting quantitative analysis of FASN during melanogenesis for 3 independent biological replicates. Mean ± SEM is plotted for 3 independent biological replicates. One-way ANOVA is applied $F(3,7) = 25.74$, *p*-value = 0.0004. (I) Representative western blot for FASN expression on D4–D6 PTU-treated cell-seeded at low density with respect to Actin. Numerical values show average fold change for 3 biological replicates. (J) Bar graph depicting quantitative analysis of FASN during melanogenesis for 3 independent biological replicates. One-way ANOVA is applied $F(2,6) = 5.288$, *p*-value = 0.0474. Quantitative data are provided in [S2 Data](#) for Panels A, B, F, H, and J. PCA, principal component analysis; PTU, 1-phenyl-2-thiourea; TAG, triacylglycerols. (TIF)

S2 Fig. Validation of transcriptional network analysis. (A) Bar graph depicting qRT-PCR of *Mitf* with respect to *Hgprt*. Mean ± SEM is plotted for 3 independent biological replicates. One-way ANOVA is applied. For *Mitf*, $F(3,8) = 16.59$, *p*-value = 0.0009. Turkey's test is performed for pairwise comparison. (B) Bar graph depicting qRT-PCR of *Tyr* with respect to

Hgprt. Mean \pm SEM is plotted for 3 independent biological replicates. One-way ANOVA is applied. For *Tyr*, $F(3,8) = 24.08$, p -value = 0.0002. Turkey's test is performed for pairwise comparison. (C) Bar graph depicting qRT-PCR of *Srebf1* with respect to *Hgprt*. One-way ANOVA is applied. For *Srebf1*, $F(3,8) = 21.72$, p -value = 0.0003. Turkey's test is performed for pairwise comparison. (D) Bar graph depicting qRT-PCR-based analysis fatty acid synthesis genes, *Fasn*, *Acaca*, *Acacb*, and *Acly*, with respect to *Hgprt*. Mean \pm SEM is plotted for 3 independent biological replicates. One-way ANOVA is applied separately for each gene. For *Fasn* $F(3,8) = 8.435$, p -value = 0.0074, for *Acaca* $F(3,8) = 9.811$, p -value = 0.0063, for *Acacb* $F(3,8) = 10.72$, p -value = 0.0035, for *Acly* $F(3,8) = 11.06$, p -value = 0.0032. (E) Bar graph depicting qRT-PCR of *Nrf2* with respect to *Gapdh*. Mean \pm SEM is plotted for 3 independent biological replicates. One-way ANOVA is applied. For *Nrf2*, $F(3,8) = 9.622$, p -value = 0.005. Turkey's test is performed for pairwise comparison. (F) Bar graph depicting qRT-PCR-based analysis *Nrf2* TGs, *Gsr* and *Gst*, with respect to *Gapdh*. Mean \pm SEM is plotted for 3 independent biological replicates. One-way ANOVA is applied separately for each gene. For *Gst*, $F(3,7) = 7.68$, p -value = 0.0128, for *Gsr*, $F(3,8) = 9.666$, p -value = 0.0049. Quantitative data are provided in [S2 Data](#) for Panels A–F. qRT-PCR, quantitative real-time polymerase chain reaction; TG, target gene. (TIF)

S3 Fig. Temporal resolution of metabolic signature of melanocytes during pigmentation.

(A) PCA plot depicting segregation of different days based on metabolite signatures. Groups 1 to 4 correspond to days 3 to 6. Four biological replicates are taken for each time point. PC1 is 48.9% and PC2 is 18.5%. (B) Heatmap depicting top 50 regulated metabolites across different days for each replicate. Blue colour arrows are used to show amino acids and nucleotides, higher on D3 and D4, while orange arrows are shown to mark cofactors and TCA metabolites, higher on D5 and D6. (C) Bar graphs depicting glucose utilization upon pigmentation induction in B16 cells cultured at low-density model. Glucose utilization is calculated by subtracting glucose in media on consecutive days (i.e., glucose concentration on (n-1) day-glucose concentration on nth day)/cell number on nth day*100. Data are represented for 3 independent replicates. Mean \pm SEM is plotted for 3 biological replicates. One-way ANOVA is applied $F(3,7) = 39.50$, **** p -value < 0.0001. (D) Schematic showing biochemical reactions and enzymes involved in conversion of pyruvate to lactate and acetyl CoA formation. (E) Bar graph depicting quantitation of amount of lactate in cellular lysate on D5 and D6 for 3 independent replicates. Mean \pm SEM is plotted for 3 biological replicates. Two-tailed Student t test is applied, $t = 3.284$, $df = 4$, * p -value = 0.0304. (F) Bar graph depicting qRT-PCR-based mRNA expression of *Pdk1*, which regulates PDH activity on D5 and D6 for 3 independent replicates. Mean \pm SEM is plotted for 3 biological replicates. Two-tailed Student t test is applied, $t = 3.541$, $df = 4$, * p -value = 0.0240. Quantitative data are provided in [S2 Data](#) for Panels C, E, and F. PCA, principal component analysis; qRT-PCR, quantitative real-time polymerase chain reaction; TCA, tricarboxylic acid cycle. (TIF)

S4 Fig. Mitochondrial fragmentation analysis in pigmented and depigmented cells. (A)

Representative confocal microscopy images showing mitochondrial morphology in pigmented day 6 cells vs. PTU-treated depigmented cells on day 6 using MitoTracker RED dye. Images were taken at 63 \times . Scale is 5 μ m. (B) Bar graph depicting the quantitation of fragmented mitochondria in pigmented vs. PTU-treated depigmented day 6 cells using ImageJ macro tool MiNA. Approximately 100 cells were taken in each replicate. Mean \pm SEM is plotted in 3 independent biological replicates. Mean \pm SEM is plotted for 3 biological replicates. Two-tailed Student t test is applied, $t = 2.262$, $df = 24$, * p -value = 0.0330. Quantitative data are provided in

[S2 Data](#) for Panel B. MiNA, Mitochondrial Network Analysis; PTU, 1-phenyl-2-thiourea. (TIF)

S5 Fig. Cloning of *Srebf1* in mCherry-C1 eGFP construct. (A) Representative agarose gel showing amplification of first and second half of *Srebf1* gene. (B) Representative agarose gel showing amplification of full-length *Srebf1* using overlap PCR. (C) Representative agarose gel showing partial digestion of *Srebf1*-pBS clone, *Srebf1* to obtain full-length fragment for sub-cloning in mCherry-C1 eGFP vector. (D) Expected size of *Srebf1* pBS clone is tabulated upon digestion with XhoI and EcoRI. (E) Representative agarose gel showing clone confirmation of mCherry-*Srebf1*-eGFP vector. (F) Expected size of mCherry-*Srebf1*-eGFP vector is tabulated upon restriction digestion. (G) Representative western blot for expression analysis of mCherry-*Srebf1*-eGFP construct upon transfection in B16 cells.

(TIF)

S6 Fig. Standardization of SREBF1 activation assay. (A) Representative fluorescence images showing eGFP, mCherry, and merge signal. Magnified nuclear images were shown to focus on SREBF1 nuclear translocation after 4 hours of insulin treatment. Around 20 cells were analyzed in each of the 3 biological replicates. (B) Dot plot depicting colocalization rate between mCherry and Hoechst signal analyzed for each cell at 1 to 4 hours after insulin treatment. Mean \pm SEM is plotted for 3 biological replicates. One-way ANOVA is applied, $F(2.516, 52.83) = 8.234$, p -value = 0.0003. Dunnett's multiple comparison test is performed. **** p -Value < 0.0001, *** p -value = 0.00081, ** p -value = 0.0011. (C) Bar graph depicting quantitation of number of cells showing positive phenotype after Insulin treatment, determined by increased colocalization rate of mCherry and Hoechst signal from 1 to 4 hours. Mean \pm SEM is plotted for combined analysis. Two-tailed Student t test is performed, $t = 5.131$, $df = 4$, ** p -value = 0.0068. Quantitative data are provided in [S2 Data](#) for Panels B and C.

(TIF)

S7 Fig. PPAR signalling do not regulate pigmentation in the B16 model. (A) Representative B16 cell pellet images showing melanin accumulation phenotype on day 6 upon inhibiting PPAR- γ with GW9662, PPAR- α with GW6471, and PPAR- β with GSK3787 ($N = 3$). Bar graph depicting melanin estimation after different inhibitor treatments. Mean \pm SEM is plotted for 3 biological replicates. One-way ANOVA is applied, $F(3, 8) = 1.728$. p -Value = 0.2383. Tukey's test is performed for pairwise analysis. ns is nonsignificant. (B) Bar graph representing qRT-PCR-based quantitation of *Ppara* and *Tyrp1* genes on D5 upon silencing of *Ppara* using smart pool siRNA. Mean \pm SEM is plotted for 3 biological replicates. One-way ANOVA is applied, $F(3, 6) = 49.29$. For NT vs. *Ppara*, *** p -value = 0.0002. For NT vs. *Tyrp1*, p -value is nonsignificant. (C) Bar graph representing qRT-PCR-based quantitation of *Pparg* and *Tyrp1* genes on D5 upon silencing of *Pparg* using smart pool siRNA. Mean \pm SEM is plotted for 3 biological replicates. One-way ANOVA is applied, $F(3, 6) = 1.188$. For NT vs. *Ppara*, * p -value = 0.0255. For NT vs. *Tyrp1*, p -value is nonsignificant. Quantitative data are provided in [S2 Data](#) for Panels A–C. qRT-PCR, quantitative real-time polymerase chain reaction; siRNA, small interfering RNA.

(TIF)

S8 Fig. Effect of lipid metabolism perturbation on melanogenesis. (A) Bar graph represents inhibitor dose standardization in B16 cells using MTT assay. Red arrows represent the dose chosen for further experiments. (B) Bar graph representing cell count on day 6 upon treatment with Orlistat, C75, T863, and PTU. Mean \pm range is plotted for 2 biological replicates. ns is nonsignificant. One-way ANOVA is applied $F(4, 5) = 3.964$. p -Value = 0.0922. (C) Bar graph depicts cell death induced in day 6 cells upon inhibitor treatment measured using Propidium

Iodide staining. Mean \pm SEM is plotted for 3 biological replicates. (D) Representative confocal microscopy images showing lipid droplet accumulation in B16 cells during pigmentation upon addition of treatments (Orlistat, C75, T863) on D3 and analysis on D5. Images were taken at 63 \times . Scale is 5 μ m. (E) Bar graph depicting qRT-PCR of *Hsl* with respect to *Hgprt*. Mean \pm SEM is plotted for 3 independent biological replicates. One-way ANOVA is applied. For *Hsl*, $F(3,8) = 15.92$, p -value = 0.001. Turkey's test is performed for pairwise comparison. (F) Bar graph representing qRT-PCR-based quantitation of *Hsl* and *Tyrp1* genes on D6 upon silencing of *Hsl* using smart pool siRNA. Mean \pm SEM is plotted for 3 biological replicates. One-way ANOVA is applied, $F(3,4) = 61$, *** p -value = 0.0009. Turkey's test is performed for pairwise comparison. (G) Schematic study design for analyzing TAG formation in primary human melanocyte culture by inhibiting DGAT1 using T863, and capturing lipid droplets content in these cells using BODIPY dye. (H) Representative confocal microscopy images showing lipid droplet accumulation in primary melanocytes upon T863 addition. Images were taken at 63 \times . Scale is 5 μ m. Quantitative data are provided in [S2 Data](#) for Panels A, B, C, E, and F. PTU, 1-phenyl-2-thiourea; qRT-PCR, quantitative real-time polymerase chain reaction; siRNA, small interfering RNA; TAG, triacylglycerol. (TIF)

S9 Fig. Role of fatty acid uptake during pigmentation. (A) Representative plot depicts median fluorescent intensity corresponding to the uptake of C-12 fluorescently labelled fatty acid from days 4 to 6. Mean \pm SEM is plotted for 3 biological replicates. One-way ANOVA is applied, $F(2,6) = 72.66$. Turkey's test is performed for pairwise comparison. For D4 vs. D5, p -value is nonsignificant. For D4 vs. D6, *** p -value < 0.0001. (B) Bar graph depicting qRT-PCR of *Fabp5* with respect to *Hgprt*. Mean \pm SEM is plotted for 3 independent biological replicates. One-way ANOVA is applied. Turkey's test is performed for pairwise comparison. For *Fabp5*, $F(3,8) = 5.374$, p -value = 0.0255. ns is nonsignificant. Quantitative data are provided in [S2 Data](#) for Panels A and B. qRT-PCR, quantitative real-time polymerase chain reaction. (TIF)

S1 Data. Data underlying panel Figs [1A](#), [1C](#), [1G](#), [1H](#), [3C](#), [3E](#), [4A](#), [4B](#), [4C](#), [4E](#), [4F](#), [5B](#), [5E](#), [5F](#), [6C](#), [6D](#), [6H](#), [6J](#), [7C](#), [7E](#), [7H](#), [7I](#), and [7J](#).

(XLSX)

S2 Data. Data underlying panel Supporting information [S1A](#), [S1B](#), [S1F](#), [S1H](#), [S1J](#), [S2A–S2F](#), [S3A–S3C](#), [S3E](#), [S3F](#), [S4B](#), [S6B](#), [S6C](#), [S7A–S7C](#), [S8A–S8C](#), [S8E](#), [S8F](#), [S9A](#), and [S9B](#) Figs.

(XLSX)

S3 Data. Data underlying panel Figs [1E](#), [1D](#), and [2](#).

(XLSX)

S4 Data. Data underlying panel [Fig 3A](#).

(XLSX)

S1 Raw Images. Raw data underlying panel Figs [1B](#), [5A](#), [5D](#), [6B](#), [6G](#), [7D](#), [S1G](#), [S1I](#), and [S6A](#).

(PDF)

Acknowledgments

We acknowledge the infrastructure supported by CSIR-IGIB for imaging facility and Mr. Manish for help with imaging. We thank Department of Biotechnology, Government of India

and ICGEB, New Delhi core research fund for providing financial support for the high field NMR spectrometer at ICGEB, New Delhi.

Author Contributions

Conceptualization: Farina Sultan, Vivek T. Natarajan, Rajesh S. Gokhale.

Data curation: Farina Sultan.

Formal analysis: Farina Sultan, Reelina Basu, Divya Murthy, Kuldeep S. Attri, Ayush Aggarwal, Pooja Kumari, Pooja Dnyane, Chetan Gadgil.

Funding acquisition: Vivek T. Natarajan, Rajesh S. Gokhale.

Investigation: Farina Sultan, Reelina Basu, Divya Murthy, Manisha Kochar.

Methodology: Farina Sultan, Kuldeep S. Attri, Pooja Kumari, Archana Singh, Neel Sarovar Bhavesh, Pankaj K. Singh.

Project administration: Rajesh S. Gokhale.

Resources: Vivek T. Natarajan, Rajesh S. Gokhale.

Supervision: Rajender K. Motiani, Vivek T. Natarajan, Rajesh S. Gokhale.

Validation: Farina Sultan, Manisha Kochar, Jyoti Tanwar.

Visualization: Ayush Aggarwal.

Writing – original draft: Farina Sultan.

Writing – review & editing: Farina Sultan, Vivek T. Natarajan, Rajesh S. Gokhale.

References

1. Costin G-E, Hearing VJ. Human skin pigmentation: melanocytes modulate skin color in response to stress. *FASEB J*. 2007; 21(4):976–94. <https://doi.org/10.1096/fj.06-6649rev> PMID: 17242160
2. Yosipovitch G, DeVore A, Dawn A. Obesity and the skin: skin physiology and skin manifestations of obesity. *J Am Acad Dermatol*. 2007; 56(6):901–16. <https://doi.org/10.1016/j.jaad.2006.12.004> PMID: 17504714
3. Duff M, Demidova O, Blackburn S, Shubrook J. Cutaneous manifestations of diabetes mellitus. *Clin Diabetes*. 2015; 33(1):40–8. <https://doi.org/10.2337/diaclin.33.1.40> PMID: 25653473
4. Cichorek M, Wachulska M. Skin melanocytes: biology and development. *Postep Dermatol Alergol*. 2013; 30(1):30–41. <https://doi.org/10.5114/pdia.2013.33376> PMID: 24278043
5. Ando H, Niki Y, Ito M, Akiyama K, Matsui MS, Yarosh DB, et al. Melanosomes are transferred from melanocytes to keratinocytes through the processes of packaging, release, uptake, and dispersion. *J Invest Dermatol*. 2012; 132(4):1222–9. <https://doi.org/10.1038/jid.2011.413> PMID: 22189785
6. Gibbs S, Murli S, De Boer G, Mulder AAT, Mommaas AM, Ponc M. Melanosome capping of keratinocytes in pigmented reconstructed epidermis—effect of ultraviolet radiation and 3-isobutyl-1-methyl-xanthine on melanogenesis. *Pigment Cell Res*. 2000; 13(6):458–66. <https://doi.org/10.1034/j.1600-0749.2000.130608.x> PMID: 11153698
7. Goding CR, Arnheiter H. MITF—the first 25 years. *Genes Dev*. 2019; 33(15–16):983–1007. <https://doi.org/10.1101/gad.324657.119> PMID: 31123060
8. Tsukamoto K, Jackson IJ, Urabe K, Montague PM, Hearing VJ. A second tyrosinase-related protein, TRP-2, is a melanogenic enzyme termed DOPAchrome tautomerase. *EMBO J*. 1992; 11(2):519–26. PMID: 1537333
9. Jimbow K, Park JS, Kato F, Hirosaki K, Toyofuku K, Hua C, et al. Assembly, target-signaling and intracellular transport of tyrosinase gene family proteins in the initial stage of melanosome biogenesis. *Pigment Cell Res*. 2000; 13(4):222–9. <https://doi.org/10.1034/j.1600-0749.2000.130403.x> PMID: 10952389

10. Berson JF, Harper DC, Tenza D, Raposo G, Marks MS. Pmel17 initiates premelanosome morphogenesis within multivesicular bodies. *Mol Biol Cell*. 2001; 12(11):3451–64. <https://doi.org/10.1091/mbc.12.11.3451> PMID: 11694580
11. Bertolotto C, Abbe P, Hemesath TJ, Bille K, Fisher DE, Ortonne JP, et al. Microphthalmia gene product as a signal transducer in cAMP-induced differentiation of melanocytes. *J Cell Biol*. 1998; 142(3):827–35. <https://doi.org/10.1083/jcb.142.3.827> PMID: 9700169
12. Chakraborty AK, Funasaka Y, Slominski A, Ermak G, Hwang J, Pawelek JM, et al. Production and release of proopiomelanocortin (POMC) derived peptides by human melanocytes and keratinocytes in culture: regulation by ultraviolet B. *Biochim Biophys Acta*. 1996; 1313(2):130–8. [https://doi.org/10.1016/0167-4889\(96\)00063-8](https://doi.org/10.1016/0167-4889(96)00063-8) PMID: 8781560
13. Rousseau K, Kauser S, Pritchard LE, Warhurst A, Oliver RL, Slominski A, et al. Proopiomelanocortin (POMC), the ACTH/melanocortin precursor, is secreted by human epidermal keratinocytes and melanocytes and stimulates melanogenesis. *FASEB J*. 2007; 21(8):1844–56. <https://doi.org/10.1096/fj.06-7398com> PMID: 17317724
14. Bondurand N, Pingault V, Goerich DE, Lemort N, Sock E, Caignec CL, et al. Interaction among SOX10, PAX3 and MITF, three genes altered in Waardenburg syndrome. *Hum Mol Genet*. 2000; 9(13):1907–17. <https://doi.org/10.1093/hmg/9.13.1907> PMID: 10942418
15. Furumura M, Potterf SB, Toyofuku K, Matsunaga J, Muller J, Hearing VJ. Involvement of ITF2 in the transcriptional regulation of melanogenic genes. *J Biol Chem*. 2001; 276(30):28147–54. <https://doi.org/10.1074/jbc.M101626200> PMID: 11382753
16. Ferguson J, Smith M, Zudaire I, Wellbrock C, Arozarena I. Glucose availability controls ATF4-mediated MITF suppression to drive melanoma cell growth. *Oncotarget*. 2017; 8(20):32946. <https://doi.org/10.18632/oncotarget.16514> PMID: 28380427
17. Meira WV, Heinrich TA, Cadena SMSC, Martinez GR. Melanogenesis inhibits respiration in B16-F10 melanoma cells whereas enhances mitochondrial cell content. *Exp Cell Res*. 2017; 350(1):62–72. <https://doi.org/10.1016/j.yexcr.2016.11.006> PMID: 27864061
18. Daniele T, Hurbain I, Vago R, Casari G, Raposo G, Tacchetti C, et al. Mitochondria and melanosomes establish physical contacts modulated by Mfn2 and involved in organelle biogenesis. *Curr Biol*. 2014; 24(4):393–403. <https://doi.org/10.1016/j.cub.2014.01.007> PMID: 24485836
19. Kim ES, Park SJ, Goh MJ, Na YJ, Jo DS, Jo YK, et al. Mitochondrial dynamics regulate melanogenesis through proteasomal degradation of MITF via ROS-ERK activation. *Pigment Cell Melanoma Res*. 2014; 27(6):1051–62. <https://doi.org/10.1111/pcmr.12298> PMID: 25065405
20. Tanwar J, Saurav S, Basu R, Singh JB, Priya A, Dutta M, et al. Modulating Mitochondrial ROS Generation. *Cell*. 2022; 11:701. <https://doi.org/10.3390/cells11040701> PMID: 35203350
21. Jung DW, Williams D, Khersonsky SM, Kang TW, Heidary N, Chang YT, et al. Identification of the F1F0 mitochondrial ATPase as a target for modulating skin pigmentation by screening a tagged triazine library in zebrafish. *Mol Biosyst*. 2005; 1(1):85–92. <https://doi.org/10.1039/b417765g> PMID: 16880968
22. Seo SH, Jo JK, Kim EJ, Park SE, Shin SY, Park KM, et al. Metabolomics reveals the alteration of metabolic pathway by alpha-melanocyte-stimulating hormone in B16F10 melanoma cells. *Molecules*. 2020; 25(15):3384. <https://doi.org/10.3390/molecules25153384> PMID: 32722640
23. Abdel-Malek Z, Swope V, Collins C, Boissy R, Zhao H, Nordlund J. Contribution of melanogenic proteins to the heterogeneous pigmentation of human melanocytes. *J Cell Sci*. 1993; 106(4):1323–31.
24. Natarajan VT, Ganju P, Singh A, Vijayan V, Kirty K, Yadav S, et al. IFN- γ signaling maintains skin pigmentation homeostasis through regulation of melanosome maturation. *Proc Natl Acad Sci U S A*. 2014; 111(6):2301–6. <https://doi.org/10.1073/pnas.1304988111> PMID: 24474804
25. Motiani RK, Tanwar J, Raja DA, Vashisht A, Khanna S, Sharma S, et al. STIM 1 activation of adenylyl cyclase 6 connects Ca²⁺ and cAMP signaling during melanogenesis. *EMBO J*. 2018; 37(5):e97597. <https://doi.org/10.15252/embj.201797597> PMID: 29311116
26. Malcov-Brog H, Alpert A, Golan T, Parikh S, Nordlinger A, Netti F, et al. UV-Protection Timer Controls Linkage between Stress and Pigmentation Skin Protection Systems. *Mol Cell*. 2018; 72(3):444–456.e7. <https://doi.org/10.1016/j.molcel.2018.09.022> PMID: 30401431
27. Shin SY, Choi JH, Jung E, Gil HN, Lim Y, Lee YH. The EGR1-STAT3 Transcription Factor Axis Regulates α -Melanocyte-Stimulating Hormone-Induced Tyrosinase Gene Transcription in Melanocytes. *J Invest Dermatol*. 2019; 139(7):1616–9. <https://doi.org/10.1016/j.jid.2018.12.020> PMID: 30648541
28. Wang H, Mannava S, Grachtchouk V, Zhuang D, Soengas MS, Gudkov AV, et al. c-Myc depletion inhibits proliferation of human tumor cells at various stages of the cell cycle. *Oncogene* 2008; 27(13):1905–13. <https://doi.org/10.1038/sj.onc.1210823> PMID: 17906696

29. Inoue J, Kumagai H, Terada T, Maeda M, Shimizu M, Sato R. Proteolytic activation of SREBPs during adipocyte differentiation. *Biochem Biophys Res Commun*. 2001; 283(5):1157–61. <https://doi.org/10.1006/bbrc.2001.4915> PMID: 11355894
30. Natarajan VT, Singh A, Kumar AA, Sharma P, Kar HK, Marrot L, et al. Transcriptional upregulation of Nrf2-dependent phase II detoxification genes in the involved epidermis of vitiligo vulgaris. *J Invest Dermatol*. 2010; 13-(12):2781–9. <https://doi.org/10.1038/jid.2010.201> PMID: 20664557
31. Negroiu G, Branza-Nichita N, Petrescu AJ, Dwek RA, Petrescu SM. Protein specific N-glycosylation of tyrosinase and tyrosinase-related protein-1 in B16 mouse melanoma cells. *Biochem J*. 1999; 344(Pt 3 (Pt 3)):659–65. PMID: 10585852
32. Mikami M, Sonoki T, Ito M, Funasaka Y, Suzuki T, Katagata Y. Glycosylation of tyrosinase is a determinant of melanin production in cultured melanoma cells. *Mol Med*. 2013; 8(3):818–22. <https://doi.org/10.3892/mmr.2013.1602> PMID: 23900309
33. Semba H, Takeda N, Isagawa T, Sugiura Y, Honda K, Wake M, et al. HIF-1 α -PDK1 axis-induced active glycolysis plays an essential role in macrophage migratory capacity. *Nat Commun*. 2016; 7:11635. <https://doi.org/10.1038/ncomms11635> PMID: 27189088
34. Kim JW, Tchernyshyov I, Semenza GL, Dang CV. HIF-1-mediated expression of pyruvate dehydrogenase kinase: a metabolic switch required for cellular adaptation to hypoxia. *Cell Metab*. 2006; 3(3):177–85. <https://doi.org/10.1016/j.cmet.2006.02.002> PMID: 16517405
35. Buck MDD, O'Sullivan D, Klein Geltink RII, Curtis JDD, Chang CH, Sanin DEE, et al. Mitochondrial Dynamics Controls T Cell Fate through Metabolic Programming. *Cell*. 2016; 166(1):63–76. <https://doi.org/10.1016/j.cell.2016.05.035> PMID: 27293185
36. Valente AJ, Maddalena LA, Robb EL, Moradi F, Stuart JA. A simple ImageJ macro tool for analyzing mitochondrial network morphology in mammalian cell culture. *Acta Histochem*. 2017; 119(3):315–26. <https://doi.org/10.1016/j.acthis.2017.03.001> PMID: 28314612
37. Dif N, Euthine V, Gonnet E, Laville M, Vidal H, Lefai E. Insulin activates human sterol-regulatory-element-binding protein-1c (SREBP-1c) promoter through SRE motifs. *Biochem J*. 2006; 400(1):179–88. <https://doi.org/10.1042/BJ20060499> PMID: 16831124
38. Adams CM, Reitz J, De Brabander JK, Feramisco JD, Li L, Brown MS, et al. Cholesterol and 25-Hydroxycholesterol Inhibit Activation of SREBPs by Different Mechanisms, Both Involving SCAP and Insigs *. *J Biol Chem*. 2004; 279(50):52772–80. <https://doi.org/10.1074/jbc.M410302200> PMID: 15452130
39. Nishimura T, Inoue T, Shibata N, Sekine A, Takabe W, Noguchi N, et al. Inhibition of cholesterol biosynthesis by 25-hydroxycholesterol is independent of OSBP. *Genes Cells*. 2005; 10(8):793–801. <https://doi.org/10.1111/j.1365-2443.2005.00879.x> PMID: 16098143
40. Yoshida M, Hirotsu S, Nakahara M, Uchiwa H, Tomita Y. Histamine is involved in ultraviolet B-induced pigmentation of guinea pig skin. *J Invest Dermatol*. 2002; 118(2):255–60. <https://doi.org/10.1046/j.0022-202x.2001.01668.x> PMID: 11841541
41. Allan AE, Archambault M, Messana E, Gilchrist BA. Topically applied diacylglycerols increase pigmentation in guinea pig skin. *J Invest Dermatol*. 1995; 105(5):687–92. <https://doi.org/10.1111/1523-1747.ep12324466> PMID: 7594645
42. Berod L, Friedrich C, Nandan A, Freitag J, Hagemann S, Harmrolfs K, et al. De novo fatty acid synthesis controls the fate between regulatory T and T helper 17 cells. *Nat Med*. 2014; 20(11):1327–33. <https://doi.org/10.1038/nm.3704> PMID: 25282359
43. Everts B, Jha AK, Huang SCC, Sergushichev A, Lampropoulou V, Ivanova Y, et al. Network integration of parallel metabolic and transcriptional data reveals metabolic modules that regulate macrophage polarization. *Immunity*. 2015; 42(3):419–30. <https://doi.org/10.1016/j.immuni.2015.02.005> PMID: 25786174
44. Imokawa G, Yada Y, Kimura M, Morisaki N. Granulocyte/macrophage colony-stimulating factor is an intrinsic keratinocyte-derived growth factor for human melanocytes in UVA-induced melanosis. *Biochem J*. 1996; 313:625–31. <https://doi.org/10.1042/bj3130625> PMID: 8573102
45. Natarajan VT, Ganju P, Ramkumar A, Grover R, Gokhale RS. Multifaceted pathways protect human skin from UV radiation. *Nat Chem Biol*. 2014; 10:542–51. <https://doi.org/10.1038/nchembio.1548> PMID: 24937072
46. Loughrasithiphol P, Siddaway R, Loffreda A, Pogenberg V, Friedrichsen H, Schepsky A, et al. Tuning Transcription Factor Availability through Acetylation-Mediated Genomic Redistribution. *Mol Cell*. 2020; 79(3):472–487.e10. <https://doi.org/10.1016/j.molcel.2020.05.025> PMID: 32531202
47. Raja DA, Gotherwal V, Burse SA, Subramaniam YJ, Sultan F, Vats A, et al. pH-controlled histone acetylation amplifies melanocyte differentiation downstream of MITF. *EMBO Rep*. 2020; 21(1):48333. <https://doi.org/10.15252/embr.201948333> PMID: 31709752

48. Suzuki M, Shinohara Y, Ohsaki Y, Fujimoto T. Lipid droplets: Size matters. *J Electron Microsc (Tokyo)*. 2011; 60(SUPPL. 1):101–16. <https://doi.org/10.1093/jmicro/dfr016> PMID: 21844583
49. Schuler G, Hönigsmann H, Jaschke E, Wolff K. Selective accumulation of lipid within melanocytes during photochemotherapy (PUVA) of psoriasis. *Br J Dermatol*. 1982; 107(2):173–82. <https://doi.org/10.1111/j.1365-2133.1982.tb00335.x> PMID: 7104216
50. Pan Y, Tian T, Park CO, Lofftus SY, Mei S, Liu X, et al. Survival of tissue-resident memory T cells requires exogenous lipid uptake and metabolism. *Nature*. 2017; 543(7644):252–6. <https://doi.org/10.1038/nature21379> PMID: 28219080
51. O'Sullivan D, van der Windt GWJ, Huang SCC, Curtis JD, Chang CH, Buck MDL, et al. Memory CD8+ T Cells Use Cell-Intrinsic Lipolysis to Support the Metabolic Programming Necessary for Development. *Immunity*. 2014; 41(1):75–88. <https://doi.org/10.1016/j.immuni.2014.06.005> PMID: 25001241
52. Keller R, Wuthrich K. Computer-aided resonance assignment (CARA). Verl Goldau Cantina Switz. 2004.
53. Kageyama A, Oka M, Okada T, Nakamura SI, Ueyama T, Saito N, et al. Down-regulation of melanogenesis by phospholipase D2 through ubiquitin proteasome-mediated degradation of tyrosinase. *J Biol Chem*. 2004; 279(26):27774–80. <https://doi.org/10.1074/jbc.M401786200> PMID: 15067002

PAPER

Boolean model for melanogenesis

To cite this article: Pooja Dnyane and Chetan Gadgil 2021 *Phys. Biol.* **18** 026004

View the [article online](#) for updates and enhancements.

You may also like

- [Reliable dynamics in Boolean and continuous networks](#)
Eva Ackermann, Tiago P Peixoto and Barbara Drossel
- [The mathematics of a quantum Hamiltonian computing half adder Boolean logic gate](#)
G Dridi, R Julien, M Hliwa et al.
- [Anisotropy in finite continuum percolation: threshold estimation by Minkowski functionals](#)
Michael A Klatt, Gerd E Schröder-Turk and Klaus Mecke



 **EDINBURGH
INSTRUMENTS**

**WORLD LEADING
MOLECULAR
SPECTROSCOPY SOLUTIONS**

edinst.com

Physical Biology



PAPER

Boolean model for melanogenesis

RECEIVED
28 July 2020REVISED
27 November 2020ACCEPTED FOR PUBLICATION
15 December 2020PUBLISHED
17 February 2021Pooja Dnyane^{1,2} and Chetan Gadgil^{1,2,3,*} ¹ Chemical Engineering and Process Development Division, CSIR-National Chemical Laboratory, Dr Homi Bhabha Road, Pune 411008, India² Academy of Scientific and Innovative Research (AcSIR), CSIR-HRDC Campus, Ghaziabad 201002, India³ CSIR-Institute of Genomics and Integrative Biology, New Delhi 110020, India

* Author to whom any correspondence should be addressed.

E-mail: cj.gadgil@ncl.res.in**Keywords:** Boolean model, melanogenesis, signal transductionSupplementary material for this article is available [online](#)

Abstract

Melanogenesis is a highly regulated process through which the pigment melanin is produced in skin cells. Irregularities in the molecular events that govern the process of skin pigmentation can cause disorders like vitiligo. In order to understand the biology of disease progression, it is important to have an in depth understanding of intracellular events. Mathematical models provide an integrated view of intracellular signalling. There are very few models to date that incorporate intracellular processes relevant to melanogenesis and only one to our knowledge that simulates the dynamics of response to varying levels of input. Here, we report the formulation of the largest Boolean model (265 nodes) for melanogenesis to date. The model was built on the basis of a detailed interaction network graph published by Raghunath *et al.* Through additional manual curation of the reported interactions, we converted the graph into a set of Boolean rules, following the procedure of the first Boolean model (62 nodes) for melanogenesis published by Lee *et al.* Simulations show that the predicted response to varying UV levels for most of the nodes is similar to the predictions of the existing model. The greater complexity allows investigation of the sensitivity of melanin to additional nodes. We carried out perturbation analysis of the network through node deletion and constitutive activation to identify sensitivity of outcomes, and compared the nodes identified as sensitive to previous reports.

1. Introduction

Skin, the largest organ in the human body, is made up of various types of cells. These cells interact in a highly coordinated manner to maintain homeostasis of skin thickness, composition, and pigmentation. Depending on their function, these cells reside within different layers of the skin, viz, the epidermis, dermis and subcutaneous fat. The epidermis is the uppermost layer of the skin. It is a mechanical and antimicrobial barrier. It also controls skin pigmentation, chiefly through the activities of melanocytes and keratinocytes [1].

The process of skin pigmentation, also known as ‘melanogenesis’, is quite complex. Among other conditions, it gets triggered when skin is exposed to external stimuli such as UV radiation. Keratinocytes, upon UV stimulation, produce various substances like alpha-MSH, SCF, prostaglandin and endothelin-

1 that enhance melanogenesis [2–4]. These substances get transported to nearby melanocytes and, through a series of signalling events, induce paracrine activation of microphthalmia-associated transcription factor (MITF). MITF in turn activates tyrosinase, the key enzyme in this process. Tyrosinase converts amino acids like tyrosine and cysteine into subunits of eumelanin or pheomelanin pigment in organelles called melanosomes. After maturation these melanosomes are transported to multiple keratinocytes with the help of melanocyte dendrites. In keratinocytes, melanosomes surround the nucleus and pigments in these organelles absorb UV radiation, thus protecting cell DNA from damage [5]. An imbalance in molecular signals that govern these events may result in disorders of pigmentation such as vitiligo, or other skin conditions ranging from rashes to psoriasis [6]. These disorders could lead to physiological impairment, and also to social ostracism

and resulting psychological problems as in the case of vitiligo, which has a significant incidence in the Indian population.

In order to develop optimal treatment protocols, a detailed understanding of the molecular events that lead to these diseases is required. Mathematical models of intracellular interactions help in furthering our understanding of the system function. These models present an integrated view of intracellular signalling, metabolism and interaction between cell types. Models are typically constructed based on available information in the literature on the interactions between individual components in the network. Such a network of interactions can either be analysed as a graph, or further information on the nature of the interactions can be added to simulate system dynamics. A 'complete' description includes the stochasticity inherent in the reactions. Ordinary differential equations resulting from a mass balance on system components are used to simulate the mean dynamics of each component. Both these approaches require knowledge of the rate constants for individual reactions. A coarser approach discretizes system states into a finite number of allowed values, at a minimum 2 in case of Boolean models.

Boolean models have been used for the analysis of several biological interaction networks, and a few are discussed here as examples. Kauffman [7] used random Boolean networks, which are ensembles of random network structures, for studying dynamical properties of gene regulatory networks. Albert and Othmer [8] developed a Boolean model for the gene network that governs embryonic segmentation in *Drosophila*. The model was able to reproduce wild-type expression pattern and ectopic expression pattern, experimentally observed in various mutants. Saez-Rodriguez *et al* [9] constructed the signalling network for T-cells by collecting data from the literature and from their own experiments. By converting this logical model into an interaction graph, the authors were able to extract important features like feedback loops, signalling paths, and network-wide interdependencies. The model was also able to capture the phenotypes of this network for both wild type and perturbed conditions. Faure *et al* [10] transformed a generic model of mammalian cell cycle into a logical regulatory graph. The model helped them in assessing the advantages and limitations of synchronous versus asynchronous updating scheme in understanding the asymptotical behaviour of regulatory networks. Several other models have also been used to analyse intracellular networks [11].

There are very few models to date that incorporate intracellular metabolism relevant to skin pigmentation in keratinocytes and melanocytes. Rodriguez-Lopez *et al* [12] formulated a kinetic model for the melanin biosynthesis pathway. The pathway comprised of 12 nodes, including metabolites from tyrosine to dopachrome. The model

explained lower catalytic efficiency of the enzyme tyrosinase on monophenols (tyrosine) than on diphenols. Emir and Kurnaz [13] devised an integrated, 18 component model for melanocyte-specific gene expression and melanogenesis. The model successfully showed that upon stimulation/inhibition of certain growth factors in the system, the melanin output can be upregulated/downregulated. Thingnes *et al* [14] defined a 7-component model for distribution of melanin in keratocytes during the process of skin tanning. It predicts the thickness of epidermal layer and how far the melanocyte dendrite grows after exposure to UV radiation. Oyehaug *et al* [15] developed a mathematical model comprising of 28 nodes to understand the switch between eumelanin and pheomelanin production depending upon an extracellular signal. Their results supported Ito's hypothesis that melanogenic switching is due to covalent binding of the intermediate dopaquinone to the enzyme glutathione reductase. Raghunath *et al* [16] constructed a graphical network of 265 nodes for melanogenesis. They used a graph theoretical analysis of this network to determine essential nodes in the network which upon deletion disrupt the signalling between source (UV and other inputs) and target (pigmentation and survival) nodes. Subramanian *et al* [17] developed a novel systems biology based computational platform called 'eSkin'. The platform contains a network of 35 manually-curated pathways and 2600 + genes. The proprietary platform was specially designed to aid skin centric analysis and interpretation of omics data. Here, as also in the Raghunath model, interactions are defined qualitatively as connections/edges, and dynamics are not simulated. In a pioneering effort, Lee *et al* [2] developed a Boolean model for melanogenesis network consisting of 62 nodes. Their analysis suggest that inhibition of beta-catenin is the most effective and safe way to reduce UV-B induced skin pigmentation.

Here, we report the formulation of a Boolean model based on the nodes included in the Raghunath *et al* network. The interactions of the 265 nodes in that network were described using 23 different terms (activation, phosphorylation etc). Through additional manual curation of the reported interactions, we have converted this description into a set of Boolean rules, and formulated the largest Boolean model for melanogenesis reported to our knowledge. We compared several aspects of the dynamics of this new model with the Lee model for melanogenesis and show that the predicted response to varying UV levels for most of the common nodes is similar to the predictions of the Lee model. Our model has 203 additional nodes, which allows investigation of the dynamics and effect of many more known mediators of melanogenesis. We also carried out a perturbation analysis of the network through node deletion and constitutive activation to identify

Table 1. Types of interactions and their distribution in network.

S. No.	Expression relation	Frequency	S. No.	Expression relation	Frequency
1	Increases level	23	13	Catalysis	7
2	Induces	25	14	Decreases	1
3	Inhibits	24	15	Decreases expression	1
4	Activates	195	16	Dissociates to	7
5	Associates	1	17	Forms complex	18
6	Binds	1	18	Gets converted to	16
7	Increases expression	80	19	Induces complex dissociation	6
8	Increases	3	20	Induces complex formation	3
9	Increases expression	1	21	Inhibits expression	1
10	Increases release	6	22	Involved in	1
11	Increases stability	1	23	Phosphorylates/activates/degrades	3
12	Regulates	5			

sensitivity of outcomes such as melanin to individual nodes, and compared the nodes identified as important to previous reports for smaller melanogenesis networks.

2. Materials and methods

2.1. Building the Boolean model

The comprehensive network model for UV-mediated skin pigmentation constructed by Raghunath *et al* [16] was used as the basis for our Boolean model. It consists of 265 components and 429 directed interactions between them. The 265 nodes represent proteins, small molecules, complexes, biological processes and environmental factors. Of these nodes, 20 are source/input nodes and 9 are output nodes. Raghunath *et al* identified essential signalling components (nodes) by performing shortest path analysis. We formulated Boolean rules corresponding to each edge of the network.

The extensive details provided by Raghunath *et al* in the form of literature references for individual interactions provide an excellent starting point for transforming this model into a Boolean model. Based on this and other available information, we constructed a Boolean model of this network. The directions of edges mentioned in the Raghunath *et al* [16] network is dependent on the functional nature of the interaction, for e.g. ‘phosphorylation’ or ‘activation’. Likewise, there are a total of 23 interaction types (table 1). We have re-visited each interaction and added further precision through formulation of Boolean rules. We believe that doing so will make the model more biologically relevant and enable simulation of system dynamics, including system response to varying UV levels. As an example of Boolean rules resulting in greater definition, when there are two or more nodes that positively influence the activity of a target node, either one of the inputs could suffice to change the activity level (i.e. an OR gate), or all could be required (AND gate), but it is also possible that a combination of AND and OR is representative of the biology (some nodes are required, some are redundant). As such, a detailed

Table 2. Individual interactions for caspase 3 in keratinocyte as defined in [16].

Input node	Target node	Interaction type
CASP8_kerat	CASP3_kerat	Activates
CASP9_kerat	CASP3_keart	Activates
MAPK14_kerat	CASP3_keart	Activates
PRKCD_kerat	CASP3_keart	Activates
PRKCH_kerat	CASP3_keart	Inhibits

Table 3. Individual interactions for CREB1 as defined in [16].

Input node	Target node	Interaction type
AKT1_melan	CREB1_melan	Activates
MAPK14_melan	CREB1_melan	Activates
PRKACA_melan	CREB1_melan	Activates
PRKG1_melan	CREB1_melan	Activates
PRK6KA1_melan	CREB1_melan	Activates

examination of the literature is necessary, since stipulating either an AND or an OR mode for the interaction will not accurately represent the biology. We did not use any general assumption while forming the Boolean rules. Given below are a few examples of how we defined interactions (see tables 2–4) to develop Boolean rules. Node nomenclature follows the format name_location, where location is either ‘kerat’ or ‘melan’ representing the keratinocyte and melanocyte respectively.

Caspases 9 and 8 are the upstream members of the apoptotic protease cascade (initiator caspases) that cleave and activate caspase 3 (executioner caspase) which subsequently carries out the mass proteolysis that leads to apoptosis [18, 19]. Caspases 9 and 8 acts through different pathways, viz intrinsic and extrinsic, and hence only one of them is required to activate downstream caspase 3. In Boolean terms, it is translated as either Casp8 OR Casp 9 is required. PRKCD is also known to translocate to mitochondria by UVB stimulation, where it triggers apoptosis by caspase 3 activation [20]. Although it is unclear how PRKCH blocks caspase 3 activity, it may be possible that the protein interacts with and activates MAPK14 and thus indirectly inhibits caspase 3 as MAPK14 can directly phosphorylate and inhibit the activities of caspase 8

Table 4. Individual interactions for pheomelanin as defined in [16].

Input node	Target node	Interaction type
Cysteiny1_DOPA_melan	Pheomelanin_melan	Gets converted to
Glutathionyl_DOPA_melan	Pheomelanin_melan	Gets converted to

and caspase 3 [20, 21]. Taking together all the information, Boolean rule for caspase 3 can be written as:

$$\text{CASP3_kerat} = (\text{CASP9_kerat} \text{ OR } \text{CASP8_kerat}) \text{ AND } ((\text{NOT}(\text{MAPK14_kerat})) \text{ OR } \text{PRKCD_kerat}).$$

The indirect regulation by PRKCH is included through its effect on MAPK14_kerat (see SI <https://stacks.iop.org/PB/18/026004/mmedia> for Boolean rule for MAPK14_kerat).

Phosphorylation of CREB is required for the activation of the transcription factor. This can be achieved through two alternate ways i.e. via cAMP/PRKACA signalling or by involvement of Akt, MAPK14, PRKG1 and PRS6KA1 [22–27]. Either cAMP or PRKACA is sufficient for CREB1 activation. In their absence, Akt, MAPK14, PRKG1 and PRS6KA1 are all required for activation via serine-133 phosphorylation. Therefore, the Boolean rule for CREB1 is:

$$\text{CREB1_melan} = (\text{cAMP_melan} \text{ OR } \text{PRKACA_melan}) \text{ OR } (\text{AKT1_melan} \text{ AND } \text{MAPK14_melan} \text{ AND } \text{PRKG1_melan} \text{ AND } \text{RPS6KA1_melan}).$$

If cysteine or glutathione is present in the system, it reacts with DOPAquinone to produce cysteinylDOPA/glutathionylDOPA and the benzothiazine derivatives of pheomelanin [28]. Hence the rule for pheomelanin is:

$$\text{Pheomelanin_melan} = \text{glutathionyl_DOPA_melan} \text{ OR } \text{cysteinyl_DOPA_melan};$$

Likewise, rules for all 265 nodes were constructed based on a manual curation. All the rules are listed in the SI, both as truth tables and logical rules. All simulations were carried out using Matlab 9.5 (R2018b, Mathworks). Synchronous updating is used for all the simulations. For both the Lee model and new model simulations, the UV input percentage was varied by fixing the percentage of updating steps when the UV node state is on to be equal to the UV percentage. Then the string of zeros and ones was randomized using the Matlab function `randperm` such that there is no pattern to the on and off state sequence.

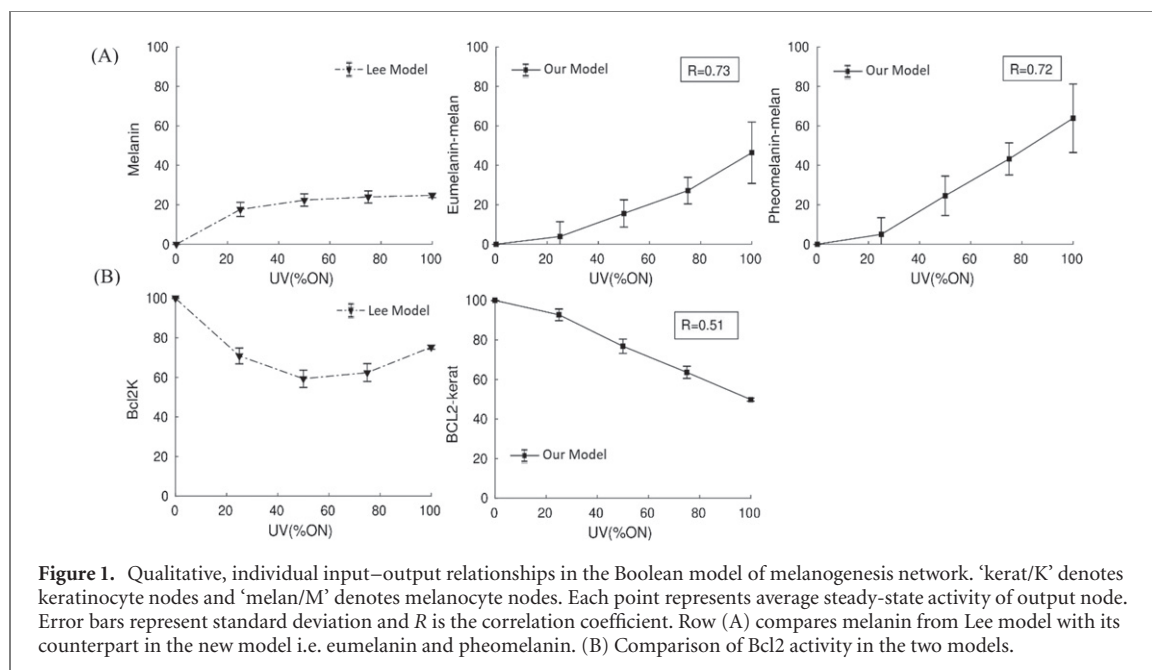
2.2. Comparison with the existing model

So far, the largest known Boolean model for melanogenesis is the pioneering model by Lee *et al* which consists of 62 nodes [2]. After comparing the networks designed by Lee *et al* and this work, it was found that 56 components are common between them. We

compared our results for node sensitivity of these 56 common nodes with the sensitivity reported by both these reports. In addition, Lee *et al* used simulations of their Boolean model to predict the response of individual nodes to different levels of UV input. We carry out simulations with synchronous updating as previously described [29] and report the similarity in profiles for the 56 common nodes in terms of the Pearson correlation coefficient for the UV-response of these nodes. Correlation between a node in this model and the corresponding node in the Lee model is calculated for steady state values/output using the equation $R_i = \text{correlation}(S_i^l, S_i^n)$, where R is the Pearson correlation coefficient, S_i^l is a vector representing steady state activity of node i in the Lee model for all levels of UVB inputs and S_i^n is a vector representing steady state activity of the same node (i) in the new model reported here. We note that the Pearson correlation coefficient is a crude measure for such a comparison of results from a qualitative model simulated with a random input sequence for each UV level. Its interpretation is intended to be qualitative in nature (i.e., roughly similar, indicated by a substantial positive value, or anticorrelated, indicated by a large negative value) rather than as a quantitative similarity measure.

2.3. Perturbation analysis

Boolean networks are often analysed to identify sensitive nodes which on perturbation disproportionately change a predefined output. In our case, we used as the predefined output pigmentation related nodes and cell survival nodes present in melanocyte and keratinocyte, identical to those used by Lee *et al*. We used two different types of perturbation methods, i.e. constitutive activation and inhibition, to identify sensitive nodes in the melanogenesis network [2]. Lee *et al* developed these methods to identify safe and effective targets in the network for reduction of pigmentation as measured by the state of the output nodes. To this end, constitutive activation and constitutive inhibition of each node was simulated by setting the node state to 1 and 0, respectively. The UV input was varied from 0% (always off) to 100% (always on). A ‘wild-type’ profile of the average state of each node at each UV level was obtained in the absence of any perturbation. Sensitivity of each node was estimated by calculating the post-perturbation change in the profile of the four output nodes: B-cell chronic lymphocytic leukemia/lymphoma 2 (Bcl2) in keratinocyte (Bcl2K), Bcl2 in melanocyte (Bcl2M), eumelanin and pheomelanin.



3. Results

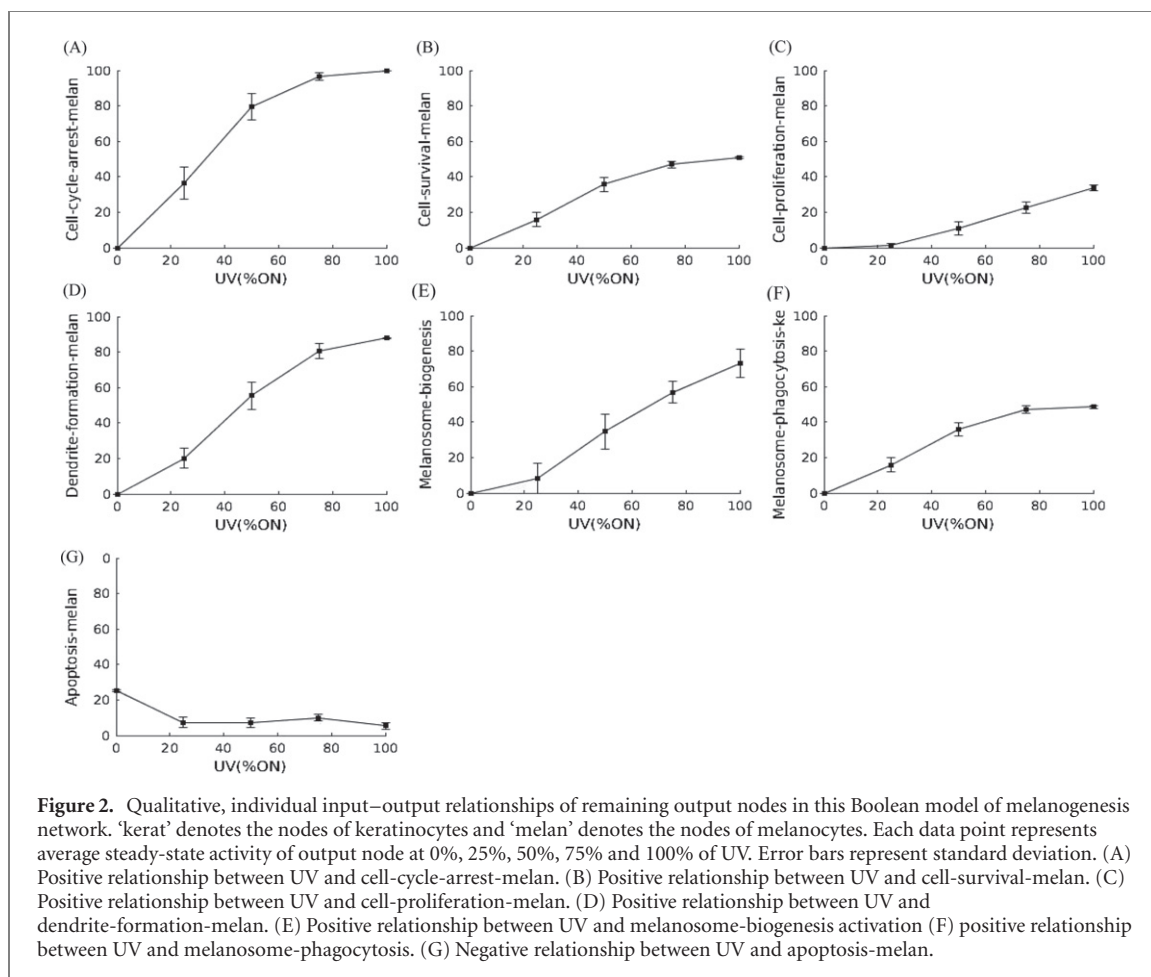
3.1. New model for melanogenesis captures the system response to UV

Although the state space of this melanogenesis network is huge (2^{265} states), by performing simulations for 2000-updating steps, we found that system attains steady state within 1000 steps. We carried out simulations for 10, 50, 100 and 150 initial conditions. Mean and standard deviation values remain almost unchanged with the use of 100 or higher initial conditions. Simulations were carried out using parameters specified in our previous work [29]. To compute the ‘steady-state’ activity of each node with varying levels of input stimulation, we ran the simulation for 1000 updating steps and used the average of the final 100 updating steps as the attractor mean value. For each simulation run, the UV input was assigned a probability of being randomly on or off. The intensity of UVA and UVB was set to 0%, 25%, 50%, 75% and 100%. Initial states of all nodes were randomized in every run (50% ‘0’ and 50% ‘1’) and mean value reported is the mean for 100 such initial conditions. The pigmentation state and the apoptotic balance of the cells were determined by observing the steady-state activities of the output nodes eumelanin, pheomelanin and BCL2-kerat.

The results (figure 1) show that this melanogenesis network model captures the qualitative features of the known biological activities of the species in the system. There are literature reports which suggest that the exposure to UV radiation increases skin pigmentation. For instance, in an experimental study, Tadocoro *et al* [30] showed that exposure to UV radiation significantly increases the level of melanin in the skin. Melanin, which exists mainly in two

forms in human body i.e. eumelanin and pheomelanin. In another study by Gillardon *et al*, [31] it was shown that UV irradiation of mammalian skin cells in culture results in decline of Bcl-2 transcripts. The apparent non-monotonicity seen in figure 1 for Bcl2-K in the Lee model simulation is heavily dependent on a single point, and up to 80% UV no significant nonmonotonicity is seen. As such, we conclude that both models predict a decrease in Bcl2-K levels with UV, which is consistent with the experimental reports. Apart from eumelanin and pheomelanin, there are 7 other terminal nodes in graphical network of Raghunath *et al* [16]. These nodes are cell-cycle-arrest-melan, cell-proliferation-melan, cell-survival-melan, dendrite-formation-melan, melanosome-biogenesis, melanosome-phagocytosis and apoptosis-melan. The model successfully captured qualitative response of these target nodes to changing UV levels (figure 2). In the study by Gillardon *et al*, [31] it was also shown that UV irradiation of mammalian skin cells causes growth arrest and cell death followed by hyperproliferation of epidermal cells.

Scott and Cassidy [32] showed that dendrite formation in melanocytes is stimulated by hormones and ultraviolet light exposure. While studying the physiology of pigmentation, Bessou *et al* [33] observed that UV irradiation accelerates melanosome transfer from dendritic melanocyte to keratinocyte. In another study, Bivik *et al* [34] demonstrated that when melanocytes are exposed to UV radiation, anti-apoptotic factors like Bcl-2 get translocated to mitochondria where they stop the release of cytochrome C in the cytoplasm and ultimately protects the cell from apoptosis. Despite the large network and formulation of Boolean rules individually for each node, the model predictions of output response to



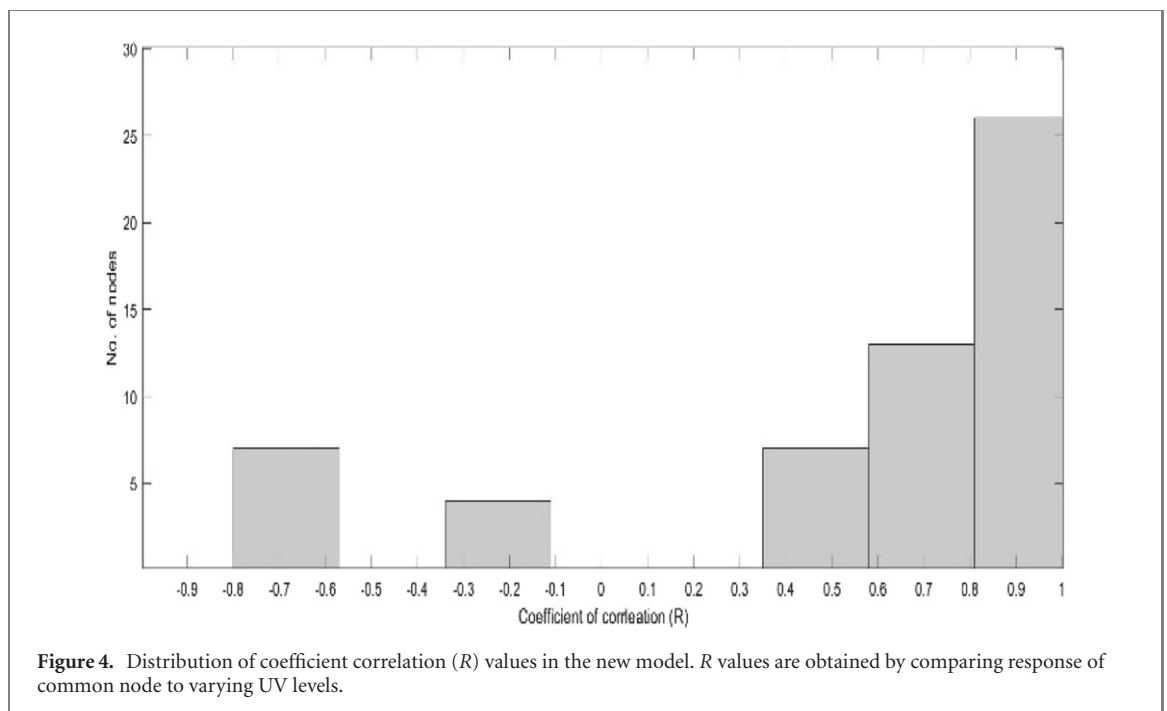
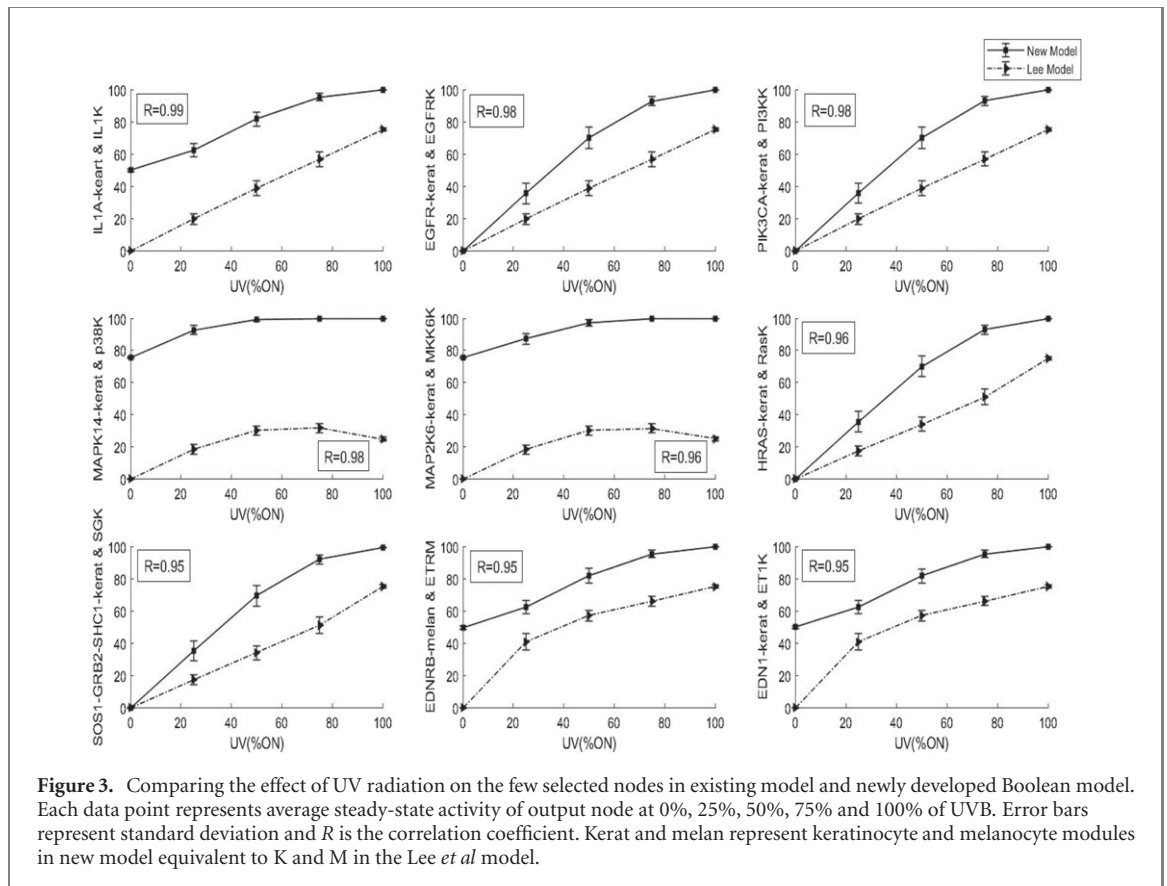
varying UV are consistent with these experimental reports.

3.2. Comparison with the Lee model

We compared the output of the Lee *et al* [2] model with our results. The similarity between the nodes are quantified using correlation coefficient. Correlation between a node in this model and the corresponding node in the Lee model is calculated for steady state values/output using the equation defined in the methods section. This measure is similar to what we have used in our previous study to identify sensitive nodes [29]. A few nodes with their corresponding correlation coefficients are shown in figure 3 [35]. Out of 56 common nodes between the models, 46 were positively correlated ($R_i > 0.3$, see figure 4). These include important nodes as defined by Lee *et al* (eumelanin, pheomelanin, Bcl-2 in keratinocytes and melanocytes). The list of negatively correlated nodes includes kinases and few other nodes like adenylate cyclase and CREB. Comparison of the Boolean rule between the two models (see SI for details) showed that for a few nodes the rules and regulating nodes are exactly similar. However, for several others, participating nodes in Boolean rule are different, which is expected due to the presence of additional nodes in the new network.

3.3. Identification of sensitive nodes in the new model

Effect of perturbations in this melanogenesis network is calculated by measuring a change in the activity profile of the output nodes eumelanin, pheomelanin Bcl2_melan and Bcl2_kerat relative to the respective unperturbed output profiles, for the inputs of 0%, 25%, 50%, 75% and 100% UVB. Since these perturbations mimic the effect of knock out and continuous activation, the perturbed nodes that caused constant activation/inactivation of output nodes (pheomelanin, eumelanin, BCL2_kerat and BCL2_melan nodes) were selected as sensitive (table 5). As specified in the methods section, value for the last 100 of the 1000 simulation steps was used. Since the system reaches an attractor state before this point, it is equivalent to the condition that for all the accessed attractor states the value of these output nodes should be either 1 or 0. Such nodes were marked as ‘sensitive’ since this is a qualitative departure from the unperturbed system dynamics. The comparison (table 5) shows that the new model has a significantly large number of sensitive nodes which is obvious given the larger size and complexity. The number of common sensitive nodes consistently identified among two models are fewer and include obvious ones like MITF and CREB which serves as the key transcription factors in regulating the



melanogenesis process. There is experimental support for the importance of nodes which are not the part of Lee *et al* model but are identified as sensitive in new model. For example, DOPAchrome and tyrosinase are identified as sensitive in this model. It is known that cysteine or glutathione reacts with DOPAquinone to produce the benzothiazine

derivatives of pheomelanin. TYR_melan(tyrosinase) catalyses the tautomerization of DOPAchrome to 5,6-dihydroxyindole-2-carboxylic acid (DHICA), which is later oxidized to eumelanin [28]. It has been experimentally shown that inhibition of lipid peroxidation by protocatechuic acid leads to inhibition of melanin production in α -MSH-induced B16 cells [36]. 4-HNE

Table 5. Nodes influencing melanin, Bcl2-melan and Bcl2-kerat activities when subjected to constitutive activation and inhibition. Underlined nodes are consistently predicted as sensitive by both models.

	Activation (Lee <i>et al</i>)	Inhibition (Lee <i>et al</i>)	Activation (new model)	Inhibition (new model)
Eumelanin	<u>MITF</u> proteinM, ASK1M, <u>cAMPM</u> , MKK6M, p38M, GSK3bM	ERKM, AktM, PI3KM, <u>RafM</u> , PDK1M, MEKM, <u>MITF</u> proteinM, bcateninM, CREBM, <u>MITF</u> mRNAM	ACTH_kerat, ADCY4_melan, alpha_MSH_kerat, <u>cAMP_melan</u> , <u>CREB1_melan</u> , indole_5_6_quinone_carboxylic_acid_melan, indole_5_6_quinone_melan, <u>MITF_melan</u> , PRKACA_melan, TP53_kerat, TYR_melan, HRAS_melan, MAP2K1_melan, MAP2K2_melan, MAPK1_melan, MAPK3_melan, <u>RAF1_melan</u> , RPS6KA1_melan, SOS1_GRB2_SHC1_melan	FourHNE_kerat, ADCY4_melan, alpha_MSH_kerat, calcium_cyt_kerat, <u>cAMP_melan</u> , CASP3_kerat, ceramide_kerat, <u>CREB1_melan</u> , DFFB_DFFA_kerat, DFFB_kerat, DNA_damage_kerat, DOPA_melan, DOPAchrome_melan, DOPAquinone_melan, IKBKA_kerat, IP3_kerat, lipid_peroxidation_kerat, MITF_EP300_melan, <u>MITF_melan</u> , NFKB1_kerat, PKC_kerat, PLC_kerat, PRKCB_melan, PRKCZ_kerat, RYR1_kerat, TNF_kerat, TYR_melan, HRAS_melan, <u>RAF1_melan</u> , SOS1_GRB2_SHC1_melan
Pheomelanin			ACTH_kerat, ADCY4_melan, alpha_MSH_kerat, cAMP_melan, <u>CREB1_melan</u> , cysteinyl_DOPA_melan, DOPAquinone_melan, glutathionyl_DOPA_melan, <u>MITF_melan</u> , PRKACA_melan, TP53_kerat, TYR_melanLG_kerat	FourHNE_kerat, ADCY4_melan, calcium_cyt_kerat, cAMP_melan, CASP3_kerat, ceramide_kerat, <u>CREB1_melan</u> , DFFB_DFFA_kerat, DFFB_kerat, DNA_damage_kerat, DOPA_melan, DOPAquinone_melan, IKBKA_kerat, IP3_kerat, lipid_peroxidation_kerat, <u>MITF_melan</u> , NFKB1_kerat, PKC_kerat, PLC_kerat, <u>PRKCB_melan</u> , PRKCZ_kerat, RYR1_kerat, TYR_melan, HRAS_melan, <u>RAF1_melan</u> , SOS1_GRB2_SHC1_melan
BCL2-kerat	ASK1K, MKK6K, p38K, AktK, EGFRK, PI3KK, PDK1K, Bcl2K, MITFproteinM		ACTH_kerat, TP53_kerat	FourHNE_kerat, calcium_cyt_kerat, CASP3_kerat, ceramide_kerat, DFFB_DFFA_kerat, DFFB_kerat, DNA_damage_kerat, IKBKA_kerat, IP3_kerat, lipid_peroxidation_kerat, NFKB1_kerat, PKC_kerat, PLC_kerat, PRKCZ_kerat, RYR1_kerat
BCL2-melan	AktM, PI3KM, PDK1M, ASK1M, <u>cAMPM</u> , MKK4M, MKK6M, p38M, JNKM, <u>MITF</u> proteinM, p53M	AktM, PI3KM, PDK1M	ACTH_kerat, ADCY4_melan, alpha_MSH_kerat, <u>cAMP_melan</u> , <u>CREB1_melan</u> , <u>MITF_melan</u> , PRKACA_melan, TP53_kerat	HRAS_melan, <u>RAF1_melan</u> , SOS1_GRB2_SHC1_melan, NGF_kerat, FourHNE_kerat, ADCY4_melan, calcium_cyt_kerat, <u>cAMP_melan</u> , CASP3_kerat, ceramide_kerat, <u>CREB1_melan</u> , DFFB_DFFA_kerat, DFFB_kerat, DNA_damage_kerat, IKBKA_kerat, IP3_kerat, lipid_peroxidation_kerat, NFKB1_kerat, PKC_kerat, PLC_kerat, PRKCZ_kerat, RYR1_kerat

is a highly reactive lipid aldehyde that is generated from ultraviolet radiation induced lipid peroxidation reactions [37]. PLC is responsible for the production of IP3 and DAG, both of which function as secondary messengers. DAG activates PKC, which in turn activates other cytosolic proteins such as NFKB [38, 39]. KIT is a keratinocyte derived growth factor secreted by keratinocytes and fibroblasts which activates a signalling pathway comprising of KIT receptor, SHC protein, GRB2 and SOS, leading to the phosphorylation of Ras, which in turn activates Raf-1 and MAPK signalling pathway [40]. This cascade of activation induces MITF phosphorylation which in turn allows the recruitment of the transcriptional coactivator CREB [41, 42] and leads to subsequent

transcription of melanogenic enzymes TYR, TYRP1 and TYRP2 [43].

4. Discussion

We developed a new 265-node Boolean model for melanogenesis, compared it with the existing model and identified sensitive nodes in the network. The model builds upon two excellent resources, the interaction network constructed by Raghunath *et al*, and the Boolean model constructed by Lee *et al*. The dynamic model closest to this work is the pioneering 62-node Lee *et al* model for skin pigmentation. It is the only Boolean model for melanogenesis available in public domain. However, the model is smaller and

does not include intricate details of the melanogenesis process. For example, the intermediate components that connect MITF to melanin production such as tyrosine, L-DOPA, cysteinyl L-DOPA, DOPAquinone and TYRP1 are not the part of Lee model [44, 45]. Biological processes such as melanosome biogenesis, dendrite formation and melanosome phagocytosis are crucial in explaining the transfer of melanin to upper layer of skin and details about these are included in the network constructed by Raghunath *et al*, which is the basis for the nodes in this model.

We find that most common nodes respond in a similar way to UV stimulus as has been reported by Lee *et al*. Despite there being many more intermediate nodes between the UV input and the output nodes, the output nodes such as melanin, Bcl-2, beta-catenin and MITF have a correlation value >0.5 . As such, we see that expansion of the network does not lead to a fundamental change in the predictions of the smaller Lee model. We believe that this work constitutes an improvement over the existing model since more details of the molecular interactions are included, and it is possible to dissect the effect of individual components that are lumped together in the Lee model.

A few nodes show a different response to increasing UV levels in the two models. A detailed discussion of all 11 anti-correlated nodes including their response to UV in the Lee model and this model, and the literature references is given in the SI. It is seen that though there are some nodes that show an unambiguously different behaviour (increasing with UV in one model and decreasing in the other), from our survey of the literature, we find that the new larger model is more consistent with the experimental literature. Several responses are seemingly non-monotonic, among which are alpha-MSH_kerat, MC1R_melan, TP53_kerat, and TP53_melan. In the Lee *et al* model, these substances show an initial increase followed by gradual decrease in expression whereas in new model their expression keeps increasing with higher dose of UV. We have also come across experimental studies that supports the prediction that expression of these substance does increase after UV stimulation. While studying the pigimentary responses in mouse melanoma cells, Chakraborty *et al* found that epidermal melanocytes and keratinocytes respond to UVR by increasing their expression of alpha-MSH and ACTH, which up-regulate the expression of MC1R [46].

After subjecting the system to two kinds of perturbation i.e. inhibition and constitutive activation we identified many sensitive nodes which drastically changes the activity of output nodes eumelanin, pheomelanin and Bcl-2. MITF, cAMP and CREB are among the few nodes that are commonly identified as sensitive in both the models (table 5). There are

several studies that claim that MITF is a key regulator of melanogenesis and its inhibition leads to termination of the process [47–49]. It is also known that cAMP and CREB are located upstream to MITF and tyrosinase [2, 50]. Therefore, modulation in their activity definitely affects the melanin level in the skin [49]. There are a few nodes that are not identified as sensitive in Lee model but here are identified as important for the Bcl2 activity in keratinocytes and melanocytes. NFKB1, ADCY4, TP53, PKC and PRKCZ are few of them. These results are consistent with the experimental data. For instance, while investigating the role of NFKB in skin biology, Fullard *et al* found that knocking out the gene or its constitutive activation lead to epidermal hyperplasia in mice [51]. The study identified NFKB as a master regulator of epidermal homeostasis. TP53 plays key role in keratinocyte-melanocyte signalling. Based on a binding site analysis of TP53, Wei *et al* showed that most of the major paracrine factors that are released from keratinocytes after UV exposure are potentially regulated by p53 and its disruption may result in deregulation cytokine signalling in keratinocytes [52]. In another study Li *et al* studied the role of PKC and its isoforms. Their result suggested that overexpression of PKC and its isoform provide a negative regulation for Akt phosphorylation and kinase activity in mouse keratinocytes and serve as modulators of cell survival pathways in response to external stimuli [53].

It would be interesting to carry out a comparative analysis of the dynamics of both the Lee model and this model to comprehensively map the number of attractors and their basins of attraction. In both cases, for 100% UV, the system reaches a number of cyclic attractors. Nodes corresponding to melanin are active only in a fraction of these states. This is the reason why simulation of both models shows that melanin does not reach 100% when the UV is always on (UV = 100%). For our model, in the 100 initial states sampled, we find 16 distinct attractors ranging in size from fixed points to 16-node cyclic attractors. Eumelanin and/or pheomelanin is active in about 8 of the 16 states comprising each of the large attractors. Despite the richness of the dynamical system attractor space, we find that the mean values of the output nodes do not differ appreciably even when larger number of initial conditions are sampled. This is consistent with the Lee model simulations that showed similar distribution of basin size with sampling size. It would be interesting to see if there is a common regulatory logic backbone underlying the two independently-constructed models.

The model presented here is the largest Boolean model for melanogenesis reported to date, with about four-fold more nodes. We believe it will provide a tool for the simulation and analysis of the complex interplay between keratinocytes and melanocytes that results in melanogenesis.

Acknowledgments

PD acknowledges funding through a senior research fellowship from CSIR. CG acknowledges funding from CSIR through project BSC0302.

ORCID iDs

Chetan Gadgil  <https://orcid.org/0000-0002-1728-0796>

References

- [1] Gould J 2018 Superpowered skin *Nature* **563** S84–5
- [2] Lee H-S, Goh M-J, Kim J, Choi T-J, Kwang Lee H, Joo Na Y and Cho K-H 2015 A systems-biological study on the identification of safe and effective molecular targets for the reduction of ultraviolet B-induced skin pigmentation *Sci. Rep.* **5** 10305
- [3] Slominski A and Pawelek J 1998 Animals under the sun: effects of ultraviolet radiation on mammalian skin *Clin. Dermatol.* **16** 503–15
- [4] Natarajan V T, Ganju P, Ramkumar A, Grover R and Gokhale R S 2014 Multifaceted pathways protect human skin from UV radiation *Nat. Chem. Biol.* **10** 542–51
- [5] Park H-Y and Yaar M 2012 *Chapter 72 Biology of Melanocytes Fitzpatrick's Dermatology in General Medicine* ed L A Goldsmith, S I Katz, B A Gilchrist, A S Paller, D J Leffell and K Wolff (New York: McGraw-Hill)
- [6] Mathes S H, Ruffner H and Graf-Hausner U 2014 The use of skin models in drug development *Adv. Drug. Deliv. Rev.* **69–70** 81–102
- [7] Kauffman S A 1969 Metabolic stability and epigenesis in randomly constructed genetic nets *J. Theor. Biol.* **22** 437–67
- [8] Albert R and Othmer H G 2003 The topology of the regulatory interactions predicts the expression pattern of the segment polarity genes in *Drosophila melanogaster* *J. Theor. Biol.* **223** 1–18
- [9] Saez-Rodriguez J *et al* 2007 A logical model provides insights into T cell receptor signaling *PLoS Comput. Biol.* **3** 1580–90
- [10] Fauré A, Naldi A, Chaouiya C and Thieffry D 2006 Dynamical analysis of a generic Boolean model for the control of the mammalian cell cycle *Bioinformatics* **22** 124–31
- [11] Wang R-S, Saadatpour A and Albert R 2012 Boolean modeling in systems biology: an overview of methodology and applications *Phys. Biol.* **9** 055001
- [12] Rodríguez-López J N, Tudela J, Varón R, García-Carmona F and García-Cánovas F 1992 Analysis of a kinetic model for melanin biosynthesis pathway *J. Biol. Chem.* **267** 3801–10
- [13] Emir U E and Kurnaz I I A 2003 An integrated model for melanocyte-specific gene expression and melanogenesis *Signal Transduct.* **3** 209–17
- [14] Thingnes J, Øyehaug L, Hovig E and Omholt S W 2009 The mathematics of tanning *BMC Syst. Biol.* **3** 60
- [15] Øyehaug L, Plahte E, Våge D I and Omholt S W 2002 The regulatory basis of melanogenic switching *J. Theor. Biol.* **215** 449–68
- [16] Raghunath A, Sambarey A, Sharma N, Mahadevan U and Chandra N 2015 A molecular systems approach to modelling human skin pigmentation: identifying underlying pathways and critical components *BMC Res. Notes* **8** 170
- [17] Subramanian I, Singh V K and Jere A 2018 Elucidating mechanistic insights into drug action for atopic dermatitis: a systems biology approach *BMC Dermatol.* **18** 3
- [18] Denning M F, Wang Y, Tibudan S, Alkan S, Nickoloff B J and Qin J-Z 2002 Caspase activation and disruption of mitochondrial membrane potential during UV radiation-induced apoptosis of human keratinocytes requires activation of protein kinase C *Cell Death Differ.* **9** 40–52
- [19] Sitailo L A, Tibudan S S and Denning M F 2002 Activation of caspase-9 is required for UV-induced apoptosis of human keratinocytes *J. Biol. Chem.* **277** 19346–52
- [20] Matsumura M, Tanaka N, Kuroki T, Ichihashi M and Ohba M 2003 The η isoform of protein kinase C inhibits UV-induced activation of caspase-3 in normal human keratinocytes *Biochem. Biophys. Res. Commun.* **303** 350–6
- [21] Alvarado-Kristensson M, Melander F, Leandersson K, Rönnstrand L, Wernstedt C and Andersson T 2004 p38-MAPK signals survival by phosphorylation of caspase-8 and caspase-3 in human neutrophils *J. Exp. Med.* **199** 449–58
- [22] Wu Y, Feinstein S I, Manevich Y, Chowdhury I, Pak J H, Kazi A, Dodia C, Speicher D W and Fisher A B 2009 Mitogen-activated protein kinase-mediated phosphorylation of peroxiredoxin 6 regulates its phospholipase A2 activity *Biochem. J.* **419** 669–79
- [23] Berthon A S, Szarek E and Stratakis C A 2015 PRKACA: the catalytic subunit of protein kinase A and adrenocortical tumors *Front. Cell Dev. Biol.* **3** 00026
- [24] D'Mello S A N, Finlay G J, Baguley B C and Askarian-Amiri M E 2016 Signaling pathways in melanogenesis *Int. J. Mol. Sci.* **17** 1144
- [25] Pugazhenthis S, Nesterova A, Sable C, Heidenreich K A, Boxer L M, Heasley L E and Reusch J E-B 2000 Akt/protein kinase B up-regulates Bcl-2 expression through cAMP-response element-binding protein *J. Biol. Chem.* **275** 10761–6
- [26] She Q-B, Ma W-Y, Zhong S and Dong Z 2002 Activation of JNK1, RSK2, and MSK1 is involved in serine 112 phosphorylation of Bad by ultraviolet B radiation *J. Biol. Chem.* **277** 24039–48
- [27] Zhang X, Yan G, Ji J, Wu J, Sun X, Shen J, Jiang H and Wang H 2012 PDE5 inhibitor promotes melanin synthesis through the PKG pathway in B16 melanoma cells *J. Cell. Biochem.* **113** 2738–43
- [28] Ebanks J, Wickett R and Boissy R 2009 Mechanisms regulating skin pigmentation: the rise and fall of complexion coloration *Int. J. Mol. Sci.* **10** 4066–87
- [29] Dnyane P A, Puntambekar S S and Gadgil C J 2017 Method for identification of sensitive nodes in Boolean models of biological networks *IET Syst. Biol.* **12** 1–6
- [30] Tadokoro T, Yamaguchi Y, Batzer J, Coelheo S G, Zmudzka B Z, Miller S A, Wolber R, Beer J Z and Hearing V J 2005 Mechanisms of skin tanning in different racial/ethnic groups in response to ultraviolet radiation *J. Invest. Dermatol.* **124** 1326–32
- [31] Gillardon F, Eschenfelder C, Uhlmann E, Hartschuh W and Zimmermann M 1994 Differential regulation of c-fos, fosB, c-jun, junB, bcl-2 and bax expression in rat skin following single or chronic ultraviolet irradiation and *in vivo* modulation by antisense oligodeoxynucleotide superfusion *Oncogene* **9** 3219–25
- [32] Scott G A and Cassidy L 1998 Rac1 mediates dendrite formation in response to melanocyte stimulating hormone and ultraviolet light in a murine melanoma model *J. Invest. Dermatol.* **111** 243–50
- [33] Bessou S, Surlève-Bazeille J-E, Sorbier E and Taïeb A 1995 *Ex vivo* reconstruction of the epidermis with melanocytes and the influence of UVB *Pigm. Cell Res.* **8** 241–9
- [34] Bivik C A, Larsson P K, Kågedal K M, Rosdahl I K and Öllinger K M 2006 UVA/B-induced apoptosis in human melanocytes involves translocation of cathepsins and Bcl-2 family members *J. Invest. Dermatol.* **126** 1119–27
- [35] St-Germain M-E, Gagnon V, Parent S and Asselin E 2004 Regulation of COX-2 protein expression by Akt in

- endometrial cancer cells is mediated through NF- κ B/I κ B pathway *Mol. Cancer* **3** 7
- [36] Chou T-H, Ding H-Y, Lin R-J, Liang J-Y and Liang C-H 2010 Inhibition of melanogenesis and oxidation by protocatechuic acid from *origanum vulgare*(oregano) *J. Nat. Prod.* **73** 1767–74
- [37] Paterson E K, Ho H, Kapadia R and Ganesan A K 2013 9-cisretinoic acid is the ALDH1A1 product that stimulates melanogenesis *Exp. Dermatol.* **22** 202–9
- [38] Huang H-C, Chiu S-H and Chang T-M 2011 Inhibitory effect of [6]-Gingerol on melanogenesis in B16F10 melanoma cells and a possible mechanism of action *Biosci. Biotechnol. Biochem.* **75** 1067–72
- [39] Adams S, Pankow S, Werner S and Munz B 2007 Regulation of NF- κ B activity and keratinocyte differentiation by the RIP4 protein: implications for cutaneous wound repair *J. Invest. Dermatol.* **127** 538–44
- [40] Imokawa G and Ishida K 2014 Inhibitors of intracellular signaling pathways that lead to stimulated epidermal pigmentation: perspective of anti-pigmenting agents *Int. J. Mol. Sci.* **15** 8293–315
- [41] Hemesath T J, Price E R, Takemoto C, Badalian T and Fisher D E 1998 MAP kinase links the transcription factor microphthalmia to c-Kit signalling in melanocytes *Nature* **391** 298–301
- [42] Rönstrand L 2004 Signal transduction via the stem cell factor receptor/c-Kit *Cell. Mol. Life Sci.* **61** 2535–348
- [43] Buscà R, Abbe P, Mantoux F, Aberdam E, Peyssonnaud C, Eychène A, Ortonne J P and Ballotti R 2000 Ras mediates the cAMP-dependent activation of extracellular signal-regulated kinases (ERKs) in melanocytes *EMBO J.* **19** 2900–10
- [44] Fang D and Au V 1999 Role of microphthalmia transcription factor in regulation of melanocyte differentiation marker TRP-1 *Biochem. Biophys. Res. Commun.* **256** 657–63
- [45] Simon J D, Peles D, Wakamatsu K and Ito S 2009 Current challenges in understanding melanogenesis: bridging chemistry, biological control, morphology, and function *Pigm. Cell Melanoma Res.* **22** 563–79
- [46] Chakraborty A, Slominski A, Ermak G, Hwang J and Pawelek J 1995 Ultraviolet B and melanocyte-stimulating hormone (MSH) stimulate mRNA production for α MSH receptors and proopiomelanocortin-derived peptides in mouse melanoma cells and transformed keratinocytes *J. Invest. Dermatol.* **105** 655–9
- [47] Park S-H, Kim D-S, Kim W-G, Ryoo I-J, Lee D-H, Huh C-H, Youn S-W, Yoo I-D and Park K-C 2004 Terrein: a new melanogenesis inhibitor and its mechanism *CMLS Cell. Mol. Life Sci.* **61** 2878–85
- [48] Chung S-Y, Seo Y-K, Park J-M, Seo M-J, Park J-K, Kim J-W and Park C-S 2009 Fermented rice bran downregulates MITF expression and leads to inhibition of α -MSH-induced melanogenesis in B16F1 melanoma *Biosci. Biotechnol. Biochem.* **73** 1704–10
- [49] Lehraiki A *et al* 2014 Inhibition of melanogenesis by the antidiabetic metformin *J. Invest. Dermatol.* **134** 2589–97
- [50] Kim A, Yang Y, Lee M-S, Yoo Y D, Lee H G and Lim J-S 2008 NDRG2 gene expression in B16F10 melanoma cells restrains melanogenesis via inhibition of Mitf expression *Pigm. Cell Melanoma Res.* **21** 653–64
- [51] Fullard N *et al* 2013 The c-rel subunit of NF- κ B regulates epidermal homeostasis and promotes skin fibrosis in mice *Am. J. Pathol.* **182** 2109–20
- [52] Wei C-L *et al* 2006 A global map of p53 transcription-factor binding sites in the human genome *Cell* **124** 207–19
- [53] Li L, Sampat K, Hu N, Zakari J and Yuspa S H 2006 Protein kinase C negatively regulates Akt activity and modifies UVC-induced apoptosis in mouse keratinocytes *J. Biol. Chem.* **281** 3237–43

Method for identification of sensitive nodes in Boolean models of biological networks

ISSN 1751-8849

Received on 27th July 2017

Accepted on 16th August 2017

E-First on 30th October 2017

doi: 10.1049/iet-syb.2017.0039

www.ietdl.org

Pooja A. Dnyane¹, Shraddha S. Puntambekar^{1,2}, Chetan J. Gadgil^{1,2,3} ✉

¹Chemical Engineering and Process Development Division, CSIR-National Chemical Laboratory, Dr. Homi Bhabha Road, Pune 411 008, India

²Academy of Scientific and Innovative Research (AcSIR), CSIR-National Chemical Laboratory Campus, Pune 411 008, India

³CSIR-Institute of Genomics and Integrative Biology, New Delhi 110 020, India

✉ E-mail: cj.gadgil@ncl.res.in

Abstract: Biological systems are often represented as Boolean networks and analysed to identify sensitive nodes which on perturbation disproportionately change a predefined output. There exist different kinds of perturbation methods: perturbation of function, perturbation of state and perturbation in update scheme. Nodes may have defects in interpretation of the inputs from other nodes and calculation of the node output. To simulate these defects and systematically assess their effect on the system output, two new function perturbations, referred to as 'not of function' and 'function of not', are introduced. In the former, the inputs are assumed to be correctly interpreted but the output of the update rule is perturbed; and in the latter, each input is perturbed but the correct update rule is applied. These and previously used perturbation methods were applied to two existing Boolean models, namely the human melanogenesis signalling network and the fly segment polarity network. Through mathematical simulations, it was found that these methods successfully identified nodes earlier found to be sensitive using other methods, and were also able to identify sensitive nodes which were previously unreported.

1 Introduction

Biological pathways are often represented as networks, the nodes being the biomolecules and edges being the connections. Dynamic models can explain how abundances of biomolecules change over time due to their interactions. Dynamic modelling approaches can be continuous or discrete. In continuous dynamic modelling, the number of nodes and reactions is limited by sparse data leading to limited identifiability of kinetic parameters [1–3]. Boolean modelling is the simplest type of discrete dynamic modelling with abundances represented by 0 (absent/low) and 1 (present/high). It does not require knowledge about the kinetic details of the interactions. The only information needed is the logic of regulatory interactions such as the activating or inhibitory nature of genetic regulations. In a Boolean network, which is a rule-based binary network, the interaction between nodes is represented using logic rules. Synchronous or asynchronous updating is used to update node states and hence simulate the system dynamics from a given set of initial node states [4]. Boolean networks with a varying number of nodes from <10 [5] to approximately 100 [6, 7] have been used to investigate biological systems.

It is often of interest to identify sensitive nodes in a regulatory network that when perturbed lead to a significant change in the network output. For instance, in models for signalling or metabolic pathways in pathogens, nodes that disproportionately affect survival are potential drug targets. The same motivation exists for identifying sensitive nodes in cancer cell pathways. The robustness (or otherwise) of a signalling network can be assessed from identification and analysis of all sensitive nodes. To estimate sensitivity, a perturbation is applied to every node or edge, and the effect on a set of node states predefined as the system output is calculated.

Previous studies on robustness of Boolean networks have used perturbation methods that can be classified in three broad classes: state perturbations, function perturbations and update rule perturbations. A vast majority of studies use state perturbation to explain system properties including node sensitivity. Shmulevich *et al.* [8] explored the effect of random gene state perturbation on entire network, i.e. any gene can flip its value for only one-time point from 0 to 1 or vice versa with probability p . Lee *et al.* [9] performed node control analysis (constitutive state perturbation) to

identify an effective target to reduce skin pigmentation. In this method, the state value of each internal regulatory node is fixed at either '0' for inhibition or '1' for constitutive activation and then the steady-state activity of output nodes is measured. Fauré *et al.* [10] simulated the effect of loss of function and gain of function mutation in mammalian cell cycle by constraining selected node within specific value intervals. Subramanian and Gadgil [11] showed that transient state perturbation in *Drosophila melanogaster* segment polarity network leads to an ectopic expression pattern. Saadatpour *et al.* [12] introduced dynamic perturbation that entails setting the node's status opposite to the existing state (diseased state) and normally updating other nodes.

Function perturbations change the normal truth table for a node or set of nodes. Function perturbations have also been used to estimate sensitivity. Garg *et al.* [13] assume that one gene (or one function) can have a fault at a given time. At a different time in the same trajectory, another gene (or function) can be faulty. The node faults [stochasticity in nodes (SINs)] are interpreted as a change of the current state at that time; moreover, the function faults [stochasticity in function (SIF)] are interpreted as using a different truth table at that time point. They find that the SIN approach predicts biologically implausible behaviour, whereas the SIF approach predicts more biologically relevant robustness. Qian and Dougherty [14] take into account 1 bit function perturbation which entails flipping the value of a single row in the truth table of a probabilistic Boolean model. Another study by the same authors used a similar approach along with the change in probabilistic parameter, i.e. change in the probability of selecting each constitutive Boolean network in the probabilistic Boolean model and changing the perturbation probabilities [15].

Change in updating scheme as a means of assessing robustness has been used by a few researchers. Chaves *et al.* [16] considered the effect of a perturbation in synchronous update scheme on the dynamics of the model for the *D. melanogaster* segment polarity genes. Perturbation in the time scales or using different kinds of updating schemes in combination with knockout strategies or state perturbation is also an effective way to identify sensitive nodes [10, 16–18]. Other studies demonstrate different kinds of perturbations not easily classifiable into these three categories. Structural perturbation strategies have been developed [12, 19] to identify essential nodes in a static network whose disruption can reverse the

abnormal state of the signalling network. Here, topological intervention involves ranking of the nodes by the effects of their loss (knockout) on the connectivity between the network's inputs and outputs. There are also many reports studying the effect of function perturbation on an ensemble of Boolean networks but not on a specific Boolean network [20, 21].

Here, we introduce two new function perturbation methods and use them to identify sensitive nodes in two specific networks. Our methods are general and applicable to any individual Boolean model or probabilistic Boolean model. These perturbations were applied to the existing melanogenesis signalling network [9] and *D. melanogaster* segment polarity network [22]. Mathematical simulations revealed that for melanogenesis network, nodes identified as sensitive by the new function perturbation methods are in agreement with state perturbation. Similarly, for *D. melanogaster* segment polarity network, results of gene mutation performed by Albert and Othmer [22] and transient state perturbation [11] coincide with the results of function perturbation. The nodes identified by each method individually as sensitive nodes are elements of the union of the set of sensitive nodes identified through constitutive activation and constitutive inhibition perturbations. In addition, the new methods identify new nodes as sensitive. We discuss the experimental support for the sensitivity of the newly identified nodes.

2 Materials and methods

2.1 Simulation of existing Boolean models

2.1.1 Melanogenesis signalling network: The melanogenesis network constructed by Lee *et al.* [9] contains two main modules – the keratinocyte and the melanocyte. There are a total of 62 nodes and 113 links (80 activating and 33 inhibiting links). Of the 62 nodes, there is one external input node [ultraviolet B (UVB) radiation]. The objective was to identify safe and effective targets in the network for reduction of pigmentation as measured by the state of the output nodes. To this end, constitutive activation and constitutive inhibition of each node was simulated by setting the node state to 1 and 0, respectively. The UV input was varied from 0% (always off) to 100% (always on). A ‘wild-type (WT)’ profile of the average state of each node at each UV level was obtained in the absence of any perturbation. Sensitivity of each node was estimated by calculating the post-perturbation change in the profile of the three output nodes: B-cell chronic lymphocytic leukemia/lymphoma 2 (Bcl2) in keratinocyte (Bcl2K), Bcl2 in melanocyte (Bcl2M) and melanin. Nodes whose constitutive activation or inhibition results in a significant reduction in the melanin node activity without significantly affecting Bcl2 activity are reported as potential targets in this paper.

We look at node-wise sensitivity for each of the three output nodes identified in this paper, and identify nodes whose constitutive activation/repression has a significant effect on each of the three output node profiles, as quantified by the magnitude of the (negative) correlation coefficient between the WT and perturbed profile or the Euclidean distance between the two profiles. The set of nodes thus identified includes the nodes identified by Lee *et al.* [9] as depigmentation targets. Next, we apply each of the new function perturbation methods to the network, keeping other simulation parameters constant; and assess the overlap between the nodes identified as sensitive by the new methods, and those identified as sensitive using constitutive activation/inhibition perturbations. Simulations were carried out using the network and rules reported in [9]. The intensities of input node UVBs were set to 0, 25, 50, 75 and 100% through a random (non-cyclic) input with the corresponding probability of being ON. Average of node state values was calculated for each UV level as an average of the last 100 of 1000 time steps for each of 100 random initial conditions. We verified that the results are robust to change in the simulation parameters.

2.1.2 Segment polarity network: The *D. melanogaster* segment polarity gene expression is defined and maintained through spatiotemporal interactions between gene products including secreted proteins, receptors and transcription factors expressed by

cells in a parasegment. A continuous state model was developed by von Dassow who concluded that the patterning was robust to the choice of reaction rate constants [23]. This idea was taken to its logical limit by Albert and Othmer [22] who developed a Boolean model of the regulatory network, thereby obviating the need for any rate parameter. Their model [22] represents 14 cells spread across four parasegments. The first and last parasegments consists of three cells, whereas the second and third parasegments consist of four cells. Each cell has 15 nodes, of which one (SLP) is treated as an input. A parasegment thus has 56 nodes.

Simulations were carried out using Boolean updating rules, initial conditions and parameters specified by Albert and Othmer [22]. Simulations were carried out till attractor state was attained. The simulations were repeated for perturbations, where individual nodes were subjected to constitutive activation/inhibition. Simulations were also carried out after applying each of the two new perturbations introduced here. The node was identified as sensitive if the system steady state on perturbation was either a qualitatively different attractor (i.e. not a point attractor) or the node states differed by 20% from the WT.

All Boolean model simulations were carried out using MATLAB 2015b.

3 Results

First, we describe the two new function perturbation methods to identify sensitive nodes, followed by application of these methods on two existing Boolean networks.

3.1 Two new function perturbation methods

Each node j in the network is associated with variable $x_j(t)$ which describes its expression level at time t . In Boolean models with synchronous updating, the future state of node j , denoted by $x_j(t+1)$, is defined by a logic rule involving the current states of its regulators (inputs), i.e. $x_j(t+1) = F_j[\underline{x}(t)]$, where F_j is a Boolean rule and \underline{x} represents the vector of all node states.

Biological processes occur in an inherently noisy environment. Here, we simulate the effect of two permanent defects in the regulatory network. Defects in nodes due to misinterpretation of one or more input signals or miscalculation of the output even when the inputs are received correctly are captured by the function of not (FoN) and not of function (NoF) perturbations (Fig. 1a). Biological regulatory networks have been compared with electrical circuits. Nodes are components of a digital circuit that read inputs and emit an output depending on the input. The NoF perturbation simulates a defective node that reads inputs correctly but gives the incorrect output. For example, consider a node where binding of two components results in activation (Fig. 1b). In a malfunctioning node with an NoF perturbation, deactivation of the otherwise active node would result from the presence of the two inputs. The FoN perturbation simulates a situation, where the node logic is functioning properly (activation when there are two non-zero inputs) but there is an error in reading the inputs such that the presence of either component is misinterpreted as absence. This results in a node that is active only when both inputs are absent. These perturbations are incorporated by flipping the output of the function (NoF) or by flipping all the inputs to the function (FoN). Fig. 1c illustrates the two new function perturbation methods of flipping the output (FoN) and misreading the inputs (NoF).

The effect of perturbing the nodes on the output is compared with the output when there is no perturbation (WT) by using similarity measures such as correlation coefficient and Euclidean distance. Correlation and distance between the WT and the perturbed network are calculated for the steady-state values/pattern of output, before and after applying the function perturbation using equations

$$R_{i,j}^k = \text{correlation}(\underline{S}_{i,j}^k, \underline{S}_i^0)$$

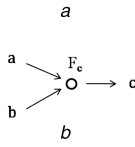
$$D_{i,j}^k = \text{distance}(\underline{S}_{i,j}^k, \underline{S}_i^0)$$

$$\text{Avg}D_{i,j}^k = \text{distance}(\underline{S}_{i,j}^k, \underline{S}_i^0)/n$$

$$x_j^0(t+1) = F_j(\mathbf{x}(t)) \begin{cases} x_j^1(t+1) = \overline{F_j(\mathbf{x}(t))} \rightarrow \text{NoF} \\ x_j^2(t+1) = F_j(\overline{\mathbf{x}(t)}) \rightarrow \text{FoN} \end{cases}$$

Original rule

Perturbed rule



c

$a(t)$	$b(t)$	$c^0(t+1)$	$c^1(t+1)$
0	0	0	1
1	0	0	1
0	1	0	1
1	1	1	0

$c^0(t+1) = F_c([a(t), b(t)])$

$c^1(t+1) = \overline{F_c([a(t), b(t)])}$ (NoF)

$a(t)$	$b(t)$	$\overline{a(t)}$	$\overline{b(t)}$	$c^2(t+1)$
0	0	1	1	1
1	0	0	1	0
0	1	1	0	0
1	1	0	0	0

$c^2(t+1) = F_c([\overline{a(t)}, \overline{b(t)}])$ (FoN)

Fig. 1 Methods of function perturbation with an example

(a) Equations for FoN and NoF, (b) Example model, (c) Both a and b are required to activate c but ‘NoF’ perturbation (c^1) will result in inhibition of c , i.e. not of output. Similarly, with ‘FoN’ perturbation (c^2) only inputs are flipped

where nature of perturbation $k \in \{0, 1, 2\}$, $i \in \{\text{output nodes}\}$ and $j \in \{\text{all nodes}\}$. R is the correlation coefficient, D is Euclidean distance and $AvgD$ is average distance across all the n levels of UV or in general over the length of the vector \underline{S}_i^0 . \underline{S}_i^k is a vector representing steady-state activity of output node i for all levels of UVB input when node j is subjected to a perturbation of type k , where $k = 0, 1, 2$ represents no perturbation (WT), NoF perturbation and FoN perturbation, respectively. \underline{S}_i^0 denotes steady-state activity of output node i for WT condition ($k = 0$) for all levels of inputs. We apply these perturbations to two existing Boolean models. The identified sensitive nodes were then compared with those given in previous studies for constitutive state perturbation.

3.2 Effect of function perturbations in melanogenesis network

Effect of function perturbations in melanogenesis network is calculated by measuring a change in the activity profile of the output nodes melanin, Bcl2M and Bcl2K relative to the respective unperturbed output profiles, for the inputs of 0, 25, 50, 75 and 100% UVB. Change in the activity profile of the output is calculated using the measures described previously. The nodes having either the top five Euclidean distance score or correlation coefficient value ≤ -0.8 were selected as sensitive (Table 1). Sensitive nodes with correlation coefficient ≤ -0.8 are depicted in Fig. 2. We also performed constitutive activation and inhibition perturbations of each node in the network, as described in [9], and checked its effect on the outputs using similar measures. When function perturbation is applied to the sensitive nodes, it resulted in a Euclidean distance score of 126–180 for melanin. This is equivalent to $AvgD \geq 25$. Similarly, for Bcl2M and Bcl2K the $AvgD$ score was in the range of 21–24 and 20–30, respectively. $AvgD$ values for constitutive activation and inhibition falls in the range of 30–36 and 7–9 for melanin, 30–32 and 12–20 for Bcl2M and 22–33 and 14–22 for Bcl2K. The comparison showed that most of the nodes identified as sensitive by function perturbations are in agreement with the results of state perturbation analysis but with a few exceptions (non-underlined nodes in Table 1). There are literature reports suggesting the importance of these nodes. For instance, an experimental study by Jost *et al.* [24] showed that inhibition of MAPK/ERK kinase (MEK) enzymatic activity in keratinocyte is associated with down-regulation of Bcl-2 expression and increased susceptibility to cell death induction. There is also literature evidence for nodes identified as sensitive by both the new methods as well as constitutive activation/inhibition perturbations. For instance, activation of cAMP response element-binding protein (CREB) is known to activate the microphthalmia-

associated transcription factor (MITF) promoter that promotes melanogenesis [25].

3.3 Effect of function perturbations in *D. melanogaster* segment polarity network

To identify sensitive nodes in segment polarity network, Boolean function was perturbed for each node in all the cells in all parasegments. It is observed that, for a few nodes, when the logic function was perturbed, the system tends to approach a cyclic attractor. This condition highly differs from WT pattern, where system approaches a point attractor. Therefore, such nodes were classified as sensitive (Table 2). For others (node perturbations resulting in point attractors), the Euclidean distance was calculated and if the distance was >3.35 , then the node was assigned as sensitive. This is equivalent to the condition that expression value for at least 20% nodes (11 out of 56) should be changed when a particular node is perturbed. Constitutive inhibition analysis performed previously has shown that null mutation of selected genes in segment polarity network result in alternate steady-state patterns such as ‘no segmentation pattern’ and ‘broad stripes pattern’ [22]. Similarly, critical and benign nodes identified by transient perturbation are those in which a perturbation leads to the ‘broad stripes pattern’ or alternate steady state [11]. We were successfully able to identify most of the nodes previously identified as sensitive using the new function perturbation methods. There are also a few exceptions where nodes identified as sensitive previously are not identified as such by FoN or NoF perturbations; and new nodes are identified as sensitive (Table 2). Our analysis indicates that patterning is sensitive to perturbation of *Cubitus interruptus*. This is in contrast to the results of Albert and Othmer. Interestingly, the experimental literature also seems to be divided, with one report suggesting that there is no requirement for cubitus interruptus (CI) before embryonic stage 11 [26] as well as another suggesting that there is an ‘absolute requirement’ for CI in hedgehog signalling [27]. It seems likely that the node sensitivity changes under different conditions, thus supporting the use of multiple perturbation methods to assess sensitivity.

4 Conclusion

We developed two new methods of dynamic function perturbation, namely FoN and NoF and applied it to two existing Boolean models – melanogenesis signalling network and segment polarity network. To our knowledge the perturbation methods closest to FoN and NoF are the SIF and SIN derived by Garg *et al.* However, there are critical differences. As implemented, NoF results in a change of state of the output node; moreover, it is equivalent to SIN for a given updating time when that node has a defect. In the NoF approach, there is a ‘permanent’ defect that persists through the simulation, whereas in SIN, different nodes may be defective at different times during a single simulation instance. We also find that predictions using NoF are consistent with other perturbation studies in contrast to the ‘implausible’ results obtained using SIN [13]. SIF perturbations assume that defects only arise in active nodes, and use as an example the unlikelyness of transcription without activation. However, leaky transcription is known to occur, and switch – on defects are possible. We include both switch-on and switch-off defects in our FoN perturbation. Conceptually, we regard such a perturbation as a defect in interpreting all the input signals. An interesting follow-up study would be to consider a defect in interpreting one input of a multi-input node. However, this would complicate the comparison between nodes with differing number of inputs. We have applied each of the two perturbations on two models of differing size and complexity (the segment polarity network with 13 nodes each in 4 cells and the melanogenesis network with 64 nodes in two cell types). We found that as both methods do not require addition of additional inputs to nodes but just involve changing the existing truth tables, implementation was not difficult. We have also verified that it is possible to use these methods to perturb a larger network (~ 100 nodes, results not shown). We have analysed the perturbed networks solely from the perspective of identification of sensitive nodes. The effect of small perturbations on attractor states and

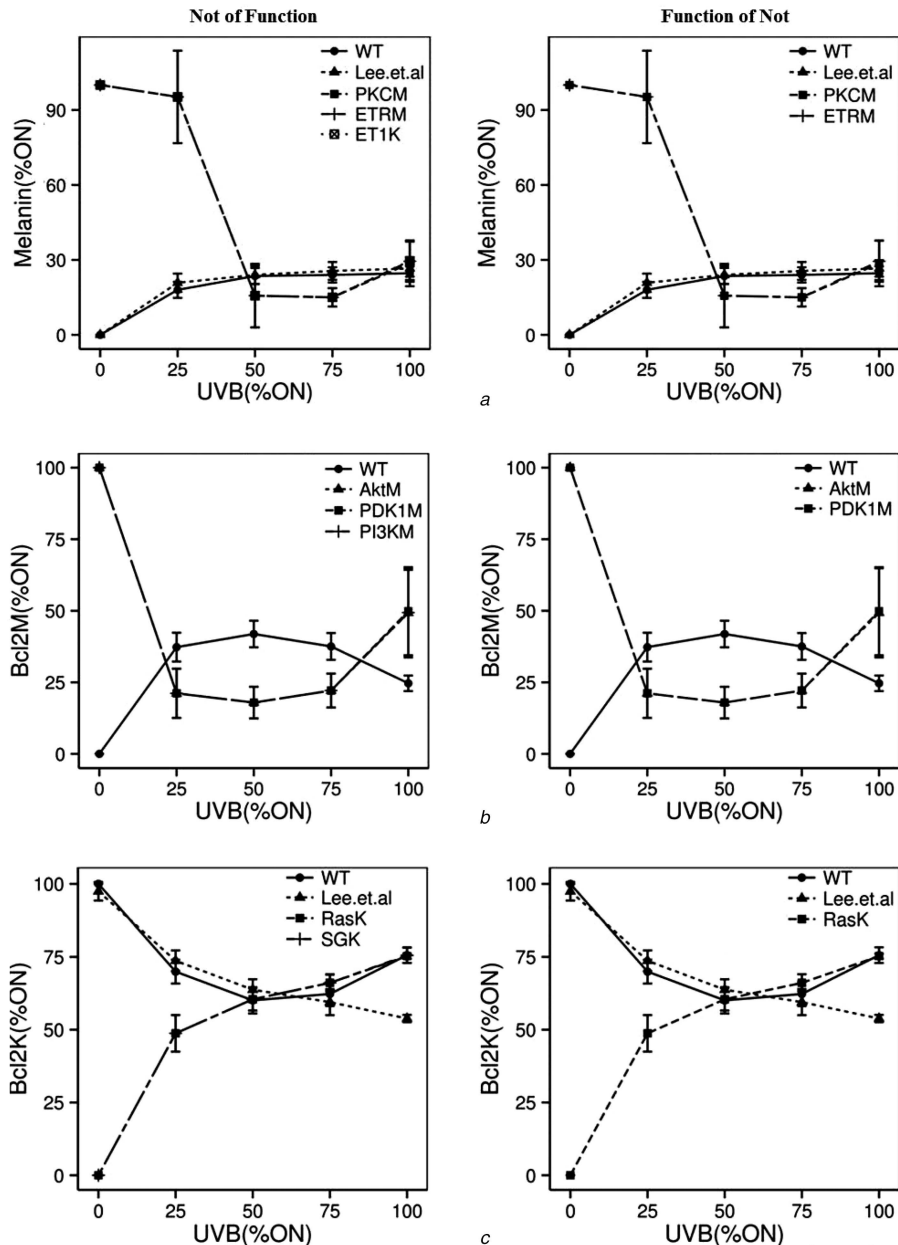


Fig. 2 Effect of function perturbation (left column – NoF and right column – FoN) of selected nodes on UVB-induced skin pigmentation and Bcl-2 expressions. Each data point represents average steady-state activity of output node at 0, 25, 50, 75 and 100% of UVB. Error bar represents standard deviation. Steady-state value of WT and Lee *et al.* WT (values of WT outputs mentioned in [9]) fall under each other's standard deviation

(a) Positive relationship between UVB and melanin synthesis (WT) is seen for $k=0$. A negative relationship is observed when function perturbations are applied to certain nodes, implying a large average distance and negative correlation. Effect of perturbing PKCM, ETRM and ET1K on melanin are quantitatively identical, (b) Nodes that greatly affect WT activity of Bcl2M on 'NoF' perturbations. Lee *et al.* WT values are not available for Bcl2M, (c) A negative relation between UVB and Bcl2K activations. Perturbation in the growth factor receptor-bound protein 2 (Grb2) and Son of Sevenless (SOS) complex (SG) and GTPase (Ras) in keratinocytes results in a quantitatively overlapping positive relationship

Table 1 Sensitive nodes in the melanogenesis signalling network

	Constitutive activation	Inhibition	NoF	FoN
melanin	<u>MITFproteinM</u> , PKCM, RasM, ET1K, ETRM, SGM, IL1K	ERKM, AktM, PI3KM, RafM, PDK1M, MEKM, MITFproteinM, bcateninM, CREBM, IL1K, ASK1M, MITFmRNAM, p38M, MKK6M	<u>MITFproteinM</u> , SGM, IL1K, RasM, ET1K, ETRM, PKCM	RasM, ET1K, MITFproteinM, ETRM, PKCM
Bcl2M	AktM, PI3KM, PDK1M, PKCM, ET1K, ETRM, RasM, SGM, IL1K	ASK1M, p38M, MKK6M, AktM, PI3KM, PDK1M, CREBM	SGM, IL1K, AktM, RasM, ET1K, ETRM, PDK1M, PI3KM	RasM, ET1K, ETRM, PKCM, PDK1M, AktM
Bcl2K	ASK1K, MKK6K, p38K, MKK4K, JNKK, p53K, RasK, ERKK, RafK, SGK	PDK1K, PI3KK, EGFRK, AktK, ASK1K	MKK6K, p38K, ASK1K, JNKK, MKK4K, RasK, SGK	MKK6K, p38K, JNKK, MEKK, RasK

The table lists nodes which highly influence melanin, Bcl2M and Bcl2K activities when perturbed with constitutive activation, inhibition, NoF and FoN. Shown are the nodes with the top five Euclidean distance score and correlation coefficient value ≤ -0.8 for each method of perturbation. Underlined nodes are identified as sensitive both by at least one method of function perturbation and one of constitutive activation/inhibition.

Table 2 Sensitive nodes in the *D. melanogaster* segment polarity network

	NoF	FoN	Transient perturbation	Gene mutation (knockout)
nodes with cyclic attractor	<u>en(1), en(2), EN(1), EN(2), wg(2),</u> <u>wg(3), wg(4), WG(3), WG(4), PTC(1),</u> <u>hh(1), hh(2), HH(1), SMO(4)</u>	<u>EN(1), EN(2), wg(3),</u> <u>wg(4), WG(3), WG(4),</u> <u>hh(1), HH(1)</u>	<u>wg(1), wg(3), wg(2),</u> <u>WG(1), WG(3), en(2),</u> <u>en(4), EN(2), EN(4), hh(2),</u> <u>hh(4), HH(2), HH(4), ptc(1),</u> <u>PTC(1), PTC(3), SMO(3)</u>	<u>wg(1), wg(2), wg(3), wg(4),</u> <u>en(1), en(2), en(3), en(4),</u> <u>hh(1), hh(2), hh(3),</u> <u>hh(4), ptc(1), ptc(2), ptc(3),</u> <u>ptc(4)</u>
nodes with point attractor	<u>en(4), EN(4), wg(1), WG(1), PTC(3),</u> <u>CI(1), hh(4), HH(2), HH(4), CIR(1),</u> <u>CIR(4), SMO(3)</u>	<u>en(1), en(4), EN(4),</u> <u>WG(1), PTC(3), CI(1),</u> <u>HH(2), HH(4), SMO(3)</u>		

Comparison of nodes identified as sensitive using 'NoF', 'FoN' with those identified as critical nodes by performing transient perturbation and gene mutation. Numbers in parenthesis indicate the cell to which they belong (1–4) with respect to the parasegment. Underlined nodes are identified as sensitive both by one of the methods of function perturbation and one of transient perturbation/gene mutation.

trajectories can lead to better insights about the stability of the phenotype [28]. Further analysis of the effects of such perturbations on the attractors and their basins of attraction would be desirable but very challenging for large networks even of the order of magnitude of the melanogenesis network. Larger Boolean networks [6, 7] have been used to analyse signalling pathways and cancer pathways. However, analysis of the attractor states of the large unperturbed networks is itself challenging, especially for networks with asynchronous updating [29]. Although methods [30, 31] for identifying attractors for large networks such as the cancer pathways network have been presented, we have focused on identification of node sensitivity and not carried out an analysis of the state space of the perturbed networks in this paper. Although we have used synchronous updating, the methods are equally applicable to asynchronous updating since they both involve a time-invariant change to the truth table. The updating order and frequency for a particular asynchronous updating scheme can be applied to the modified truth table corresponding to NoF and FoN perturbations.

To examine the ability of FoN and NoF perturbations to identify sensitive nodes in the network, we compared the results obtained by our methods with those of existing ones. Sensitivity is expected to be a function of the nature of the perturbation applied to the network. However, in the case of melanogenesis, a few nodes were robustly identified as sensitive irrespective of perturbation method applied to them, e.g. melanin activity was found to be sensitive to MITFproteinM; moreover, PDK1M and AktM were found to be critical for maintaining Bcl2M level. FoN perturbation results in identification of MEKK as a sensitive node, important for Bcl2K activity, consistent with a reported experimental result. In the case of segment polarity network, we assigned nodes as 'sensitive' if perturbation in them results in variation from WT pattern. We were able to identify few new nodes which are important in maintaining WT steady-state pattern, e.g. imbalance between cubitus interruptus transcriptional activator (CIA) and cubitus interruptus transcriptional repressor (CIR) in posterior cells of parasegment leads to the mutant state [16]. We were able to identify CI as a sensitive node, which is in agreement with some (but not other) experimental reports. As contradictory reports are likely to indicate that the sensitivity differs depending on the experimental condition tested, such data suggests that multiple perturbation methods may capture differing biological situations, and hence a comprehensive determination of node sensitivity may require different perturbation methods to be applied to the network.

Most of the nodes identified as sensitive by our methods are also identified as such by constitutive activation/inhibition. This suggests that our method is more stringent than constitutive activation/repression; and relaxing the Euclidean distance cut-off criteria would result in identification of more sensitive nodes (inclusion of non-underlined nodes in Tables 1 and 2). There is no theoretical result to our knowledge suggesting an optimal perturbation method. Indeed, a variety of stochastic perturbations resulting from intrinsic and external sources are encountered by individual cells and developing organisms. Hence, depending on the question sought to be answered, either a specific perturbation corresponding to a specific experiment (for instance gene knockout) is applied to assess the effect on the network output or a suite of perturbation methods is applied to study node and network

robustness. In this paper, we have presented two methods that we believe would be useful additions to this suite of perturbation methods for Boolean networks. These methods result in further support for the nodes previously identified as sensitive by other perturbation methods. However, more interestingly, they also lead to the identification of sensitive nodes not identified as such by existing perturbation methods assessed here. This suggests that these new methods query system dynamics and response in a way differing from existing methods. Hence, these methods are expected to be a useful addition to the set of perturbations used to assess node and network sensitivities.

5 Acknowledgments

PD and CG acknowledge funding from CSIR (BSC0302). SP acknowledges support from DBT-BINC (Senior Research Fellowship).

6 References

- Glass, L., Kauffman, S.A.: 'The logical analysis of continuous, non-linear biochemical control networks', *J. Theor. Biol.*, 1973, **39**, pp. 103–129
- Karlebach, G., Shamir, R.: 'Modelling and analysis of gene regulatory networks', *Nat. Rev. Mol. Cell Biol.*, 2008, **9**, pp. 770–780
- Thomas, R.: 'Boolean formalization of genetic control circuits', *J. Theor. Biol.*, 1973, **42**, (3), pp. 563–585
- Wang, R., Saadatpour, A., Albert, R.: 'Boolean modeling in systems biology: an overview of methodology and applications', *Phys. Biol.*, 2012, **9**, pp. 055001
- Pal, R., Datta, A., Bittner, M.L., *et al.*: 'Intervention in context-sensitive probabilistic Boolean networks', *Bioinformatics*, 2005, **21**, (7), pp. 1211–1218
- Fumiã, H.F., Martins, M.L.: 'Boolean network model for cancer pathways: predicting carcinogenesis and targeted therapy outcomes', *PLoS One*, 2013, **8**, (7), p. e69008
- Ryll, A., Samaga, R., Schaper, F., *et al.*: 'Large-scale network models of Il-1 and Il-6 signalling and their hepatocellular specification', *Mol. Biosyst.*, 2011, **7**, (12), pp. 3253–3270
- Shmulevich, I., Dougherty, E.R., Zhang, W.: 'Gene perturbation and intervention in probabilistic Boolean networks', *Bioinformatics*, 2002, **18**, pp. 1319–1331
- Lee, H.-S., Goh, M.-J., Kim, J., *et al.*: 'A systems-biological study on the identification of safe and effective molecular targets for the reduction of ultraviolet B-induced skin pigmentation', *Sci. Rep.*, 2015, **5**, p. 10305
- Fauré, A., Naldi, A., Chauviya, C., *et al.*: 'Dynamical analysis of a generic Boolean model for the control of the mammalian cell cycle', *Bioinformatics*, 2006, **22**, pp. 124–131
- Subramanian, K., Gadgil, C.: 'Robustness of the Drosophila segment polarity network to transient perturbations', *IET Syst. Biol.*, 2010, **4**, pp. 169–176
- Saadatpour, A., Wang, R.-S., Liao, A., *et al.*: 'Dynamical and structural analysis of a T cell survival network identifies novel candidate therapeutic targets for large granular lymphocyte leukemia', *PLoS Comput. Biol.*, 2011, **7**, p. e1002267
- Garg, A., Mohanram, K., Di Cara, A., *et al.*: 'Modeling stochasticity and robustness in gene regulatory networks', *Bioinformatics*, 2009, **25**, pp. 101–109
- Qian, X., Dougherty, E.R.: 'Effect of function perturbation on the steady-state distribution of genetic regulatory networks: optimal structural intervention', *IEEE Trans. Signal Process.*, 2008, **56**, pp. 4966–4976
- Qian, X., Dougherty, E.R.: 'On the long-run sensitivity of probabilistic Boolean networks', *J. Theor. Biol.*, 2009, **257**, pp. 560–577
- Chaves, M., Albert, R., Sontag, E.D.: 'Robustness and fragility of Boolean models for genetic regulatory networks', *J. Theor. Biol.*, 2005, **235**, pp. 431–449
- Kwon, Y.K., Cho, K.H.: 'Quantitative analysis of robustness and fragility in biological networks based on feedback dynamics', *Bioinformatics*, 2008, **24**, pp. 987–994